DIFFUSION AND DOMAINS

DIFFUSION AND DOMAINS: MEMBRANE STRUCTURE AND DYNAMICS STUDIED BY NEUTRON SCATTERING

By

CLARE L. ARMSTRONG, M.Sc.

A Thesis
Submitted to the School of Graduate Studies
in Partial Fulfillment of the Requirements
for the Degree
Doctor of Philosophy

McMaster University

DOCTOR OF PHILOSOPHY (2013) McMaster University
(Physics) Hamilton, Ontario

TITLE: Diffusion and Domains:
Membrane Structure and Dynamics Studied by Neutron Scattering

AUTHOR: Clare L. Armstrong, M.Sc.(McMaster University)

SUPERVISOR: Dr. Maikel C. Rheinstädter

NUMBER OF PAGES: xi, 139

Abstract

Biological membranes play host to a number of processes essential for cellular function and are the most important biological interface. The structurally complex and highly dynamic nature of the membrane poses significant measurement challenges, requiring an experimental technique capable of accessing very short, nanometer length scales, and fast, micro-pico second time scales.

The experimental work presented in this thesis uses a variety of neutron scattering techniques to study the structure and dynamics of biologically relevant model membrane systems. The main body of this work can be sub-divided into two distinct topics: (1) lateral diffusion of lipid molecules in a bilayer; and (2) the measurement of domains in the membrane.

Diffusion is the fundamental mechanism for lipids and proteins to move throughout the lipid matrix of a biological membrane. Despite a strong effort to model lipid diffusion, there is still no coherent model which describes the motion of lipid molecules from less than a lipid-lipid distance to macroscopic length scales. The experiments presented on this topic attempt to extend the range over which diffusion is typically measured by neutron scattering, to initiate the development of a more complete lipid diffusion model.

Lipid domains and rafts are thought be platforms for many cellular functions; however, their small size and transient nature makes them notoriously difficult to observe. The penultimate chapter of this thesis provides evidence supporting the existence of domains in a model lipid/cholesterol system by probing of the dynamics of the system. The challenge of observing these structures directly was addressed by modifying the traditional neutron triple-axis spectrometry setup to increase its sensitivity to systems with short-range order. This technique was employed to examine the coexistence of fluid and gel domains in a single-component lipid bilayer system, as well as the presence of highly ordered lipid domains in a model membrane containing cholesterol.

Scientific Contributions

First Author Publications

- *"The Observation of Highly Ordered Domains in Membranes with Cholesterol"*

  Clare L. Armstrong, Drew Marquardt, Hannah Dies, Norbert Kučerka, Zahra Yamani, Thad A. Harroun, John Katsaras, An-Chang Shi, and Maikel C. Rheinstädter, (submitted to PLoS ONE).

- *"Incoherent Neutron Spin-Echo Spectroscopy as an Option to Study Long-Range Lipid Diffusion"*

  Clare L. Armstrong, Laura Toppozini, Hannah Dies, Antonio Faraone, Michihiro Nagao, and Maikel C. Rheinstädter, ISRN Biophysics, **2013**, 439758, 2013.

- *"Effect of cholesterol on the lateral nanoscale dynamics of fluid membranes"*

  Clare L. Armstrong, Matthew A. Barrett, Arno Hiess, Tim Salditt, John Katsaras, An-Chang Shi, and Maikel C. Rheinstädter, Eur. Biophys. J., **41**, 901-913, 2012.

- *"Co-existence of gel and fluid lipid domains in single-component phospholipid membranes"*

  Clare L. Armstrong, Matthew A. Barrett, Laura Toppozini, Norbert Kučerka, Zahra Yamani, John Katsaras, Giovanna Fragneto, and Maikel C. Rheinstädter, Soft Matter, **8**, 4687-4694, 2012.

- *"Short range ballistic motion in fluid lipid bilayers studied by quasi-elastic neutron scattering"*

  Clare L. Armstrong, Marcus Trapp, Judith Peters, Tilo Seydel, and Maikel C. Rheinstädter, Scientific Highlight, ILL Annual Report 2011, 42-43, 2011.

- *"Short range ballistic motion in fluid lipid bilayers studied by quasi-elastic neutron scattering"*

  Clare L. Armstrong, Marcus Trapp, Judith Peters, Tilo Seydel, and Maikel C. Rheinstädter, Soft Matter, **7**, 8358-8362, 2011.

- *"Protein-Protein Interactions in Membranes"*

  Clare L. Armstrong, Erik Sandqvist, and Maikel C. Rheinstädter, Protein & Peptide Letters, **18**, 344-353, 2011.

- *"Diffusion in single supported lipid bilayers studied by quasi-elastic neutron scattering"*

  Clare L. Armstrong, Martin D. Kaye, Michaela Zamponi, Eugene Mamontov, Madhusudan Tyagi, Timothy Jenkins, and Maikel C. Rheinstädter, Soft Matter, **6**, 5864-5867, 2010.

- *"Membrane Mediated Protein-Protein Interactions"*

  Clare L. Armstrong, Erik Sanqvist, Karin Schmalzl, and Maikel C. Rheinstädter, Physics in Canada, **66.3**, 189, 2010.

Additional Works

- *"The Production of Fibers and Films from Solubilized Hagfish Slime Thread Proteins"*

  Atsuko Negishi, Laurent Kreplak, **Clare L. Armstrong**, Maikel C. Rheinstädter, Loong-TakLim, Todd E. Gillis, and Douglas S. Fudge, Biomacromolecules, **13**, 3475-3482, 2012.

- *"Partitioning of ethanol into lipid membranes and its effect on fluidity and permeability as seen by X-ray and neutron scattering"*

  Laura Toppozini, **Clare L. Armstrong**, Matthew A. Barrett, Songbo Zheng, Lindy Luo, Hirsh Nanda, Victoria Garcia Sakai, and Maikel C. Rheinstädter, Soft Matter, **8**, 11839-11849, 2012.

- *"Hydration Water Freezing in Single Supported Lipid Bilayers"*

  Laura Toppozini, **Clare L. Armstrong**, Martin D. Kaye, Madhusudan Tyagi, Timothy Jenkins, and Maikel C. Rheinstädter, ISRN Biophysics, **2012**, 520307, 2012.

Acknowledgements

First and foremost, I would like to express my gratitude to my supervisor, Dr. Maikel Rheinstädter. Maikel has an unprecedented level of dedication to his students and a truly contagious enthusiasm for science. He has given me countless opportunities to be directly involved with all aspects of our research projects, helping me to become a well rounded and confident experimentalist.

Thanks to my committee members, Drs. Bruce Gaulin and Cecile Fradin. I feel incredibly fortunate to have two such accomplished researchers as my advisors, and am very grateful for the valuable insight they have provided me with throughout the course of my degree. There are two more McMaster faculty in particular that I would like to acknowledge. Thanks to Dr. An-Chang Shi, for pleasant and productive collaborations, and Dr. Kari Dalnoki-Veress for being a constant source of encouragement and support from the moment I stepped onto the McMaster campus.

There are a number of collaborators and instrument scientists, without whom these projects would not have been possible. Again, I feel very privileged to have been given the opportunity to work with such world class researchers. I would especially like to thank Drs. Norbert Kučerka and Zahra Yamani for their hard work and commitment to our experiments, as well as Drew Marquardt, who went well above and beyond for us when he stepped up to the plate during Norbert's leave. I would also like to thank Dr. John Katsaras for his expertise, fruitful collaborations, and for simply being a delight to work with.

To my lab-mates, Martin Kaye (my original partner in crime), Matt Barrett, and Laura Toppozini, I cannot thank you enough for your support, discussions, hard work, and willingness to turn every experiment or conference into an adventure. I would also like to thank Hannah Dies, our undergraduate extraordinaire.

Thanks to all of the Hamiltonians who have helped me decompress when things got too stressful; in particular, Phil, Patrick, Claire, Josh, Andreas, Allan, Sandy, Louca, Rory, and Laura. I'm pretty lucky to have stumbled into such an amazing and supportive group of friends.

Lastly, I would like to extend my appreciation to my parents, Blaine and Maureen, my childhood friend Andy, and, most of all, James for giving me love and support throughout the duration of this marathon.

Contents

List of Figures

List of Tables

LIST OF TABLES

Chapter 1

Introduction

Cellular membranes separate the internal and external environments of the cell. While this is an important role that membranes fulfil, they are also responsible for a myriad of other tasks necessary for proper cell function. The membrane controls what enters and leaves the cell. For small molecules, like water or carbon dioxide, it acts as a semi-permeable barrier, allowing for passive (or sometimes directed [1]) diffusion into and out of the cell. The lipid matrix of the membrane hosts a variety of integral proteins, some of which act as trans-membrane channels to transport larger molecules, like carbohydrates or amino acids. Ion channels in the membrane serve to create a charge gradient with respect to the external environment, which can be a crucial energy source for the synthesis of ATP [2]. Inhomogeneities in the lipid matrix, such as highly concentrated regions of certain types of lipids or macromolecules, can lead to the formation of so-called rafts. These rafts are believed to act as platforms for essential processes, which will be discussed in the following chapter.

To better understand these cellular membrane functions, a thorough understanding of this structurally complex and highly dynamic system is required. Such a task is not without its own set of challenges, namely, the measurement of molecular organization in a system that does not possess long-range order, and is undergoing micro-pico second fluctuations.

Neutron scattering, a technique initially developed for the study of hard condensed matter systems, is constantly evolving to meet the measurement challenges posed by the field of biophysics. The last ten years have seen a multi-billion dollar reinvestment

into neutron facilities globally, and with that the development of instruments (such as small angle and neutron spin-echo spectrometers) designed with a focus on the measurement of relevant length and time scales necessary for understanding biological and soft matter systems.

1.1 Thesis Overview

This thesis presents work which can be divided into two distinct topics: (1) Membrane dynamics (more specifically, the lateral diffusion of lipid molecules in a bilayer); and (2) Domains in the membrane (referring to the structure of both transient lipid and lipid/cholesterol domains). While the papers presented in these two sections may seem only loosely related, there is another running theme that underlies all of these projects, and that is "pushing the limits of traditional neutron spectrometry".

An introduction to the biological systems studied in this body of work, as well as the basics of neutron scattering, will be covered in Chapter 2. The specific details of the experimental portion of the different projects will be given in Chapter 3. This includes different methods of sample preparation and construction, and the general theory behind each of the neutron spectrometers used to collect data for the published articles.

Chapter 4 addresses the topic of lateral lipid diffusion in the membrane. It includes three projects: diffusion in single lipid bilayers, short-range ballistic diffusion in lipid membranes, and mesoscopic lipid diffusion studied using incoherent neutron spin-echo spectrometry. These three works contribute to an understanding of how the mechanism behind lipid motion changes at different length scales.

Chapter 5 includes works related to the study of domains in biological membranes. This chapter contains three articles which present evidence for the existence of domains in membrane systems, but also introduces a neutron scattering technique developed for the measurement of small, transient structures. The first article in this section presents data indicative of a non-uniform distribution of cholesterol in a model lipid/cholesterol system, suggesting the coexistence of fluid, gel and liquid ordered phases. This evidence can been seen in the dynamics of the system, as three distinct energy dispersion curves were observed simultaneously relating to each phase.

The second and third papers probe the structure of their systems, rather than the dynamics. The second paper introduces a technique developed to measure fluctuating systems with short-range order. By examining a single-component lipid bilayer near its phase transition temperature, a coexistence of fluid and gel nanodomains was observed, confirming that the system undergoes a first order phase transition. The last paper presented combines themes from the previous two, as it probes the structure of a lipid bilayer system containing cholesterol. This experiment led to the observation of highly ordered lipid domains in the presence of cholesterol, again, suggesting a non-uniform distribution of the macromolecule in the bilayer.

Lastly, Chapter 6 will include future outlooks and possible experiments that could stem from the work presented here, as well as concluding remarks.

Chapter 2

Theoretical Background

2.1 Biological Systems

For decades, the fluid mosaic description of the cell membrane, developed by Singer and Nicholson in 1972, has been the standard model for the structure and function of biological membranes. It suggests that the membrane is a homogeneous passive bilayer, where the fluid matrix is composed of freely diffusing lipids and the mosaicities in the system are primarily peripheral and integral membrane proteins [3] (see Figure 2.1). However, it has become increasingly apparent that this model is too simple to explain many of the complex substructures thought to be essential for cellular function. Clusters of certain types of lipids and macromolecules, which form rafts in the fluid lipid matrix, are believed to serve a variety of purposes, such as platforms for signal transduction, cell adhesion, cell trafficking, and lipid/protein sorting [4–13]. Elucidating the function and formation of these structures hinges on a complete understanding of the structure and dynamics of the lipid matrix. As such, model membrane systems are often used as a tool for the characterization of a simplified version of the cell membrane, before considering the much more complicated multi-component biological membrane.

2.1.1 Lipids

Lipids are considered to be one of the four building blocks of life (along with nucleic acids, proteins and carbohydrates) [15], so it is no surprise that lipid systems

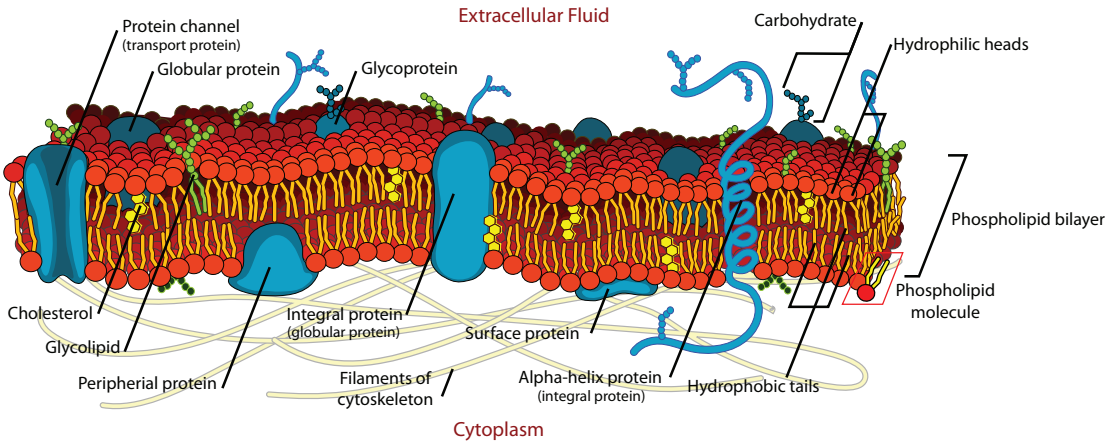

Figure 2.1: Schematic diagram of a biological membrane displaying the complexity and multi-component nature of the system [14].

have been so thoroughly studied in the past. They consist of a hydrophilic headgroup and hydrophobic hydrocarbon tails. Because of their amphiphilic nature, lipid molecules spontaneously aggregate, when in aqueous environments, into well known bilayer structures. The properties of the lipid matrix will influence the function of macromolecules (like proteins) inserted into the bilayer [16], as well as protein-protein interactions which are thought to be lipid membrane mediated [17].

Lipid molecules are classified by their chemically functional backbone and can be subdivided into eight categories, four of which commonly contribute to the membrane's composition: glycerophospholipids, glycerolipids, sphingolipids, and sterols [18]. Sterols, in particular cholesterol, are of significance to the membrane's physical properties (such as stiffness), as well as the formation of inhomogeneities in the membrane. This topic will be discussed further in the next section. Of the three remaining aforementioned lipids, focus will be drawn towards glycerophospholipids for two reasons: (1) they are the primary constituent in biological membranes; and (2) all work presented in Chapters 4 and 5 utilized glycerophospholipid model membranes.

A glycerophospholipid (often simply referred to as a phospholipid) is composed of gylcerol based lipid, with one or two hydrocarbon chains, and a phosphate attached to the headgroup. The length of the chains (or tails) is defined by the number of carbons which extend beyond the glycerol backbone of the molecule. Phospholipids have chain lengths that commonly range from 12-24 carbons.

The "saturation" of the lipid refers to whether or not any of the carbons in the lipid tails are double bonded. Saturated lipids have no double bonds, thus each carbon atom is "saturated" with hydrogen. Because the carbons in the saturated chains have tetrahedral bond angles, the lipid tails can take on an all-trans configuration resulting in a relatively linear structure, as pictured in Figure 2.2. Unsaturated lipids have one or more double bonds, which increases the C-C=C bond angle to 120°, causing kinks in the lipid tails. These kinks require the tails to inhabit a larger volume, resulting in a higher level of disorder in the hydrophobic membrane core.

The subgroup of phospholipids used in the work presented in this thesis was phosphatidylcholine, which have an additional choline molecule in the headgroup. The two specific lipids used, 1,2-dimyristoyl-*sn*-glycero-3-phosphatidylcholine (DMPC) and 1,2-dipalmitoyl-*sn*-glycero-3-phosphatidylcholine (DPPC), are shown in Figure 2.2 a) and b). These lipids are commonly found in human tissue and are well established model systems [19].

The hydrophilic/hydrophobic nature of lipid molecules is what drives them to self assemble into different structures (micelles, vesicles, bilayers), which minimize their free energy. The bilayer separates the interior of the cell from its surroundings, with the polar head groups in contact with the aqueous internal and external environments of the cell and the lipid tails in the center of the bilayer forming its hydrophobic core. Depending on the temperature and hydration level of the system, a bilayer will assume different phases. Schematic representations of these phases, along with a phase diagram displaying their temperature and hydration dependence can be found in Figure 2.3.

The notation used to describe the membrane state is denoted by the symmetries of corresponding liquid crystalline phases: L_α, $\mathrm{L}_{\beta'}$, and $\mathrm{P}_{\beta'}$. The phase that is typically thought of as being "physiologically relevant" in biological membranes is the fluid (L_α) phase. This phase occurs at higher temperatures and when the system is sufficiently hydrated ($\gtrsim$70%). In the fully hydrated fluid phase, lipids in the bilayer are extremely dynamic. The lipid chains will undergo fluctuations creating an increased area per lipid and more a disordered system. These factors also promote movement in the lateral direction of the lipid bilayer, making it easier for lipids to diffuse.

The temperature at which the bilayer changes from a fluid to a gel ($\mathrm{L}_{\beta'}$) state

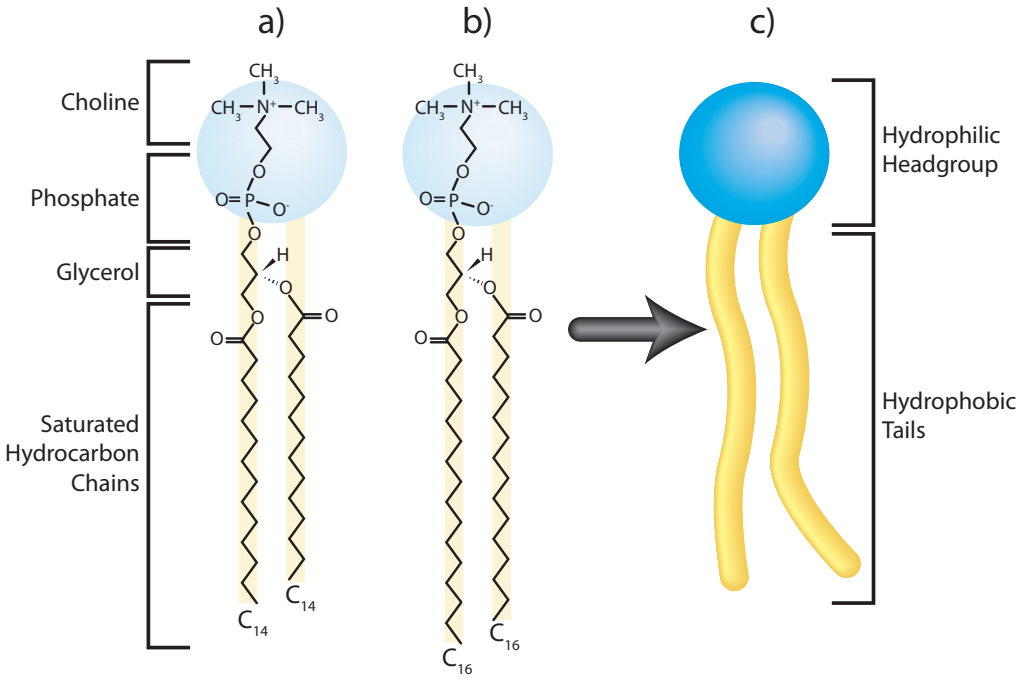

Figure 2.2: Representations of the phosphatidylcholine lipids used to create the bilayers studied in Chapters 4 and 5. a) and b) Chemical representations of DMPC and DPPC molecules, respectively. c) Schematic diagram demonstrating how these lipids are considered. The specific chemical nature of each lipid is generalized to a simplified model with a rigid polar headgroup attached to two flexible non-polar tails.

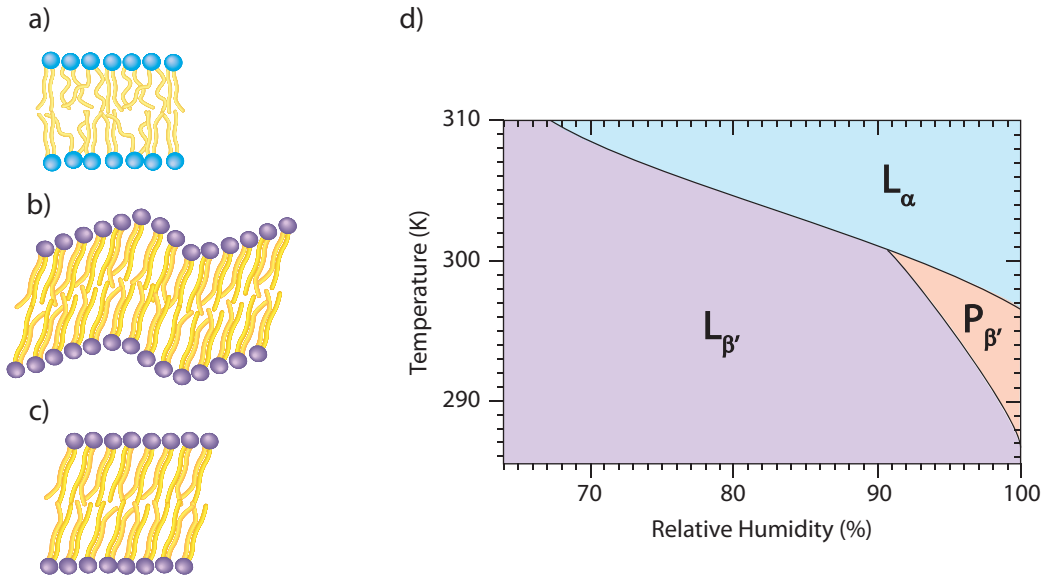

Figure 2.3: Lamellar lipid phases. Schematic diagram of the a) fluid L_α, b) ripple $P_{\beta'}$ and c) gel $L_{\beta'}$ phases of a lipid bilayer. d) Phase diagram of DMPC displaying the temperature and humidity dependence on the bilayer phase. (Adapted from Smith *et al.*, 1990 [20].)

is referred to as the main transition temperature, T_m. This transition temperature is strongly influenced by the length of the hydrocarbon tails. For instance, DMPC has a tail length of 14 carbons and a transition temperature of T_m=296.6 K, while DPPC has 16 carbons and T_m=314.4 K. Thus, at temperatures below T_m the bilayer assumes the gel phase. A fundamental characteristic of this phase is that the tails assume a straight, all-trans configuration. This is a key difference from the fluid phase, as above the T_m gauche defects are introduced in the hydrocarbon chains making the tails more mobile. The reduced thermal energy in the gel phase results in highly ordered lipid tails, leading to a hexagonal closed packing arrangement of the hydrocarbon chains [21]. Differences in the physical dimensions of lipid bilayers in their fluid and gel phases are shown in Table 2.1.

The ripple $P_{\beta'}$ phase is a particular gel phase which occurs at temperatures between the fluid and gel phase in some phospholipids, such as DMPC and DPPC, when the bilayer is under high hydration. In this high hydration scenario, the main phase transition temperature actually refers to the temperature at which the system transitions from the fluid to the ripple phase. This phase is characterized by addi-

	D'_B Å	A_L Å^2
DMPC (fluid) [23]	43.4	60.6
DMPC (gel) [24]	48.4	47.5
DPPC (fluid) [25]	47.2	62.9
DPPC (gel) [21]	52.4	47.9

Table 2.1: Noteworthy dimension of DMPC and DPPC lipid bilayers. The main transition temperature of DMPC is near room temperature (T_m=296.6 K) [26, 27], while the transition temperature of DPPC is much higher (T_m=314.4 K) [28, 29]. D'_B represents the steric bilayer thickness. It is determined from the position of the headgroup in electron density (X-ray) or scattering length (neutron) density profiles. A_L is the area per lipid. This table illustrates the increase in bilayer thickness and decrease in lipid area as the system transitions from the fluid to the gel phase.

tional small, one dimensional height modulations with amplitudes of ∼10-20 Å, and wavelengths of ∼120-160 Å [22]. The gel and ripple phases exhibit similar elastic properties, diffusion coefficients and nanoscale dynamics.

2.1.2 Cholesterol

Cholesterol is an essential structural component of the cellular membrane. It is composed of a small hydrophilic hydroxyl group attached to a single hydrophobic tail. The cholesterol tail, unlike the lipid tails, is quite rigid as it is made of a series of sterol rings with a short fatty acid chain at the end (see Figure 2.4). In what is called the "umbrella model" [30, 31], the bulky, primarily hydrophobic, molecule tends to reside in an upright orientation among the lipid tails, causing them to straighten. As such, it can strongly influence the rigidity, permeability and molecular organization of the lipid bilayer. At high enough concentrations, cholesterol will the drive the lipid bilayer into a liquid-ordered (l_o) phase, which is characterized by rapid hydrocarbon chain reorientation with high conformational order [32].

The physiological concentration of cholesterol in biological membranes varies widely, with concentrations in healthy plasma membrane tissue ranging from 20-50% [33]. This broad range of cholesterol content in real biological systems motivates the question, "Is this molecule heterogeneously or homogeneously dispersed throughout the lipid bilayer?". Cholesterol is thought to be a key participant in the formation of

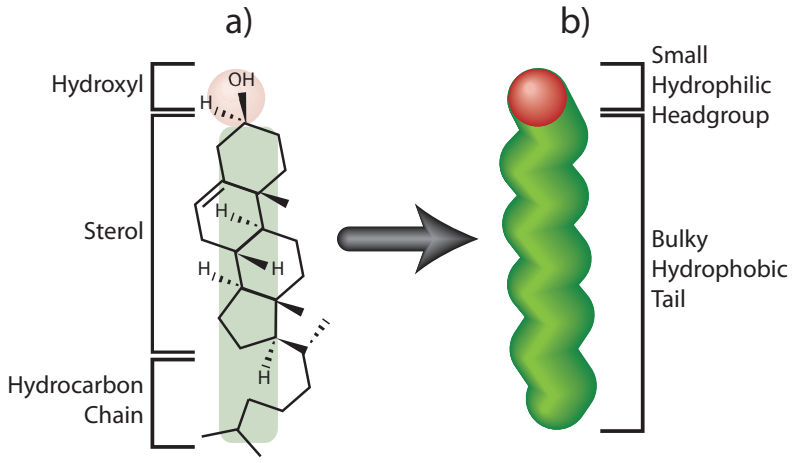

Figure 2.4: a) Chemical representation of a cholesterol molecule. b) Schematic diagram of the cholesterol molecule displaying its relatively small hydrophilic headgroup and single rigid sterol tail.

lipid rafts [5], suggesting that it is not simply uniformly dispersed in the membrane. However, in model systems containing high concentrations of cholesterol, experimental evidence suggests that the membrane assumes a uniform l_o phase [34, 35]. This point of interest was the driving force behind the work presented in Paper VI, and is, therefore, thoroughly addressed in Section 5.4.

2.2 Neutron Scattering

Neutron scattering was initially developed in the 1940's as a method for probing condensed matter systems. Bertram N. Brockhouse and Clifford G. Shull were two instrumental pioneers in the development of this technique, and as such, were recipients of the Nobel Prize in Physics in 1994 for their contributions to the field. Although it's primary use early on was for the system of condensed matter, it has become an increasingly useful and important tool for elucidating the structure and dynamics in soft matter and biological systems. Labelling of molecular components by selective deuteration is widely used in structural investigations. Inelastic neutron scattering allows for the observation of dynamics occurring over nanometer length scales, and nano to picosecond time scales. In the context of biological membranes, this corresponds to distances ranging from less than the lipid nearest-neighbour dis-

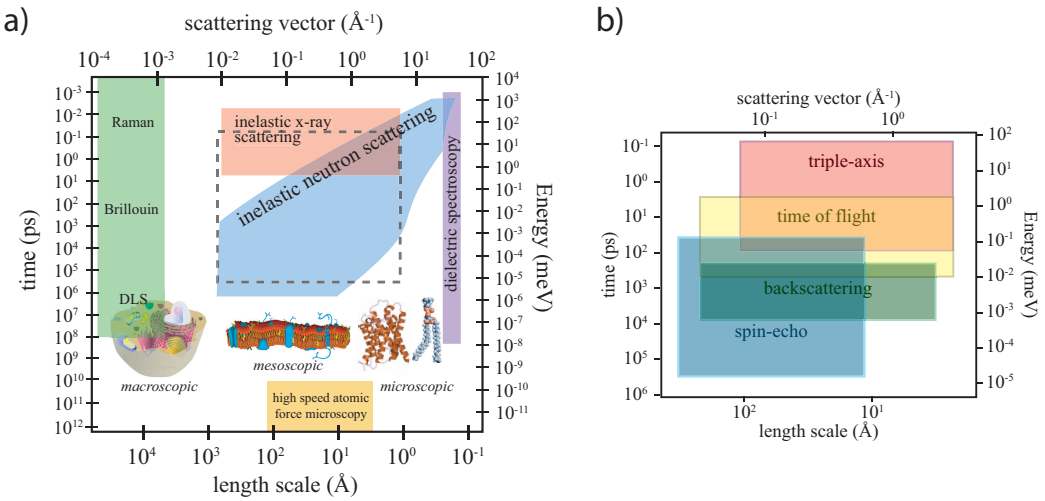

Figure 2.5: a) Length and time scales, with the corresponding energy and momentum transfer ranges, accessible by different experimental techniques commonly used in soft matter systems. Inelastic neutron scattering spans a broad range of both length and time scales that are highly relevant for the study of biological membrane dynamics. The area enclosed by the grey dashed box is enlarged in b). b) Break down of the different inelastic neutron scattering spectrometers which are used to access such a broad range of length and time scales. (Adapted from Armstrong *et al.*, 2011 [17].)

tance to lengths extending across several (∼5-8) lipid diameters. The fast time scales accessible through this technique enable the examination of short-range motion and the dynamics of fluctuating, transient structures. The broad range of length and time scales that can be measured by inelastic neutron scattering are shown in Figure 2.5.

Neutrons are part of the atomic nucleus and, while hypothesized as early as 1920, were not experimentally discovered until 1932. As the name suggests, they are charge neutral. This lack of charge enables neutrons to penetrate deeply into materials and scatter from atomic nuclei, unlike electrons and X-rays, which have much smaller penetration depths and scatter from the electron cloud surrounding the atoms. In a sense, neutrons provide an ideal probe for a variety of studies as they: (1) are deeply penetrating, enabling the study of bulk material; (2) have wavelengths similar to inter-atomic spacings; and (3) are non-damaging, making them appealing for the study of biological systems. Some physical properties of neutrons are detailed in

Quantity	Value
mass	1.675×10^{-27}kg
charge	0
spin	$\frac{1}{2}$
velocity	2200m/s (thermal)
magnetic moment	-9.649$\times 10^{-27}$ J/T

Table 2.2: Neutron properties.

Table 2.2 [36].

There are two primary sources of neutron production which result in a high enough flux to make them useful for neutron scattering experiments: reactor sources and spallation sources. Reactor sources produce neutrons through the nuclear fission of Uranium atoms. Each fission event produces roughly 1 experimental neutron [36], thus creating a continuous beam of neutrons. Spallation sources produce neutrons by bombarding a heavy metal target with high energy protons. This creates a pulse of $\sim$20-30 neutrons after each proton collision [36]. Because the time between pulses is precisely known, spallation sources lend themselves quite well to time-of-flight experiments.

2.2.1 Scattering Theory

A neutron, with kinetic energy $E = \frac{1}{2}mv^2$, will have a de Broglie wavelength of $\lambda = \frac{2\pi\hbar}{mv}$. This wavelength is used to define the wavevector of the neutron, $\mathbf{k}$, where

$$|k| = \frac{2\pi}{\lambda} \ (\textit{in the direction of } \mathbf{v}). \tag{2.1}$$

Thus the energy of the particle can be written in terms of its wavevector,

$$E = \frac{\hbar^2 k^2}{2m}. \tag{2.2}$$

Typically, neutrons are defined by a specified energy or wavelength range. Neutrons produced in reactor or spallation sources usually have kinetic energies equivalent to the thermal energy corresponding to room temperature. By equilibrating the neutrons in a cold or hot thermal bath, different types of neutrons can be produced.

Source	Energy (meV)	Temperature (K)	Wavelength (Å)
cold	0.1 - 10	1 - 120	30 - 3
thermal	5 -100	60 - 1000	4 - 1
hot	100 - 500	1000 - 6000	1 - 0.4

Table 2.3: Energy range classifications for neutrons.

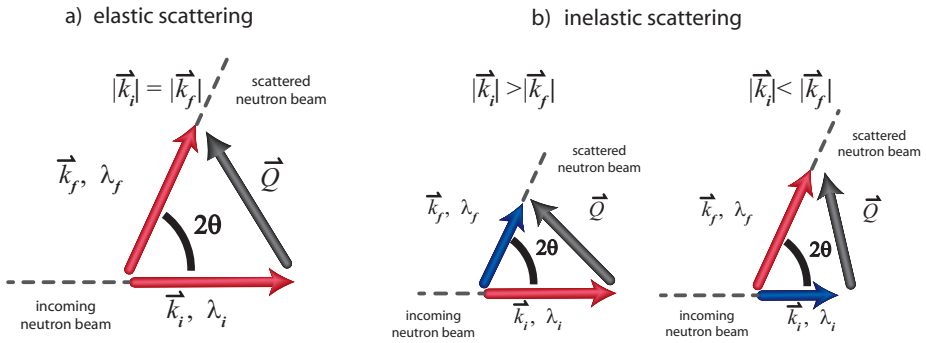

Figure 2.6: Scattering triangles displaying a) elastic and b) inelastic scattering scenarios. The scattering vector is defined as the difference between the final and initial wavevectors.

This is often achieved by allowing the neutrons to interact with a container of hydrogen or deuterium cooled to ∼20 K to produce slow neutrons, or with ∼2000 K graphite, increasing their kinetic energy to produce fast neutrons. Table 2.3 displays the commonly accepted energy ranges for cold, thermal and hot neutrons.

Scattering occurs when the neutron interacts with the sample, resulting in an exchange of momentum and kinetic energy. The scattering vector is defined as the difference between the outgoing ($\mathbf{k_f}$) and incoming ($\mathbf{k_i}$) wavevectors,

$$\mathbf{Q} = \mathbf{k_f} - \mathbf{k_i}. \tag{2.3}$$

If there is no energy transfer between the neutron and the sample, the neutron has undergone elastic scattering and the magnitude of the initial wavevector will be preserved. In the case of inelastic scattering, the neutron will have either donated or absorbed energy from the sample. These scenarios are depicted in Figure 2.6.

When considering elastic scattering from a periodic structure, resulting in con-

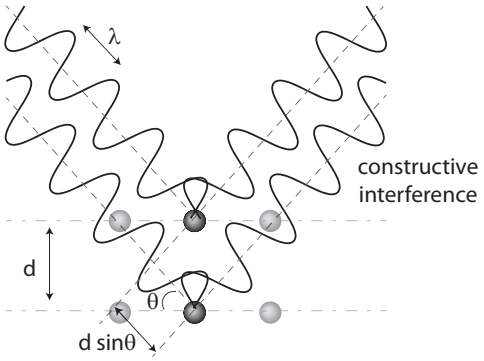

Figure 2.7: When elastic scattering occurs from a lattice, the Bragg condition is satisfied if the path length difference between two scattering waves is an integer number of wavelengths, resulting in constructive interference.

structive interference, the scattering vector can be written in terms of the scattering angle and the wavelength by combining the trigonometric relation $\frac{\mathbf{Q}}{2} = k_i \sin\theta$ (which can be seen in Figure 2.6) with Equation 2.1 to yield

$$|\mathbf{Q}| = \frac{4\pi \sin\theta}{\lambda}. \tag{2.4}$$

This condition is satisfied if the path length difference between the scattered waves is an integer number of wavelengths (see Figure 2.7). Equation 2.4, the well-know Bragg's law, is more commonly written in terms of the real-space lattice spacing, d,

$$n\lambda = 2d \sin\theta, \tag{2.5}$$

where $d = \frac{2\pi}{Q}$.

An important concept to introduce when considering any type of scattering is the scattering cross section. The neutron scattering cross section essentially describes the probability of a neutron interacting with a target nucleus. In a typical neutron scattering experiment, the quantity of interest is the number of neutrons scattered in a specific energy range, into a given solid angle. A measure of this intensity is the partial differential cross section, $\frac{\mathrm{d}^2\sigma}{\mathrm{d}\Omega \mathrm{d}E_f}$, where σ is the total cross section, $\mathrm{d}\Omega$ is the solid angle defining the direction of scattering, and the final energy range is between E_f and E_f+dE_f. The total cross section is independent of both energy and scattering

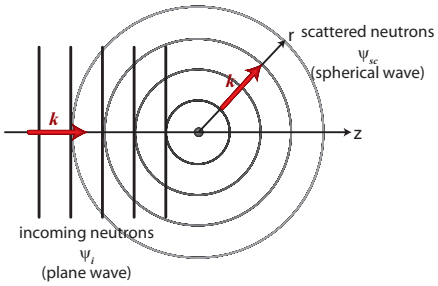

Figure 2.8: Neutron scattering from a single stationary nucleus. The incoming neutron can be expressed as a plane wave. Because the interaction distance between the neutron and nucleus is much smaller than the neutron wavelength, the resulting scattered wave will be spherically symmetric.

angle, as it refers to the total number of neutrons scattered in all directions and at all energies,

$$\sigma_{tot} = \int_0^{4\pi} \int_0^{\infty} \left(\frac{\mathrm{d}^2\sigma}{\mathrm{d}\Omega \mathrm{d}E_f} \right) \mathrm{d}E_f \mathrm{d}\Omega. \tag{2.6}$$

If we consider the elastic scattering from a single stationary atom, the incoming neutron beam can be described as a plane wave with the wavefunction Ψ_i,

$$\Psi_i = \exp(ikz), \tag{2.7}$$

where the wavevector, $\mathbf{k}$, is oriented along the z-axis (as shown in Figure 2.8). Because typical nuclear forces responsible for scattering act on length scales of $\sim 10^{-15}$ m, and the wavelength of a thermal neutron beam is much larger, $\sim 10^{-10}$ m, the scattered wave will be spherically symmetric:

$$\Psi_{sc} = -\frac{b}{r} \exp(ikr). \tag{2.8}$$

The amplitude of the scattered wave, b, is a constant referred to as the scattering length.

The differential cross section ($\frac{\mathrm{d}\sigma}{\mathrm{d}\Omega}$) is described as follows:

$$\frac{\mathrm{d}\sigma}{\mathrm{d}\Omega} = \frac{\#\text{ of neutrons scattered into } \mathrm{d}\Omega \text{ per second}}{\Phi\ \mathrm{d}\Omega}, \tag{2.9}$$

and can be calculated in this simplified scenario using expressions for the incident

and scattered flux, as defined by the wavefunctions in Equations 2.7 and 2.8.

In the case of elastic scattering (i.e. the neutron velocity, v, is the same before and after scattering),Φ, the incident neutron flux, can be written as

$$\Phi = v|\Psi_i|^2 = v. \tag{2.10}$$

(Note that the dimension of a wavefunction describing a particle in three dimension is $\mathrm{m}^{-3/2}$.) The number of neutrons scattered into a solid angle defined by an area, $\mathrm{d}A$, per second is given by

$$v\ \mathrm{d}A|\Psi_{sc}|^2 = v\ \mathrm{d}A\frac{b^2}{r^2} = vb^2\ \mathrm{d}\Omega, \tag{2.11}$$

where $\mathrm{d}\Omega = \frac{\mathrm{d}A}{r^2}$. Subbing Equations 2.10 and 2.11 into the expression for the differential cross section (Equation 2.9) gives

$$\frac{\mathrm{d}\sigma}{\mathrm{d}\Omega} = \frac{vb^2\ \mathrm{d}\Omega}{v\ \mathrm{d}\Omega} = b^2. \tag{2.12}$$

Thus, the total scattering cross section of a nucleus will be the cross section of a sphere with the radius of the scattering length, b,

$$\sigma_{tot} = 4\pi b^2. \tag{2.13}$$

It should be noted that there is no direct correlation between the scattering cross section and the number of neutrons in the nucleus of an element. Therefore, neutron scattering lengths are experimentally determined parameters. This is quite different from trends that are seen in atomic cross sections for X-ray scattering. Because X-ray scattering involves photons interacting with the electron cloud surrounding a nucleus, there is an obvious trend between atomic number and scattering cross section (i.e. elements higher up on the periodic table are inevitably stronger X-ray scatterers). Contrary to this trend, the element with the largest neutron scattering cross section is hydrogen. A comparison between the drastically different neutron and X-ray scattering cross sections of common elements can be seen in Figure 2.9.

Since all biological materials have high hydrogen content, neutron scattering is an appealing technique. In addition to this, the coherent and incoherent scattering

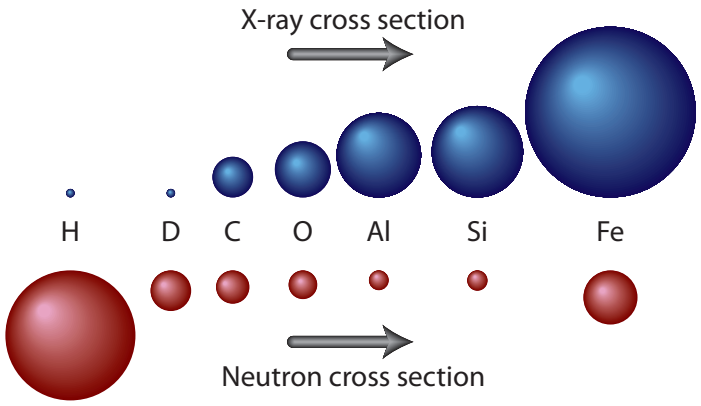

Figure 2.9: Comparison between X-ray and neutron scattering cross sections. X-ray scattering cross sections have a monatomic dependence on the number of electrons in the system and, thus increase with atomic number. Neutron cross sections vary erratically with atomic number [36]. It should be noted that by using absorption edges, the scattering contribution of one element can be drastically enhanced over another. This aspect is not represented in the figure above.

properties of hydrogen play an important role in adding "labels" to certain molecules or functional groups through selective deuteration, which will be discussed in Section 2.2.4.

2.2.2 Coherent and Incoherent Neutron Scattering

Two factors contribute to differences in the atomic nuclei structure of atoms of the same chemical element: (1) different isotopes; and (2) different orientations of the nuclear spin (for elements with non-zero nuclear spin). Therefore, even monatomic samples can contain nuclei with different scattering lengths. Coherent scattering is the scattering which would occur if every nucleus in the system had a scattering length equal to the average scattering length, giving rise to the coherent cross section,

$$\sigma_{coh} = 4\pi\langle b\rangle^2. \tag{2.14}$$

The incoherent scattering cross section can be obtained by adding the necessary component such that the incoherent and coherent scattering cross sections combine

to give the total scattering cross section,

$$\begin{aligned}\sigma_{inc} &= \sigma_{tot} - \sigma_{coh}, \\ \sigma_{inc} &= 4\pi \left(\langle b^2 \rangle - \langle b \rangle^2 \right). \end{aligned} \tag{2.15}$$

The coherent and incoherent partial differential scattering cross sections are defined as follows:

$$\left(\frac{\mathrm{d}^2\sigma}{\mathrm{d}\Omega \mathrm{d}E_f} \right)_{coh} = \frac{\sigma_{coh}}{4\pi} \frac{k_f}{k_i} \frac{1}{2\pi\hbar} \sum_{jj'} \int_{-\infty}^{\infty} \langle \exp\{-i\mathbf{Q}\cdot\mathbf{R}_{j'}(0)\} \ \exp\{i\mathbf{Q}\cdot\mathbf{R}_j(t)\} \rangle \exp(-i\omega t) \mathrm{d}t, \tag{2.16}$$

$$\left(\frac{\mathrm{d}^2\sigma}{\mathrm{d}\Omega \mathrm{d}E_f} \right)_{inc} = \frac{\sigma_{inc}}{4\pi} \frac{k_f}{k_i} \frac{1}{2\pi\hbar} \sum_{j} \int_{-\infty}^{\infty} \langle \exp\{-i\mathbf{Q}\cdot\mathbf{R}_j(0)\} \ \exp\{i\mathbf{Q}\cdot\mathbf{R}_j(t)\} \rangle \exp(-i\omega t) \mathrm{d}t. \tag{2.17}$$

Equation 2.16 involves a summation over the j^{th} and j'^{th} particles, accounting for interactions which may occur between these two sets of particles at different times. This takes into consideration correlations between the positions of both the same nuclei at different times *and* different nuclei at different times. Thinking of this in terms of the wave-like nature of the neutron, coherent scattering preserves the relative phases of the scattered waves, thus giving rise to interference effects.

Incoherent scattering, on the other hand, only involves the correlation between the positions of the same nuclei at different times (i.e. Equation 2.17 only includes the summation over j). In this case, the neutrons do not preserve the phase relationship between the incident and scattered waves and thus, cannot constructively or destructively interfere. Therefore, the incoherent scattering intensity is simply the sum of all of the individual scattering intensities.

2.2.3 Scattering Functions

With the coherent and incoherent partial differential cross sections introduced, the nuclear scattering and correlation functions can now be defined. These functions are commonly referred to in experimental settings and help bring physical significance to the cross section expressions.

The intermediate scattering function is defined as follows:

$$I(\mathbf{Q},t) = \frac{1}{N}\sum_{jj'}\langle \exp\{-i\mathbf{Q}\cdot\mathbf{R}_{j'}(0)\}\ \exp\{i\mathbf{Q}\cdot\mathbf{R}_{j}(t)\}\rangle, \tag{2.18}$$

where N is the number of scatterers in the system. This function is used to relate the time-dependent pair correlation function ($G(\mathbf{r},t)$) and the scattering function ($S(\mathbf{Q},\omega)$):

$$G(\mathbf{r},t) = \frac{1}{(2\pi)^3}\int I(\mathbf{Q},t)\ \exp(-i\mathbf{Q}\cdot\mathbf{r})\ \mathrm{d}\mathbf{Q}, \tag{2.19}$$

$$S(\mathbf{Q},\omega) = \frac{1}{2\pi\hbar}\int I(\mathbf{Q},t)\ \exp(-i\omega t)\ \mathrm{d}t. \tag{2.20}$$

Based on the definition of $I(\mathbf{Q},t)$, it should be obvious that these function pertain to coherent scattering. As such, as set of similarly defined functions exist corresponding to incoherent scattering, where the self intermediate scattering function is given by

$$I_{self}(\mathbf{Q},t) = \frac{1}{N}\sum_{j}\langle \exp\{-i\mathbf{Q}\cdot\mathbf{R}_{j}(0)\}\ \exp\{i\mathbf{Q}\cdot\mathbf{R}_{j}(t)\}\rangle, \tag{2.21}$$

from which the self time-pair correlation function ($G_{self}(\mathbf{r},t)$) and incoherent scattering function ($S_{inc}(\mathbf{Q},\omega)$) can be written :

$$G_{self}(\mathbf{r},t) = \frac{1}{(2\pi)^3}\int I_{self}(\mathbf{Q},t)\ \exp(-i\mathbf{Q}\cdot\mathbf{r})\ \mathrm{d}\mathbf{Q}, \tag{2.22}$$

$$S_{inc}(\mathbf{Q},\omega) = \frac{1}{2\pi\hbar}\int I_{self}(\mathbf{Q},t)\ \exp(-i\omega t)\ \mathrm{d}t. \tag{2.23}$$

Comparing Equations 2.16 and 2.17 with Equations 2.20 and 2.23 respectively, it is clear that the coherent and incoherent scattering functions are very closely related to the partial differential cross sections:

$$\left(\frac{\mathrm{d}^2\sigma}{\mathrm{d}\Omega\mathrm{d}E_f}\right)_{coh} = \frac{\sigma_{coh}}{4\pi}\frac{k_f}{k_i}NS(\mathbf{Q},\omega), \tag{2.24}$$

$$\left(\frac{\mathrm{d}^2\sigma}{\mathrm{d}\Omega\mathrm{d}E_f}\right)_{inc} = \frac{\sigma_{inc}}{4\pi}\frac{k_f}{k_i}NS_{inc}(\mathbf{Q},\omega). \tag{2.25}$$

The scattering functions can, therefore, be directly measured in a neutron scattering

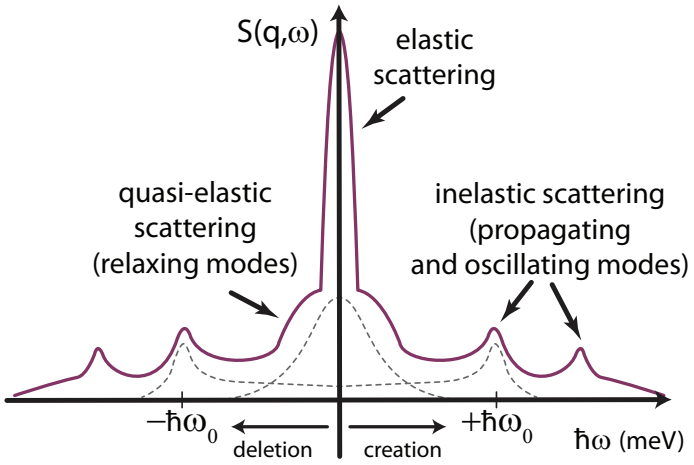

Figure 2.10: Schematic of a typical scattering function displaying the characteristic finger prints of elastic, inelastic (coherent), and quasi-elastic (incoherent) scattering. (Adapted from Rheinstädter, 2009 [37].)

experiment.

A schematic of a typical neutron excitation spectrum is displayed in Figure 2.10. There is a sharp peak centered about $\hbar\omega = 0$ corresponding to elastic scattering, in which no energy transfer occurs. Inelastic excitations exhibit themselves as satellite peaks, occurring as pairs at frequencies of $-\hbar\omega_0$ and $+\hbar\omega_0$, caused by the creation and deletion of dynamical modes (i.e. the neutron causing an excitation in the system, or an excitation in the system donating energy to the neutron). These inelastic excitations can be the result of propagating (acoustical) or oscillating (optical) modes and are often described by a damped harmonic oscillator model, where the width of the inelastic peak is related to the life time of the excitation. Quasi-elastic scattering refers to inelastic contributions which do not have a characteristic excitation frequency. It is typically incoherent scattering related to relaxation processes in the system that do not have a restoring force (like diffusion). The fingerprint of quasi-elastic scattering is a Lorentzian broadening of the central peak.

2.2.4 Selective Deuteration

Whether a system scatters coherently or incoherently will depend on the scattering lengths (b) of each nuclei in the system, as was mentioned above. The value of b

depends on both the spin of the nucleus at the scattering site and the spin state of the combined nucleus and neutron system. For instance, if a nucleus has a non-zero spin I, then the nucleus-neutron system can either have a spin state of $|I + \frac{1}{2}|$ or $|I - \frac{1}{2}|$, and each will have a different value of b. In the case where the nucleus has a zero spin, then the nucleus-neutron system will have a spin of $|\frac{1}{2}|$, and there will only be one possible value of b.

To clarify this point, let's consider a simple system composed of only one element. Although this system is made up of a single element, it is possible for the value of b to vary between the individual nuclei for two reasons: (1) the nucleus of the element has a non-zero nuclear spin; or (2) there are isotopes of the element present in the system which also may have different nuclear spins. Therefore, if the nuclear spins in the system are randomly oriented, resulting in different scattering lengths, a neutron scattered from one nucleus will not be able to constructively (or destructively) interfere with a neutron scattered from another nucleus. This incoherent scattering from the "same" type of nucleus occurs because the neutron essentially "sees" the different nuclear spins.

Now let's consider the same single element system, but simplify it even further by saying that it is completely pure (no isotopes) and this particular element has a zero nuclear spin. In this case, every nucleus will have the same scattering length, resulting in coherent scattering. Because all of the nuclei are identical to the neutrons, they will be able to interfere with neutrons scattered from different sites (see Figure 2.11).

This ability to scatter both coherently and incoherently is a property of neutrons which lends itself well to the study of local and collective dynamics occurring in a given system. For instance, incoherent quasi-elastic neutron scattering gives us access to relaxation processes in the system, like diffusion, while coherent inelastic neutron scattering can be used to detect correlated motion in biological systems, such as phonon modes.

Another feature which lends itself particularly well for the study of biological systems, was briefly touched on earlier; neutrons interact very strongly with hydrogen. The incoherent cross section for hydrogen is larger than any other nuclide, while its coherent cross section is quite small. This makes it easy to detect, but also creates an effective method of selectively measuring certain components or dynamics in the

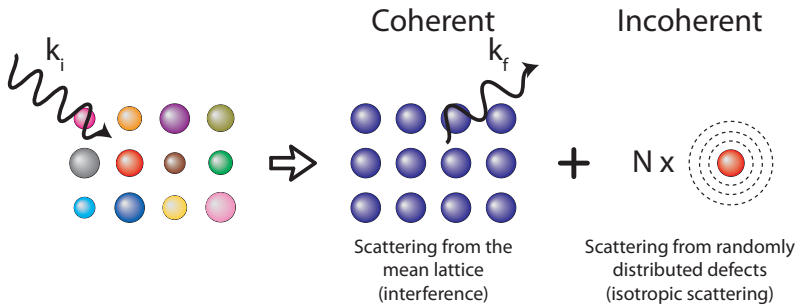

Figure 2.11: Total scattering will be a combination of coherent and incoherent contributions. The coherent scattering is from the regular mean lattice (i.e. the average scattering length, $\langle b \rangle$) and will give rise to Bragg peaks when scattering occurs at certain angles. The incoherent contribution is caused by isotropic scattering from nuclei with different scattering lengths, which will be proportional to the number of atoms in the system, N, and the mean deviation of the scattering length from $\langle b \rangle$. (Adapted from Dhont *et al.*, 2002 [38].)

Atom	Coherent (barns)	Incoherent (barns)	Total (barns)
^{1}H (Hydrogen)	1.7583	80.27	82.03
^{2}H (Deuterium)	5.592	2.05	7.64

Table 2.4: Neutron scattering cross sections of hydrogen and deuterium (1 barn=10^{-24}cm^2).

system. Deuterium, while for the most part functionally identical to hydrogen in a biological membrane, has a coherent scattering cross section which is not only larger than its incoherent cross section, but also larger than the coherent cross section of its protonated counter part. A graphic representation of the differences between coherent and incoherent cross sections of common elements found in biological systems are shown in Figure 2.12 and the numerical values of the cross sections for hydrogen and deuterium are found in Table 2.4 [39].

This enables the fabrication of systems which will have enhanced scattering from specific dynamics. To study the diffusive motion of lipids in a membrane, protonated lipid bilayers can be created, which are hydrated with D_2O. This makes the measurements sensitive to the incoherent scattering of the lipids molecules, while the deuterated water no longer has a significant incoherent contribution to obscure the signal. If the goal is to probe collective motions, chain deuterated lipids can be used

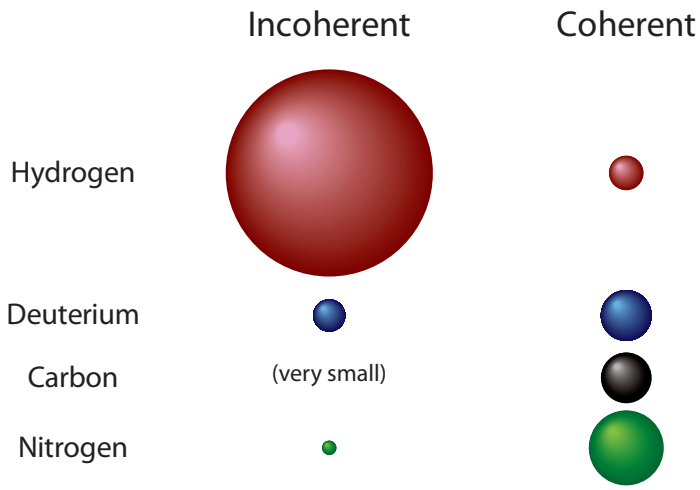

Figure 2.12: Comparison of the coherent and incoherent scattering cross sections of elements commonly found in biological systems. The most notable difference is that between the coherent and incoherent cross sections of hydrogen and deuterium [36].

to create bilayers, making the experiment sensitive to the collective motion of the lipid tails. These scenarios are depicted in Figure 2.13.

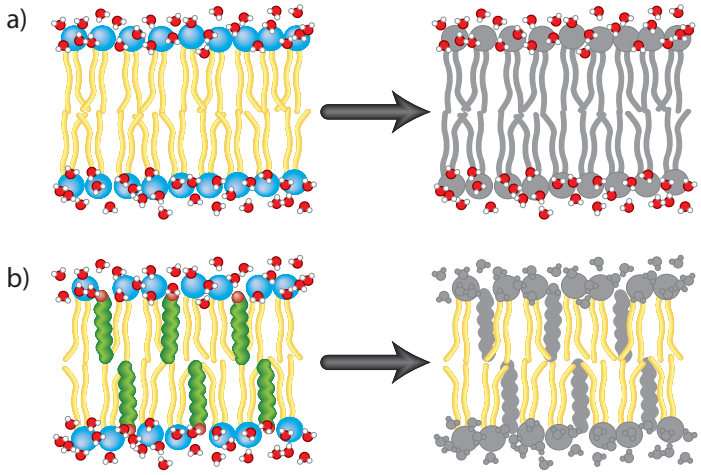

Figure 2.13: Examples of selective deuteration. The images on the right are schematics of what would be enhanced in a scattering experiment. Molecules shown in colour are deuterated and, thus, contribute to the coherent signal. Molecules that are greyed-out are protonated and have a strong incoherent signal. a) Selective deuteration for a typical lipid diffusion experiment. b) Selective deuteration for an experiment to probe lipid tail structure and collective dynamics.

Chapter 3

Experimental Background

3.1 Sample Preparation

All samples used in this thesis were solid supported, single or multi-lamellar, highly oriented membranes re-constituted from different types of lipids and cholesterol. Creating quality, highly oriented lipid bilayer systems requires a clean, dust-free work environment to minimize substrate defects and contamination. All samples prepared for this body of work began with the deposition of sample solution on to treated Si⟨100⟩-wafers. The treatment of the wafers, to achieve hydrophilic or hydrophobic substrates, as well as the method of sample deposition, was dictated by the type sample that was to be created.

3.1.1 Chemicals and Materials

Si substrates

The silicon wafers used for substrates were purchased from Montco Silicon Technologies Inc. All wafers used were 2 ″ (50.8 ± 0.5 mm) in diameter with a thickness of 256-306 μm. The orientation of the Si was ⟨100⟩. The wafers used for the single lipid bilayer samples were double-side polished, while all other samples used single-side polished wafers.

Ultra pure water

The ultra pure water was obtained from our in house Cascade LS Water System. The water is characterized by a resistivity of 18.2 MΩ·cm.

Acidic cleaning solution

The solution used to clean the Si wafers, creating a hydrophilic substrate, was 70% concentrated sulphuric acid (H_2SO_4) and 30% hydrogen peroxide (H_2O_2).

Buffer solution

The buffer solution used to create a suspension of lipid vesicles was a 1:1:1 mixture of 5×10^{-3} mol/L Hepes, 5×10^{-3} mol/L magnesium chloride ($MgCl_2$) and 100×10^{-3} mol/L potassium chloride (KCl).

Solvent solution

The solvent solution used to dissolve lipids for deposition onto a hydrophobic substrate was a 1:1 mixture of chloroform and 2,2,2 trifluoroethanol (TFE).

Biomolecules

Biomolecules were purchased from Avanti Polar Lipids Inc. 1,2-dimyristoyl-*sn*-glycero-3-phosphatidylcholine (product # 8850345P), referred to as DMPC, was the lipid used for all of the diffusion experiment presented in Chapter 4. 1,2-dipalmitoyl-D62-*sn*-glycero-3-phosphatidylcholine (product # 860355P), deuterated DPPC or DPPC-d62, was used in the samples for the study of lipid domains shown in Chapter 5. Cholesterol (product # 700000P) was also used in Paper VI.

3.1.2 Single Supported Lipid Bilayers

Single supported lipid bilayers provide a simplistic model for the study of membrane properties. A common method for creating this type of sample is through vesicle fusion. This process involves the deposition of vesicles, suspended in a water based buffer solution, onto a substrate. The vesicles adsorb on the substrate, rupture and

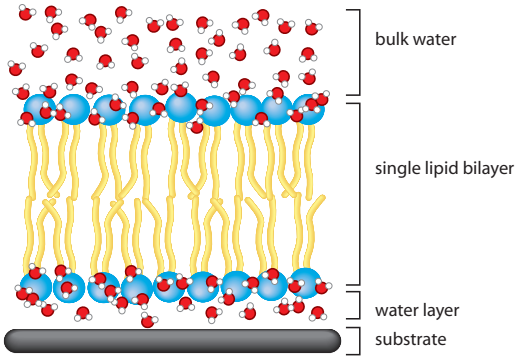

Figure 3.1: Schematic representation of a single supported lipid bilayer, displaying the water cushion between the bilayer and the substrate.

form a single lipid bilayer with a thin (∼10-20 Å) water layer between the lower bilayer leaflet and the substrate, which acts to preserve membrane fluidity [40] (see Figure 3.1). Despite this water layer, the bilayer will still "feel" the presence of the substrate, thus this system does not mimic the most biologically relevant scenario. For instance, in this system, bilayer undulations are strongly suppressed. Nevertheless, efforts to fully understand the single supported lipid bilayer system are warranted, as they have many applications in the bioengineering industry for the production of biosensors and functionalized surfaces [41, 42].

The aim of this project was to study lipid diffusion in a single lipid bilayer. This was the first successful study of this kind. Because of the minuteness of the inelastically scattered signal, the signal intensity was multiplexed by using 100 double-side polished Si substrates with a single bilayer applied to each side of the wafer, resulting in 200 single lipid bilayers.

This particular sample has such a limited amount of material on each wafer, that substrate smoothness is paramount for the production of uniform bilayer. The vesicle fusion process requires a strongly hydrophilic substrate to encourage the vesicles to adhere to the silicon surface. Surface hydrophilicity can be increased by immersing the Si wafers in an acidic cleaning solution (see Section 3.1.1) heated to T=363 K for 30 minutes. This ensures that any organic contaminates on the wafers are removed, without disturbing the substrate's native silicon oxide layer. To prevent any chance of contamination before lipid deposition, the wafers can be kept in ultra pure water

until they are ready to be used. The existing protocols for the preparation of single solid supported bilayers had to be improved for the preparation of 100 2″ wafers simultaneously.

A suspension of lipid vesicles is prepared by first making a buffer solution (see Section 3.1.1) and heating it to T=328 K. Lipid powder is then added to this solution at a concentration of 1.5 mg/mL. For the experiment detailed in Section 4.1, the lipid used was DMPC. The sample solution will take on a milky appearance due to the formation of giant multi-lamellar vesicles. To ensure that single lipid bilayers are formed once the vesicles come in contact with the substrate, the solution must be sonicated to break the large vesicles into small uni-lamellar vesicles. This requires ∼15-24 hours of sonication until the solution appears transparent.

The hydrophilic Si wafers are then completely submerged in the solution for one hour, while the temperature of the solution is maintained at T>T_m to ensure the lipids stay in their fluid phase. The cleaned wafers were kept in the slotted plastic container that they were shipped in, and the lipid solution was poured over the wafers, filling the container. This kept the wafers from coming into contact with each other, while allowing both sides of the polished wafer to be immersed in the lipid solution.

After being submerged in the lipid solution for one hour, the wafers will have patches of single lipid bilayer on the surface, in addition to entire vesicles and possibly even regions of multi-lamellar bilayer formation. Thoroughly rinsing the wafers several times with ultra pure water will remove all excess vesicles, but will have little effect on the single lipid bilayer that is in direct contact with the Si substrate. This process (depicted in Figure 3.2) initially produces a system of single lipid bilayer patches which will eventually transition into a large uniform single lipid bilayer after annealing. The lipid containing wafers are annealed for ∼72 hours at T=328 K in air.

Sample Construction for the Single Supported Lipid Bilayer Experiment

Once annealed, the wafers were stacked in an aluminum sample can (see Figure 3.3). Because this experiment was designed to examine the lateral diffusion of the lipid molecules in the membrane, the incoherent scattering from the lipid tails was emphasized by using protonated lipids. To minimize the effects of incoherent scattering from the hydration water, the sample was hydrated with deuterated water (D_2O).

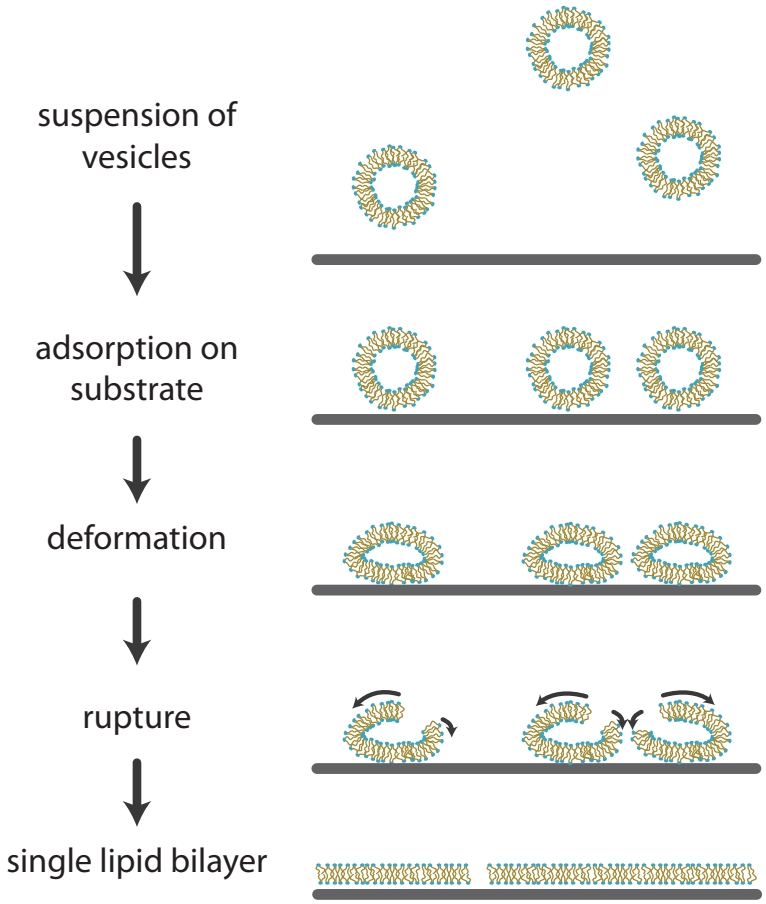

Figure 3.2: Steps leading to the formation of a single supported lipid bilayer through the vesicle fusion process. (Adapted from Hamai *et al.*, 2006 [43].)

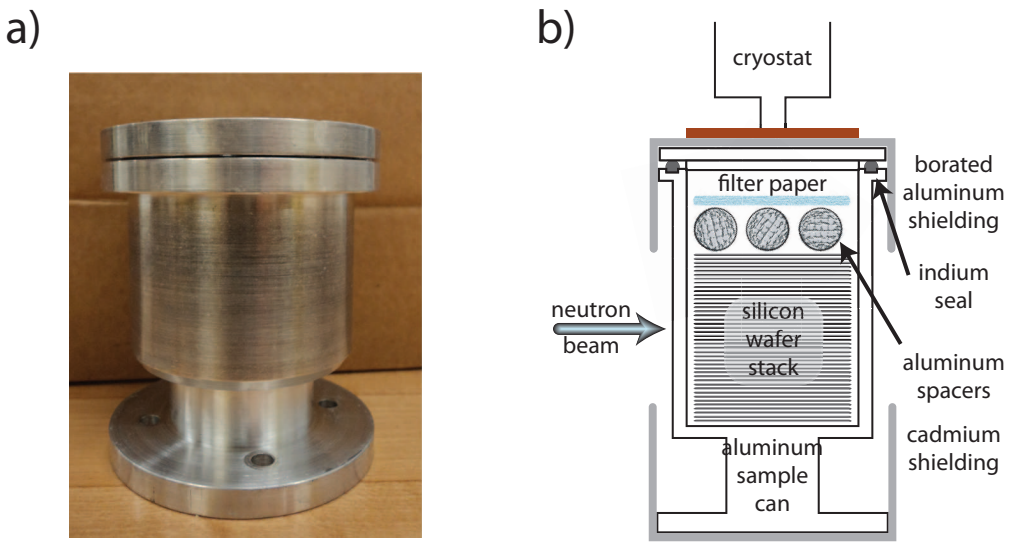

Figure 3.3: Sample environment for the "diffusion in single lipid bilayers" experiment. a) Photograph of the bare aluminum sample can. b) Cross sectional diagram of the fully constructed sample.

Porous aluminum spacers were placed between the top of the wafer stack and the hydration source to prevent any direct contact. The hydration source was a piece of filter paper saturated with 120 μL of D_2O, which, once the sample can was sealed, was very effective in hydrating the sample from the vapour state.

Before putting the sample into the neutron beam, special precautions were taken to ensure that the can was properly shielded. Cadmium shielding was applied to the bottom of the can to avoid surplus aluminum in the beam, but more importantly shielding was applied to the top of the can to ensure that the filter paper would not inadvertently be in the beam. This experiment had such a small amount of sample material ($\sim$0.7 mg) that it was essential to minimize all possible sources of background scattering.

3.1.3 Multi-Lamellar Supported Lipid Bilayers

Multi-lamellar membrane stacks are often used in scattering experiments. As neutrons (and X-rays) penetrate through the stack, the intensity of elastically and inelastically scattered neutrons can be drastically enhanced by this type of sample preparation.

A multi-lamellar or stacked membrane system has a fundamentally different sam-

ple preparation. Rather than creating a suspension of lipid vesicles, the lipid powder is dissolved into organic, non-polar solvents. This solution is deposited onto the substrates, thus requiring a cleaning procedure which leaves the surface hydrophobic to promote spreading of the solvent over the entire wafer. For this type of sample the Si wafers are cleaned by alternate sonications in ultra pure water and methanol at T=313 K. The sonication cycle is repeated at least twice (always ending with a sonication in methanol). To perform the sonications, each 2″ wafer is placed into its own 50 mL beaker with just enough water (or methanol) to cover the wafer. The beakers are then loaded into the heated sonicator for 12 minutes. The purpose of having the wafers separated into their own beakers is to prevent the substrates from coming into contact with each other during the sonication process and damaging their surfaces. Again, to minimize any chance of contamination after cleaning, the wafers are put back into the plastic tray that they are shipped in and stored under ultra pure water. This not only preserves the newly treated surface, but having the wafers upright and separated in the tray makes it easier to manipulate them once it is time to remove them from the water.

The lipid solution is prepared by dissolving lipid powder in a solvent solution (see Section 3.1.1). It was found that it was easiest to prepare the samples in 8 wafer batches, thus the solution was also prepared in batches. Once the wafers are removed from the water, they are immediately dried with pure nitrogen gas and covered to prevent surface contamination before deposition.

The solution should be deposited onto the wafers with the lipids in the fluid state. This is easily accommodated in the case of preparing a multi-lamellar DMPC sample, as the main transition temperature of DMPC is T_m=296.6 K [26], thus the deposition can occur at room temperature. 1 mL of 20 mg/mL lipid solution is carefully pipetted on to each wafer. Creating a uniform distribution requires spreading the solution such that it comes in contact with the edge of the wafers (without spilling), then slowly adding the remaining solution to the center of the wafer. This process is depicted in Figure 3.4.

This procedure is slightly more challenging when using a lipid with a higher transition temperature, like DPPC (T_m=314.4 K [28]). To ensure that the lipids are being deposited in the fluid state, the solution and substrates must be heated. This is done

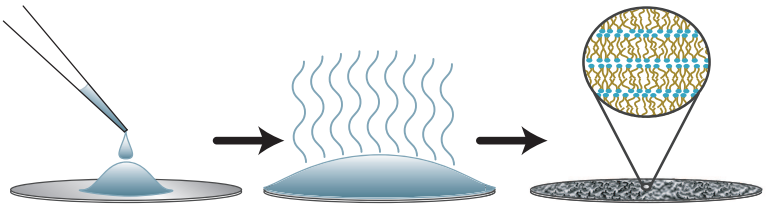

Figure 3.4: Diagram of the lipid deposition process leading to the production of a highly oriented multi-lamellar sample. Depositing 20 mg of lipid material on the wafer will result in a stack of ∼3000 highly oriented membranes.

by placing the marble blocks, which hold the substrates during deposition, on top of a water flow element attached to a heated water bath (see Figure 3.5). Once the wafers are dried and covered on the marble slab, they should be allowed to sit for ∼5 minutes, along with the lipid solution, to ensure that they are warm.

Pipetting the lipid solution onto the heated wafers is a non-trivial process. The solvent will evaporate very quickly (in less than a minute), nevertheless the solution must be deposited fast enough to achieve full coverage on the wafer without spilling. If full contact between the solution and the edge of the wafer is not met, the film will retreat, leaving large blank areas on the wafer. To combat the difficulties encountered in this process, it was found that using more solution in the deposition made it easier to achieve full coverage. Therefore, for the DPPC samples 1.2 mL of a 16.67 mg/mL lipid solution was used. Both of the processes detailed above result in 20 mg of material on each wafer.

After the lipid solution has dried, the wafers are placed in individual petri dishes and kept in vacuum overnight at T=313 K to remove all traces of solvent. The wafers are then ready to be stacked into the sample holders. Two "c-shaped", 0.3 mm thickness, aluminum spacers are placed in between each wafer, as shown in Figure 3.6. This ensures that the hydration water is able to reach all of the wafers. The last wafer on the stack is placed membrane side down, to protect the sample surface during transport. Pieces of alumnium are used to wedge the stack securely into the holder. This ensures that the wafers will not tip out when the holder is mounted upright. The samples are then hydrated by placing the full holder in a sealed container with an open dish containing ∼10 mL of water. The sealed hydration containers are place in

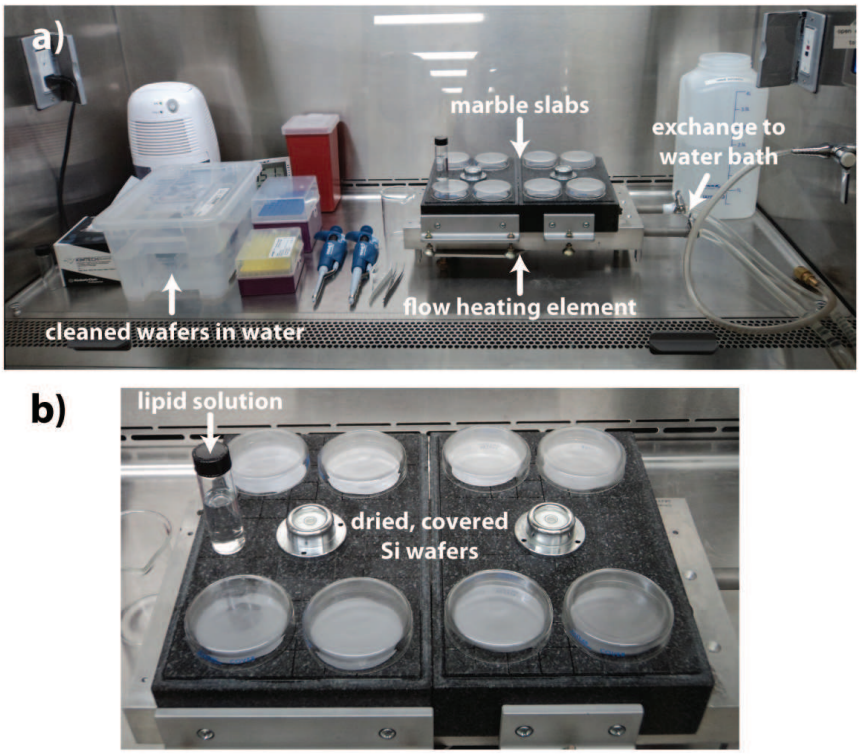

Figure 3.5: a) Ideal work station setup for the production of multi-lamellar samples. b) Heating stage used when preparing samples with lipids that have a main transition temperature above room temperature.

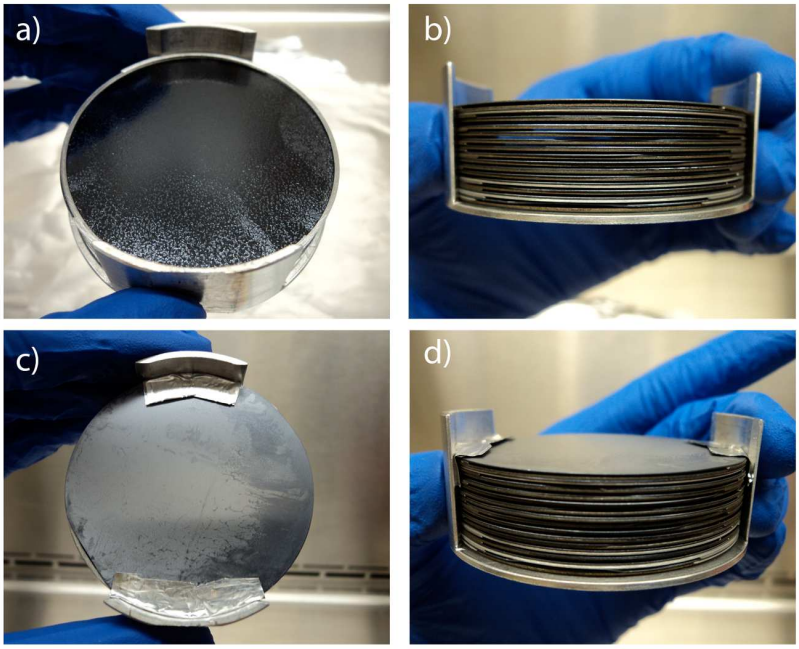

Figure 3.6: a) Top and b) side view of a sandwich sample being constructed. The aluminum spacers are placed such that there is a gap on each side of the wafer to allow for the hydration water to reach the sample. c) Top and d) side view of the fully constructed sample showing the placement of aluminum wedges to hold the wafers in place when vertically mounted.

an oven and the temperature is slowly ramped up (5 K/hour) from room temperature to ∼5-10 K above the lipid's main transition temperature for 24-36 hours.

Multi-lamellar samples prepared for neutron triple-axis experiments

The sandwich samples prepared for use on the N5 triple-axis spectrometer were part of an experiment to measure the coherent scattering from the lipid tails. As such, the lipids used in these samples were tail deuterated DPPC-d62. To minimize the incoherent scattering background, and to preserve the deuterium content of the lipids, the samples were hydrated with D_2O. Both experiments performed on N5 used a specialized humidity controlled sample environment. The sample was mounted vertically in the chamber such that when it is placed in the neutron beam, it can simply be rotated by 90° to conduct in-plane or out-of-plane measurements (see Figure 3.7). This ensures that the state of the sample is preserved even when switching between scat-

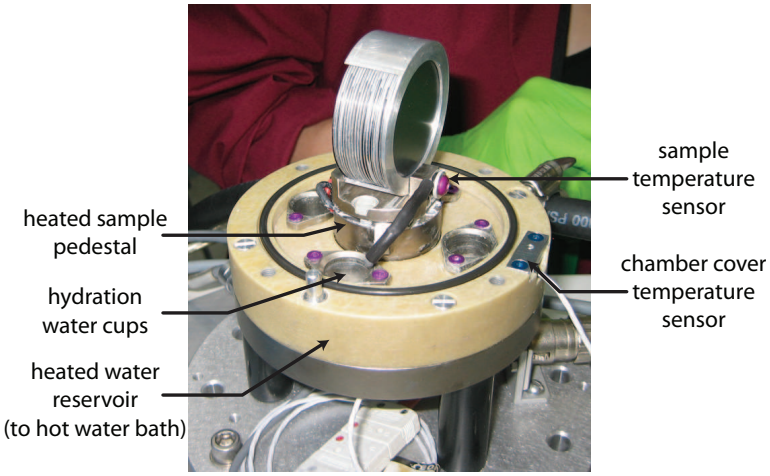

Figure 3.7: Humidity controlled sample environment with independent control over the sample, humidity water, and cover temperatures. The temperature of the sample was controlled with a Peltier device located beneath the sample and a sensor attached to the side of the sample pedestal. The humidity water was heated by a flow through reservoir attached to a hot water bath. The temperature of the aluminum chamber cover (not shown) was controlled with another Peltier device, placed on the top of the cover, and a sensor which was in contact with the bottom rim of the cover.

tering modes. Peltier elements are placed directly below the sample and in contact with the chamber cover, and a hot water bath is used to manipulate the temperature of the humidity water reservoirs that surround the sample. By independently controlling the temperatures of these three elements, precise temperature and humidity conditions were achieved.

Multi-lamellar samples prepared for the long-range diffusion, neutron spin-echo experiment

The sandwich sample prepared for the study of long-range lateral diffusion in lipid bilayers needed to be sensitive to the incoherent scattering from the lipids. Therefore, similar to the single lipid bilayer experiment, the sample was composed of protonated DMPC, hydrated with D_2O. After the stacked sample was hydrated overnight, it was placed in an open aluminum sample can with a dry Kim wipe wedged along the side of the stack, resealed in its hydration container, and left for another 12-24 hours. Once hydrated in the sample can, 60 μL of D_2O was used to wet the Kim wipe (this

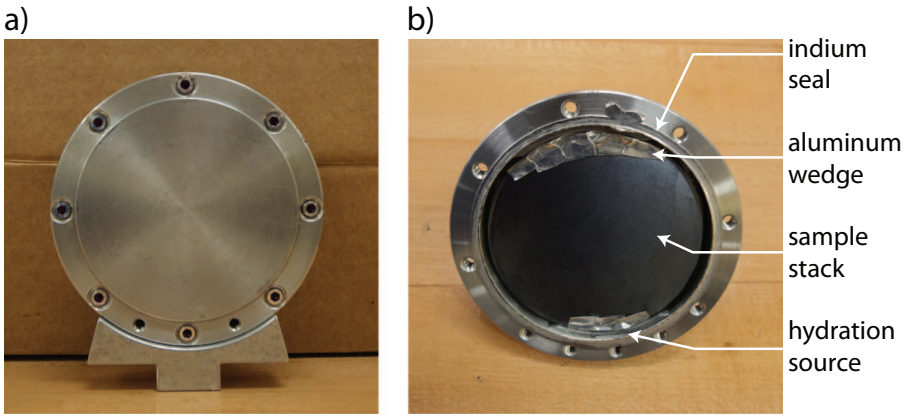

Figure 3.8: Sample used for the NSE experiment. a) Sealed aluminum sample can. b) Open sample can. Eight Si wafers are stacked in a holder with aluminum spacers placed between each wafer. A D_2O saturated Kim wipe (shown at the bottom of the photo) was used as a hydration source.

would act as a hydration source for the experiment), and the can was immediately sealed (see Figure 3.8).

3.2 Neutron Instrumentation

3.2.1 Triple-Axis Spectrometer

The neutron triple-axis spectrometer (TAS) is a versatile instrument, the development of which was pioneered by Nobel laureate Bertram N. Brockhouse. The three axes referred to in its name are the rotational axes of: the monochromator crystal, the sample, and the analyzer crystal. It is by rotating these components that the TAS is capable of selecting the incident wavevector ($\mathbf{k_i}$), scattering angle (θ) and final wavevector ($\mathbf{k_f}$) to probe various points in ($\mathbf{Q}$, $\hbar\omega$) space at different sample orientations. By holding either $\mathbf{k_i}$ or $\mathbf{k_f}$ fixed and allowing θ to vary, a "constant $\mathbf{Q}$" scan can be performed, where the intensity of the scattered neutrons is a function of energy transfer ($\hbar\omega$). Similarly, "constant energy" scans can be performed by rotating both the monochromator and analyzer to maintain constant $\mathbf{k_i}$ and $\mathbf{k_f}$ magnitudes. Here the changing scattering angle will result in a scan through various $\mathbf{Q}$ values. It should be noted that this technique is best used for surveying small regions in

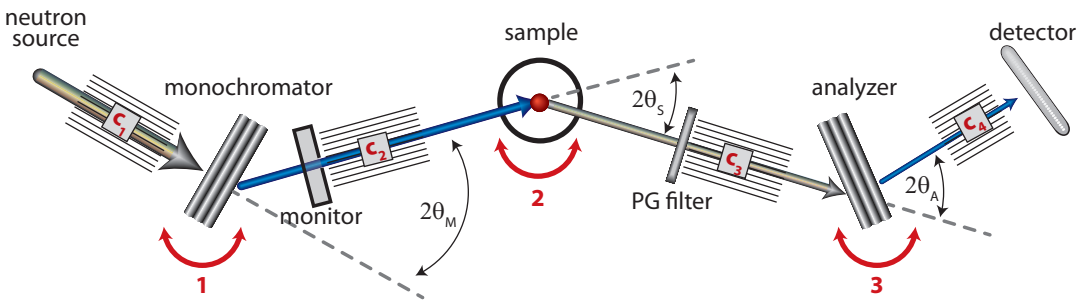

Figure 3.9: Geometry of a TAS. The axes of rotation are denoted with red arrows. The different c_i's show where collimators can be placed.

phase space, as measuring one point at a time yields a relatively low collection rate. However, TAS offers good resolution, low background and high versatility.

A simplified general version of the TAS geometry is shown in Figure 3.9. It is common practice to have a monitor between the monochromator and the sample. A monitor is simply a neutron detector with a very low efficiency to reduce absorption and reduction of neutron flux. Its presence ensures that the detector will accumulate signal until a specified number of monitor counts been measured, thus circumventing problems arising from flux changes of the incoming white beam.

Monochromator and Analyzer

A monochromator is a crystal with a well defined d-spacing used to select the wavelength (or energy) of the incident neutron beam through Bragg diffraction from the lattice planes. By rotating the monochromator crystal, a specified $\mathbf{k_i}$ can be defined. The analyzer is a second monochromating crystal. Its placement after the sample defines the $\mathbf{k_f}$ of the scattered neutrons to be detected. Depending on the monochromator that is being used, it can also be advantageous to have a filter in the beam to remove any higher-order neutrons. (Pyrolytic graphite (PG) is an extremely effective material for this purpose [44], as can been seen in Paper VI.)

Ideally, the material used for a monochromator should have a large scattering length density, low absorption coefficient, and small incoherent scattering cross section. Typical materials for monochromators include PG, silicon, germanium and copper [44]. Due to the inherent beam divergence of the incoming white beam in-

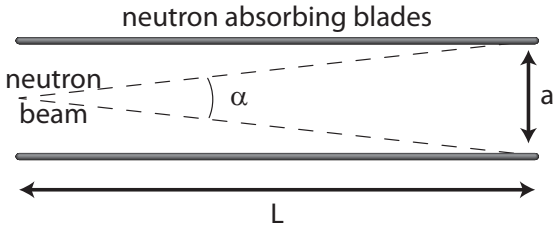

Figure 3.10: Schematic of a Soller collimator showing the relation of the beam divergence to the length and spacing of the collimation blades.

cident on the monochromator, the use of a perfect single crystal would result in an unacceptable loss in intensity (i.e. too many neutrons would be "thrown away"). For this reason mosaic crystals are often employed. A mosaic crystal is composed of small single crystallites, whose orientations vary slightly. Typical values for the mosaicity, i.e., the distribution of normal vectors of the crystallites, are on the order of 3-5%. The small misalignments of the crystallites make the monochromator better at accommodating the divergence of the neutron beam, as well as increasing the bandwidth of accepted wavelengths. This results in an increased flux; however it is at the cost of wavelength resolution.

Collimation

The beam divergence can be improved with the use of collimators; however, an extremely tight collimation will reduce neutron flux. As can be seen in Figure 3.9, there are several places along the TAS beam path where collimators can be used. Soller collimators define the horizontal beam divergence using an array of parallel neutron absorbing blades of a specified length. The spacing between the blades can be increased or decreased to relax or tighten the collimation, respectively. Thus, the angular divergence (α) of the collimated beam is given by

$$\tan\left(\frac{\alpha}{2}\right) = \frac{a}{2L}, \text{ which simplifies to } \alpha = \frac{a}{L}, \tag{3.1}$$

where a is the spacing between the blades and L is the blade length, as depicted in Figure 3.10.

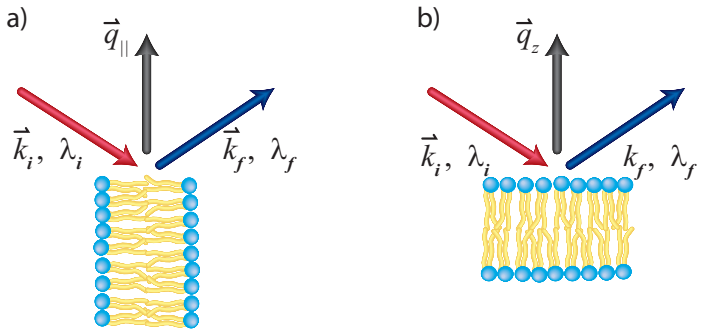

Figure 3.11: a) In-plane and b) out-of-plane scattering geometries for membrane systems.

Oriented Samples

If the sample is a highly oriented 2-dimensional system, as is the case with all of the membrane systems examined in this work, the total scattering vector, **Q**, can be thought of as a sum of its in-plane ($q_{||}$) and out-of-plane (q_z) components. By carefully orienting such a sample in the neutron beam, one can ensure that the primary contribution to the scattering vector is the result of either in-plane *or* out-of-plane scattering. This gives a way to segregate signals resulting from scattering caused by structures in the plane of the bilayer (i.e. lipid tail spacing), or perpendicular to the membrane plane, (i.e. lamellar d_z-spacing).

A particularly advantageous feature of the TAS geometry is the sample's rotational degree of freedom. The experiments presented in Papers V and VI examine the structure of highly oriented, solid supported lipid bilayer systems under physiological conditions. Preserving the physical state of the sample, between measurements which characterize the system's in-plane and out-of plane structure, is paramount. By simply rotating the entire sample stage by 90°, the scattering vector can be placed either in the plane of the membrane (Figure 3.11 a) or perpendicular to the plane of the membrane (Figure 3.11 b). Thus, the TAS setup can be switched from an in-plane to a reflectivity mode without disrupting the sample environment or compromising the state of the bilayer system.

3.2.2 Backscattering

Neutron backscattering spectrometers offer a method of measuring the inelastic scattering in a system over a broad dynamic range ($\sim 10^2$ μeV), with an extremely high energy resolution ($\sim$0.1-20 μeV) [45]. This energy range corresponds to dynamics occurring in the nanosecond regime [46], bridging the gap between the short picosecond time scales measured by time-of-flight (TOF) spectrometers and the long 10-100 ns regime accessible using neutron spin-echo. This particular range makes it a useful tool for the study of diffusive motions in lipid membrane systems.

For many neutron spectrometers, the energy resolution is improved by creating a well-defined monochromatic incident beam; however, this often results in a low neutron flux. The characteristic feature of the backscattering geometry is that its high energy resolution is achieved by using a Bragg angle (2θ) close to 180° (hence, "backscattering") for the analysis of the scattered neutron wavelength, which is achieved with a bank of analyzer crystals. The backscattering condition yields an extremely well defined wavelength (or energy) resolution of the beam. This property can be seen directly by the differentiation of Bragg's law:

$$\begin{aligned} \lambda &= 2d\sin\theta \\ \frac{\Delta\lambda}{\lambda} &= \frac{2\sin\theta\ \Delta d\ +\ 2d\cos\theta\ \Delta\theta}{2d\sin\theta} \\ \frac{\Delta\lambda}{\lambda} &= \frac{\Delta d}{d} + \frac{\Delta\theta}{\tan\theta}. \end{aligned} \tag{3.2}$$

As θ goes to 90°, $\tan\theta$ approaches ∞, making the second term in Equation 3.2 negligible. The wavelength resolution is now, to first order, independent of the beam divergence, $\Delta\theta$, and is only dependent on the mosaicity of the analyzer crystal, Δd. The resolution is optimized by using perfect, silicon crystals with $\Delta d/d$ values on the order of 10^{-4} [46].

There are two types of backscattering spectrometers that were used in this body of work: a TOF-XTL spectrometer and an XTL-XTL spectrometer. The distinction between the two will be described in the following sections. TOF stands for the use of neutron time-of-flight techniques to determine the neutrons' velocity. As neutrons move with moderate velocities, on the order of 1000 m/s, their time of flight over a

well defined path can be used to precisely determine their velocity (and energy). XTL (short for crystal) refers to monochromatization using single crystal monochromators or analyzers to determine the wavelength of the incoming or scattered neutrons.

XTL-XTL Backscattering Spectrometer

The XTL-XTL backscattering spectrometer employs single crystals with near 180° Bragg angles for both the monochromator and analyzers. A schematic of this experimental geometry is shown in Figure 3.12. It should be noted that to achieve a perfect backscattering condition, the neutron beam has to pass through the sample twice. This setup only works well for weakly scattering samples (on the order of 10% scatterers). Most instruments work in an almost perfect backscattering configuration, with angles slightly deviating from 180° by positioning the neutron detector slightly above or below the scattering plane to avoid passage of the scattered neutron beam through the sample.

To perform an energy scan, different incoming wavelengths must be selected. The neutron wavelength could be varied by changing the Bragg angle, $2\theta_M$; however, maintaining $2\theta_M \sim 180°$ is essential for backscattering. A Doppler drive is sometimes used to create a finite bandwidth of wavelengths by moving the monochromator crystal back and forth. This motion results in a transfer of kinetic energy, either from the monochromator to the neutrons or vice versa, resulting in a beam of neutrons with a distribution of velocities. In the case of the backscattering spectrometer used for the work shown in Paper II (IN13), the wavelength distribution was created by varying the temperature of a thermally expanding monochromator crystal (CaF_2).

TOF-XTL Backscattering Spectrometer

The TOF-XTL backscattering spectrometer is an instrument that is well adapted for spallation sources, as it uses a pulsed, white neutron beam. In this geometry (shown in Figure 3.13) the neutron energies in the incoming beam are defined through TOF methods. The energy of the selected scattered beam is then known from the scattering angle of the analyzer crystals. Should a narrower wavelength bandwidth be required in the incident neutron beam, a series of choppers can be used to act as a velocity selector.

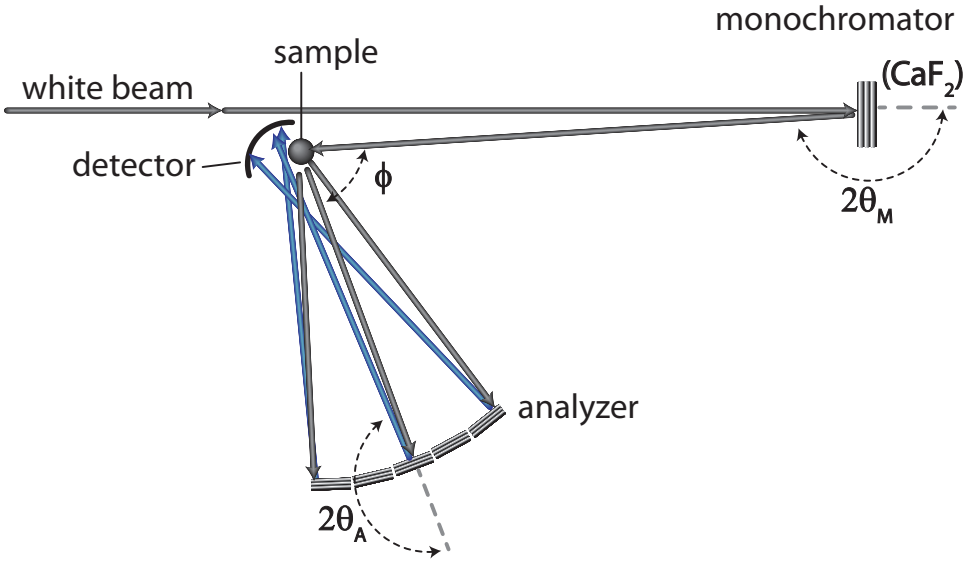

Figure 3.12: Experimental geometry of an XTL-XTL backscattering spectrometer. The Bragg angles for the monochromator and analyzers crystals are $2\theta_M$ and $2\theta_A$, respectively, and the scattering angle from the sample is denoted as ϕ. This setup is similar to that used in the works of Section 4.2 (IN13).

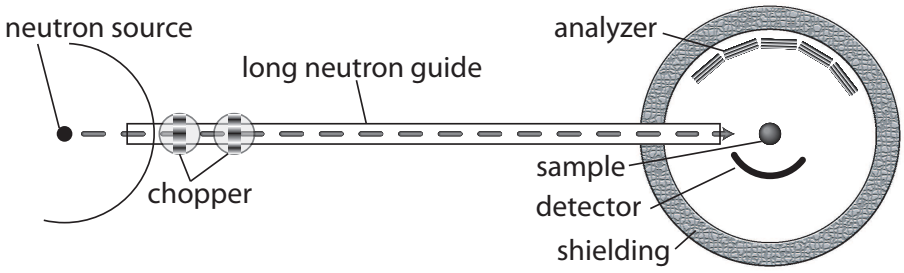

Figure 3.13: Experimental geometry of a TOF-XTL backscattering spectrometer. This setup is similar that used in the works of Section 4.1 (BASIS).

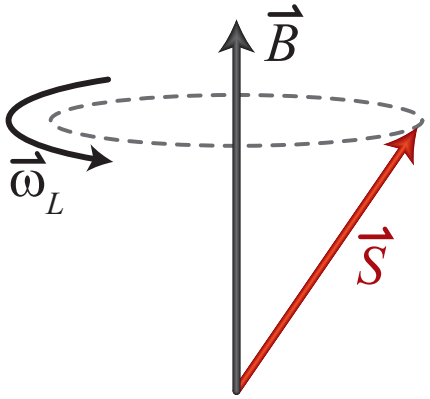

Figure 3.14: Larmor precession of a spin around a magnetic field

3.2.3 Neutron Spin-Echo

Neutron spin-echo (NSE) spectrometry, developed by Ferenc Mezei [47], is a technique that has become highly popularized for the study of soft matter systems [48]. It is capable of monitoring the slowest time scales of all inelastic neutron scattering techniques (as slow as 100s of nanoseconds), by using neV energy resolution. These qualities make it particularly useful for studying the dynamics of large molecules, like polymers, but also dynamics in biological systems. One key feature which differentiates NSE from other neutron scattering techniques is that the characteristic quantity that is measured is the intermediate scattering function (ISF), $I(\mathbf{Q}, t)$, rather than $S(\mathbf{Q}, \omega)$, giving direct access to the, often more physically meaningful, relaxation time, τ.

NSE uses the Larmor precession of a neutron spin in a magnetic field to determine how its velocity is changed by the scattering event. A magnetic spin moment, within a magnetic field, will precess around the axis in which the field points (as shown in Figure 3.14). The frequency of precession, ω_L, is given by

$$\omega_L = -\gamma B, \tag{3.3}$$

where B is the magnetic field and γ is the gyromagnetic ratio ($\gamma = \frac{-eg}{2m}$), which is the same for all neutrons.

A sketch of a typical NSE spectrometer is shown in Figure 3.15. The neutron

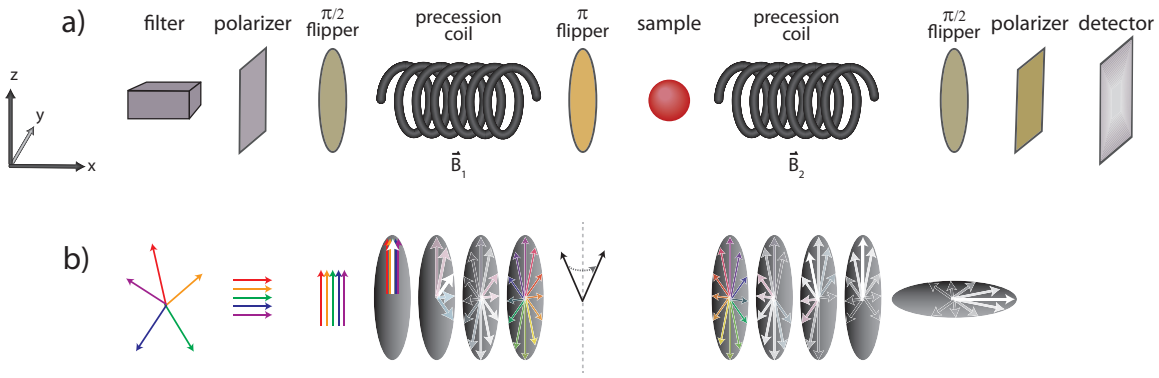

Figure 3.15: a) Sketch of a standard neutron spin-echo spectrometer. b) Depiction the neutron spin state as it passes through the components above.

source emits neutrons with a wide range of velocities and spins which point in various directions. A filter selects neutrons with a ∼10-20% wavelength (or velocity) spread. An advantage of the spin-echo technique is that the spin-echo condition is fulfilled for all wavelengths. It decouples energy resolution from the monochromaticity of the neutron beam. The intensity is drastically increased as compared to other techniques, without compromising the energy resolution.

The neutron beam is polarized with a Mezei cavity, which uses an array of mirrors and polarizers to align neutron spins along the x-axis (see Figure 3.15). A $\pi/2$ spin flipper aligns spins along the z-axis. The neutrons now propagate through a region of carefully aligned, homogeneous magnetic field, B_1, oriented along x-axis. This causes the neutron spins to precess around the field direction with the same frequency, ω_L (as depicted in Figure 3.14). The large magnetic fields and long guide enable the neutrons to perform upwards of 10^5-10^6 full rotations resulting in an energy resolution on the order of neV. The angle of rotation of the neutron spin, φ, is inversely proportional to the velocity of neutron travelling through the magnetic field,

$$\varphi = \gamma \int \frac{\mathbf{B}\mathrm{dl}}{v}. \tag{3.4}$$

Because a distribution of neutron velocities was initially selected, the spins will rotate through a range of different angles, creating a uniform spectrum of spin angles in the y-z plane.

Conceptually it is easy to think of a spin-echo experiment having two long magnetic coils of with magnetic fields in opposite directions. One field would wind up the spin before the sample, and the other field would unwind it after it has interacted with the sample. In reality, having two such strong opposing magnetic fields within close proximity to each other would cause a non-uniform field close to the sample. To circumvent this problem, after the neutrons have precessed through the first magnetic field, they then pass through a π flipper. This rotates the spins by 180° around z-axis, making it such that a second magnetic field, B_2 also oriented along x-axis, will *effectively* precess the spins in the opposite direction. Once the neutrons' spins have been flipped they will interact with the sample, before passing through the second magnetic field. The spins are then realigned along the x-axis by another $\pi/2$ spin flipper. The reoriented spins pass though a polarizer that selects neutrons with spins aligned in x-direction, which are then detected.

Therefore, a neutron spin-echo spectrometer essentially measures the change in neutron polarization [47]. If all scattering is elastic (no velocity change occurs as a result of sample interaction), then the precession angle of a neutron through the first coil, φ_1, will be the same as the precession angle through the second coil, φ_2, as long as $B_1 = B_2$. Elastic scattering will resulting in a total precession angle of $\Delta\varphi = \varphi_1 - \varphi_2 = 0$ for all incoming neutron velocities, and the initial polarization will be retrieved.

If inelastic scattering occurs, the scattered neutrons will have a different distribution of velocities and will precess through different angles in the second coil, thereby creating a distribution of spin angles about z-axis after precession ($\Delta\varphi \neq 0$). The angular distribution of scattered neutrons leads to a decrease in the detected neutrons after polarization, as not all neutrons will return to their initial polarization state. If the neutron scatters inelastically by a small energy transfer $\hbar\omega$, there will be a linear change in $\Delta\varphi$ ($\Delta\varphi = \tau \cdot \omega_L$), with τ being a real time in the case of quasi-elastic scattering [49]. By slightly varying the strength of B_2, the polarization of the neutron beam can be measured for different Fourier times (τ). When normalized to a perfectly elastic scatterer, such as graphite, the polarization directly corresponds to the intermediate scattering function, $I(\mathbf{Q}, t)$. For example, in the case of a quasi-elastic response, with a Lorentzian lineshape (half-width Γ), the polarization will then show

a single exponential decay,

$$P_{NSE} = \frac{I(\mathbf{Q}, t)}{I(\mathbf{Q}, 0)} = e^{-\Gamma t}. \tag{3.5}$$

As was stated above, this direct measurement of $I(\mathbf{Q}, t)$ in the time domain is a distinguishing characteristic of NSE, as most other neutron spectroscopic techniques involve the measurement of $S(\mathbf{Q}, \omega)$ in the frequency domain, and rely on a Fourier transform to access the time domain.

Chapter 4

Lipid Diffusion in Membranes

Diffusion is the fundamental mechanism for lipids, macromolecules, and proteins to move throughout the lipid matrix of a biological membrane. It also plays an important role in the formation of various macromolecular structures, thus, examining the dynamics of a biological membrane system will give insight into the nature of transient structures, such as lipid rafts. Membrane embedded proteins are responsible for a myriad of essential processes in the cell and are strongly influenced by the dynamics of the surrounding lipid matrix, as well as interactions with neighbouring proteins [50]. The composition of the lipid bilayer itself will result in different diffusion conditions, and the addition of macromolecules, such as cholesterol, may have an advantageous or detrimental effect on how lipids and proteins are able to move and interact [51]. Therefore, to better understand how different membrane structures are formed and how proteins disperse in the membrane, lipid dynamics need to be characterized over a broad range of distances, from micrometer to molecular length scales.

Although lipid diffusion has been extensively studied in the past, there is no coherent model describing the motion of molecules from nanometer to micrometer distances. For example, there are still large discrepancies between lipid diffusion coefficients measured by neutron scattering and fluorescence spectroscopy techniques. The diffusion coefficients measured in membranes by fluorescence spectroscopy [52] tend to be about an order of magnitude slower that those measured by neutron backscattering [53]. It has been suggested, by Rheinstädter *et al.*, that a component

of the over all lipid motion may associated with the coherent movement of loosely bound clusters of lipid molecules, which are ∼30 Å in diameter [54]. The diffusion of a cluster of lipids would be slower than the diffusion of an individual lipid within this cluster. Therefore, it is possible that the fluorescence measurements are sensitive to the slower motion of a lipid moving as part of a coherent cluster over long length scales, while the faster, short length scale dynamics of a lipid moving independently are more effectively probed by neutron scattering experiments.

One of the reasons it is difficult to consolidate the data obtained from these two types of experiments is the challenge associated with measuring dynamics over mesoscopic length scales. As can be seen in Figure 2.5, the resolution of optical techniques is limited by the wavelength of light, and, therefore, they are primarily sensitive to dynamics occurring over micrometer length scales. Neutron scattering can probe length scales ranging from Ångströms to tens of nanometers. This essentially leaves a "blind spot" in the measurement of dynamics occurring over the tens to hundreds of nanometer range.

In addition to the discrepancies in the measurement of long-range lipid motion, there are competing models for lipid motion on very short length scales, fractions of a lipid-lipid distance (i.e. on the other side of the typically measured neutron diffusion window). It is widely accepted that lipids diffuse via a continuous Brownian motion over length scales down to the nearest-neighbour distance. Below that, however, there are a few theories as to what the primary mechanism for short-range lipid motion might be. The "rattling-in-the-cage" model suggests that the lipid molecule moves in a "cage" formed by its neighbouring molecules, before escaping and becoming trapped in another cage, thereby undergoing continuous diffusion over longer length scales. Recently, Busch *et al.* reported evidence for a flow-like process contributing to the motion of lipid molecules in a bilayer system [55], in contradiction to the rattling-in-the-cage model. Such a flow-like process should have a dramatic effect on the motion at shorter length scales.

To gain insight into what the mechanism for lipid motion is at different length scales, a goal of this thesis was to extend the measurable diffusion window by using different neutron techniques. This will foster the process of formulating a more coherent model for lipid and protein diffusion over a broad range of length scales.

The following publications address the challenges associated with the measurement of lateral, in-plane dynamics in solid supported lipid bilayers, as well as present experiments designed to extend the diffusion window observable by neutron scattering.

4.1 Paper I: Diffusion in Single Supported Lipid Bilayers Studied by Quasi-Elastic Neutron Scattering

Clare L. Armstrong, Martin D. Kaye, Michaela Zamponi, Eugene Mamontov, Madhusudan Tyagi, Timothy Jenkins, and Maikel C. Rheinstädter *"Diffusion in single supported lipid bilayers studied by quasi-elastic neutron scattering"*, Soft Matter, **6**, 5864-5867, 2010.

4.1.1 Preface to Paper I

We first chose to examine a very simple model system to study the lipid diffusion process: a uniform single supported lipid bilayer. While this may not be the most biologically relevant sample, it is an important one to understand as this will be a building block from which we can create more complicated customized systems to study.

Because single supported lipid bilayers were being examined, there was also the challenge of conducting an inelastic neutron scattering experiment with very little sample material ($\sim$0.7 mg). Therefore, in addition to characterizing the dynamics of the lipid matrix, this experiment afforded us the opportunity to determine how little sample material could be used while still obtaining a signal from neutron scattering experiment. This may not seem terribly important for examining a simple lipid sample, as both protonated and deuterated lipids are commercially available in reasonable quantities. However, being able to perform an experiment with minimal amounts of material is an important factor to consider in the study lipid-protein systems, as many deuterated and highly topical proteins are not only extremely expensive ($\sim$\$100k), but also difficult to synthesize in large amounts.

There were three main factors that enabled us to examine this system:

First was the sample construction. In order to maximize the amount of sample material the neutron beam sees, we created a stack of single supported bilayers. Our sample was formed by depositing a single lipid bilayer onto each side of 100 double side polished Si wafers, resulting in 200 single solid supported bilayers.

Second was our choice of instrument. The experiment was performed at the backscattering spectrometer, BASIS, at the Spallation Neutron Source (SNS) in Oakridge, the world's most powerful neutron source. At the moment, the SNS is the only source with a high enough flux necessary to detect such a small about of material. The instrument itself, BASIS, also had the appropriate energy resolution to be sensitive to the nanosecond dynamics that we were interested in.

The last crucial experimental consideration was the orientation of the sample. Rather than placing the plane of the sample perpendicular to the beam, as is normally done, the sample was oriented such that the scattering plane was in the plane of the membrane. By doing so, all lateral wavevectors, which are sensitive to lateral diffusion, were detected simultaneously.

The experiment lead us to the conclusion that single supported lipid bilayers exhibit continuous lipid diffusion over nanometer length scales; however, we also observed an enhanced diffusion at nearest-neighbour distances thought to be related to a hopping diffusion. This enhanced diffusion was postulated to be system dependant and due to the higher level of structural order that occurs as a result of substrate effects in the single supported lipid bilayer system.

Author Contributions

- *Designed research:* Maikel C. Rheinstädter
- *Sample fabrication:* **Clare L. Armstrong**, Martin D. Kaye, and Maikel C. Rheinstädter
- *Performed experiment:* **Clare L. Armstrong**, Martin D. Kaye, Michaela Zamponi, Eugene Mamontov, Madhusudan Tyagi, Timothy Jenkins, and Maikel C. Rheinstädter
- *Analysed data:* **Clare L. Armstrong**, Martin D. Kaye, and Maikel C. Rheinstädter

- *Wrote the manuscript:* **Clare L. Armstrong** and Maikel C. Rheinstädter

COMMUNICATION www.rsc.org/softmatter | Soft Matter

Diffusion in single supported lipid bilayers studied by quasi-elastic neutron scattering†

Clare L. Armstrong,*[a] Martin D. Kaye,[a] Michaela Zamponi,[bc] Eugene Mamontov,[b] Madhusudan Tyagi,[d] Timothy Jenkins[d] and Maikel C. Rheinstädter[ae]

Received 6th July 2010, Accepted 17th September 2010
DOI: 10.1039/c0sm00637h

It seems to be increasingly accepted that the diversity and composition of lipids play an important role in the function of biological membranes. A prime example of this is the case of lipid rafts; regions enriched with certain types of lipids which are speculated to be relevant to the proper functioning of membrane embedded proteins. Although the dynamics of membrane systems have been studied for decades, the microscopic dynamics of lipid molecules, even in simple model systems, is still an active topic of debate. Neutron scattering has proven to be an important tool for accessing the relevant nanometre length scale and nano to picosecond time scales, thus providing complimentary information to macroscopic techniques. Despite their potential relevance for the development of functionalized surfaces and biosensors, the study of single supported membranes using neutron scattering poses the challenge of obtaining relevant dynamic information from a sample with minimal material. Using state of the art neutron instrumentation we were, for the first time, able to model lipid diffusion in single supported lipid bilayers. We find that the diffusion coefficient for the single bilayer system is comparable to the multi-lamellar lipid system. More importantly, the molecular mechanism for lipid motion in the single bilayer was found to be a continuous diffusion, rather than the flow-like ballistic motion reported in the stacked membrane system. We observed an enhanced diffusion at the nearest neighbour distance of the lipid molecules. The enhancement and change of character of the diffusion can most likely be attributed to the effect the supporting substrate has on the lipid organization.

Although phospholipid membranes have been studied for decades[1] there is still no consistent picture of lipid dynamics, even in simple model systems. While techniques such as fluorescence recovery after photobleaching (FRAP) and fluorescence correlation spectroscopy (FCS) are capable of measuring the diffusion of lipid molecules on micrometre length scales, quasi-elastic neutron scattering (QENS) has proven to be an important tool to study nanoscale dynamics and diffusion on a nanometre length scale. In their seminal 1989 paper, Pfeiffer *et al.*[2] studied the local dynamics of lipid molecules in stacked fluid lipid membranes using incoherent neutron scattering techniques. Here a detailed model of lipid dynamics, including rotations, librations and diffusion, was proposed. More recently, this topic was revisited by Busch *et al.*[3] using state of the art neutron scattering techniques. Their primary finding was that the molecular mechanism for long range lipid diffusion in stacked membranes is a flow-like motion rather than the traditional diffusive motion. Ballistic motion was speculated to be a more efficient search strategy as compared to a Brownian motion.[4,5]

Despite their potential relevance to bioengineering applications, such as biosensors and surface functionalization[6,7] dynamical neutron scattering experiments in single supported bilayers have been limited in the past, as the minimal amount of sample material in a single bilayer results in a low scattering signal. Recent developments in neutron scattering instruments, and increasingly powerful neutron sources, now make it possible to observe dynamics in single bilayers. How the interaction between membrane and substrate affects lipid organization and dynamics, as compared to multi-lamellar or free-standing membranes, is a fundamental question.

We have studied the nanosecond lipid diffusion in a single phospholipid bilayer supported on a silicon wafer. From quasi-elastic neutron scattering, acquired using a backscattering spectrometer, the mechanism of the lipid diffusive motion could be modeled. While flow-like motion was reported in stacked bilayer systems,[3] we find evidence for a continuous diffusion with an enhanced diffusion at the nearest neighbor distance.

Single-supported bilayers of the model system 1,2-dimyristoyl-sn-*glycero*-3-phoshatidylcholine (DMPC) were prepared by vesicle fusion and hydrated by heavy water (D_2O).[8] 100 double-side polished, 2″, 300 μm thick, Si(100)-wafers were cleaned by immersion in an $H_2O_2^+$ sulfuric acid mixture (volume fraction of 70%

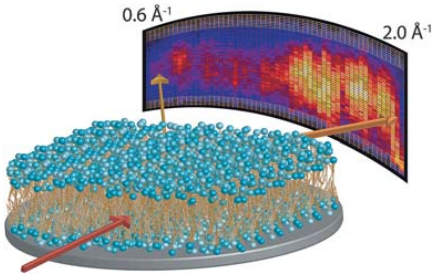

Fig. 1 A sketch of the experimental setup. Each solid supported single bilayer is aligned such that the plane of the membrane is in the scattering plane. In-plane q between 0.6 and 2.0 $Å^{-1}$ are then measured simultaneously.

[a]*Department of Physics and Astronomy, McMaster University, Hamilton, ON, Canada. E-mail: armstc5@mcmaster.ca; Fax: (+905) 546-1252; Tel: (+905)525-9140 x26376*
[b]*Spallation Neutron Source, ORNL, Oak Ridge, TN, USA*
[c]*Jülich Center for Neutron Science, FZ Jülich, Jülich, Germany*
[d]*NIST Center for Neutron Research, NIST, Gaithersburg, MD, USA*
[e]*Canadian Neutron Beam Center, NRC, Chalk River, ON, Canada*
† Electronic supplementary information (ESI) available: Details regarding the data analysis. See DOI: 10.1039/c0sm00637h

concentrated H_2SO_4, 30%H_2O_2 at 90 °C for 30 min). This strongly oxidizing combination removes all organic contaminants on the surface, but does not disturb the native silicon oxide layer. The wafers were then rinsed and stored under distilled water before use. 200 ml of a 5×10^{-3} mol L^{-1} Hepes, 5×10^{-3} mol L^{-1} $MgCl_2$, and 100×10^{-3} mol L^{-1} KCl buffer solution was prepared and heated to 55 °C. DMPC was added to the buffer solution up to a concentration of 1.5 mg ml^{-1}. The milky solution, which initially contained giant multi-lamellar vesicles, was sonicated (50% duty cycle, power level 4) for 15 h until the solution became transparent and small uni-lamellar vesicles formed. The hydrophilic Si wafers were then completely immersed in the solution for 1 h. The lipid solution was kept at 55 °C during the whole process to keep the bilayers in their fluid phase. After 1 h the wafers were thoroughly rinsed with ~2 L of distilled water to remove excess vesicles from the surface. Through this procedure, small bilayer patches initially develop on the substrate, which eventually undergo a transition into a large uniform single bilayer after approximately 20–25 min.[8] The substrates were then annealed for 72 h at 55 °C in an oven in air before mounting in an aluminium sample can, and rehydrated.

Because the sample was hydrated with D_2O, the incoherent neutron scattering experiment is sensitive to local dynamics of the (protonated) lipid molecules. About 75% of the scattering comes from hydrogen atoms attached to the lipid acyl chains in the hydrophobic membrane core, and about 25% from hydrogen atoms located in the head group region. To increase the scattering signal, 100 wafers (resulting in 200 single bilayers) were mounted horizontally into the spectrometer, such that the neutron beam was always in the plane of the membrane ($q_{||}$). In contrast to previous studies, this type of sample orientation probes $q_{||}$ values between 0.6 and 2.0 $Å^{-1}$ simultaneously, corresponding to lateral length scales of 3 Å to 10 Å. The experimental setup is shown in Fig. 1. The sample was sealed in an aluminium sample can and placed inside a closed-cycle refrigerator (CCR) during the experiment. A sufficient amount of D_2O was added before closing to ensure full hydration of the bilayers (26 water molecules per lipid molecule), approximately 100 μL.

Elastic incoherent neutron scattering experiments were carried out using the high flux neutron backscattering spectrometer HFBS at the NIST Center for Neutron Research (NCNR), Gaithersburg, in its standard setup with Si (111) monochromator and analyzer crystals corresponding to an incident and analyzed neutron energy of 2.08 meV ($\lambda = 6.27$ Å). At the ~0.8 μeV resolution used, only hydrogen movements with characteristic times slower than 1 ns are monitored. The hydrogen atoms reflect the movements of larger groups to which they are attached, such as lipid head groups and carbon tails. Freezing and melting of molecular degrees of freedom can easily be identified, as they lead to jumps or kinks in the recorded intensity. Because the elastic intensity is related to the molecular mean-square thermal fluctuations $\langle \delta u^2 \rangle$, $S_{inc}^{el}(Q) \propto \exp\left(- \left\langle \frac{\delta u^2(T)}{6} \right\rangle Q^2 \right)$, each point on an elastic scan provides a value for the mean-square displacement (MSD) at a particular temperature.[9] The MSD was calculated and is shown in Fig. 2 over a temperature range of 240–355 K. Data were taken while heating the sample at a rate of 0.08 K min^{-1}. The inset in Fig. 2 depicts a sketch of a hydrated single supported bilayer as suggested by Nováková *et al.* from X-ray reflectivity. Each lipid molecule was found to be associated with 26 water molecules. Eight water molecules per lipid were found to be located within the head group region, while 18 water molecules per lipid form a hydration layer on the surface of the bilayer. There was also evidence of the presence of water molecules between the substrate and the lower leaflet.[10]

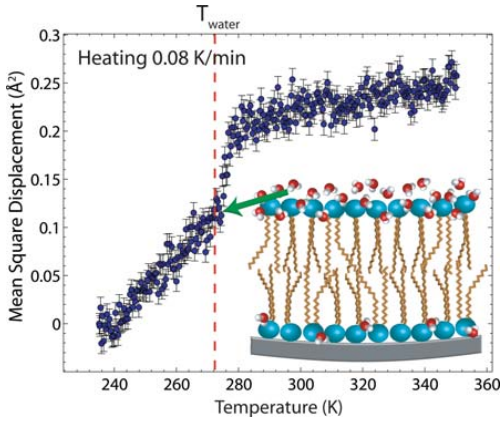

Fig. 2 The MSD of the lipid molecules over a temperature range of 240 to 355 K. The error bars shown are the result of statistical uncertainty. Melting of the hydration water was observed at approximately 273 K. No additional phase transition was observed at higher temperatures.

A melting transition at about $T_{water} = 273$ K was observed (see Fig. 2), which can most likely be assigned to the melting of the membrane hydration water. In multi-lamellar DMPC systems the transition from the gel into the fluid phase occurs at $T_m = 23.4$ °C = 296.6 K in fully hydrated bilayers and appears as a pronounced step in the MSD.[11,12] No such transition was observed. It was reported that the transition temperature may shift up to 318 K for nanometre sized patches of single supported bilayers.[13,14] The transition from the gel into the fluid phase involves a drastic increase in volume and area of the lipid molecules. For patches, the volume and area difference of the lipid molecules between the two phases can most likely relax over defects in the bilayer coverage.[13] In our samples, the transition was possibly suppressed due to large uniform and defect free single bilayers. While we cannot exclude the possibility that the upper and lower leaflets have different transition temperatures, the technique used should be sensitive enough to detect a transition in the individual leaflets. The diffusion constant that we determined is an order of magnitude faster than diffusion reported in the gel phase of multi-lamellar systems[2] and corresponds well with the diffusion constants reported in fluid multi-lamellar membranes, as discussed below. At 303 K, the single DMPC bilayers can, therefore, tentatively be characterized to be in a fluid state with an enhanced structural order; however, further structural investigations are required to unambiguously determine the structural state of the bilayer.

To measure the slow nanosecond dynamics, μeV energy resolved spectra were measured on the BASIS backscattering spectrometer at the Spallation Neutron Source, at Oak Ridge National Laboratory. The experiments were performed using a 60 Hz chopper setting with the incident wavelength bandwidth centered at of 6.4 Å. The Si (111) crystal analyzers provide an energy resolution of ~3 μeV, FWHM of the elastic peak, and a Q-range of 0.6 to 2.0 $Å^{-1}$. The dynamic range used was −80 to 80 μeV. Typical counting times were ~24 h.

Different diffusion models have been proposed. For a continuous diffusion, the quasi-elastic broadening is described by a Lorentzian

peak shape, with a full width at half maximum (FWHM) that shows a $q_{\|}^2$ dependence,

$$FWHM_L(q_{\|}) = 2\hbar D q_{\|}^2 \quad (1)$$

where D is the diffusion constant.[15]

A flow motion, as suggested in ref. 3,4 is described by a Gaussian component, where the width of the function has a linear $q_{\|}$ dependence,

$$FWHM_G\left(q_{\|}\right) = 2\sqrt{2ln(2)}\hbar v_o q_{\|}. \quad (2)$$

Here v_o refers to the ballistic velocity of the lipid molecules. In an unconstrained motion, v_o would correspond to the thermal velocity, $\sqrt{2k_BT/m}$.

Fig. 3 (a) and (b) depict exemplary spectra at $q_{\|} = 0.9$ and 1.3 Å^{-1}. The total scattering can be described by a narrow central component due to instrumental resolution and a quasi-elastic broadening between ~1–24 μeV. There is also evidence for a smaller broad component, similar to what has been observed by Busch *et al.* This broad component, most likely due to vibrations and librations of the lipid molecules, has a width of ~200 μeV, but is clearly out of the dynamic range of the instrument. The narrow component was assigned to the lateral diffusion of the lipid molecules. The broadening could well be fitted using a Lorentzian function rather than a Gaussian. The data were fit with three components: an asymmetric Gaussian and a background, a narrow (1–24 μeV) Lorentzian function to describe the lipid diffusion, and a broad (~200 μeV) Lorentzian function. The instrumental resolution was determined by fitting data measured in the frozen state of the bilayers, at $T = 240$ K, using the asymmetric Gaussian function to accommodate the slight asymmetry in the resolution function of the BASIS spectrometer†. The parameters were then used to fit the quasi-elastic broadening observed at $T = 303$ K.

Fig. 4 plots the FWHM of the Lorentzian, following deconvolution with the instrumental resolution, as a function of $q_{\|}^2$. The data can well be fit by a straight line, making it possible to determine the diffusion constant using eqn (1), $D = 60 \pm 10 \times 10^{-12}$ m^2 s^{-1}. The data deviate from the straight line around $q_{\|} = 1$ Å^{-1}, giving rise to faster dynamics. Diffusion seems to be enhanced at nearest neighbour distance of the lipid molecules of about 6 Å (2π/1 Å^{-1}).

When comparing to eqn (1) and (2), the most likely mechanism for diffusion in single supported bilayers seems to be continuous diffusion rather than the flow-like motion reported for multi-lamellar

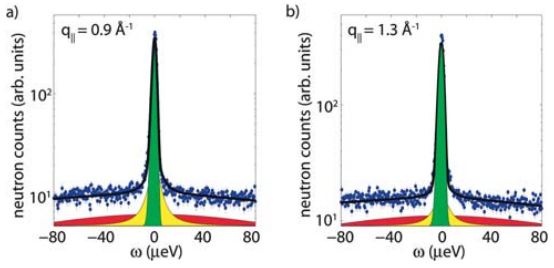

Fig. 3 Spectra for a) $q_{\|} = 0.9$ Å^{-1} and b) 1.3 Å^{-1}. The error bars shown are the result of statistical uncertainty. Data were fitted (black) with the instrumental resolution (green), a Lorentzian quasi-elastic broadening (yellow) and an additional broad Lorentzian (red).

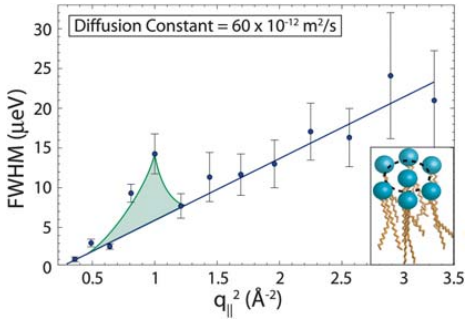

Fig. 4 FWHM of the Lorentzian as a function of $q_{\|}^2$. When excluding data points around $q_{\|} = 1$ Å^{-1}, data can be fit using a linear function. Diffusion seems to be enhanced around $q_{\|} = 1$ Å^{-1}, as indicated by the peak. Error bars correspond to a 10% confidence level in the Lorentzian fit. The inset shows a sketch of the lipid packing that might give rise to an enhanced nearest neighbour diffusion.

membranes stacks. The peak like feature around 1 Å^{-1} in Fig. 4 shows evidence for an enhanced diffusion of the lipid molecules, possibly triggered by voids in the ordered arrangement of lipids. The diffusion constant we found lies well within the range of diffusion constants of fluid phospholipid bilayers reported in the literature (18–180 × 10^{-12} m^2 s^{-1} [2,3,16,17]). However, because we cannot resolve a possible difference in the diffusion constants of the lipids in the upper and lower leaflets of the bilayer, we cannot exclude the possibility that the diffusion in the lower leaflet is suppressed by the presence of the substrate, while the diffusion in the upper leaflet may be enhanced by a highly ordered fluid phase of the lipids, thereby averaging to a diffusion constant which is comparable to multilamellar systems.

This change of character and enhanced nearest neighbour diffusion is most likely to be due to the highly ordered fluid phase of the lipids caused by the confinement of the defect free bilayer on the substrate. Note that the diffusion constants, as determined by incoherent neutron scattering, are usually an order of magnitude above the values obtained by macroscopic techniques in single[18,19] and multi-lamellar systems.[20] This may be due to coherent motion of lipid molecules, which are speculated to move as loosely bound clusters rather than individual molecules.[4,21]

This experiment has also demonstrated the feasibility of performing inelastic neutron scattering experiments on single supported bilayer systems. Complex membranes containing different membrane embedded proteins, as well as cholesterol, can be prepared. By tuning bilayer properties, such as elasticity, the impact of membrane properties on protein function may be elucidated. Inelastic neutron scattering experiments were once limited by the availability of sample material. The sample used for this study contained less than 1 mg of lipids. This opens up new opportunities for dynamical neutron scattering experiments in relevant and highly topical membrane/protein systems.

Acknowledgements

This research was supported by the Natural Sciences and Engineering Research Council of Canada (NSERC), the National Research

Council Canada (NRC) and the Canada Foundation for Innovation (CFI). This work utilized facilities at the NIST Center for Neutron Research supported in part by the NSF under agreement No. DMR-0454672. Research at Oak Ridge National Laboratory's Spallation Neutron Source was sponsored by the Scientific User Facilities Division, Office of Basic Energy Sciences, U. S. Department of Energy.

References

1 G. Pabst, N. Kučerka, M.-P. Nieh, M. C. Rheinstädter and J. Katsaras, *Chem. Phys. Lipids*, 2010, **163**, 460–479.
2 W. Pfeiffer, T. Henkel, E. Sackmann and W. Knorr, *Europhys. Lett.*, 1989, **8**, 201–206.
3 S. Busch, C. Smuda, L. Pardo and T. Unruh, *J. Am. Chem. Soc.*, 2010, **132**, 3232–3233.
4 E. Falck, T. Róg, M. Karttunen and I. Vattulainen, *J. Am. Chem. Soc.*, 2008, **130**, 44–45.
5 A. James, M. Plank and R. Brown, *Phys. Rev. E: Stat., Nonlinear, Soft Matter Phys.*, 2008, **78**, 051128.
6 E. Sackmann, *Science*, 1996, **271**, 43–48.
7 M. Tanaka and E. Sackmann, *Nature*, 2005, **437**, 656–663.
8 R. Richter, A. Mukhopadhyay and A. Brisson, *Biophys. J.*, 2003, **85**, 3035–3047.
9 D. J. Bicout and G. Zaccai, *Biophys. J.*, 2001, **80**, 1115–1123.
10 E. Nováková, K. Giewekemeyer and T. Salditt, *Phys. Rev. E: Stat., Nonlinear, Soft Matter Phys.*, 2006, **74**, 051911.
11 M. Weik, U. Lehnert and G. Zaccai, *Biophys. J.*, 2005, **89**, 3639–3646.
12 M. C. Rheinstädter, T. Seydel, F. Demmel and T. Salditt, *Phys. Rev. E: Stat., Nonlinear, Soft Matter Phys.*, 2005, **71**, 061908.
13 A. F. Xie, R. Yamada, A. A. Gewirth and S. Granick, *Phys. Rev. Lett.*, 2002, **89**, 246103.
14 A. Charrier and F. Thibaudau, *Biophys. J.*, 2005, **89**, 1094–1101.
15 M. Bée, *Quasielastic Neutron Scattering: Principles and Applications in Solid State Chemistry, Biology and Materials Science*, Taylor & Francis, 1988.
16 A. Buchsteiner, T. Hauß, S. Dante and N. Dencher, *Biochim. Biophys. Acta, Biomembr.*, 2010, **1798**, 1969–1976.
17 S. König, W. Pfeiffer, T. Bayerl, D. Richter and E. Sackmann, *J. Phys. II*, 1992, **2**, 1589–1615.
18 M. Roark and S. E. Feller, *Langmuir*, 2008, **24**, 12469–12473.
19 C. Scomparin, S. Lecuyer, M. Ferreira, T. Charitat and B. Tinland, *Eur. Phys. J. E*, 2009, **28**, 211–220.
20 R. Merkel, E. Sackmann and E. Evans, *J. Phys.*, 1989, **50**, 1535–1555.
21 M. C. Rheinstädter, J. Das, E. J. Flenner, B. Brüning, T. Seydel and I. Kosztin, *Phys. Rev. Lett.*, 2008, **101**, 248106.

Supplementary Material (ESI) for Soft Matter

Electronic Supplimentary Information for: Diffusion in single supported lipid bilayers studied by quasi-elastic neutron scattering

Clare L. Armstrong*[*a], Martin D. Kaye[a], Michaela Zamponi[b,c], Eugene Mamontov[b], Madhusudan Tyagi[d], Timothy Jenkins[d], and Maikel Rheinstädter[a,e]

[a] *Department of Physics and Astronomy, McMaster University, Hamilton, ON, Canada*
[b] *Spallation Neutron Source, Oak Ridge National Laboratory, Oak Ridge, TN, USA*
[c] *Jülich Center for Neutron Science, Forschungszentrum Jülich, Jülich, Germany*
[d] *NIST Center for Neutron Research, NIST, Gaithersburg, MD, USA*
[e] *The Canadian Neutron Beam Center, Chalk River Laboritories, Chalk River, ON, Canada*

Resolution Fitting Procedure

The 240 K low teperature data was used as the resolution for this experiment. This data was fit with an asymmetric Gaussian function to accomodate the slight asymmetry in the resolution of the BASIS spectrometer. This function was introduced by Lan and Jorgenson (2001). The asymmetry in the Gaussian is introduced by incorporating an exponential function into one side of the Gaussian peak, as shown by the following equation[1]:

$$y = y_o + H(x_o - x)Ae^{-\left[\frac{(x-x_O)^2}{2\sigma^2+\tau|x-x_O|}\right]} + H(x - x_o)Ae^{-\left[\frac{(x-x_O)^2}{2\sigma^2}\right]}, \qquad \textbf{(1)}$$

where y_o is the constant background, H is a Heavyside function, x_o is the center of the Gaussian function, A is the amplitude of the Gaussian, σ is the varience, and τ is the time constant of the exponential decay, which determines the asymmetry.

For each q value, the low temperature data were fit using Equation (1). The resolution was then used to fit the high temperature data.

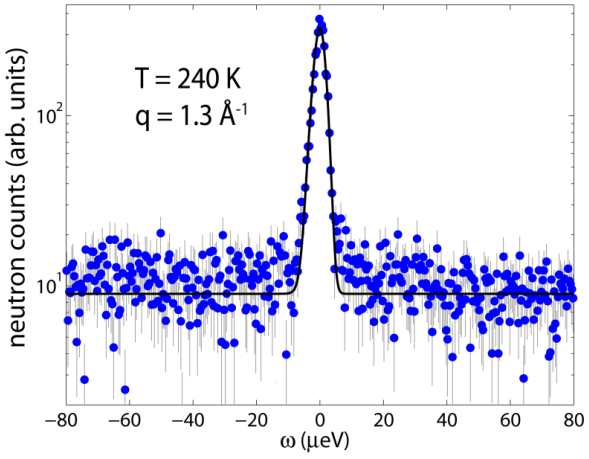

Figure ESI-1: Data obtained from the 240 K low temperature lipid sample at q = 1.3 Å^{-1} plotted on a log scale. The data was fit using the asymmetric Gaussian function described in the text. The resolution function is then used to fit the high temperature data.

Supplementary Material (ESI) for Soft Matter

Sample can with uncoated wafers

Prior to measuring the sample, data was taken on the aluminum can filled with uncoated Si wafers as a control sample. The results of this data collection are plotted on the same graph as the low temperature resolution and fit, in Figure ESI-2. It was found that this control sample showed no quasi-elastic scattering. When compared to the low temperature data, about 65% of the elastic signal stems from the substrates. The sample bilayers contribute about 35% to the scattering signal.

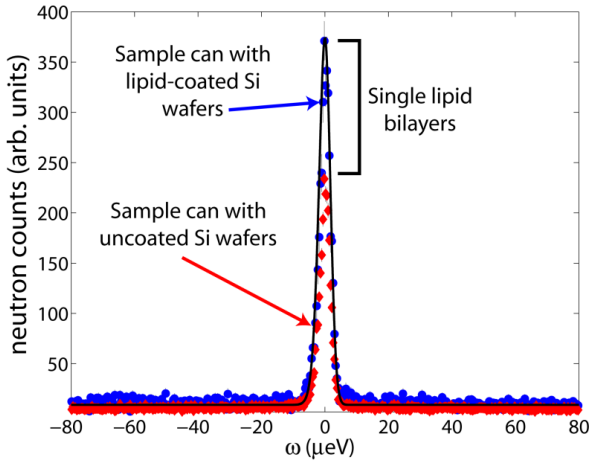

Figure ESI-2: Data from the low temperature lipid-coated Si wafers (blue) and the uncoated Si wafers (red) in the aluminum sample can. The lipid coated sample has a higher intensity elastic peak due to the additional contribution of the frozen dynamics of the lipid system.

[1] K. Lan and J.W. Jorgenson, *J. Chromatogr. A,* 2001, **915**, 1-13

4.2 Paper II: Short Range Ballistic Motion in Fluid Lipid Bilayers Studied by Quasi-Elastic Neutron Scattering

Clare L. Armstrong, Marcus Trapp, Judith Peters, Tilo Seydel, and Maikel C. Rheinstädter *"Short range ballistic motion in fluid lipid bilayers studied by quasi-elastic neutron scattering"*, Soft Matter, **7**, 8358-8362, 2011.

4.2.1 Preface to Paper II

The study of lipid diffusion on very short length scales (less than the nearest-neighbour distance) requires the use of a spectrometer that can access correspondingly high Q values. The thermal backscattering spectrometer, IN13, at the Institut Laue-Langevin (ILL) has a much larger Q range than typical (cold) backscattering spectrometers and is capable of measuring Q values from 0.2 to 4.9 Å^{-1} ($\sim$1.3 - 31.5 Å). The experiment was conducted on a stacked membrane sample, composed of protonated DMPC lipids and hydrated with D_2O, to minimize the incoherent scattering contributions from the water. Again, because of the highly oriented nature of the membranes, it was possible to align the sample such that the scattering vector was in the plane of the bilayers ($q_{||}$).

The low $q_{||}$ range data exhibited the same type motion that was observed in the single supported lipid bilayer system from the previous paper: Lorentzian shaped quasi-elastic energy broadening with a $q_{||}^2$ dependence, indicative of continuous diffusion over nanometer length scales. However, at higher $q_{||}$ values, there was a distinct change in character of the dynamics. Above $q_{||}$ $\sim$2.5 Å^{-1} ($\sim$2.5 Å) the quasi-elastic broadening was better fit with a Gaussian curve, rather than a Lorentzian, with an energy broadening that exhibited a linear $q_{||}$ dependence. This behaviour implies that the initial mechanism for the lipid motion on sub-nanometer length scales is ballistic.

From the relationship between the Gaussian energy broadening and $q_{||}$, a value for the lipid velocity was extracted. This value was compared to the velocity given by the equipartition theorem for a free particle, with the mass of the lipid molecule. The purely ballistic velocity of a free particle was found to be two orders of magnitude

larger than the experimentally determined lipid velocity. This suggests that the short-range lipid motion is more flow-like than purely ballistic. This finding has lead us to consider the possibility of a "nano-viscosity" or "nano-friction" influencing the lipid dynamics at length scales less than the nearest-neighbour distance.

Author Contributions

- *Designed research:* Judith Peters and Maikel C. Rheinstädter
- *Sample fabrication:* Marcus Trapp
- *Performed experiment:* Marcus Trapp, Tilo Seydel, Judith Peters, and Maikel C. Rheinstädter
- *Analysed data:* **Clare L. Armstrong**
- *Wrote the manuscript:* **Clare L. Armstrong** and Maikel C. Rheinstädter

Soft Matter

Cite this: *Soft Matter*, 2011, **7**, 8358

www.rsc.org/softmatter

PAPER

Short range ballistic motion in fluid lipid bilayers studied by quasi-elastic neutron scattering†

C. L. Armstrong,‡*[a] M. Trapp,‡[bc] J. Peters,[def] T. Seydel[f] and M. C. Rheinstädter[ag]

Received 18th April 2011, Accepted 7th July 2011
DOI: 10.1039/c1sm05691c

Diffusion is the primary mechanism for movement of lipids and proteins in the lateral direction of a biological membrane. In this paper we have used quasi-elastic neutron scattering to examine the diffusion process of lipid molecules in fluid DMPC membranes. We found that the motion over length scales greater than the lipid diameter could be characterized as a continuous diffusion process, with a diffusion coefficient of $D = 64 \times 10^{-12}$ m^2/s. The continuous diffusion model has been successfully used in the past to describe the motion of lipid over long length scales. However, the focus of this measurement was to determine how the character of the molecular motion changes on length scales shorter than the nearest neighbour distance. At very short length scales (<2.37 Å), we see first experimental evidence for a short-range flow-like ballistic motion.

1 Introduction

Diffusion is not only the primary mechanism for proteins to move through the lipid matrix, but it also plays an important role in the formation of various macromolecular structures, such as lipid rafts and nanoenvironments for proteins.

It is commonly accepted that the Brownian motion of lipid molecules over long length scales (length scales larger than the nearest neighbour distance of the lipid molecule) is characterized by a continuous diffusion process.[1–5] On very short length scales, the motion of the molecules is often modeled as a "rattling in the cage" motion,[6,7] as shown in Fig. 1b), where the molecule is constraint in its local environment for a certain time before leaving the cage. This model has been used successfully to fit, in particular, diffusion determined by neutron scattering experiments.[8] However, our understanding of molecular diffusion in membranes has been challenged by new results from experiments and simulations. From computer simulations, sub-diffusive and ballistic regimes were observed on very short time scales and, respective, small distances.[9] It has also been reported that lipids move coherently in loosely bound clusters, rather than as independent molecules.[10,11] A "hopping" diffusion of lipids into nearest neighbor sites was reported in single supported bilayers.[12] Recently, it has been suggested that there is also a flow-like component to the motion of the lipid molecules over long length scales.[13] While continuous diffusion can be pictured as the Brownian motion of individual lipid molecules, a flow-like motion involves the coherent movement of several lipid molecules, as pictured in Fig. 1c). If a flow like motion is present, it should be apparent at all length scales, and be particularly

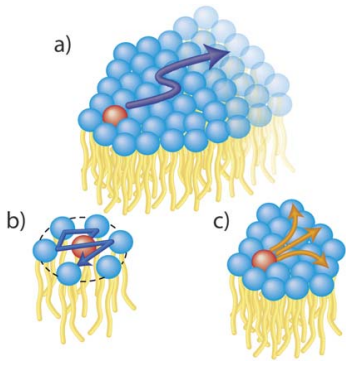

Fig. 1 Models depicting the motion of lipid molecules at different length scales. The motion at longer length scales is characterized by continuous diffusion (a). Previously accepted models suggest a "rattling in the cage" ballistic motion (b) at short length scales, while recent measurements show evidence for a flow-like ballistic motion (c).

[a]*Department of Physics and Astronomy, McMaster University, Hamilton, ON, L8S 4M1, Canada. E-mail: armstc5@mcmaster.ca; rheinstadter@mcmaster.ca; Fax: +1-(905)546-1252; Tel: +1-(905)525-9140 ext.23134*
[b]*Angewandte Physikalische Chemie, Universität Heidelberg, Im Neuenheimer Feld 253, 69120 Heidelberg, Germany*
[c]*Helmholtz-Zentrum Berlin für Materialien und Energie, Lise-Meitner Campus, Hahn-Meitner-Platz 1, 14109 Berlin, Germany*
[d]*Université Joseph Fourier, BP 53, F-38041 Grenoble Cédex 9, France*
[e]*Institut de Biologie Structurale, J.-P. Ebel, UMR 5075, CNRS-CEA-UJF, 41 rue Jules Horowitz, 38027 Grenoble Cédex 1, Grenoble, France*
[f]*Institut Laue-Langevin, 6 rue Jules Horowitz, B.P. 156, 38042 Grenoble Cedex 9, France*
[g]*Canadian Neutron Beam Centre, NRC, Chalk River, ON, Canada*

† Electronic Supplementary Information (ESI) available: Details regarding the data analysis. See DOI: 10.1039/c1sm05691c/

‡ These authors contributed equally to this work.

pronounced at shorter length scales where the continuous diffusive motion is no longer dominant.

Quasi-elastic neutron scattering is a powerful tool for observing short range lipid dynamics at time scales on the order of pico-nanoseconds, enabling the characterization of this type of motion. We measured lipid diffusion in a phospholipid model membrane over distances from 1.3 Å to 22 Å using quasi-elastic neutron scattering on the backscattering spectrometer IN13.[14] With typical lipid distances of about 8 Å, the experiments cover motions of the lipid molecules from about 1/5 to almost 3 times the lipid-lipid distance. While we observe the well established continuous diffusion at large distances, we find experimental evidence for a ballistic motion of the lipids at distances smaller than 2.37 Å. The velocity of the lipids (1.12 m s^{-1}) is significantly smaller than their thermal velocity (87 m s^{-1}), thus indicating a flow-like ballistic motion at small length scales.

2 Experimental details

Multi-lamellar bilayers of the model system 1,2-dimyristoyl-*sn*-glycero-3-phoshatidylcholine (DMPC) were prepared on Si wafers and hydrated with heavy water. By using selective deuteration, the experiment was mainly sensitive to the incoherent scattering of diffusing lipid molecules.[15]

The DMPC powder was dissolved in a 3 : 1 chloroform-trifluoroethanol mixture following a protocol described by Ding and co-workers.[16] The dissolution was kept at −20 °C overnight. Measuring the in-plane motions of the lipids in the membrane required the use of highly oriented samples. This was achieved by preparing the lipids on silicon wafers. The wafers had a thickness of ∼380 μm and Si(111) orientation.

The lipid solution was sprayed onto wafers, producing a system of highly oriented stacked membranes. After the deposition, the wafers were dried over silica gel for 2 days in a desiccator. The sample was rehydrated from pure D_2O at 40 °C to achieve full hydration (corresponding to at least 12 water molecules per lipid[17]), resulting in a lamellar spacing of d ∼ 59.3 Å as measured by a θ–2θ scan.[18]

After rehydration six wafers were stacked together in order to achieve a total amount of about ∼100 mg lipid. This amount of sample is needed to achieve sufficiently high statistics in a reasonable measuring time. The total sample thickness of the six wafers with the deposited DMPC was 3 mm. The sample cell was sealed using indium wire and the weight of the sample was monitored before and after the experiment, with no change observed.

The experiment was performed at the Collaborative Research Group (CRG) thermal neutron backscattering spectrometer IN13 at the high flux reactor of the Institut Laue-Langevin (ILL), Grenoble.[14] This instrument is unique in its capability of accessing very high Q-values, corresponding to very small distances in the bilayer sample, in combination with a high dynamic range of about −100 to 100 μeV. The incident wavelength was λ = 2.23 Å, with an incident neutron energy of about 16 meV. This setup yields a uniquely broad range of momentum transfers, Q (0.28 $Å^{-1}$ < Q < 4.9 $Å^{-1}$), corresponding to distances 1.3 < d < 22 Å. The 8 μeV elastic energy resolution corresponds to a 0.10 ns time scale. The experiment was therefore sensitive to pico-nanosecond diffusive motions of lipid molecules over a wide range of distances. A detailed description of the instrument and selected applications in the field of biophysics can be found in Natali *et al.*[14]

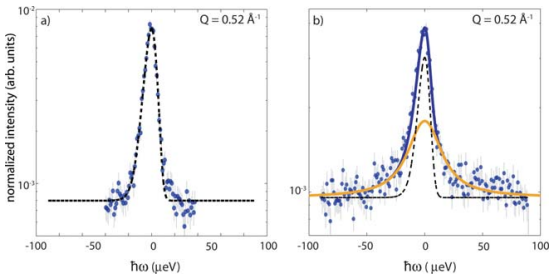

Fig. 2 Typical data analysis used for low Q values. a) Vanadium resolution with asymmetric Gaussian fit (black). b) Lipid sample at 310 K fit with the asymmetric resolution function (black) and a Lorentzian function convoluted with the resolution (orange). The total fit is shown in blue. The deconvoluted FWHM of the Lorentzian at this Q value was determined to be 27.5 μeV.

The lipid sample as well as a sample holder containing six cleaned silicon wafer for background subtraction, were measured in an energy range of ±90 μeV. The instrumental resolution was determined by measuring a 2 mm vanadium sample in the range of ±40 μeV as shown in Fig. 2. The incident energy of the neutrons was varied by changing the temperature of the crystal monochromator of the instrument. This procedure introduces a small asymmetry in the resolution function which will be discussed in more detail in the data analysis section. All measured samples were aligned at an angle of 135° with respect to the incident neutron beam, with the scattering vector Q in the plane of the bilayers (Q_{‖}). Transmission of the sample was measured and found to be in the order of 93%, so multiple scattering effects were not taken into consideration for the data treatment. All scans were measured at 310 K, in the fluid phase of the DMPC bilayers.

3 Data analysis

Fig. 2a) depicts the instrumental energy resolution of the IN13 spectrometer as determined from a Vanadium sample, which is usually well described by a Gaussian peak shape. To accommodate the slightly asymmetric resolution function, the resolution was fit with an asymmetric Gaussian function. The asymmetry was introduced by incorporating an exponential function into one side of the Gaussian peak[19] to get

$$y = y_o + H(\hbar\omega_o - \hbar\omega)Ae^{-\left(\frac{(\hbar\omega-\hbar\omega_o)^2}{2\sigma^2+\tau|\hbar\omega-\hbar\omega_o|}\right)} + H(\hbar\omega-\hbar\omega_o)Ae^{-\left(\frac{(\hbar\omega-\hbar\omega_o)^2}{2\sigma^2}\right)}, \quad (1)$$

where A is the amplitude, ω_o the elastic energy peak position, σ the Gaussian standard deviation, H is a Heaviside function, and τ the asymmetry parameter. For $\tau = 0$, a Gaussian peak function

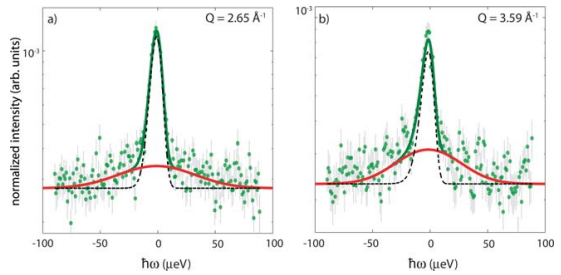

Fig. 3 Exemplary high Q data fit with the resolution function (black) and a Gaussian quasi-elastic broadening (red), see text for details. The total fit is shown in green. a) Q = 2.65 Å^{-1} b) Q = 3.59 Å^{-1}. While the quasi-elastic broadening is larger at Q = 2.65 Å^{-1} as compared to Q = 0.52 Å^{-1} in Fig. 2b), the broadening at higher Q (3.59 Å^{-1}) becomes significantly smaller again. FWHM for all measured Q are shown in Fig. 4.

is obtained. The energy resolution in Fig. 2a) is slightly asymmetric, with a τ value of 3.29.

The scattering obtained from the lipid sample is described by a narrow central component, corresponding to the instrumental resolution (~8 μeV), a constant background, and a quasi-elastic broadening due to relaxational dynamics of the lipid molecules. Two different functions were used to fit the quasi-elastic broadening, depending on the Q range.

Typical data obtained at low Q-values are shown in Fig. 2b). The intensity was normalized to Vanadium to correct for detector efficiency. For the low Q values (Q < 2.65 Å^{-1}) the broadening (25–72 μeV) was fit with a Lorentzian function, convoluted with the Gaussian instrumental resolution. It should be noted that the FWHM of the Lorentzian functions quoted in the paper are the deconvoluted values.

Exemplary data from the high Q scans are shown in Fig. 3. Because the neutron flux of the instrument is significantly lower at high Q values, these scans had significantly lower statistics than the small Q scans. There was a distinct change in the trend of the FWHM of the Lorentzian functions when fitting the high Q values (Q > 2.65 Å^{-1}). After a detailed data analysis (which is provided in the Electronic Supplementary Information†), we concluded that the high Q values were better fit with a Gaussian function rather than a Lorentzian.

Fig. 4 displays the FWHM for all measured Q-values as function of Q^2. In this plot the FWHM of the low Q data (Q < 2.65 Å^{-1}), fit with a Lorentzian function (blue), scale linearly with Q^2, a behaviour which is indicative of continuous diffusion. The broadening for higher Q-values was found to drop from about 70 μeV to 40 μeV and then raise again to 60 μeV. The FWHM of the Gaussian functions used to fit the high Q data (green) were found to fall on a square root curve§. The relationship between the Q scaling of the FWHM and the character of motion will be discussed in more detail in the following section. Note that we cannot exclude additional faster dynamics outside of the energy window of the IN13 instrument.

§ The Gaussian standard deviation σ is related to the FWHM of the Gaussian peak by $\mathrm{FWHM}_G = 2\sqrt{2\ln 2}\sigma$.

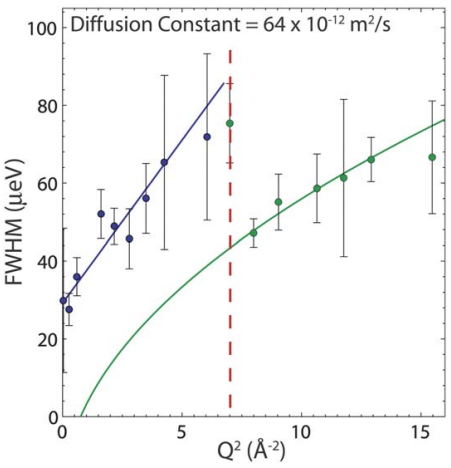

Fig. 4 FWHM of the quasi-elastic broadening plotted as function of Q^2. The linear Q^2 relationship at low Q (blue) is indicative of continuous diffusion. The high Q data (green) show a quasi-elastic broadening described by a Gaussian peak shape. The corresponding FWHM scale linearly with Q. The corresponding fit (green) displays as square root when plotted against Q^2. The transition between continuous and ballistic diffusion is observed at Q = 2.65 Å^{-1}, marked by the red dashed line.

4 Discussion

There are different models used to describe diffusion.[8] For a particle diffusing via random Brownian motion, the displacement of the particle can be characterized as a function of time,

$$\sigma_d = \sqrt{2Dt} \tag{2}$$

where D is the translational diffusion coefficient of the system. With this characteristic length scale, one can define a self time-dependent pair-correlation function for incoherent scattering,

$$F_d(r,t) = (4Dt)^{-\frac{3}{2}} exp\left(\frac{-r^2}{4Dt}\right), \tag{3}$$

which is a solution of Fick's law,

$$\frac{\partial F_d(r,t)}{\partial t} = D\nabla^2 F_d(r,t). \tag{4}$$

This results in an intermediate scattering function which decays exponentially,

$$I_d(Q,t) = \exp(-Q^2 Dt), \tag{5}$$

and can be Fourier transformed to give a Lorentzian incoherent scattering function

$$S_d(Q,\omega) = \frac{1}{\pi\hbar}\left(\frac{Q^2 D}{(Q^2 D)^2 + \omega^2}\right). \tag{6}$$

Thus, quasi-elastic scattering which exhibits itself as Lorentzian broadening with a FWHM that has a Q^2 dependence, is indicative of a continuous diffusion process ($FWHM_L = 2\hbar DQ^2$). This behavior was observed for the low Q values, shown in Fig. 4 as

the data fit with a blue line. From this linear fit a diffusion coefficient could be extracted and was found to be D = 64 × 10^{-12} m^2/s. This value is comparable to diffusion coefficients quoted in the literature for similar systems.[1,4,12,13,20] We note that the linear fit in Fig. 4 does not pass through the origin, as one would expect, and the offset is larger than the instrumental resolution. This effect is often observed in the literature, however no consistent explanation has been offered.

Taking advantage of the unique high Q-range accessible on the IN13, it was found that the data for Q values >2.65 $Å^{-1}$ no longer agreed with the continuous diffusion model and the broadening is better fit with a Gaussian curve. This feature is indicative of a change in character of the lipid motion.

In the case of a ballistic motion, the displacement of the particle can be written as a function of time, simply defined by its velocity,

$$\sigma_b = vt, \tag{7}$$

which will change the form of the self pair-correlation function,

$$F_b(r,t) = \left(2\pi v^2 t^2\right)^{-\frac{3}{2}} exp\left(\frac{-r^2}{2v^2t^2}\right). \tag{8}$$

The spacial Fourier transform of this now gives an intermediate scattering function which is a Gaussian,

$$I_b(Q,t) = exp\left(\frac{-Q^2v^2t^2}{2}\right). \tag{9}$$

Thus, the incoherent scattering function will also have a Gaussian form,

$$S_b(Q,\omega) = \frac{1}{\sqrt{2\pi}Qv\hbar} exp\left(\frac{-\omega^2}{2Q^2v^2}\right). \tag{10}$$

In this new model, the velocity of the particle can be extracted from the linear Q dependence of the FWHM of the Gaussian function ($FWHM_G = 2\sqrt{2ln2}\hbar vQ$). This fit is shown as the green curve in Fig. 4, which displays as a square root when plotted against Q^2. The data suggest a transition from continuous diffusion to ballistic diffusion at Q = 2.65 $Å^{-1}$, corresponding to a length scale of 2.37 Å, about 1/3 of the typical lipid-lipid distance. If this ballistic motion is driven by thermal energies, neglecting friction, the expected velocity of the molecule should be that of a free particle, and thus dictated by the thermal energy as given from the equipartition theorem $\left(k_BT = \frac{1}{2}mv^2\right)$. Using the mass of a single lipid molecule (1.1258 × 10^{-24} kg) results in a velocity of $v_{thermal} = 87$ m s^{-1} at $T = 310$ K. From the fit in Fig. 4, the experimentally determined velocity was $v_{exp} = 1.12$ m s^{-1}.

The experimentally determined velocity is about two orders of magnitude slower than the thermal velocity. The primary mechanism for short range motion of lipids is thus too slow for a purely thermal free particle motion, and is, rather, the result of a flow-like process.

The initial movement of a lipid molecule in a tightly packed fluid state most likely requires the re-arrangement of the nearest neighbour molecules. Diffusion of lipid molecules at distances smaller than a lipid diameter could then be pictured as a flow-like process, which involves the coherent motion of several lipid molecules. This picture is in agreement with previously reported results on possible motional coherence in fluid phospholipid bilayers.[11] Here lipids were reported to fluctuate as coherently coupled, ~30 Å large patches rather than individual molecules.

The ballistic regime was observed in the data in Fig. 4 for length scales less then 2.37 Å. Our data can be compared to results from Molecular Dynamics (MD) simulations by Flenner *et al.* who studied lipid diffusion over a wide range of time scales (10^{-16} s to 10^{-6} s).[9] At very short timescales, *i.e.* very early stages of the diffusion process (10^{-14} s), a ballistic diffusion regime was observed. This regime was followed by a sub-diffusive regime and lead into the well known continuous diffusion process at longer times. Considering typical diffusion constants of ~10^{-11} m^2 s^{-1}, the simulated ballistic regime corresponds to length scales of only ~0.003 Å, and thus occurs at a significantly shorter length scale than found in this experiment. We argue that the MD simulations qualitatively describe lipid diffusion over a broad range of time scales; however, due to imperfections in the force fields, discrepancies in area per lipids used in the simulations, as well as insufficient sampling, the absolute values obtained by Flenner *et al.* may differ from our experimental results. While we find experimental evidence for a ballistic regime, determining a possible sub-diffusive behavior would require fitting non-Lorentzian peak shapes to the quasi elastic data. The unavoidable statistical error of the data in Fig. 2 and 3, unfortunately, did not allow for the unambiguous determination small deviations from a purely Lorentzian peak shape. The existence of a possible sub-diffusive regime can experimentally not be confirmed at this point and will be addressed in future experiments.

While we observe a flow-like motion at very small length scales, long distance flow-like diffusion has been reported recently.[13] We note that data with a very small statistical error were needed for the Bayesian data analysis to detect a small Gaussian broadening of the instrumental resolution. The instrument used in our study was optimized to study diffusion at very high Q values. The data quality (as shown in Fig. 2b) did not allow the same kind of analysis to determine a possible flow-like diffusion over long length scales. We note that the low Q data in Fig. 4 can be reasonably fit using the continuous Brownian diffusion model. This model is also widely used in the literature to determine diffusion coefficients from neutron scattering experiments. It can, therefore, be speculated that flow and continuous lipid diffusion possibly coexist in fluid membranes at long distances. Our data presents the first experimental evidence that flow-like diffusion dominates at small distances of up to about 1/3 of a lipid-lipid distance. Strong interactions between the lipids may eventually lead to a change in character of the motion to a continuous diffusion process.

5 Conclusions

We studied pico-nanosecond diffusion of lipid molecules in the fluid phase of DMPC phospholipid model membranes using quasi-elastic incoherent neutron scattering experiments. Using unique neutron instrumentation, the measurements covered lateral length scales from 1.3 to 22 Å, 1/5 to about 3 lipid-lipid distances. At large distances, we observe continuous diffusion with a diffusion coefficient of D = 64 × 10^{-12} m^2 s^{-1}, in excellent

agreement to values reported in the literature. For distances smaller than 2.37 Å, the character of the diffusion changes from continuous to ballistic diffusion with a velocity of 1.12 m s^{-1}, much smaller than the thermal velocity. Motion of lipid molecules at very small distances was, therefore, characterized as a flow-like ballistic motion.

References

1 S. König, W. Pfeiffer, T. Bayerl, D. Richter and E. Sackmann, *J. Phys. II*, 1992, **2**, 1589–1615.
2 S. König, E. Sackmann, D. Richter, R. Zorn, C. Carlile and T. Bayerl, *J. Chem. Phys.*, 1994, **100**, 3307–3316.
3 S. König, T. Bayerl, G. Coddens, D. Richter and E. Sackmann, *Biophys. J.*, 1995, **68**, 1871–1880.
4 W. Pfeiffer, T. Henkel, E. Sackmann and W. Knorr, *Europhys. Lett.*, 1989, **8**, 201–206.
5 W. Pfeiffer, S. König, J. Legrand, T. Bayerl, D. Richter and E. Sackmann, *Europhys. Lett.*, 1993, **23**, 457–462.
6 W. Vaz and P. Almeida, *Biophys. J.*, 1991, **60**, 1553–4.
7 J. Wohlert and O. Edholm, *J. Chem. Phys.*, 2006, **125**, 204703.
8 M. Bée, *Quasielastic Neutron Scattering: Principles and Applications in Solid State Chemistry, Biology and Materials Science*, Taylor & Francis, 1988.
9 E. Flenner, J. Das, M. C. Rheinstädter and I. Kosztin, *Phys. Rev. E: Stat., Nonlinear, Soft Matter Phys.*, 2009, **79**, 011907.
10 E. Falck, T. Róg, M. Karttunen and I. Vattulainen, *J. Am. Chem. Soc.*, 2008, **130**, 44–45.
11 M. C. Rheinstädter, J. Das, E. J. Flenner, B. Brüning, T. Seydel and I. Kosztin, *Phys. Rev. Lett.*, 2008, **101**, 248106.
12 C. L. Armstrong, M. D. Kaye, M. Zamponi, E. Mamontov, M. Tyagi, T. Jenkins and M. C. Rheinstädter, *Soft Matter*, 2010, **6**, 5864–5867.
13 S. Busch, C. Smuda, L. Pardo and T. Unruh, *J. Am. Chem. Soc.*, 2010, **132**, 3232–3233.
14 F. Natali, J. Peters, D. Russo, S. Barbieri, C. Chiapponi, A. Cupane, A. Deriu, M. T. D. Bari, E. Farhi, Y. Gerelli, P. Mariani, A. Paciaroni, C. Rivasseau, G. Schir and F. Sonvico, *Neutron News*, 2008, **19**, 14.
15 V. F. Sears, *Neutron News*, 1992, **3**, 26–37.
16 L. Ding, T. Weiss, G. Fragneto, W. Liu, L. Yang and H. Huang, *Langmuir*, 2005, **21**, 203.
17 H. Pfeiffer, H. Binder, G. Klose and K. Heremans, *BBA-Biomembranes*, 2003, **148**, 1609.
18 M. Trapp, T. Gutberlet, F. Juranyi, T. Unruh, B. Demé, M. Tehei and J. Peters, *J. Chem. Phys.*, 2010, **133**, 164505.
19 K. Lan and J. Jorgenson, *J. Chromatogr., A*, 2001, **915**, 1–13.
20 A. Buchsteiner, T. Hauß, S. Dante and N. Dencher, *Biochim. Biophys. Acta, Biomembr.*, 2010, **1798**, 1969–1976.

Electronic Supplementary Material (ESI) for Soft Matter

Electronic Supplementary Information for: Short range ballistic motion in fluid lipid bilayers studied by quasi-elastic neutron scattering

C.L. Armstrong[a], M. Trapp[b,c], J. Peters[d,e,f], T. Seydel[f] and M.C. Rheinstädter[a,g]

[a]*Department of Physics and Astronomy, McMaster University, Hamilton, ON, Canada*
[b]*Angewandte Physikalische Chemie, Universität Heidelberg, Im Neuenheimer Feld 253, 69120 Heidelberg, Germany.*
[c]*Helmholtz-Zentrum Berlin für Materialien und Energie, Lise-Meitner Campus, Hahn-Meitner-Platz 1, 14109 Berlin, Germany.*
[d]*Université Joseph Fourier, F-38041 Grenoble Cedex 9, France.*
[e]*Institut de Biologie Structurale, J.-P. Ebel, UMR 5075, CNRS-CEA-UJF, 41 rue Jules Horowitz, 38027 Grenoble Cedex 1, Grenoble, France.*
[f]*Institut Laue-Langevin, 6 rue Jules Horowitz, B.P. 156, 38042 Grenoble, Cedex 9, France.*
[g]*The Canadian Neutron Beam Centre, Chalk River Laboratories, Chalk River, ON, Canada*

1. Potential continuous diffusion at high Q-values

In a first attempt, all Q-values were fit using the continuous diffusion model assuming Lorentzian shaped quasi-elastic broadening only. The fitting procedure is described in detail in the main paper. The fitted FWHM for all Q values are shown in ***Figure ESI-1***.

This model provides a good fit for Q-values smaller than 2.65 $Å^{-1}$. A typical fit is shown in Figure 2b) of the main paper for a Q value of 0.52 $Å^{-1}$. When plotted as function of Q^2, the data points for Q values smaller than 2.65 $Å^{-1}$ follow a linear trend, as predicted for continuous diffusion (see ***Equation 6***). The FWHM decreases and starts to deviate from the Q^2 curve for Q-values larger than 2.65 $Å^{-1}$ (corresponding to a length scale of 2.37 Å). As the signal intensity decreases with increasing Q, the uncertainties in the high Q fits become larger, as can be seen by the error bars in ***Figure ESI-1***. The fitted values for the FWHM are consistently smaller than for the low Q and scatter around a value of 25 μeV.

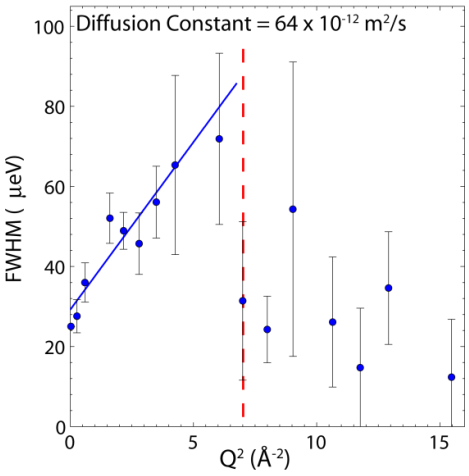

Figure ESI-1: *FWHM of Lorentzian functions used to fit all of the Q values. There is a distinct change in character of the motion occurring at ~2.37Å*

From this, two conclusions can be drawn. Firstly, the character of the motion changes at Q=2.65 $Å^{-1}$ and the FWHM no longer follow the Q^2 behaviour predicted by the continuous diffusion model. Secondly, the high Q data in ***Figure ESI-1*** do not fall on a straight line. A second, continuous diffusion regime corresponding to the high Q data, within the dynamic window of IN13, can be excluded. Given the values of the FWHM for the high Q values in Figure ESI-1, the observed motion at high Q values is significantly slower than the continuous diffusion at small Q values.

Electronic Supplementary Material (ESI) for Soft Matter

2. *Ballistic diffusion at small distances*

Because the continuous diffusion model did not provide a satisfying description of the high Q data, a ballistic diffusion model, according to ***Equation 10***, was taken into consideration. Q values higher than 2.65 $Å^{-1}$ were fit assuming Gaussian quasi-elastic broadening. The FWHM, as determined from the fits, are shown in ***Figure 4*** in the main paper.

The ballistic model provides good quality fits with lower uncertainties as compared to the continuous diffusion model as will be discussed in the next section. The FWHM of the peaks are significantly smaller for high Q, as compared to the trend from the low Q values. We note that the observation of a critical Q-value of 2.65 $Å^{-1}$ is robust and independent of the applied model. In addition, the fitted FWHM show a linear Q dependence, as predicted by the ballistic diffusion model. Because the data at Q=2.65 $Å^{-1}$ is right at the transition between the two regimes, it was found to not follow the trend of either model; however it was better fit with a Gaussian function.

3. *Quantitative comparison between the two models*

In order to quantitatively compare the continuous and ballistic diffusion model the quality of the fits of the high Q data, using Gaussian and Lorentzian peak shapes, must be compared.

Table ESI-1 lists the uncertainties in the determination of the FWHM and χ^2 values for the Gaussian and Lorentzian fits. Due to the intrinsically large uncertainty in the data, both models can be used to fit the data. However, the Gaussian model provides mostly smaller values for the uncertainty and χ^2.

Q	χ^2 of Gaussian fit	Gaussian FWHM uncertainty (μeV)	χ^2 of Lorentzian fit	Lorentzian FWHM uncertainty (μeV)
2.6455	0.99726	10.19	1.0370	19.79
2.8278	1.1984	3.62	1.2618	8.31
3.0062	0.96619	7.20	0.97619	36.78
3.2627	1.3364	8.84	1.2795	16.25
3.4305	1.3750	20.19	1.3309	14.88
3.5935	1.0343	5.68	1.1496	14.08
3.9329	1.1858	14.51	1.1890	14.45

Table ESI-1: *χ^2 values and uncertainties (corresponding to a 95% confidence interval) in the FWHM as determined from the Gaussian and Lorentzian fits.*

Electronic Supplementary Material (ESI) for Soft Matter

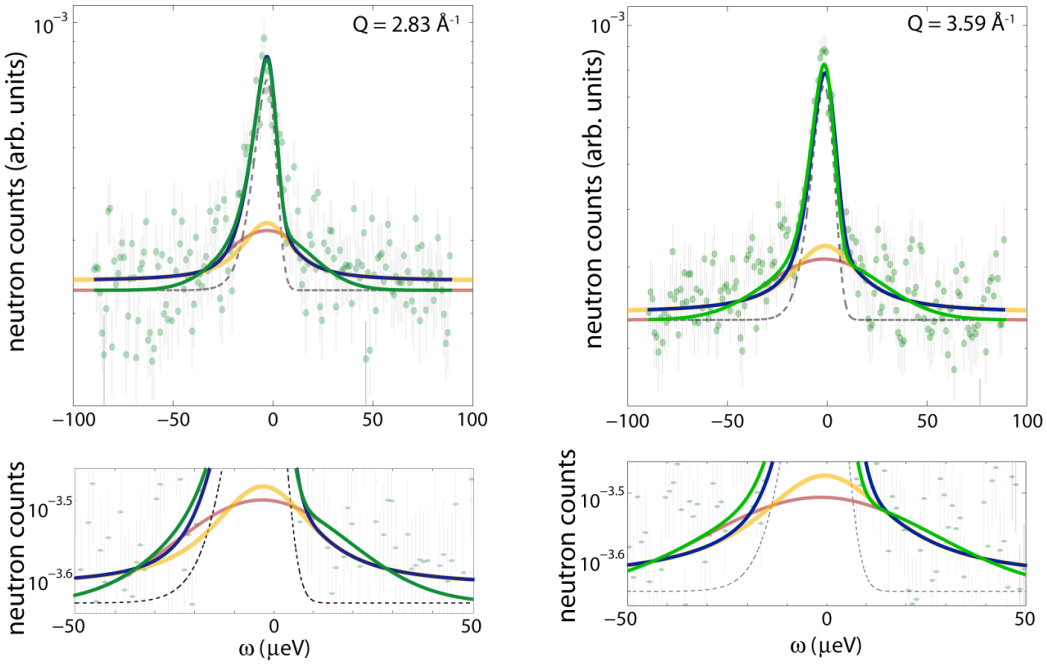

Figure ESI-2: *Comparison of the Gaussian and Lorentzian function fits at a) Q = 2.83 Å^{-1} and b) Q = 3.59 Å^{-1}. The red curve is the Gaussian function and the total Gaussian fit, with the resolution included, is the green curve. The yellow curve is the Lorentzian function, with the total Lorentzian fit shown in blue.*

Fits of two exemplary Q values are shown in ***Figure ESI-2.*** By visual inspection the Gaussian peak seems to better describe the shape of the quasi-elastic broadening at energy transfers of 10-40 μeV as the Lorentzian peak shape is narrower in the centre and falls of more quickly thereby missing the data points which the Gaussian is able to accommodate.

In summary, the dynamics at high-Q values can be fit using both a Gaussian and Lorentzian quasi-elastic broadening. In both models the fitted FWHM starts to deviate from the low-Q trend towards significantly smaller FWHM values beyond a critical Q-value of 2.65 Å^{-1}. Within the uncertainties of this experiment, the Gaussian fits were found to provide a better description of the high-Q data. The uncertainties in the fits are mostly smaller with the Gaussian function and the data show a linear Q-behaviour.

The fitted values of the FWHM scatter around 25 μeV when using the Lorentzian fits without a clear trend, such as a Q^2 behaviour. We, therefore, conclude that the ballistic motion is the appropriate model to describe the high Q data within the uncertainty of this experiment.

4.3 Paper III: Incoherent Neutron Spin-Echo Spectroscopy as an Option to Study Long-Range Lipid Diffusion

Clare L. Armstrong, Laura Toppozini, Hannah Dies, Antonio Faraone, Michihiro Nagao, and Maikel C. Rheinstädter *"Incoherent Neutron Spin-Echo Spectroscopy as an Option to Study Long-Range Lipid Diffusion"*, ISRN Biophysics, **2013**, 439758, 2013.

4.3.1 Preface to Paper III

In an effort to close the gap between measurements obtained by inelastic neutron scattering and fluorescence microscopy techniques, an experiment was designed to determine the feasibility of using incoherent neutron spin-echo spectroscopy as a viable option for measuring long-range lipid diffusion.

NSE is used to probe the coherent dynamics of soft matter systems over long time scales (∼100s of nanoseconds) [48]. A significant challenge of this particular work was to determine if the incoherent spin-echo signal was large enough be detected over the coherent scattering signal. Incoherent scattering events have a 2/3 probability of undergoing a spin flip. This effectively reduces the incoherent signal, as 2/3 of the scattering intensity is converted into "non-polarized" background. Additionally, NSE can not explicitly separate the incoherent and coherent dynamics that are measured; however this problem can be overcome by ensuring that the incoherent signal is dominant. This point is addressed in more detail in the paper.

For this reason, the sample used to measure long-range lipid dynamics was a stacked membrane system composed of protonated DMPC, to enhance the incoherent signal. The oriented nature of the sample allowed for the detection of lateral lipid dynamics by measuring the in-plane scattering vector ($q_{||}$). Even with this choice of sample, data collection required long counting times (∼24-36 hours per lateral $q_{||}$ value) in order to achieve statistically significant data.

The experiment presented here was a proof of concept trial, which would act to justify applying for further beam time on an NSE spectrometer, to obtain a more

substantial data set. This preliminary work was conducted at NIST using the NG5-NSE spectrometer. The following paper shows the characterization of the sample and details the accessible $q_{||}$-range at which the incoherent signal is dominant.

Although the data collected was limited to a single $q_{||}$ value, we found evidence of two distinct types of motion in the system: (1) fast dynamics corresponding to the motion of a single lipid molecule; and (2) slow dynamics thought to be related to the diffusion of a loosely bound cluster of lipids. The fast processes is in good agreement with the data obtained from backscattering experiments. In the previous two papers only one diffusion process was observed; however, the quality of the backscattering data did not allow for the unambiguous assignment of more than one process.

To better understand these dynamical processes and extract their associated diffusion coefficients, a more in depth incoherent NSE experiment will need to be conducted. In doing this, it should be possible to consolidate the observations from neutron backscattering and fluorescence spectroscopy experiments.

Author Contributions

- *Designed research:* Maikel C. Rheinstädter
- *Sample fabrication:* **Clare L. Armstrong**, Laura Toppozini, and Hannah Dies
- *Performed experiment:* **Clare L. Armstrong**, Laura Toppozini, Antonio Faraone, Michihiro Nagao, and Maikel C. Rheinstädter
- *Analysed data:* **Clare L. Armstrong** and Antonio Faraone
- *Wrote the manuscript:* **Clare L. Armstrong**, Anotonio Faraone, and Maikel C. Rheinstädter

Hindawi Publishing Corporation
ISRN Biophysics
Volume 2013, Article ID 439758, 9 pages
http://dx.doi.org/10.1155/2013/439758

Research Article

Incoherent Neutron Spin-Echo Spectroscopy as an Option to Study Long-Range Lipid Diffusion

Clare L. Armstrong,[1] Laura Toppozini,[1] Hannah Dies,[1] Antonio Faraone,[2,3] Michihiro Nagao,[2,4] and Maikel C. Rheinstädter[1,5]

[1] *Department of Physics and Astronomy, McMaster University, Hamilton, ON, Canada L8S 4M1*
[2] *NIST Center for Neutron Research, NIST, Gaithersburg, MD 20899-6100, USA*
[3] *Department of Materials Science and Engineering, University of Maryland, College Park, MD 20742, USA*
[4] *Center for Exploration of Energy and Matter, Indiana University, Bloomington, IN 47408-1398, USA*
[5] *Canadian Neutron Beam Centre, National Research Council of Canada, Chalk River, ON, Canada K0J 1J0*

Correspondence should be addressed to Clare L. Armstrong; armstc5@mcmaster.ca
and Maikel C. Rheinstädter; rheinstadter@mcmaster.ca

Received 4 February 2013; Accepted 25 February 2013

Academic Editors: E. Dague and K. Nishizawa

Diffusion is the fundamental mechanism for lipids and other molecules to move in a membrane. It is an important process to consider in modelling the formation of membrane structures, such as rafts. Lipid diffusion is mainly studied by two different techniques: incoherent neutron scattering and fluorescence microscopy. Both techniques access distinctly different length scales. While neutron scattering measures diffusion over about 3 lipid diameters, microscopic techniques access motions of lipids over micrometer distances. The diffusion constants which are determined by these two methods often differ by about an order of magnitude, with the neutrons usually seeing a faster lipid diffusion. Different theories are used to describe lipid diffusion in the two experiments. In order to close the "gap" between these two techniques, we propose to study lipid diffusion at mesoscopic length scales using a neutron spin-echo (NSE) spectrometer. We have conducted an experiment in highly oriented, solid supported lipid bilayers to prove the feasibility of performing incoherent NSE on biological samples. Lateral lipid diffusion was measured in a fluid phase model membrane system at a length scale of 12 Å. Using the high-energy resolution of the NSE technique, we find evidence for two dynamic processes.

1. Introduction

Diffusion not only is the primary mechanism for proteins to move through the lipid matrix, but it also plays an important role in the formation of various macromolecular structures, such as lipid rafts and nanoenvironments for proteins. It is commonly accepted that the Brownian motion of lipid molecules over long length scales (length scales larger than the nearest neighbour distance of the lipid molecule) is characterized by a continuous diffusion process [1–5]. Although this is a well-studied fundamental process, our understanding of molecular diffusion in membranes is still being challenged by new results from experiments and simulations. From computer simulations, subdiffusive and ballistic regimes have been predicted on short time scales and correspondingly small distances [6, 7]. And ballistic lipid motion in fluid membranes has indeed been recently reported from quasielastic neutron scattering (QENS) using a neutron backscattering spectrometer [8]. Furthermore, it has been reported that lipids move coherently in loosely bound clusters, rather than as independent molecules [9–11]. A "hopping" diffusion of lipids into nearest neighbour sites was observed in single supported bilayers [12], and, recently, it has also been suggested that there is a flow-like component to the motion of the lipid molecules over long length scales [11]. In biology, diffusion often occurs in crowded media, which was found to lead to *anomalous* diffusion [13, 14].

The standard techniques currently used to examine diffusion of different membrane components are neutron scattering techniques and fluorescence spectroscopy. Usually,

the goal of these techniques is to determine the diffusion time, τ_D, of the particles of interest in the membrane and their subsequent diffusion coefficient, D. As depicted in Figure 1, the two techniques cover distinctly different length and time scales: fluorescence correlation spectroscopy (FCS) covers motions on micrometer length scales and over microsecond time scales, and neutron beams access dynamics on nanometer lengths and nanosecond times. The diffusion constants determined with the two techniques usually differ by about an order of magnitude, neutrons measuring a faster diffusion as compared to FCS.

It is experimentally challenging to close the gap between the two techniques and follow diffusion of lipid molecules and proteins on mesoscopic length scales. A strong effort is currently being made to enhance the resolution of light microscopes using stimulated emission depletion microscopy [15]. A new generation of neutron backscattering instruments is currently being constructed; however, the accessible length scale, usually determined by the beam size and beam divergence at small scattering angles, is limited to ≈20 Å. The neutron spin-echo (NSE) technique, with its high energy resolution and the possibility to reach scattering vectors, Q, corresponding to tens of Å, is a promising candidate to study long-range diffusion.

Neutrons are scattered by the nuclei. Two factors contribute to differences in the atomic nuclei structure of atoms of the same chemical element: (1) different isotopes and (2) different orientations of the nuclear spin (for elements with nonzero nuclear spin). Therefore, even monatomic samples can contain nuclei with different scattering lengths. Coherent scattering is the scattering which would occur if every nucleus in the system had a scattering length equal to the average scattering length, while the incoherent contribution is caused by isotropic scattering from nuclei with different scattering lengths. The coherent and incoherent scattering contributions give insight into different dynamical processes. Coherent scattering reveals information regarding the correlations between the positions of different atomic nuclei at different times. Thus, it is a method of measuring correlations and interactions in a system. Bragg scattering for instance is the result of coherent scattering. Incoherent scattering only involves correlations between the positions of the same nuclei at different times; therefore, it is a measure of the dynamics of the individual particle. Self-diffusion of lipids and proteins is a dynamical process which will exhibit itself in the incoherent contributions to the scattering [16].

The goal of this experiment was to determine the feasibility of studying lateral lipid diffusion in the plane of the membrane using an NSE spectrometer. To separate in-plane from out-of-plane motions, and to ensure that only lateral lipid diffusion is measured, highly oriented membranes were prepared on silicon wafers and the wafers were carefully aligned in the spectrometer. Because the dynamics of the lipid's self-diffusion will exhibit itself in the incoherent scattering, an incoherent NSE signal must be measured. Protonated membranes hydrated with heavy water were used to enhance the incoherent scattering. We note that, despite the experimental challenges, incoherent NSE experiments have recently been reported [17, 18] in aqueous solutions and polymers. We, for the first time, have applied this technique to study lateral diffusion of lipid molecules in a fluid lipid bilayer.

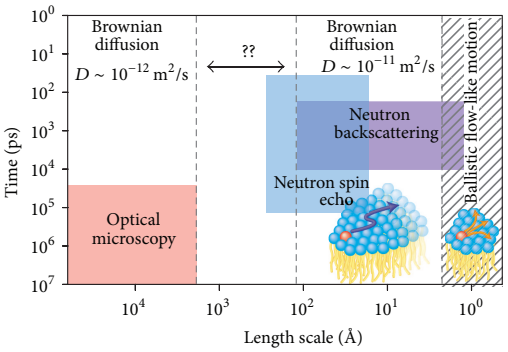

FIGURE 1: The diffusion of lipids in a bilayer has been measured by various optical and neutron techniques. There still remains a gap (from ≈10 nm to ≈200 nm) in the characterization of lipid motion between the regimes accessible by fluorescence measurements and neutron backscattering, resulting in a clear difference in the diffusion coefficients observed on each side of this gap. Neutron spin echo (NSE) can access significantly longer length scales than other neutron techniques to give insight into the character of motion at mesoscopic length scales.

2. Materials and Methods

2.1. Sample Preparation. Protonated membranes, hydrated with heavy water, were prepared to maximize the incoherent scattering of the lipid molecules. Highly oriented multilamellar stacks of 1,2-dimyristoyl-sn-glycero-3-phosphocholine (DMPC) were deposited on 2″ (diameter 5.08 cm) double-side polished Si wafers with a thickness of 300 μm. A solution of 20 mg/mL DMPC in 1 : 1 chloroform and 2,2,2-trifluoroethanol (TFE) was prepared. The Si wafers were cleaned by alternate 12-minute sonications in ultrapure water and methanol at 313 K. This process was repeated twice. As depicted in Figure 2(a), 1 mL of the lipid solution was pipetted onto each Si wafer and allowed to dry. The wafers were kept in vacuum overnight to remove all traces of the solvent. The samples were then hydrated with heavy water, D_2O, and annealed in an incubator at 308 K for 24 hours. Following this protocol, each wafer contained roughly 3,000 highly oriented stacked membranes with a total thickness of ≈10 μm.

Eight such Si wafers were stacked with 0.6 mm aluminium spacers placed in between each wafer to allow the membranes to be hydrated, creating a 10% scatterer (see Figure 2(b)). The "sandwich" sample was sealed in an aluminium sample can with a D_2O hydration source.

2.2. Neutron Spin-Echo Experiment. Among neutron scattering spectroscopic techniques, NSE is the one with the highest energy resolution. Figure 3 shows a sketch of a typical NSE experimental setup.

In the most common cases [19], the incoming neutron beam, with a wavelength spread of ≈15%, is polarized along

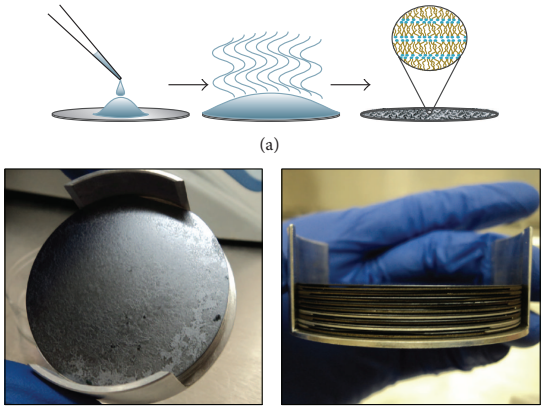

FIGURE 2: (a) A DMPC solvent solution was deposited onto Si wafers. The solvent was allowed to evaporate completely, resulting in highly oriented bilayers. (b) The wafers were then assembled into a sandwich sample in an aluminium holder with aluminium spacers, which was hydrated with D_2O from the vapour phase.

the neutrons' velocity direction (x in Figure 3). At the beginning of the instrument, a $\pi/2$ flipper rotates the spins direction to be perpendicular to the scattering plane (i.e., along z). Then, the neutron beam travels within the first precession coil through a magnetic field aligned along x. Thus, the spins perform a Larmor precession in the yz plane. The angle between the neutron spin direction at the beginning and the end of the first precession coil depends on the time spent within the magnetic field and hence on its velocity. Before being scattered by the sample, the neutron spin is rotated by 180 degrees around the z-axis by the π flipper. The neutrons are then scattered by the sample and travel through the second precession coil within a field equal to that of the first coil. Inside the second coil, the Larmor precession effectively unwinds the neutron spin. If the scattering event is elastic, the neutron spin direction at the end of the second coil is the same as the one at the beginning of the first coil (which is along the z-direction). A second $\pi/2$ flipper rotates the neutron spin onto the xy plane. The polarization of the beam is finally determined by the analyzer-detector system. Again, if the scattering is elastic, the initial polarization of the scattered beam (which is nominally one) is regained.

When quasielastic scattering occurs the, neutrons' spins do not return to their initial state and it can be shown that the resulting beam polarization is proportional to the sample's intermediate scattering function (ISF), $I(Q, t)$. The value of t, often referred to as Fourier time, is proportional to the precession field intensity. Thus, by changing the precession field, NSE can measure the ISF directly in the time domain, whereas other neutron spectrometers, which work in the energy domain, determine the dynamic structure factor, $S(Q, E)$.

Usually, for each investigated Fourier time, the condition of equality between the two precession fields is determined

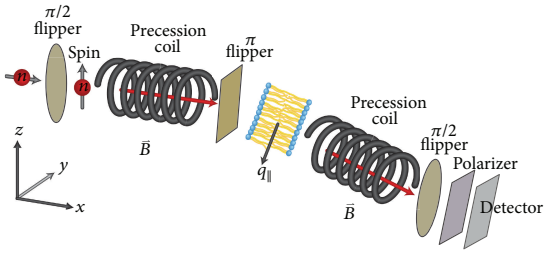

FIGURE 3: Schematic of a NSE experimental setup.

by sweeping the current (phase current) of a coil located inside one of the two spectrometer arms. Thus, the detected intensity follows the typical echo pattern (see Figure 4). The absolute minimum of the echo marks the echo condition for which the two precession fields are the same.

Incidentally, by switching the $\pi/2$ flippers off the precession, field intensity is essentially set to zero, which implies that the Fourier time value is zero as well. This effectively means that by switching the $\pi/2$ flippers off and by measuring the π flipper ON (spin flip intensity, SF) and OFF (nonspin flip intensity, NSF), a polarized diffraction measurement can be performed without changing the instrumental setup. In this way, the coherent and incoherent scattering intensity can be determined [20].

Because of the requirement of having a homogeneous field along the neutrons' flight path, except for a few noticeable exceptions [21], the NSE detector covers a small fraction of 4π. Thus, experiments requiring a large Q range coverage are less efficiently performed on an NSE spectrometer, as opposed to a backscattering spectrometer. This is often the case for incoherent scattering experiments where the Q dependence of the scattering function gives precious indications as to the nature of the observed dynamics. Also, the incoherent scattering event has a 2/3 probability of flipping the scattered neutron spin, effectively reducing the incoherent NSE signal by 2/3. However, NSE may have advantages for the study of oriented samples, as will be discussed below.

Using polarized neutrons, it is possible to determine the fraction of coherent and incoherent scattering as a function of the scattering vector, $\vec{Q}$. Unfortunately, in spite of the use of polarized neutrons, NSE cannot separate experimentally the incoherent from coherent dynamics because the neutron spin is employed to encode the energy exchanged with the sample. This limitation is a common issue with other spectrometers which do not use polarized neutrons. With this in mind, as long as the incoherent scattering is dominant, this problem can be overcome by collecting data with statistical significance.

The neutron scattering experiment was performed using the NSE spectrometer, on the Neutron Guide 5 (NG5), at the NIST Center for Neutron Research, Gaithersburg, MD, USA. The NG5-NSE was operated at a wavelength of $\lambda = 6$ Å, with a $\Delta\lambda/\lambda \approx 17.5\%$.

The sample was placed in a closed cycle refrigerator which can control the sample temperature with an accuracy of

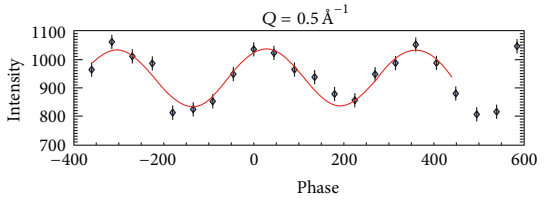

FIGURE 4: An incoherent echo for $q_{\|} = 0.5$ Å^{-1}. The third and second last points report the SF counts (measured twice), whereas the last point represents the NSF counts. The fact that the SF counts are smaller than the NSF counts is a direct evidence that the incoherent scattering is dominant at this Q value. The echo has a negative amplitude which indicates that the observed dynamics come from the incoherent scattering. Error bars shown throughout the paper represent ±1 standard deviation.

TABLE 1

Peak order	q_z (Å^{-1})	δq_z
1	0.1163	0.0001
2	0.2322	0.0009
3	0.35	0.01
4	0.47	0.05

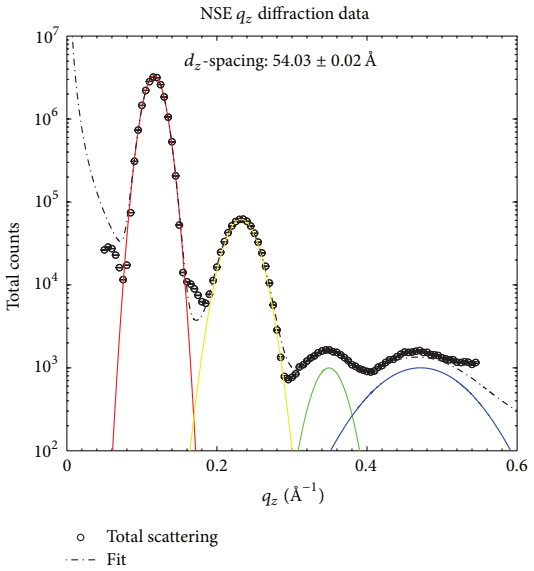

FIGURE 5: Out-of-plane diffraction data. The d_z-spacing of d_z = 54.03 Å, as determined from the fit, corresponds to a hydration of 99.4% relative humidity (RH) [23].

±0.1 K. The sample was mounted vertically in the neutron beam such that the scattering vector ($\vec{Q}$) could either be placed in the membrane plane ($q_{\|}$), or perpendicular to the membrane (q_z), by simply rotating the sample by 90 degrees. In this way, both out-of-plane and in-plane structures can easily be measured.

In order to normalize the ISF and to correct the instrumental resolution, $I(Q,t)$ is usually divided by a measurement of a perfectly elastic scatterer. In our case, the resolution was measured by cooling the sample to 70 K to freeze all molecular motions. The scattering of a sample at such low temperature can be considered to be elastic within the time window of this experiment. The advantage of using the actual sample for normalization is that size and geometry of the resolution sample are preserved. A scan of the empty can was also measured and subtracted from the data. The data were reduced using the software DAVE [22].

2.3. Sample Characterization. The quality of the multilamellar membrane samples was checked prior to the inelastic experiments. The lamellar spacing and mosaicity of the multilamellar membranes were determined by measuring out-of-plane and rocking scans in situ. The NSE spectrometer was used in diffraction mode, with the $\pi/2$ flippers off, and the data reported are the average of the NSF and SF counts. Figure 5 shows an out-of-plane scan along the q_z-axis at $T = 303$ K, in the fluid phase of the membranes. Four pronounced Bragg peaks were observed and their positions were determined from fits of Gaussian peak profiles. The q_z-positions are listed in Table 1.

A d_z-spacing of 54.03 ± 0.02 Å was determined and this corresponds to a hydration of 99.4% RH, close to full hydration of the bilayers [23]. We note that the out-of-plane Bragg peaks are significantly broadened as compared to measurements on dedicated neutron reflectometers. The reason for this broadening is that NSE spectrometers use a broad wavelength band of $\Delta\lambda/\lambda \approx 17.5\%$, which leads to an inherent broadening of Bragg reflections. However, the centre of the peaks can well be determined to measure the d_z-spacing of the stacked membranes.

The quality of the sample was checked in rocking scans, as shown in Figure 6. The distribution of membrane normal vectors can be estimated from the peak width to be smaller than ≈1°. The samples are, therefore, characterized as highly oriented membranes. This is a prerequisite to distinguish lateral diffusion from out-of-plane dynamics of the lipid molecules.

3. Results

3.1. Polarized Diffraction. The feasibility of detecting incoherent signals critically depends on the ratio between the coherent and incoherent scattering at the different in-plane, $q_{\|}$, positions. Low-angle diffraction was measured and is shown in Figure 7. An empty can, consisting of silicon wafers without membranes, and instrumental background were subtracted from the data. The incoherent scattering of the lipid molecules in the plane of the bilayers is dominant at $q_{||}$ values down to 0.1 Å^{-1}, corresponding to a lateral length scale of about 60 Å. The packing of the lipid acyl chains in the plane of the membrane leads to a correlation peak at a $q_{||}$ value of $q_{||} \approx 1.40$ Å^{-1} [24–26], with a strong coherent scattering contribution, even in protonated bilayers. This potentially

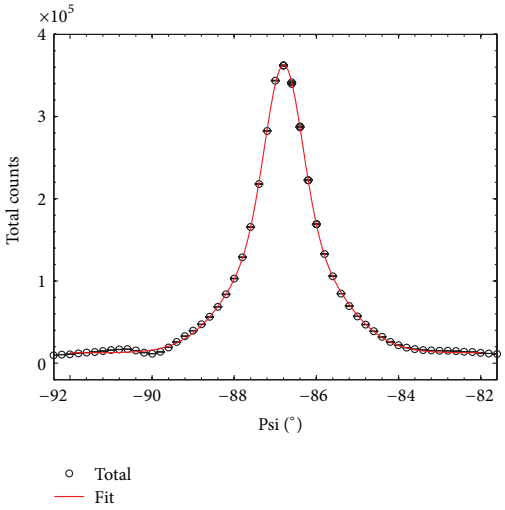

FIGURE 6: Rocking curve centred at $q_z = 0.117$ Å^{-1}, the first out-of-plane Bragg peak in Figure 5 The FWHM of the peak was fitted to be ≈1°.

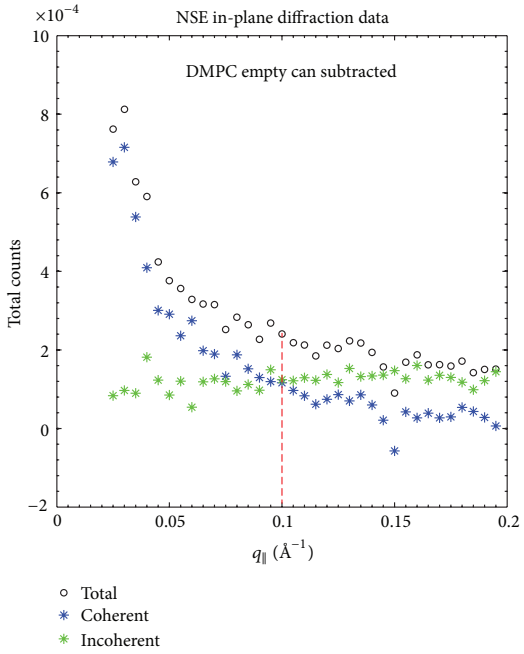

FIGURE 7: Polarized in-plane diffraction data of DMPC with empty can background subtraction. The incoherent scattering signal is dominant above $q_{||} = 0.1$ Å.

leaves a $q_{||}$ range of $0.1\,\text{Å}^{-1} < q_{||} < 1.4\,\text{Å}^{-1}$, corresponding to length scales of $5\,\text{Å} < q_{||} < 60\,\text{Å}$ for the study of lipid diffusion using incoherent NSE.

For this first test, we have decided to examine dynamics at a $q_{||}$ value of $q_{||} = 0.5\,\text{Å}^{-1}$ to prove the feasibility of incoherent NSE experiments in supported membrane systems. Dynamics at this $q_{||}$ value were previously measured using neutron backscattering such that our results could be directly compared in Section 4.

3.2. Incoherent Neutron Spin Echo. A typical spin echo is shown in Figure 4. Because of the weak incoherent signals, long counting times were used. Sample, background, and empty can were measured for ≈24 hours each resulting in a total counting time of ≈3 days at this $q_{||}$ value. Longer counting times can be expected at smaller $q_{||}$ values, where the ratio between incoherent and coherent intensity is less favourable.

The period of the echo is inversely proportional to the wavelength of the neutrons, λ. By fitting a sinusoidal curve, the amplitude and the average signal are determined. The ISF is obtained from $I(q_{||}, t) = (\text{SF} + \text{NSF})/(\text{SF}-\text{NSF})$. A series of echoes was measured for different spin-echo times, t, between 10 picoseconds and 1 nanosecond. The incoherent ISF is shown in Figure 8. Data start at an $I(q_{||}, t)$ value of $I(q_{||}, t) \approx 0.9$ at small times and decays towards longer spin-echo times.

In a first attempt (Figure 8(a)) data were fit using a single exponential decay,

$$\frac{I(q_{||}, t)}{I(q_{||}, 0)} = Ae^{(-t/\tau)}, \tag{1}$$

in agreement with a single, Brownian diffusion process. However, the corresponding fit in Figure 8(a) does not provide satisfactory agreement with the data.

In an attempt to describe the data more adequately, a tentative fit of two exponential functions was used,

$$\frac{I(q_{||}, t)}{I(q_{||}, 0)} = A_1 e^{(-t/\tau_1)} + A_2 e^{(-t/\tau_2)}, \tag{2}$$

to allow for two dynamical processes. The corresponding fit in Figure 8(b) provides better agreement with the data within the error bars of this experiment. A_1 and A_2 are the amplitudes of the two exponential decays; τ_1 and τ_2 are the corresponding relaxation times. No background was needed to fit the data, which indicates that the incoherent dynamics decay within the time window of this experiment. The fitted parameters are listed in the Table 2.

4. Discussion

NSE has been traditionally used to investigate coherent dynamics of polymers and complex systems at Q values corresponding to the small angle region; see [27] for a recent review. However, NSE was recently also successfully used [17, 18] to investigate incoherent dynamics. We applied incoherent NSE to study the diffusion of lipid molecules in a fluid lipid membrane. By using long counting times, high quality data could be measured. For this first experiment we have chosen a lateral $q_{||}$ value of $q_{||} = 0.5\,\text{Å}^{-1}$ in order to compare the results to those previously obtained by the neutron backscattering technique.

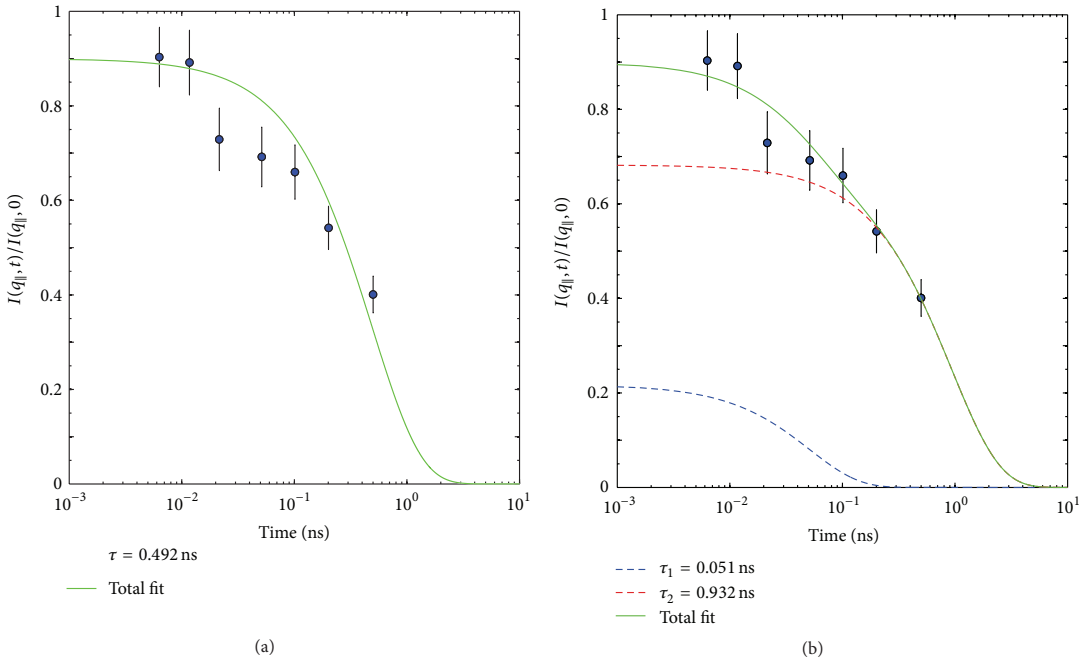

FIGURE 8: $I(q_{||},t)$ for $q_{||} = 0.5$ Å^{-1}. (a) $I(q_{||},t)$ data fit with a single exponential. (b) $I(q_{||},t)$ data fit with a double exponential to individually fit the dynamics occurring at long time scales (dashed red curve) and short time scales (dashed blue curve).

TABLE 2: Parameters used to fit the data shown in Figures 8(a) and 8(b).

Model	A_1	τ_1 (ns)	$\delta\tau_1$ (ns)	ΔE_1 (μeV)	$\delta\Delta E_1$ (μeV)	A_2	τ_2 (ns)	$\delta\tau_2$ (ns)	ΔE_2 (μeV)	$\delta\Delta E_2$ (μeV)
Single exponential	0.90	0.49	0.08	2.7	0.4					
Double exponential	0.22	0.05	0.02	26	11	0.68	0.9	0.2	1.4	0.3

Figure 9 shows τ_1 and τ_2 together with quasielastic energy broadening data previously published for DMPC in its fluid phase, at $T = 303$ K [8]. Only one diffusion process was observed in the experiment by Armstrong et al. The data quality resulting from this experiment did not allow for the unambiguous assignment of more than one process; however, the diffusion constant obtained from this analysis was in good agreement with coefficients quoted in the literature for similar systems [1, 4, 11, 12, 28]. The fit in Figure 9 corresponds to a diffusion coefficient of 64×10^{-12} m^2/s. It has been noted that the line of fit in Figure 9 does not pass through the origin, as one would expect from the Brownian diffusion model [8], and the offset is larger than the instrumental resolution. This behaviour is often observed in the literature on experiments using backscattering spectrometers; however, no consistent explanation has been offered.

The relaxation times obtained by NSE were converted to the quasielastic broadening values shown in Table 2 using

$$\Delta E_{\mathrm{FWHM}} = \frac{2\hbar}{\tau}, \tag{3}$$

which can be obtained by simply Fourier transforming the self ISF, resulting in a Lorentzian function which has a FWHM that is the quasielastic energy broadening.

This equation can be simplified to

$$\Delta E_{\mathrm{FWHM}} = \frac{2\hbar}{\tau} \cdot \frac{10^{15}}{e} = \frac{2}{1.52\tau}, \tag{4}$$

where the units of ΔE_{FWHM} and τ are μeV and ns, respectively. These energies are included in Figure 9 as stars, which correspond to the two dynamical processes measured at $q_{||} = 0.5$ Å^{-1}. The relaxation time found by fitting $I(q_{||},t)$ using a single exponential in Figure 8(a) is also included.

The relaxation time determined by the single exponential fit of $\tau = 0.49$ ns occurs at a ΔE value of $\Delta E = 2.7$ μeV, much smaller than the process reported by the backscattering technique. However, we note that the corresponding model in Figure 8(a) did not provide a good fit to the data. We, therefore, attempted to fit the data by two exponential functions in Figure 8(b).

The fast process at $\tau_1 = 0.05$ ns ($\Delta E = 26$ μeV) agrees well with the dynamics observed in the backscattering experiment

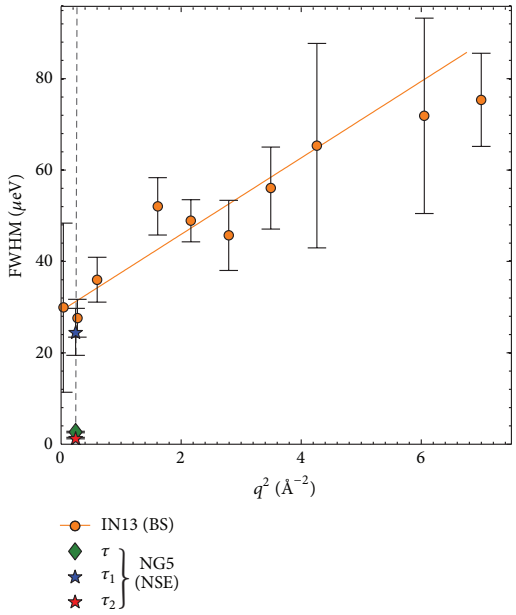

FIGURE 9: Quasielastic energy broadening (FWHM) as function of $q_{||}^2$. The yellow data and fit were obtained from an experiment performed on the same system using neutron backscattering [8]. The diamond corresponds to the energy broadening which relates to the tau value from the single exponential used to fit $I(Q,t)$ in Figure 8(a). The two stars correspond to the tau values obtained from the double exponential fit shown in Figure 8(b).

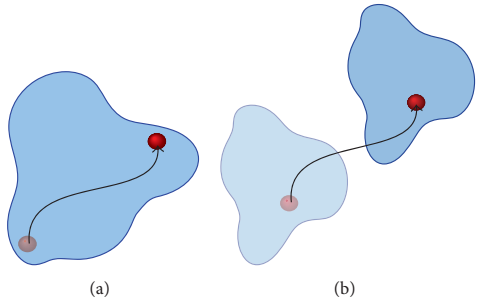

FIGURE 10: Schematic diagram illustrating the two diffusion processes thought to occur in this system. (a) The faster diffusion process of an individual lipid moving, confined within a domain. (b) The slower diffusion process of a lipid moving as part of a larger domain.

at this length scale in Figure 9. It, therefore, seems that the energy offset observed in the backscattering experiment is not related to the instrumental resolution of the backscattering instrument, as speculated previously.

An energy offset at small $q_{||}$ has been reported for confined diffusion, such as diffusion in a sphere or cylinder [29–31]. At smaller length scales (large $q_{||}$), the particles follow a typical Brownian diffusion process. However, when the displacement becomes comparable to the size of the confinement, the particles start to "feel" their confinement and the quasielastic energy broadening becomes constant, leading to an offset. The faster process can, therefore, be tentatively assigned to lipid motion confined to a certain area in the membrane. This observation is in agreement with recent results, which suggest that lipids move coherently in loosely bound clusters of ≈30 Å diameter, rather than as independent molecules [9–11].

The second, slow process at $\tau_2 = 0.9$ ns ($\Delta E = 1.4\,\mu$eV) was not observed in the backscattering data in Figure 9. Slow, long-range diffusion was reported by Busch et al. [11] using the neutron time-of-flight technique. The energy broadening of ≈1 μeV at a Q value of 0.5 Å^{-1} determined by Bayesian analysis of the small broadening of the instrumental resolution corresponds well with the value for τ_2.

The two processes identified in Figure 8(b) can, therefore, be tentatively assigned to a slow, unconstrained lipid diffusion and a second, faster process related to confined lipid diffusion. As depicted in Figure 10, these processes may be related to diffusion of a lipid molecule within a coherently coupled patch, and diffusion of the whole patch. While the confined process (Figure 10(a)) occurs on small length scales, the purely Brownian process in Figure 10(b)) most likely occurs over larger distances and can possibly be observed using FCS.

We note that the purpose of the present experiment was to prove the feasibility of incoherent NSE experiments in solid supported membrane systems and to compare the results to data previously obtained by neutron backscattering. The determination of slopes, from which diffusion coefficients can be calculated, involves the measurement of several $q_{||}$-values, and is beyond the scope of the present experiment. We can not, therefore, make a statement about diffusion constants or the molecular mechanism of diffusion at this time.

Further experiments are required to determine the precise shape of $\Delta E(q_{||})$ in an effort to more accurately assign the underlying diffusion mechanisms. To determine the molecular mechanism of lipid diffusion, several $q_{||}$ values between 0.1 Å^{-1} and 1.4 Å^{-1} will be measured in future experiments.

5. Conclusion

This experiment proves the feasibility of measuring the diffusion of lipid molecules in oriented membrane systems using incoherent NSE spectrometry.

There are several advantages of using NSE spectrometers to measure diffusion in membranes as compared to backscattering spectrometers. NSE covers a large dynamic range, from 0.005 ns to 15 ns. By using oriented samples, lateral diffusion can well be separated from out-of-plane motions. And finally, data quality is not limited by the instrumental resolution.

This technique will, in the future, be used to determine lipid diffusion on length scales up to 60 Å, a regime previously inaccessible by neutron probes. This length scale is significantly larger than lipid-lipid distances and will allow for the

testing and designation of different lipid diffusion models to the membrane system.

At present, incoherent NSE experiments in membrane systems are hindered by the inherently long counting times required to resolve the small incoherent signals. However, diffusion of lipids and proteins in membranes under physiological conditions is an important topic in membrane biophysics with implications in cancer and Alzheimer's research, making these types of measurements highly relevant. Incoherent NSE can push the limit of length scales accessible via neutron scattering, thus enabling the study of diffusion over mesoscopic distances and closing the gap between neutron and fluorescence experiments.

Acknowledgments

This work utilized facilities supported in part by the National Science Foundation under Agreement no. DMR-0944772. This research was funded by the Natural Sciences and Engineering Research Council of Canada (NSERC), the National Research Council Canada (NRC), the Canada Foundation for Innovation (CFI), and the Ontario Ministry of Economic Development and Innovation (OMEDI). H. Dies is the recipient of an NSERC-USRA, and M. C. Rheinstädter is the recipient of an Early Researcher Award of the Province of Ontario.

References

[1] S. König, W. Pfeiffer, T. Bayerl, D. Richter, and E. Sackmann, "Molecular dynamics of lipid bilayers studied by incoherent quasi-elastic neutron scattering," *Journal de Physique II*, vol. 2, pp. 1589–1615, 1992.

[2] S. König, E. Sackmann, D. Richter, R. Zorn, C. Carlile, and T. M. Bayerl, "Molecular dynamics of water in oriented DPPC multilayers studied by quasielastic neutron scattering and deuterium-nuclear magnetic resonance relaxation," *The Journal of Chemical Physics*, vol. 100, no. 4, pp. 3307–3316, 1994.

[3] S. König, T. M. Bayerl, G. Coddens, D. Richter, and E. Sackmann, "Hydration dependence of chain dynamics and local diffusion in L-α-dipalmitoylphosphtidylcholine multilayers studied by incoherent quasi-elastic neutron scattering," *Biophysical Journal*, vol. 68, no. 5, pp. 1871–1880, 1995.

[4] W. Pfeiffer, T. Henkel, E. Sackmann, and W. Knorr, "Local dynamics of lipid bilayers studied by incoherent quasi-elastic neutron scattering," *Europhysics Letters*, vol. 8, no. 2, p. 201, 1989.

[5] W. Pfeiffer, S. König, J. Legrand, T. Bayerl, D. Richter, and E. Sackmann, "Neutron spin echo study of membrane undulations in lipid multibilayers," *Europhysics Letters*, vol. 23, no. 6, p. 457, 1993.

[6] E. Flenner, J. Das, M. C. Rheinstädter, and I. Kosztin, "Subdiffusion and lateral diffusion coefficient of lipid atoms and molecules in phospholipid bilayers," *Physical Review E*, vol. 79, Article ID 011907, 11 pages, 2009.

[7] J. H. Jeon, H. M. S. Monne, M. Javanainen, and R. Metzler, "Anomalous diffusion of phospholipids and cholesterols in a lipid bilayer and its origins," *Physical Review Letters*, vol. 109, Article ID 188103, 5 pages, 2012.

[8] C. L. Armstrong, M. Trapp, J. Peters, T. Seydel, and M. C. Rheinstädter, "Short range ballistic motion in fluid lipid bilayers studied by quasi-elastic neutron scattering ," *Soft Matter*, vol. 7, pp. 8358–8362, 2011.

[9] E. Falck, T. Róg, M. Karttunen, and I. Vattulainen, "Lateral diffusion in lipid membranes through collective flows," *Journal of the American Chemical Society*, vol. 130, no. 1, pp. 44–45, 2008.

[10] M. C. Rheinstädter, J. Das, E. J. Flenner, B. Brüning, T. Seydel, and I. Kosztin, "Motional coherence in fluid phospholipid membranes," *Physical Review Letters*, vol. 101, Article ID 248106, 4 pages, 2008.

[11] S. Busch, C. Smuda, L. C. Pardo, and T. Unruh, "Molecular mechanism of long-range diffusion in phospholipid membranes studied by quasielastic neutron scattering," *Journal of the American Chemical Society*, vol. 132, no. 10, pp. 3232–3233, 2010.

[12] C. L. Armstrong, M. D. Kaye, M. Zamponi et al., "Diffusion in single supported lipid bilayers studied by quasi-elastic neutron scattering," *Soft Matter*, vol. 6, no. 23, pp. 5864–5867, 2010.

[13] F. Roosen-Runge, M. Hennig, F. Zhang et al., "Protein self-diffusion in crowded solutions," *Proceedings of the National Academy of Sciences of the United States of America*, vol. 108, no. 29, pp. 11815–11820, 2011.

[14] D. S. Banks and C. Fradin, "Anomalous diffusion of proteins due to molecular crowding," *Biophysical Journal*, vol. 89, no. 5, pp. 2960–2971, 2005.

[15] S. W. Hell and J. Wichmann, "Breaking the diffraction resolution limit by stimulated emission: stimulated-emission-depletion fluorescence microscopy," *Optics Letters*, vol. 19, no. 11, pp. 780–782, 1994.

[16] M. Bée, *Quasielastic Neutron Scattering: Principles and Applications in Solid State Chemistry, Biology and Materials Science*, Taylor & Francis, Boca Raton, Fla, USA, 1988.

[17] E. Mamontov, A. Faraone, E. W. Hagaman, K. S. Han, and E. Fratini, "A low-temperature crossover in water dynamics in an aqueous LiCl solution: diffusion probed by neutron spin-echo and nuclear magnetic resonance," *Journal of Physical Chemistry B*, vol. 114, no. 50, pp. 16737–16743, 2010.

[18] A. Wischnewski, M. Monkenbusch, L. Willner, D. Richter, and G. Kali, "Direct observation of the transition from free to constrained single-segment motion in entangled polymer melts," *Physical Review Letters*, vol. 90, no. 5, Article ID 058302, 4 pages, 2003.

[19] F. Mezei, Ed., *Neutron Spin Echo*, Springer, Berlin, Germany, 1980.

[20] A. M. Gaspar, S. Busch, M. S. Appavou et al., "Using polarization analysis to separate the coherent and incoherent scattering from protein samples," *Biochimica et Biophysica Acta*, vol. 1804, no. 1, pp. 76–82, 2010.

[21] B. Farago, "IN11C, medium-resolution multidetector extension of the IN11 NSE spectrometer at the ILL," *Physica B*, vol. 241–243, pp. 113–116, 1997.

[22] R. T. Azuah, L. R. Kneller, Y. Qiu et al., "DAVE: a comprehensive software suite for the reduction, visualization, and analysis of low energy neutron spectroscopic data," *Journal of Research of the National Institute of Standards and Technology*, vol. 114, no. 6, pp. 341–358, 2009.

[23] N. Chu, N. Kučerka, Y. Liu, S. Tristram-Nagle, and J. F. Nagle, "Anomalous swelling of lipid bilayer stacks is caused by softening of the bending modulus," *Physical Review E*, vol. 71, Article ID 041904, 8 pages, 2005.

[24] M. C. Rheinstädter, C. Ollinger, G. Fragneto, F. Demmel, and T. Salditt, "Collective dynamics of lipid membranes studied by inelastic neutron scattering," *Physical Review Letters*, vol. 93, no. 10, Article ID 108107, 4 pages, 2004.

Chapter 5

Domains in Biological Systems

Although a multicomponent system, it was once thought that the macromolecular constituents of the cell membrane were evenly dispersed in the fluid matrix, giving rise to a relatively homogeneous membrane structure [3]. However, there seems to be increasing evidence that this is not the case [56]. Density fluctuations and segregation of lipids, as well as clustering of macromolecules, can lead to the formation of functionally important domains.

A better understanding of the function and formation of domains requires the development of a technique that is able to overcome the challenges associated with their measurement [57]. The domains which are the focus of the study presented in this document are small, transient structures. Their size, on the order of tens of nanometers, is beyond the resolution of standard optical microscopy techniques. Newly developed super resolution microscopy methods, such as stimulated-emission-depletion fluorescence microscopy, are yielding promising results which could be applied to the study of rafts in the future [58]. Nanodomains have been observed by atomic force microscopy in single supported bilayer systems [59], however the strong interaction between the bilayer and the substrate may stabilize the domains, increasing their lifetime to time scales on the order of seconds or minutes. The dynamic nature of domains in stack bilayer systems, which undergo nano-micro second fluctuations, make them difficult to observe using raster scanning techniques. While neutron scattering is capable of accessing both the length and time scales required to observe such structures, some alterations must be made to the typical TAS setup to increase its sensitivity to this

type of short-range order. The details of this technique can be found in Section 5.2, and Papers V and VI demonstrate its use.

Although it seems intuitive to probe the structure of a system in an effort to find evidence for the existence of domains, our first indication that the bilayer was not assuming a homogeneous state was observed while probing the dynamics of the system. These results are presented in Paper IV.

5.1 Paper IV: Effect of Cholesterol on the Lateral Nanoscale Dynamics of Fluid Membranes

Clare L. Armstrong, Matthew A. Barrett, Arno Hiess, Tim Salditt, John Katsaras, An-Chang Shi, and Maikel C. Rheinstädter *"Effect of cholesterol on the lateral nanoscale dynamics of fluid membranes"*, Eur. Biophys. J., **41**, 901-913, 2012.

5.1.1 Preface to Paper IV

The purpose of this work was to determine the effect of cholesterol on the dynamics of a lipid bilayer system. The samples examined in this project were DMPC stack bilayer systems with low (5 mol%) and high (40 mol%) cholesterol concentrations. The experiments were conducted using two different TAS at the ILL: IN8 (a thermal neutron spectrometer with a 1 meV resolution, capable of detecting excitation energies up to 20 meV), and IN12 (a cold neutron spectrometer with a 0.2 meV energy resolution, sensitive to lower-energy excitations up to 5 meV). With the use of these two spectrometers, the dynamics of the system could be mapped out over a broad energy and $q_{||}$ range.

Both the low and high cholesterol data displayed three distinct energy dispersion curves, which were assigned to the gel phase, fluid phase, and a liquid ordered (l_o) phase due to the presence of cholesterol. This not only suggests that there is a coexistence of fluid and gel phases in the system, but also that the cholesterol is non-uniformly dispersed in the bilayer. If the cholesterol were evenly distributed throughout the bilayer, we would expect to simply observed the fluid and gel dispersion curves, with evidence of increased order and rigidity at high cholesterol concentrations. This

non-uniform dispersement results in regions of higher cholesterol concentration which are thought to give rise to the l_o phase. The energy dispersion curve of this phase appears to have a higher degree of structural order than the gel phase, but an increased "softness" relating to the interactions associated with nanoscale dynamics. Thus, the l_o phase seems to combine properties of rigid gel and soft fluid bilayers.

Author Contributions

- *Designed research:* Maikel C. Rheinstädter
- *Sample fabrication:* Maikel C. Rheinstädter
- *Performed experiment:* Arno Hiess, Tim Salditt, and Maikel C. Rheinstädter
- *Analysed data:* **Clare L. Armstrong**
- *Developed scattering density code:* Matthew A. Barrett and Maikel C. Rheinstädter
- *Wrote the manuscript:* **Clare L. Armstrong**, An-Chang Shi, John Katsaras, and Maikel C. Rheinstädter

Eur Biophys J
DOI 10.1007/s00249-012-0826-4

ORIGINAL PAPER

EBSA
Biophysics in Europe

Effect of cholesterol on the lateral nanoscale dynamics of fluid membranes

Clare L. Armstrong · Matthew A. Barrett · Arno Hiess · Tim Salditt · John Katsaras · An-Chang Shi · Maikel C. Rheinstädter

Received: 2 March 2012 / Revised: 3 May 2012 / Accepted: 7 May 2012

Abstract Inelastic neutron scattering was used to study the effect of 5 and 40 mol% cholesterol on the lateral nanoscale dynamics of phospholipid membranes. By measuring the excitation spectrum at several lateral $q_{\|}$ values (up to $q_{\|} = 3$ Å^{-1}), complete dispersion curves were determined of gel, fluid and liquid-ordered phase bilayers. The inclusion of cholesterol had a distinct effect on the collective dynamics of the bilayer's hydrocarbon chains; specifically, we observed a pronounced stiffening of the membranes on the nanometer length scale in both gel and fluid bilayers, even though they were experiencing a higher degree of molecular disorder. Also, for the first time we determined the nanoscale dynamics in the high-cholesterol liquid-ordered phase of bilayers containing cholesterol. Namely, this phase appears to be "softer" than fluid bilayers, but better ordered than bilayers in the gel phase.

Keywords Lipid membrane · Cholesterol · Lateral membrane dynamics · Nanoscale dynamics · Liquid-ordered phase · Inelastic neutron scattering · Dispersion relation

Special Issue: Scattering techniques in biology: marking the contributions to the field from Peter Laggner on the occasion of his 68th birthday.

C. L. Armstrong (✉) · M. A. Barrett · A.-C. Shi · M. C. Rheinstädter
Department of Physics and Astronomy, McMaster University, ABB-241, 1280 Main Street West, Hamilton, ON L8S 4M1, Canada
e-mail: armstc5@mcmaster.ca

A. Hiess
European Spallation Source ESS AB, P.O. Box 176, 22100 Lund, Sweden

T. Salditt
Institute for X-Ray Physics, Georg-August-University Göttingen, Friedrich-Hund-Platz 1, 37077 Göttingen, Germany

J. Katsaras
Neutron Sciences Directorate, Oak Ridge National Laboratory, Oak Ridge, TN 37831-6100, USA

J. Katsaras · M. C. Rheinstädter (✉)
Canadian Neutron Beam Centre, National Research Council, Chalk River, ON K0J 1J0, Canada
e-mail: rheinstadter@mcmaster.ca

Introduction

Cholesterol is an essential structural component of eukaryotic cell membranes capable of modulating their permeability and molecular organization. It is either obtained from foods of animal origin or synthesized in the endoplasmic reticulum, a multifold membranous structure that is also capable of producing phospholipids, including different types of membranes (Ridsdale et al. 2006). In association with lipid rafts (i.e., functional domains), cholesterol has also been implicated in cell signaling processes (Simons 1997; Brown 2000; Petrie et al. 2000; Papanikolaou et al. 2005; Pike 2006).

Cholesterol and saturated lipid species preferentially partition into liquid-ordered domains, away from unsaturated, liquid-disordered lipid species. In particular, cholesterol, because of its rigid planar structure, preferentially interacts with sphingolipids (e.g., sphingomyelin) and their highly ordered saturated hydrocarbon chains, but not exclusively (Pike 2009). Moreover, cholesterol has been shown to interact strongly with phosphatidylcholine (PC) lipids that have saturated hydrocarbon chains (Vist 1990).

Published online: 23 June 2012

In pure lipid bilayers, cholesterol modulates the molecular organization of lipids, namely by disrupting the regular packing of gel phase di-saturated PC membranes and restricting the reorientation of these same membranes when in the liquid-disordered phase (Vist 1990). However, at sufficiently high concentrations of cholesterol (i.e., >25 mol%), the so-called liquid-ordered state, which is characterized by rapid hydrocarbon chain reorientation but high conformational order, is formed over a wide range of temperatures smearing out the traditional gel and liquid crystalline phases (Fig. 1) (Mouritse 2010).

Although cholesterol is known to modulate the behavior of membranes, in the recent past it has been shown that lipid bilayers made of polyunsaturated fatty acids (PUFAs, namely, di-20:4 PC) can cause cholesterol to sequester to the bilayer center (i.e., laying flat with its hydroxyl group in the middle of the bilayer) (Harroun et al. 2006, 2008), a location that is significantly different from cholesterol's nominal upright orientation, where its hydroxyl group is located near the lipid/water interface (Léonard et al. 2001). However, the addition of just 5 mol% of dimyristoyl phosphatidylcholine (DMPC, di-14:0 PC) to those same PUFA bilayers causes cholesterol to revert to its nominal upright orientation (Kučerka 2009). This has been explained in terms of the "umbrella" model (Petrie et al. 2000; Papanikolaou et al. 2005), which suggests that cholesterol molecules associate strongly with ordered hydrocarbon chains (usually ones that are fully saturated) in such a manner that they are shielded from contact with the aqueous environment by the lipid head group. It seems obvious then that, although cholesterol can modulate the structural (e.g., chain packing) and mechanical (e.g., bending modulus) properties of bilayers, the bilayers themselves can, on the other hand, also modulate cholesterol's behavior.

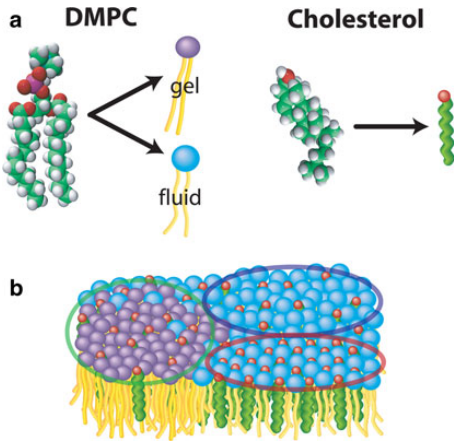

Fig. 1 **a** Schematic representations of DMPC and cholesterol molecules. In the gel phase, the lipids tails are in the all-trans configuration. At the main transition temperature lipid hydrocarbon tails "melt", resulting in fluid phase bilayers. **b** Schematic model of the possible phases present in DMPC/cholesterol systems. The gel, fluid and liquid-ordered phases are highlighted by the *green*, *blue* and *red circles*, respectively

We have studied the short wavelength fluctuations in DMPC membranes containing 5 and 40 mol% cholesterol using inelastic neutron scattering. Complete dispersion relations of gel, fluid and liquid-ordered membranes were obtained by measuring the excitation at different lateral momentum transfers. From experimentally obtained spectra, we were able to extract the "softness" of the hydrocarbon membrane core on the nanometer length scale, a length scale comparable to molecular distances within the membrane. We found that the bilayer's hydrocarbon core became significantly less fluid in the presence of cholesterol. In the liquid-ordered state, however, the system not only assumed a high degree of molecular order (associated with the high cholesterol content), but there was a concomitant softening of the nanoscale elastic properties, a feature more akin to fluid bilayers.

Materials and methods

Sample preparation

Highly oriented multi-lamellar stacks of 1,2-dimyristoyl-sn-glycero-3-phosphocholine (DMPC) and cholesterol were prepared on 2-inch-diameter, 300-μm-thick, single-side polished Si wafers. The coherent scattering of the lipid hydrocarbon chains was enhanced by using tail deuterated lipids, i.e., DMPC-d54. The use of protonated cholesterol enabled the experiment to detect changes in hydrocarbon chain structure and dynamics. A 20 mg/ml suspension of DMPC-d54 and cholesterol dissolved in 1:1 chloroform and 2,2,2-trifluoroethanol (TFE) was prepared. Two different samples were fabricated for this study; specifically, a sample containing 5 mol% cholesterol and another with 40 mol% cholesterol, a concentration found in biological membranes. The Si wafers were cleaned by alternate 12-min sonications in ultra-pure water and ethanol at 313 K. This process was repeated twice. Then 1 ml of the lipid solution was deposited on each Si wafer and allowed to dry. The wafers were kept in a vacuum overnight to remove all traces of the solvent. The samples were then hydrated with heavy water (D_2O) and annealed at 303 K for 24 h. Following this protocol, each wafer contained roughly 3,000 highly oriented membranes, totaling $\sim$10 μm in thickness.

Twenty sample-containing Si wafers were stacked with 0.6-mm aluminium spacers placed in between each wafer to enable proper hydration of the membranes. The stack of

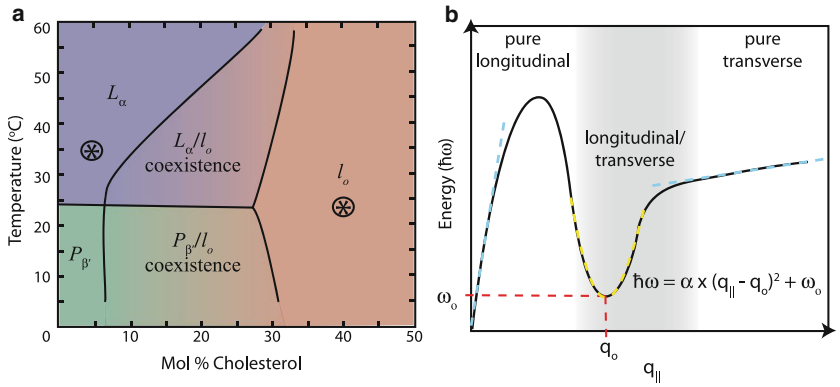

Fig. 2 **a** Schematic phase diagram of a DMPC cholesterol system as reported by, e.g., Vist 1990; Almeida et al. 1992; Thewalt and Bloom 1992; de Meyer 2009; de Meyer et al. 2010. Besides the well-known gel and fluid phase, the so-called liquid-order phase, is observed at high cholesterol concentrations. The 5 mol% cholesterol sample is in the L_α phase, while the 40 mol% sample is clearly in the l_o phase, as depicted by the ⊛. **b** A typical lateral dispersion curve observed in lipid systems (see, e.g., Chen et al. 2001; Weiss et al. 2003; Chen et al. 2003; Rheinstädter et al. 2004a; Tarek et al. 2001; Hub et al. 2007; Kaye et al. 2011). The $q_{||}$ range around the minimum is well described by a parabolic fit. The dispersion is linear at small $q_{||}$ values due to high-frequency sound propagation with longitudinal polarization. The high-$q_{||}$ regime is also linear; however, a transverse polarization has been previously observed

Si wafers were kept in a temperature- and humidity-controlled aluminium chamber, a so-called humidity chamber, during the course of the experiment. Hydration of the lipid membranes from the vapor phase was achieved by separately adjusting the temperature of the heavy water reservoir, the "sandwich" stack of Si wafers and the sample chamber's cover. Temperature and humidity sensors were installed close to the sample, and a water bath was used to control the temperature of the water reservoirs. Using this setup, a lamellar repeat spacing (d_z-spacing) of 53.1 Å was achieved for the fluid phase low cholesterol sample, which is comparable to the fluid phase of pure DMPC. For example, from the published values for d_z as a function of relative humidity (RH) published for pure DMPC (Kučerka 2005), the hydration of the DMPC bilayers in this experiment is estimated to be ∼99.5% (100% RH corresponds to fully hydrated bilayers) (Katsaras 1998).

The samples were mounted vertically in the neutron beam such that the scattering vector (**Q**) could either be placed in the plane of the membrane ($\mathbf{q}_{||}$) or perpendicular to the membrane ($\mathbf{q}_z$). Out-of-plane and in-plane structure could be measured by simply rotating the sample by 90°.

The phase diagram of phospholipid membranes containing different amounts of cholesterol remains an active field of research (Vist 1990, Almeida et al. 1992; Thewalt and Bloom 1992; de Meyer 2009; de Meyer et al. 2010). A schematic phase diagram of DMPC/cholesterol membranes is shown in Fig. 2a. It has been speculated that the relatively stiff cholesterol molecules align parallel to the hydrocarbon lipid tails and suppress lipid tail fluctuations (Róg et al. 2009), thereby affecting the membrane's dynamical properties. Most studies agree that three phases are observed, depending on temperature and cholesterol concentration: the rigid gel (ripple) $P_{\beta'}$ phase, the fluid L_α phase and the liquid-ordered l_o phase. The gel and fluid phases are well known from single component phospholipid bilayers. However, the l_o phase is solely observed at high concentrations of cholesterol. This bilayer phase is somewhat peculiar as it appears to be well ordered (similar to the gel phase); however, the lipids exhibit a diffusion coefficient that is comparable to that of fluid bilayers.

At low cholesterol content the bilayers undergo a phase transition from the gel to the fluid phase, as in pure lipid bilayers. The temperature of this so-called main transition T_m is slightly shifted towards higher temperatures. However, at high cholesterol concentrations ($\gtrsim$40 mol%), the main transition of liquid-ordered membranes was found to be suppressed, while at intermediate cholesterol concentrations (i.e., between about 10–30 mol%) most studies report a coexistence between gel and l_o, or L_α and l_o phases. The 5 mol% cholesterol sample was measured at $T = 308$ K (35 °C), while all scans for the 40 mol% sample were conducted at $T = 297$ K (24 °C). These temperatures were selected based on the schematic phase diagram in Fig. 2a. In an attempt to measure the system in one phase, temperatures were chosen far from the speculated phase boundaries. The phases at which these samples were studied are shown in Fig. 2a. The 5 mol% sample is, therefore, made up of fluid phase DMPC bilayers. As the phase transition was found to be suppressed in the l_o phase, the temperature is not a critical parameter for the high cholesterol sample.

Neutron-scattering experiment

Experiments were conducted using two different triple-axis spectrometers (TAS) co-located at the Institut Laue-Langevin high flux neutron reactor (Grenoble, France). The three axis of the spectrometers refer to the axes of rotation of the monochromator, the sample and the analyzer. The incident and final neutron energies are defined by the Bragg reflections from pyrolytic graphite (PG) crystals. Divergence of the neutron beam is controlled by several neutron Soller collimators. A schematic of the instrument configuration is shown in Fig. 3. In-plane and out-of-plane structure and dynamics can be measured simultaneously on a TAS by simply rotating the sample by 90°.

Neutrons with energies up to 20 meV were measured on the thermal TAS IN8 instrument with an energy resolution of $\sim$1 meV. Cold neutron spectrometers are inherently higher energy resolution instruments and enable the measurement of low-energy excitations (up to $\sim$5 meV). These measurements were conducted on the cold TAS IN12, which has an energy resolution of $\sim$0.2 meV.

The energy and $q_{||}$ resolution of a neutron triple-axis spectrometer are determined by the incident neutron energy, the divergence of the neutron beam and the wavelength resolution of the monochromator and analyzer. The incident energies, energy range, $q_{||}$ range and resolution of the two spectrometers used for this study are listed in Table 1. By combining a cold and thermal TAS, a $(\hbar\omega, q_{||})$ range of 0.4 $\text{Å}^{-1} < q_{||} < 3$ Å^{-1} and energies of up to $\sim$20 meV were accessible. As a result, our experiments were sensitive to picosecond dynamics in the plane of the membrane, covering length scales from between 2 and $\sim$20 Å. These distances range from less than a lipid-lipid interaction to one encompassing almost three lipid molecules.

Results

Neutron diffraction

Our setup permitted for the determination of the out-of-plane and in-plane structure of 2 mol% cholesterol/membrane samples. By rotating the sandwich sample by 90°, the scattering geometry can be switched (with respect to the Si substrates) from transmission to grazing incidence. To study in-plane structure ($\mathbf{q}_{||}$), the scattering vector $\mathbf{Q}$ is located in the plane of the membrane (i.e., transmission geometry). In grazing incidence, $\mathbf{Q}$ is normal to the Si and membrane plane ($\mathbf{q}_z$), enabling us to study out-of-plane structure.

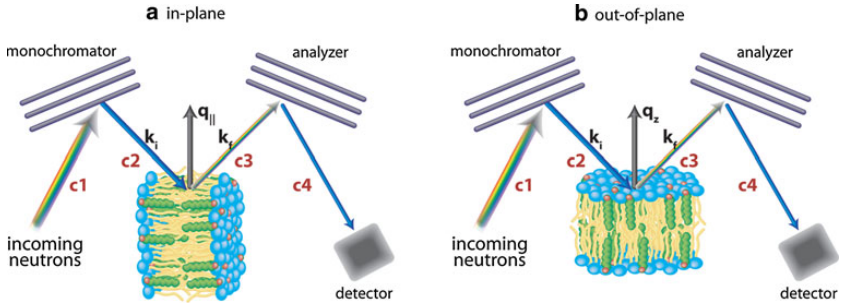

Fig. 3 Schematic representation of a triple axis spectrometer geometry. **a** Orientation of the sample for in-plane scans such that $\mathbf{Q}$ is in the plane of the membrane ($\mathbf{q}_{||}$). **b** Orientation of the sample for out-of-plane scans such that $\mathbf{Q}$ is perpendicular to the plane of the membrane ($\mathbf{q}_z$). $\mathbf{k_i}$ and $\mathbf{k_f}$ are the incident and final wave vectors, respectively; $c1$–$c4$ indicate the positions of the neutron collimators that were used to control the $\mathbf{Q}$ and energy resolutions

Table 1 $q_{||}$ and q_z and energy resolutions of the two spectrometers used in this study

Instrument	Incident neutron energy (meV)	Accessible energy range (meV)	Energy resolution (meV)	Accessible $q_{||}$ range (Å^{-1})	$q_{||}$ resolution (Å^{-1})
IN12	4.7	0–5	0.165	0–3	0.01
IN8	14.7	0–25	1.01	0–3	0.02

Instrumental setup, including collimation, was 30′–monochromator–30′–sample–30′–analyzer–60′–detector on IN12 and ø–monochromator–30′–PG filter–sample–30′–analyzer–ø–detector on IN8

In-plane structure

The lipid acyl chain positional correlation peak is the result of closely packed acyl chains making up the hydrophobic core of the membrane, as shown in Fig. 4a. The Bragg peaks from the two samples are well fit by Lorentzians. The peak in the 40 mol% sample is more pronounced and slightly shifted toward smaller $q_{||}$-values. This implies an enhanced order of the lipid tails at 40 mol% cholesterol. The distance between two lipid chains increases from 4.53 Å ($q_{||} = 1.39$ Å^{-1}) to 4.59 Å ($q_{||} = 1.37$ Å^{-1}), as determined from the fits to the Bragg peaks ($d = 2\pi/q_{||}$). The widths of the Bragg peaks also increase, albeit slightly, from $\Delta q_{||} = 0.13$ Å^{-1} to $\Delta q_{||} = 0.14$ Å^{-1}, which indicates a larger distribution of nearest-neighbor distances. The presence of cholesterol molecules seems to have little effect on hydrocarbon chain packing. The packing of lipid acyl chains is the result of a balance between attractive and repulsive forces resulting from tail fluctuations, i.e., between the free energy and entropy of the hydrocarbon tails. Incorporation of cholesterol molecules should, in theory, drastically increase the area per lipid. However, the area per lipid in the presence of cholesterol is comparable to lipid areas found in pure lipid bilayers, as cholesterol is believed to suppress hydrocarbon chain fluctuations.

It should be noted that the curves in Fig. 4a have not been shifted with respect to each other. The background in the 40 mol% sample is drastically increased because of the presence of protonated cholesterol, which contributes to the strong incoherent background.

Out-of-plane structure

Specular reflectivity allows for the determination of bilayer structure perpendicular to the plane of the membrane [see, e.g., Pabst 2010; Fragneto 2007]. The intensity of the

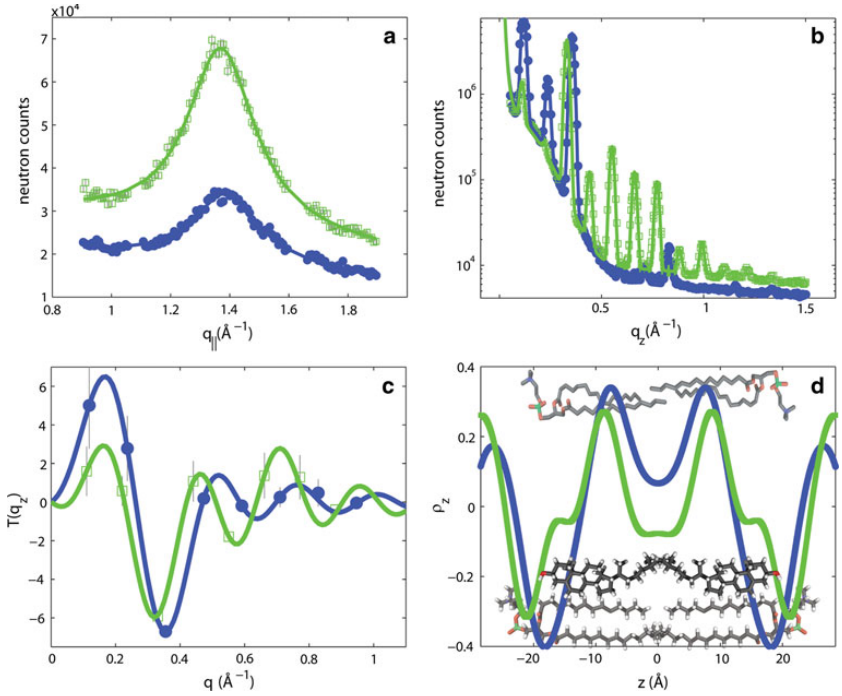

Fig. 4 Overview of the diffraction data: the *blue solid lines* and data points correspond to the 5 mol% cholesterol sample, while the *green solid lines* and data points refer to the 40 mol% cholesterol sample. **a** In-plane scattering ($q_{||}$) used to measure the acyl chain-chain positional correlation peak. Two spurious Bragg peaks from the humidity chamber at $\sim$1.1 Å^{-1} and $\sim$1.65 Å^{-1} were omitted from the scans. The *solid lines* are the Lorentzian fits to the experimental data. **b** Out-of-plane scattering (q_z) and the observation of several Bragg peaks. The position and area of each Bragg peak was determined through the fitting of a Gaussian, including the q^{-4} background. **c** $T(q_z)$, as determined by Eq. (4). Data points correspond to the integrated intensities of the different out-of-plane Bragg peaks from (**b**). The phases v_n are determined by the sign of $T(q_z)$ at the q_z position of the corresponding Bragg reflection. **d** Scattering density profile, ρ_z, calculated using Eq. (3). The location of the cholesterol molecules within the lipid bilayer can be deduced by the ρ_z of the two different mol% cholesterol membranes (5 mol%, blue; 40 mol%, *green*). Lipid and cholesterol molecules are shown schematically. The data shown were collected using the IN8 thermal TAS

reflected beam as a function of the perpendicular momentum transfer, q_z, is given by:

$$R(q_z) = \frac{16\pi^2}{q_z^2}|\hat{\rho}(q_z)|^2, \tag{1}$$

where $\hat{\rho}(q_z)$ is the one-dimensional Fourier transform of the neutron scattering length density and is defined by:

$$\hat{\rho}(q_z) = \int_{-\infty}^{\infty} \exp(iq_z z)\rho(z)dz. \tag{2}$$

Because the membranes are stacked (i.e., there is a convolution with the lamellar structure factor), the Fourier transform is not continuous, but discrete. The different Fourier components are observed in the experiment as the integrated intensities of the out-of-plane Bragg peaks. $\rho(z)$ is approximated by a 1D Fourier analysis (Tristram-Nagle et al. 2002) as follows:

$$\begin{aligned}\rho(z) &= \rho_W + \frac{F(0)}{d_z} + \frac{2}{d_z}\sum_{n=1}^{N} F(q_n)v_n \cos(q_n z) \\ &= \rho_W + \frac{F(0)}{d_z} + \frac{2}{d_z}\sum_{n=1}^{N} \sqrt{I_n q_n} v_n \cos\left(\frac{2\pi n z}{d_z}\right),\end{aligned} \tag{3}$$

where N is the highest order Bragg peak observed experimentally, and ρ_W is the scattering length density of bulk water. The integrated peak intensities, I_n, are multiplied by q_n to retrieve the form factors, $F(q_n)$ (Nagle 1989, Nagle et al. 1996). We note that Eq. (3) is used to calculate absolute scattering length densities if the curves are normalized by using $F(0)$ and ρ_W. As the setup used in this study is not optimized for quantitative reflectivity measurements, we present relative rather than absolute scattering length densities. By comparing the two samples, these measurements can be used to determine the position of molecules within the bilayers, as will be shown below.

The bilayer form factor $F(q_z)$, which is in general a complex quantity, is real in the case of centro-symmetry. The ubiquitous crystallographic phase problem, therefore, simplifies to $F(q_z) = \pm|F(q_z)|$, where the phases, v_n, can only take on values of ± 1. Assigned values for v_n are needed to reconstruct the scattering length density profile from the data following Eq. (3). When the membrane form factor $F(q_z)$ is measured at several q_z values, a continuous function, $T(q_z)$, which is proportional to $F(q_z)$, can be fit to the data (Nagle 1989; Nagle et al. 1996; King 1971; Adachi 2000):

$$T(q_z) = \sum_n \sqrt{I_n q_n}\ \mathrm{sinc}(\pi d_z q_z - \pi n). \tag{4}$$

Once an analytical expression for $T(q_z)$ has been determined from fitting the various Bragg peaks, the v_n values can be determined from $T(q_z)$. The d_z-spacing between two neighboring membranes in the stack can be determined from the positions of the Bragg reflections ($d_z = 2\pi/\Delta q_z$) along the out-of-plane axis, q_z.

Figure 4b shows out-of-plane scans for the 5 and 40 mol% cholesterol samples. Up to ten distinct Bragg peaks are observed and are used to reconstruct the scattering length density. Figure 4c, d displays $T(q_z)$ and relative scattering length densities as determined using Eqs. (4) and (3). $T(q_z)$ was fitted to the experimentally determined peak intensities using Eq. (4) to calculate an array of v_n values out of the corresponding 2^{10} combinations, assuming a phase of $+1$ or -1. Figure 4c shows the best fits to the data. Both samples were well fitted using the following combination of phases: $11\bar{1}\bar{1}1\bar{1}1\bar{1}\bar{1}$. The resulting scattering length densities are plotted in Fig. 4d. This type of sample preparation (chain deuterated lipids hydrated by heavy water) accentuates the water contribution, i.e., the layer between the membranes at $\sim$24 Å. The minima at about 20 Å correspond to the protonated lipid head groups. The scattering length density then increases toward the bilayer centre, i.e., $z = 0$. The sharp dip at the centre of the 5 mol% cholesterol sample is the tell-tale sign of a fluid membrane, i.e., the increasing number of kink-defects lower the density of the lipid tails in the bilayer centre.

At 40 mol% cholesterol, a peak at $\sim$18 Å appears, and the density at the membrane centre experiences a further decrease, showing a plateau, however, instead of a dip. Lipid and cholesterol molecules can tentatively be fit to this structure, and are schematically illustrated in Fig. 4d. The peak at $\sim$18 Å is most likely related to the presence of the hydrophilic head of the cholesterol molecule (Léonard et al. 2001). Since cholesterol makes up 40 mol% of the membrane, the density of carbon atoms in the centre of the membrane is further reduced, as cholesterol has a single chain compared to the two acyl chains of a lipid molecule. It seems, however, that the presence of cholesterol suppresses lipid tail fluctuations, as the scattering length density in the membrane centre remains constant. Our data (Fig. 4) support the notion that cholesterol molecules assume an upright orientation (Léonard et al. 2001) with their hydrophilic head residing in the lipid head group region. The data in Fig. 4 are in excellent agreement with neutron diffraction results in cholesterol-containing polyunsaturated lipid membranes (18:0-22:6n3-PC) (Mihailescu et al. 2011), where the cholesterol molecule was also found in an upright position. This observation is also consistent with the commonly accepted umbrella model of cholesterol interaction with lipid bilayers (Huang 1999).

Membrane dynamics

Motions in lipid membranes range from long wavelength undulation and bending modes, with typical relaxation

times on the order of nanoseconds and lateral length scales of several hundred lipid molecules (i.e., tens of nanometers), to short wavelength density fluctuations in the picosecond range and nearest-neighbor length scales (Rheinstädter et al. 2004a, Pfeiffer et al. 1989; König et al. 1992; Pfeiffer et al. 1993; König et al. 1994, 1995; Lipowsky and Sackmann 1995; Lindahl and Edholm 2000; Bayerl 2000; Salditt 2000; Rheinstädter et al. 2005, 2006, 2007) Different techniques have been used to study the different types of motions. For example, local dynamics in lipid bilayers (i.e., individual lipid molecules), such as vibration, rotation, libration (hindered rotation) and diffusion, have been investigated by incoherent neutron scattering (König et al. 1992, 1994, 1995; Pfeiffer et al. 1993; Meinhold et al. 2007) and nuclear magnetic resonance (NMR) (Bloom and Bayerl 1995; Nevzorov and Brown 1997) in order to determine the short wavelength translational and rotational diffusion constants. On the other hand, collective bilayer undulations have been examined by coherent scattering experiments using neutron spin-echo spectrometers (Pfeiffer et al. 1993, Rheinstädter et al. 2005, Meinhold et al. 2007, Takeda et al. 1999) and Dynamic Light Scattering (DLS) (Hirn et al. 1999; Hirn and Bayerl 1999; Hildenbrand and Bayerl 2005). TAS has been shown to be a well suited technique for the study of collective membrane dynamics (Rheinstädter et al. 2004a; Kaye et al. 2011; Rheinstädter et al. 2006b; Rheinstädter et al. 2009; Armstrong et al. 2011; Rheinstädter et al. 2004; Rheinstädter 2008). The dynamics that we are interested in are the propagation of short-wavelength density waves in the plane of the membrane, which can be thought of in terms of phonon-like excitations. These collective molecular motions determine, for instance, the elasticity of membranes (Rheinstädter et al. 2006a) and are speculated to be relevant for interactions between membrane embedded proteins (Rheinstädter et al. 2009) and membrane transport properties (Rheinstädter et al. 2004a; Kaye et al. 2011; Paula et al. 1996). Propagating modes lead to peaks in the neutron spectra at well-defined excitation energies. By measuring the excitation energies at different $q_{\|}$ values, i.e, different length scales, complete dispersion relations can be determined. However, we would like to point out that these types of dynamics are different from relaxational dynamics. A well-known example of a relaxation process in lipid membranes is the diffusion of lipids and other molecules in the plane of the membrane. The eigenfrequency of a relaxation dynamic is $\hbar\omega = 0$, which leads to a quasi-elastic broadening of the central line of the neutron spectra. Relaxational dynamics are usually slow (on the order of nano- to microseconds), while the propagating modes take place on the picosecond time scale. The two types of dynamics can be well distinguished in inelastic neutron scattering experiments. For example, diffusion is determined by measuring the broadening of the quasi-elastic peak, while in the case of propagating wave-like excitations (which are of particular interest to us), they are observed as inelastic peaks at excitation energies $\hbar\omega \neq 0$ meV.

A typical lipid dispersion relation in lipid membranes is shown in Fig. 2b. This in-plane dispersion relation was determined using several techniques in DMPC and DLPC—i.e., inelastic X-ray scattering (Chen et al. 2001, 2003; Weiss et al. 2003), inelastic neutron scattering (Rheinstädter et al. 2004a, Rheinstädter et al. 2004) and molecular dynamics (MD) simulations (Tarek et al. 2001; Hub et al. 2007; Kaye et al. 2011). The lipid dispersion curve has a generic shape, namely at small $q_{\|}$ values (long length scales) there is a linear region $\hbar\omega \propto q_{||}$ as the excitation propagates in the form of long-wavelength sound waves. The dispersion then goes through a maximum before a minimum is observed close to the nearest-neighbor distance (~ 1.5 Å^{-1}) of two lipid acyl tails. Beyond this minimum, a second linear regime is observed at high $q_{\|}$. Recently Kaye et al. 2011. studied the polarization of these excitations by combining neutron scattering and MD simulations. In a longitudinal wave, the C-atoms of the hydrocarbon tails are displaced along the direction of the propagating wave—in a transverse wave, particles are displaced perpendicular to the propagation direction. According to Kaye et al. (2011), the long-wavelength modes are purely longitudinal in nature. At high in-plane momentum transfers $q_{\|}$ (i.e., beyond the dispersion minimum), pronounced transverse properties were observed. However, in the vicinity of the dispersion minimum, the excitations have a mixed, longitudinal and transverse character. Because these excitations have been associated with the transport of small molecules in bilayers (Paula et al. 1996), the longitudinal and transverse fluctuations have been speculated to be relevant for the in-plane and trans-membrane transport of small molecules, such as water (Kaye et al. 2011, Paula et al. 1996).

Two types of inelastic scans were conducted. Specifically, constant-$q_{\|}$ scans, in which a $q_{\|}$ value is selected and held constant while the energy transfer $\hbar\omega$ is scanned, and constant-energy scans, for which the spectrometer is tuned to a certain energy transfer, $\hbar\omega$, and the momentum transfer $q_{\|}$ is varied. Both types are usually employed to measure dispersion relations. As a general rule, energy scans are usually used when the dispersion relation is flat. On the other hand, constant-$q_{\|}$ scans are usually better suited to measure steep parts of the dispersion. Examples of constant-energy and constant-$q_{\|}$ scans are shown in Fig. 5. The position of the excitations as function of $\hbar\omega$ and $q_{\|}$ is then determined from the positions of peaks in these scans. The constant-energy scans at $q_{\|} = 1.2$ Å^{-1} in Fig. 5a show two well-defined peaks at ~ 1.3 and ~ 2.1 meV in the

5 mol% cholesterol sample. Four peaks can be fit to the spectrum at a higher cholesterol concentration (as shown in Fig. 5b) at energies between 1 and 4 meV. The corresponding fitting functions consist of narrow Gaussian components centered at an energy transfer $\hbar\omega = 0$, which are used to describe the instrumental energy resolution (see Table 1), a broader Lorentzian component as a result of relaxational dynamics (also present in the systems studied) and damped harmonic oscillators (dho) for the excitations.

Figure 5c depicts constant-$q_{\|}$ scans in the two samples. Both scans show a broad component centered at $\sim q_{\|} = 1.38$ Å^{-1} and two narrow satellite peaks. As will be shown below, the broad peak is related to a minimum in the dispersion relation, i.e, a flat, horizontal region, while the narrow peaks are associated with the steeper branches. The solid lines in Fig. 5c are fits using Gaussian peak profiles—two narrow and a broad Gaussian peak were fitted to the two scans.

The use of a thermal TAS increases the available energy range. Figure 5d shows energy scans at $q_{\|} = 3$ Å^{-1} and an energy transfer of up to 20 meV. An excitation at $\sim$16 meV is visible as a pronounced peak in the spectra. This excitation was predicted by Tarek et al. (2001) and refers to an optical phonon associated with the dynamics of the terminal methyl end groups. The observed energy values are in excellent agreement with the theoretical values.

Several constant-$q_{\|}$ and constant-energy scans were performed on the two spectrometers to carefully scan the accessible energy and $q_{\|}$ range for excitations. These excitations could be assigned to dynamics in the gel, fluid and liquid-ordered states of the membrane.

Dispersion relations

Figure 6 shows all of the measured excitations (as function of energy transfer $\hbar\omega$ and momentum transfer $q_{\|}$) in the 5 and 40 mol% cholesterol samples as determined from the inelastic scans shown in Fig. 5. Excitation data measured using the cold and thermal TAS are depicted by circular

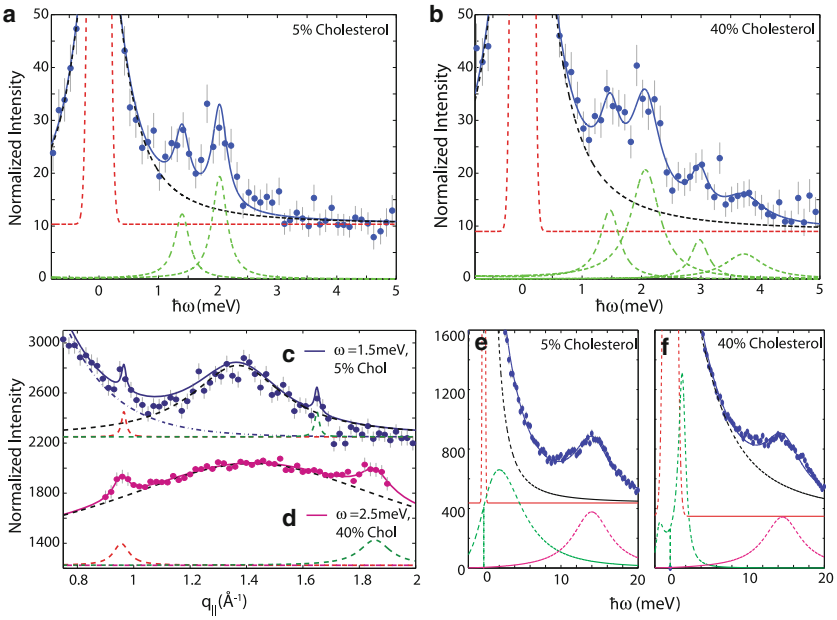

Fig. 5 Overview of the inelastic data: constant-$q_{\|}$ scan at $q_{\|} = 1.2$ Å^{-1}. The instrumental resolution is fit with a Gaussian (*red*), and the relaxation dynamics by a Lorentzian (*black*) function. The satellite excitations peaks are fit with damped harmonic oscillators (*green*), with the total fit shown in *blue*. **a** Data of 5 mol% and **b** 40 mol% cholesterol concentration samples. Constant-energy scan showing peaks fitted with Lorentzian curves: **c** 5 mol% cholesterol at $\hbar\omega$ = 1.5 meV. The Lorentzian fits are depicted by *dashed black*, *red* and *green curves*, with an exponential used to fit the background (*dashed blue*). The total fit is shown as a *solid blue line*. **d** 40 mol% cholesterol at $\hbar\omega$ = 2.5 meV. The Lorentzian fits are indicated by *dashed black*, *red* and *green curves*, with the constant background and the total fit depicted by *dashed magenta* and *solid magenta lines*, respectively. High-energy constant-$q_{\|}$ scans at $q_{\|} = 3$ Å^{-1}—the instrumental resolution is fit using a Gaussian (*red*), while a Lorentzian (*black*) function is used to describe the relaxation dynamics. The satellite excitation peaks are fit with damped harmonic oscillators (*green and magenta*), with the total fit shown in *blue*. **e** 5 mol% and **f** 40 mol% cholesterol concentrations. The green curves correspond to the low energy excitations from *a*, *b* and *c*, which cannot be resolved using the high-energy setup

and diamond-shaped symbols, respectively. The excitations were grouped into three different dispersion relations as follows: Pronounced and narrow excitations were assigned to the gel phase as the more ordered state of the lipid tails is expected to lead to well-defined excitations. Broad inelastic peaks are more likely the result of fluctuations in the fluid phase. The corresponding dispersion relations are similar to those shown in Fig. 2b. There was, however, a set of excitations (Fig. 6) that did not follow the gel or fluid dispersion curves, and was clearly outside of the error bars for those excitations. We tentatively assigned those excitations to the liquid-ordered state.

The data for the 5 mol% cholesterol sample (Fig. 4a) can be compared to the dispersion relations for gel and fluid DMPC and DPPC bilayers, as previously reported from inelastic X-rays (Chen et al. 2001, 2003; Weiss et al. 2003), neutron scattering (Rheinstädter et al. 2004a; Kaye et al. 2011) and MD simulations (Tarek et al. 2001; Hub et al. 2007). The shape of the gel dispersion curve agrees very well with ones in the literature. The energy value in the dispersion minimum is slightly increased (from 1 meV to $\sim$1.5 meV) in the presence of cholesterol. Only one excitation could clearly be identified at $q_{\|}$ values of $\lesssim$0.9 Å^{-1}, and we assigned this excitation to the gel phase as we expect it to be the most pronounced. Therefore, the fluid and liquid-ordered dispersion relations do not have data points below $q_{\|} \sim 1$ Å^{-1}. As reported previously (Rheinstädter et al. 2004a), compared to the gel dispersion curve, the fluid dispersion curve appears to be less pronounced, with a higher energy value in the dispersion minimum, and lower (softer) energies at high $q_{\|}$ values. This new dispersion curve, which we assigned to the liquid-ordered state shows, not only a very low minimum energy, but also very low energy values at high $q_{\|}$.

All energy values for the 40 mol% cholesterol sample appear to be shifted to higher energies (Fig. 6b), the trademark of more rigid interactions, which lead to higher eigenfrequencies. In both the high and low cholesterol samples, three dispersion curves could be identified and assigned to the gel, fluid and tentatively to the liquid-ordered phases. In order to analyze the differences between the different states in the low and high cholesterol samples, the energy values around the dispersion minimum were fitted using a parabola:

$$\hbar\omega = \alpha \times (q_{||} - q_0)^2 + \omega_0. \quad (5)$$

The region around the minimum of the dispersions shown in Fig. 6 was fitted using Eq. (5). The fitted values for α and ω_o are listed in Table 2.

Because the bilayers were hydrated by heavy water, the experiment is potentially also sensitive to collective hydration water dynamics. We note, however, that we expect the corresponding signals to be small. The range of hydration water excitations, as reported from inelastic neutron scattering (Paciaroni et al. 2008), is shown in Fig. 6a, b. Two of the data points in Fig. 6b can most likely be assigned to hydration water dynamics.

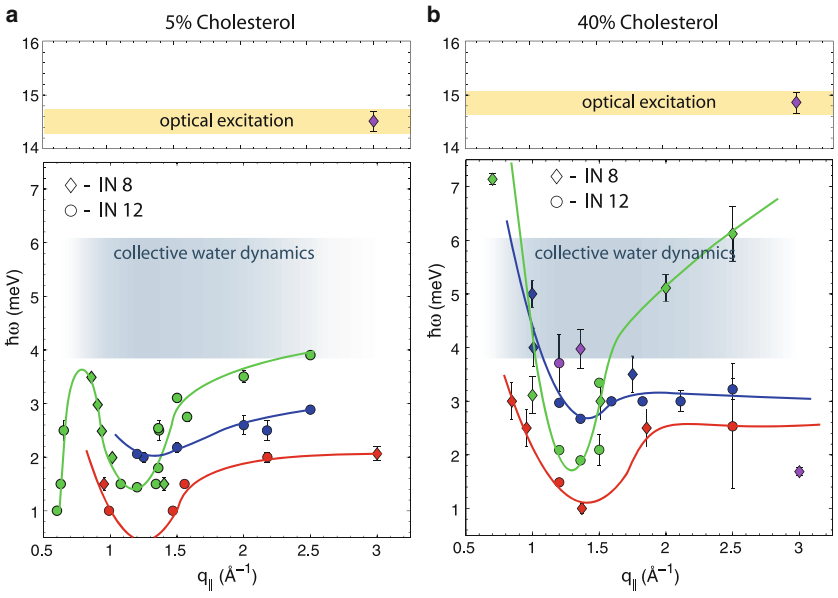

Fig. 6 Energy dispersion curves for DMPC bilayers with **a** 5 mol% cholesterol and **b** 40 mol% cholesterol. The dispersion curve corresponding to the gel phase is shown in *green* and the fluid phase in *blue*. The liquid-ordered phase, arising from the high concentration of cholesterol in the sample, is depicted by the *red curve*. The *blue band* at $\sim$4–6 meV represents the region where excitations due to hydrating water are observed (Paciaroni et al. 2008). The *yellow band* represents an optical excitation at 14–15 meV, which was predicted by MD simulations (Tarek et al. 2001)

Table 2 Results of parabolic fits using Eq. (5) to the dispersion minima in Fig. 6

	α	(meV × Å^2)	ω_0 (meV)	
	5 mol% chol	40 mol% chol	5 mol% chol	40 mol% chol
Gel	16.3	30.3	1.38	1.80
Fluid	4.9	10.7	1.99	2.63
Liquid-ordered l_o	9.8	6.6	0.44	1.09

α is the slope of the parabola, and ω_0 is the energy offset. α can be thought of as a nanoscale bilayer "stiffness" on length scales corresponding to lipid tail-tail distances

Discussion

The lateral short-wavelength dynamics of the lipid tails in the hydrophobic membrane core have previously been studied in DMPC (Weiss et al. 2003; Chen et al. 2003; Rheinstädter et al. 2004a; Hub et al. 2007; Brüning et al. 2010; Kaye et al. 2011) and DLPC (Chen et al. 2001; Tarek et al. 2001) membranes, and the corresponding dispersion relations have been determined by inelastic X-ray scattering (IXS), inelastic neutron scattering and computer simulations. In this article we have determined complete energy dispersion curves for a DMPC membrane containing different amounts of cholesterol, a system previously studied by IXS (Weiss et al. 2003; Chen et al. 2003). The shape of the dispersion curves observed from the neutron and X-ray experiments is similar to that of a pure bilayer system (Fig. 2b). The same type of excitation curve has also been reported recently in bilayers with ethanol (Kaye et al. 2011). It can therefore be concluded that this type of dispersion relation is generic to lipid membranes, even in the presence of molecules, such as ethanol and cholesterol. Ethanol and cholesterol represent two different classes of molecules, i.e., ethanol molecules predominantly reside in the lipid-head group region, while cholesterol molecules interact extensively with the membrane's hydrophobic core. Although the dynamics of the lipid chains are altered by the presence of cholesterol, nevertheless, the membrane's basic characteristics seem to be preserved.

The lateral dynamics dispersion curve exhibits three characteristic regimes: a linear regime at small $q_{||}$, a minimum at a wavelength corresponding to the nearest-neighbor lipid tail distance, and finally, a second linear regime at large $q_{||}$. The linear regime at small $q_{||}$-values is related to a long wavelength sound-like propagation in the plane of the membrane. The corresponding excitations are thus longitudinal. The speed of sound is determined from the initial linear slope of the dispersion curve at small $q_{||}$-values up to the first maximum (see Fig. 2). Dynamics at small $q_{||}$ values are usually difficult to access in inelastic neutron scattering experiments because of the so-called kinematic restriction. It is related to the fact that energy and momentum of the neutrons are conserved during the scattering process and the parabolic shape of the energy as a function of $q_{||}$, $\hbar\omega = \hbar^2/(2m_n) \times q_{||}^2$, as for instance discussed in (Rheinstädter et al. 2004). While the absolute energies of the 5 mol% cholesterol dispersion relation in Fig. 6a fall into the accessible range, the energies significantly increase in the presence of 40 mol% cholesterol, such that the corresponding excitations were no longer accessible. The determination of the speed of sound is, therefore, beyond the scope of this study. Dynamics at higher $q_{||}$ values around the dispersion minimum and beyond are the domain of inelastic neutron scattering. The final linear regime of the dispersion relation corresponds to a propagating mode with predominantly transverse properties. In the case of pure lipid membranes, the slope or propagation velocity in this region is small. The maxima and minimum in the dispersion curve correspond to a crossover behavior, connecting these two propagating modes at small and large $q_{||}$. In particular, the flat region at the dispersion minimum may be related to a non-propagating standing-wave resulting from lipid tail dynamics with mixed longitudinal and transverse properties. The characteristics of these modes in pure lipid membranes have been previously reported (Kaye et al. 2011).

The introduction of cholesterol to the lipid membrane leads to additional propagating modes, as shown in Fig. 5. Because the inclusion of additional components increases the system's degrees of freedom, it is natural to expect that the addition of cholesterol will result in more dynamic modes, as shown in Fig. 6. One interesting observation is that the dispersion curves all exhibit the same features, i.e., two linear regimes at small and large $q_{||}$ connected by a crossover regime with two maxima and a minimum. This strongly suggests that these features are generic to such systems. We therefore speculate that they are related to the fact that lipid membranes are self-assembled layered structures whose properties are closely related to that of smectic liquid crystals.

It is interesting to note that the dispersion curve, shown in Fig. 6, resembles the energy of a quasiparticle in superfluid helium, where the parabolic minimum part of the spectrum is termed the roton [see, e.g., (Annet 2004)]. The different behavior of the dispersion curves indicates different modes of molecular motions. Comparing to superfluid helium, we can speculate that the linear phonon-like dispersion curve implies that the motion of the molecules are rigidly coupled, leading to a propagating sound-like wave. On the other hand, the parabolic dispersion curve near the minimum may indicate a different type of collective mode in which a moving molecule couples strongly

to its neighbors. As one molecule moves, the neighboring molecules must move out of its way, leading to a different collective mode of motion, as depicted in Fig. 7. Phenomenologically, the minimum of the dispersion curves is well described by a parabola [Eq. (5)]. The coefficient α of the parabola can thus be viewed as a parameter characterizing the generalized rigidity of the system on the nanometer-length scale. It is interesting to note that increasing the cholesterol content in the system leads to larger α in the gel and fluid branches of the dispersion curve, and a smaller α in the liquid-ordered branch. The energy offset ω_0 in the dispersion minimum, corresponding to the roton energy gap, can be related to the excitation energy of a "soft-mode." The occurrence of a soft mode often indicates a structural phase transition if the energy cost of this mode goes to zero, i.e., $\omega_0 = 0$. A smaller value of ω_0 might then be related to a structure with a higher degree of order; a full analysis of this feature will be presented in a future paper.

Some qualitative conclusions can be drawn from the data and the phenomenological analysis: From the values for α and ω_0 shown in Table 2, one can speculate that the gel phase has, not surprisingly, a higher degree of order and is considerably stiffer than the fluid phase. The addition of cholesterol has two distinct effects: it makes the chain dynamics in both phases stiffer (α increases by a factor of $\sim$2 between 5 and 40 mol% cholesterol), while at the same time, ω_0 also increases significantly, pointing to a more disordered molecular structure. The high cholesterol content liquid-ordered phase combines low values for α, corresponding to soft nanoscale dynamics, and at the same time, low values of ω_o, indicating a high level of order in the system. As has been previously speculated, the liquid-ordered phase seems to combine properties of rigid gel and soft fluid bilayers. In IXS experiments (Weiss et al. 2003; Chen et al. 2003), the addition of cholesterol leads to a significant increase in the high-frequency sound speed, pointing to a more rigid state at large length scales (small $q_{\|}$-values).

In Fig. 6 we observe the coexistence of excitations of gel, fluid and liquid-ordered phases. The separation of saturated and unsaturated phosphatidylcholine/cholesterol mixtures into nanometer-sized liquid-ordered and liquid-disordered phases was reported recently from MD simulations (de Meyer et al. 2010; Risselada 2008; Herrera 2012). Cholesterol was also found to collectively self-organize in phospholipid membranes (Martinez-Seara et al. 2010), which can also lead to a dynamic phase separation on the nanometer scale. These small (3–50 nm) and transient (nano- microsecond) heterogeneities in membranes are very difficult to resolve with standard experimental techniques. Inelastic neutron-scattering experiments on DMPC reported evidence for the co-existence of small nanometer gel and fluid domains in the temperature range of the main phase transition (Rheinstädter et al. 2004a)—based on the co-existence of the corresponding excitations in the spectra. Such domains were also found in MD simulations (Murtola et al. 2006; Ehrig et al. 2011). Recently, Armstrong et al. (2012) have used the coherence length of neutrons to observe co-existing gel and fluid domains in a phospholipid bilayer over a range of temperatures. The authors speculated that these small transient domains could be responsible for the so-called pseudo-critical behavior in phospholipid bilayers. The results in Fig. 6 now represent experimental evidence for the coexistence of gel, fluid and liquid-ordered phases in DMPC membranes containing different amounts of cholesterol. The corresponding domains can be speculated to be nanometer sized and short-lived.

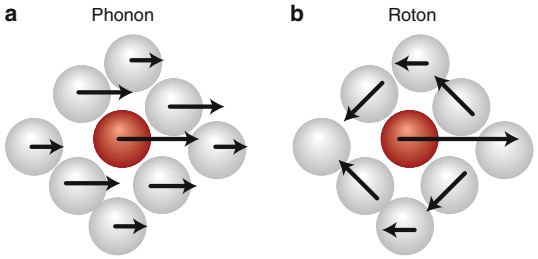

Fig. 7 **a** Molecular dynamics of particles participating in the propagating sound-like wave, i.e., the longitudinal phonon at small $q_{\|}$-values (*long length scales*) and **b** in the "roton" at $q_{\|}$-values in the dispersion minimum. These dynamics are expected to show a mixed, longitudinal and transverse character as neighboring particles couple strongly. Figure adapted from Annett (2004)

Conclusion

In summary, we present a neutron-scattering study of the lateral nanoscale dynamics in phospholipid membranes containing 5 and 40 mol% cholesterol. By measuring the excitation spectrum at several lateral $q_{\|}$ values (up to $q_{\|} = 3$ Å^{-1}), complete dispersion relations corresponding to gel, fluid and liquid-ordered bilayers were determined. The dispersion relations have a generic shape in single component lipid bilayers, i.e., there is an initial linear regime because of high-speed sound propagation and a second linear regime at high $q_{\|}$. The two linear regimes are connected by a maximum before a minimum is observed around nearest-neighbor distances between to lipid tails. The generic shape of these dispersion curves is preserved in the presence of cholesterol. A coexistence of excitations corresponding to gel, fluid and liquid-ordered phases was also observed. We therefore speculate the coexistence of

nanometer-sized, and possibly transient, gel, fluid and l_o domains in membranes containing cholesterol. Such nanodomains have long been previously suggested, with evidence coming from computer simulations and more recently from experiment (Simons 1997; Murtola et al. 2006; Ehrig et al. 2011; Armstrong et al. 2012; Engelma 2005; Eggeling et al. 2009; Lingwood 2010).

The region around the dispersion minimum was fitted using a phenomenological parabolic fitting method. The two parameters, i.e., the slope and the energy offset, were related to the bilayer's elastic properties on distances corresponding to hydrocarbon tail distances and molecular order. The inclusion of cholesterol has a distinct effect on the collective dynamics of the lipid hydrocarbon chains. Namely, we observe a pronounced stiffening of the membrane on nanometer length scales in both the gel and fluid phases, and also greater molecular disorder. For the first time, we have determined the nanoscale dynamics in the high-cholesterol liquid-ordered phase of DMPC bilayers. This phase seems to combine the properties of the gel and fluid phases, appearing softer than the fluid phase, but better ordered than the gel phase. Future experiments will offer a more complete description of these features, and a quantitative model will be put forth regarding the molecular properties of multi-component lipid bilayers.

Acknowledgments This research was funded by the Natural Sciences and Engineering Research Council of Canada (NSERC), the National Research Council Canada (NRC), the Canada Foundation for Innovation (CFI) and the Ontario Ministry of Economic Development and Innovation. John Katsaras is supported by Oak Ridge National Laboratory's (ORNL) Program Development (PD) and Laboratory Directed Research and Development (LDRD) programs.

References

Adachi T (2000) A new method for determining the phase in the X-ray diffraction structure analysis of phosphatidylcholine:alcohol. Chem Phys Lipids 107:93–97

Almeida P, Vaz W, Thompson T (1992) Lateral diffusion in the liquid phases of dimyristoylphosphatidylcholine/cholesterol lipid bilayers: a free volume analysis. Biochemistry 31:6739–6747

Annett JF (2004) Superconductivity, superfluids and condensates. Oxford University Press, Oxford

Armstrong CL, Sandqvist E, Rheinstadter MC (2011) Protein-protein interactions in membranes. Protein Pept Lett 18:344–353

Armstrong C, Barrett M, Toppozini L, Kucerka N, Yamani Z, Katsaras J, Fragneto G, Rheinstädter MC (2012) Co-existence of gel and fluid lipid domains in single-component phospholipid membranes. Soft Matter 8:4687–4694

Bayerl T (2000) Collective membrane motions. Curr Opin Colloid Interface Sci 5:232–236

Bloom M, Bayerl T (1995) Membranes studied using neutron scattering and NMR. Can J Phys 73:687–696

Brown DA, London E (2000) Structure and function of sphingolipid- and cholesterol-rich membrane rafts. J Biol Chem 275:17221–17224

Brüning B, Rheinstädter MC, Hiess A, Weinhausen B, Reusch T, Aeffner S, Salditt T (2010) Influence of cholesterol on the collective dynamics of the phospholipid acyl chains in model membranes. Eur Phys J E 31:419–428

Chen S, Liao C, Huang H, Weiss T, Bellisent-Funel M, Sette F (2001) Collective dynamics in fully hydrated phospholipid bilayers studied by inelastic X-ray scattering. Phys Rev Lett 86:740–743

Chen PJ, Liu Y, Weiss TM, Huang HW, Sinn H, Alp EE, Alatas A, Said A, Chen SH (2003) Studies of short-wavelength collective molecular motions in lipid bilayers using high resolution inelastic X-ray scattering. Biophys Chem 105:721–741

de Meyer F, Smit B (2009) Effect of cholesterol on the structure of a phospholipid bilayer. Proc Natl Acad Sci USA 106:3654–3658

de Meyer FJM, Benjamini A, Rodgers JM, Misteli Y, Smit B (2010) Molecular simulation of the dmpc-cholesterol phase diagram. J Phys Chem B 106:10451–10461

Eggeling C, Ringemann C, Medda R, Schwarzmann G, Sandhoff K, Polyakova S, Belov VN, Hein B, von Middendorf C, Schönle A, Hell SW (2009) Direc observation of the nanoscale dynamics of membrane lipids in a living cell. Nature 457:1159–1162

Ehrig J, Petrov EP, Schwille P (2011) Phase separation and near-critical fluctuations in two-component lipid membranes: Monte Carlo simulations on experimentally relevant scales. New J Phys 13:045019

Engelman DM (2005) Membranes are more mosaic than fluid. Nature 438:578–580

Fragneto G, Rheinstädter M (2007) Structural and dynamical studies from bio-mimetic systems: an overview. CR Phys 8:865–883

Harroun T, Katsaras J, Wassall S (2006) Cholesterol hydroxyl group is found to reside in the center of a polyunsaturated lipid membrane. Biochemistry 45:1227–1233

Harroun T, Katsaras J, Wassall S (2008) Cholesterol is found to reside in the center of a polyunsaturated lipid membrane. Biochemistry 47:7090–7096

Herrera FE, Pantano S (2012) Structure and dynamics of nano-sized raft-like domains on the plasma membrane. J Chem Phys 136:1–33

Hildenbrand MF, Bayerl TM (2005) Differences in the modulation of collective membrane motions by ergosterol, lanosterol, and cholesterol: a dynamic light scattering study. Biophys J 88:3360–3367

Hirn RB, Bayerl TM (1999) Collective membrane motions in the mesoscopic range and their modulation by the binding of a monomolecular protein layer of streptavidin studied by dynamic light scattering. Phys Rev E 59:5987–5994

Hirn R, Bayerl T, Rädler J, Sackmann E (1999) Collective membrane motions of high and low amplitude, studied by dynamic light scattering and micro-interferometry. Faraday Discuss 111:17–30

Huang J, Feigenson GW (1999) A microscopic interaction model of maximum solubility of cholesterol in lipid bilayers. Biophys J 76:2142–2157

Hub JS, Salditt T, Rheinstädter MC, de Groot BL (2007) Short range order and collective dynamics of DMPC bilayers. acomparison between molecular dynamics simulations, X-ray, and neutron scattering experiments. Biophysical J 93:3156–3168

Katsaras J (1998) Adsorbed to a rigid substrate, dimyristoylphosphatidylcholine multibilayers attain full hydration in all mesophases. Biophys J 75:2157–2162

Kaye MD, Schmalzl K, Nibali VC, Tarek M, Rheinstädter MC (2011) Ethanol enhances collective dynamics of lipid membranes. Phys Rev E 83:050,907

King GI, Worthington CR (1971) Analytic continuation as a method of phase determination. Phys Lett 35A:259–260

König S, Pfeiffer W, Bayerl T, Richter D, Sackmann E (1992) Molecular dynamics of lipid bilayers studied by incoherent quasi-elastic neutron scattering. J Phys II France 2:1589–1615

König S, Sackmann E, Richter D, Zorn R, Carlile C, Bayerl T (1994) Molecular dynamics of water in oriented dppc multilayers studied by quasielastic neutron scattering and deuterium-nuclear magnetic resonance relaxation. J Chem Phys 100:3307–3316

König S, Bayerl T, Coddens G, Richter D, Sackmann E (1995) Hydration dependence of chain dynamics and local diffusion in l-alpha-dipalmitoylphosphtidylcholine multilayers studied by incoherent quasi-elastic neutron scattering. Biophys J 68:1871–1880

Kučerka N, Marquardt D, Harroun T, Nieh MP, Wassall S, Katsaras J (2009) The functional significance of lipid diversity: orientation of cholesterol in bilayers is determined by lipid species. J Am Chem Soc 131:16358–16359

Kučerka N, Liu Y, Chu N, Petrache HI, Tristram-Nagle S, Nagle JF (2005) Structure of fully hydrated fluid phase DMPC and DLPC lipid bilayers using X-ray scattering from oriented multilamellar arrays and from unilamellar vesicles. Biophys J 88:2626–2637

Léonard A, Escrive C, Laguerre M, Pebay-Peyroula E, Néri W, Pott T, Katsaras J, Dufourc EJ (2001) Location of cholesterol in dmpc membranes. a comparative study by neutron diffraction and molecular mechanics simulation. Langmuir 17:2019–2030

Lindahl E, Edholm O (2000) Mesoscopic undulations and thickness fluctuations in lipid bilayers from molecular dynamics simulations. Biophys J 79:426–433

Lingwood D, Simons K (2010) Lipid rafts as a membrane-organizing principle. Science 327:46–50

Lipowsky, R, Sackmann, E (eds) (1995) Structure and dynamics of membranes, handbook of biological physics. vol 1, Elsevier, Amsterdam

Martinez-Seara H, Róg T, Karttunen M, Vattulainen I, Reigada R (2010) Cholesterol induces specific spatial and orientational order in cholesterol/phospholipid membranes. PLoS ONE 5:e11162

Meinhold L, Smith JC, Kitao A, Zewail AH (2007) Picosecond fluctuating protein energy landscape mapped by pressure-temperature molecular dynamics simulation. Proc Natl Acad Sci USA 104:17261–17265

Mihailescu M, Soubias O, Worcester D, White S, Gawrisch K (2011) Structure and dynamics of cholesterol-containing polyunsaturated lipid membranes studied by neutron diffraction and nmr. J Membr Biol 239:63–71

Mouritsen O (2010) The liquid-ordered state comes of age. Biochim Biophys Acta 1798:1286–1288

Murtola T, Róg T, Falck E, Karttunen M, Vattulainen I (2006) Transient ordered domains in single-component phospholipid bilayers. Phys Rev Lett 97:238102

Nagle JF, Wiener MC (1989) Relations for lipid bilayers. Biophys J 55(55):309–313

Nagle J, Zhang R, Tristram-Nagle S, Sun W, Petrache H, Suter R (1996) X-ray structure determination of fully hydrated lα phase dipalmitoylphosphatidylcholine bilayers. Biophys J 70:1419–1431

Nevzorov A, Brown M (1997) Bilayers from comparative analysis of 2H and 13C NMR relaxation data as a function of frequency and temperature. J Chem Phys 107:10288–10310

Pabst G, Kučerka N, Nieh MP, Rheinstädter M, Katsaras J (2010) Applications of neutron and X-ray scattering to the study of biologically relevant model membranes. Chem Phys Lipids 163(6):460–479

Paciaroni A, Orecchini A, Cornicchi E, Marconi M, Petrillo C, Haertlein M, Moulin M, Schober H, Tarek M, Sacchetti F (2008) Fingerprints of amorphous ice-like behavior in the vibrational density of states of protein hydration water. Phys Rev Lett 101:148104

Papanikolaou B, Papafotika A, Murphy C, Papamarcaki T, Tsolas O, Drab M, Kurzchalia TV, Kasper M, Christoforidis S (2005) Cholesterol-dependent lipid assemblies regulate the activity of the ecto-nucleotidase cd39. J Biol Chem 28:26406–26414

Paula S, Volkov A, Van Hoek A, Haines T, Deamer D (1996) Permeation of protons, potassium ions, and small polar molecules through phospholipid bilayers as a function of membrane thickness. Biophys J 70:339–348

Petrie R, Schnetkamp P, Patel K, Awasthi-Kalia M, Deans J (2000) Transient translocation of the b cell receptor and src homology 2 domain-containing inositol phosphatase to lipid rafts: evidence toward a role in calcium regulation. J Immunol 165:1220–1227

Pfeiffer W, Henkel T, Sackmann E, Knorr W (1989) Local dynamics of lipid bilayers studied by incoherent quasi-elastic neutron scattering. Europhys Lett 8:201–206

Pfeiffer W, König S, Legrand J, Bayerl T, Richter D, Sackmann E (1993) Neutron spin echo study of membrane undulations in lipid multibilayers. Europhys Lett 23:457–462

Pike L (2006) Rafts defined: a report on the keystone symposium on lipid rafts and cell function. J Lipid Res 47:1597–1598

Pike L (2009) The challenge of lipid rafts. J Lipid Res 50:S323–S328

Rheinstädter MC (2008) Collective molecular dynamics in proteins and membranes. Biointerfaces 3:FB83–FB90

Rheinstädter MC, Ollinger C, Fragneto G, Demmel F, Salditt T (2004a) Collective dynamics of lipid membranes studied by inelastic neutron scattering. Phys Rev Lett 93:108107

Rheinstädter MC, Ollinger C, Fragneto G, Salditt T (2004) Collective dynamics in phospholipid bilayers investigated by inelastic neutron scattering: exploring the dynamics of biological membranes with neutrons. Phys B 350:136–139

Rheinstädter MC, Seydel T, Demmel F, Salditt T (2005) Molecular motions in lipid bilayers studied by the neutron backscattering technique. Phys Rev E 71:061,908

Rheinstädter MC, Häussler W, Salditt T (2006a) Dispersion relation of lipid membrane shape fluctuations by neutron spin-echo spectrometry. Phys Rev Lett 97:048103

Rheinstädter MC, Seydel T, Häußler W, Salditt T (2006b) Exploring the collective dynamics of lipid membranes with inelastic neutron scattering. J Vac Sci Technol A 24:1191–1196

Rheinstädter MC, Seydel T, Salditt T (2007) Nanosecond molecular relaxations in lipid bilayers studied by high energy resolution neutron scattering and in-situ diffraction. Phys Rev E 75:011907

Rheinstädter MC, Schmalzl K, Wood K, Strauch D (2009) Protein-protein interaction in purple membrane. Phys Rev Lett 103:128104

Ridsdale A, Denis M, Gougeon PY, Ngsee JK, Presley JF, Zha X (2006) Cholesterol is required for efficient endoplasmic reticulum-to-golgi transport of secretory membrane proteins. Mol Biol Cell 17:1593–1605

Risselada HJ, Marrink SJ (2008) The molecular face of lipid rafts in model membranes. Proc Natl Acad Sci USA 105:17367–17372

Róg T, Pasenkiewicz-Gierula M, Vattulainen I, Karttunen M (2009) Ordering effects of cholesterol and its analogues. Biochim Biophys Acta 1788:97–121

Salditt T (2000) Structure and fluctuations of highly oriented phospholipid membranes. Curr Opin Colloid Interface Sci 5:19–26

Simons K, Ikonen E (1997) Functional rafts in cell membranes. Nature 387:569–572

Takeda T, Kawabata Y, Seto H, Komura S, Gosh S, Nagao M, Okuhara D (1999) Neutron spin echo investigations of membrane undulations in complex fluids involving amphilphiles. J Phys Chem Solids 60:1375–1377

Tarek M, Tobias D, Chen SH, Klein M (2001) Short wavelength collective dynamics in phospholipid bilayers: a molecular dynamics study. Phys Rev Lett 87:238101

Thewalt JL, Bloom M (1992) Phosphatidylcholine: cholesterol phase diagrams. Biophys J 63:1176–1181

Tristram-Nagle S, Liu Y, Legleiter J, Nagle JF (2002) Structure of gel phase dmpc determined by X-ray diffraction. Biophys J 83:3324–3335

Vist R, Davis JH (1990) Phase equilibria of cholesterol/dipalmitoylphosphatidylcholine mixtures: 2 h nuclear magnetic resonance and differential scanning calorimetry. Biochemistry 29:451–464

Weiss T, Chen PJ, Sinn H, Alp E, Chen S, Huang H (2003) Collective chain dynamics in lipid bilayers by inelastic X-ray scattering. Biophys J 84:3767–3776

5.2 Low-Energy/High-Spatial Resolution Triple-Axis Spectrometry

Typically, triple-axis spectrometers are configured to achieve the highest possible energy resolution. The energy can be expressed as a function of wavelength by combining Equations 2.2 and 2.1 [60],

$$E = \frac{2\pi^2\hbar^2}{m\lambda^2} \approx \frac{81.81}{\lambda^2}, \tag{5.1}$$

where E is in meV and λ is in Å. Thus, the energy resolution can be written as follows:

$$\begin{aligned} \Delta E = 2 \cdot \frac{2\pi^2\hbar^2}{m\lambda^3} \cdot \Delta\lambda = 2E\frac{\Delta\lambda}{\lambda}, \\ \frac{\Delta E}{E} = \frac{2\Delta\lambda}{\lambda}. \end{aligned} \tag{5.2}$$

Striving for a high-energy resolution inevitably results in a neutron beam with a long longitudinal coherence length, ξ, as the coherence length is dependent on the wavelength spread, and therefore, energy resolution of the incoming neutrons, [61]

$$\xi = \frac{\lambda^2}{\Delta\lambda} \approx \sqrt{\frac{81.81}{E}}\left(\frac{2E}{\Delta E}\right) \approx 18\frac{\sqrt{E}}{\Delta E}. \tag{5.3}$$

Operating in this high energy resolution mode is particularly effective for examining systems which possess long-range order, such as crystals. The long coherence length of the neutron probe will produce multiple higher order Bragg peaks from a system with a well-ordered structure. The coherence length can essentially be thought of as defining the integration volume (or area in the case of a two-dimensional membrane system) over which the scattered waves can be coherently summed. However, if the system is composed of small, randomly dispersed, yet highly ordered domains, using a large integration area is not the most effective method of probing the short-range structural order in the system. The total scattering signal will be the *coherent* average of the scattering from within the integration area, thus the coherent signal from the small domains will be overwhelmed by the coherent signal resulting from the surrounding matrix. For this reason the TAS setup, which is commonly employed to

probe long-range order in hard condensed matter systems, was modified to increase the sensitivity of the spectrometer to the short-range order often found in biological samples.

Changing the spectrometer to operate with a lower energy resolution will result in a shorter coherence length, a feature which is not often thought to be desirable when probing hard condense matter systems. However, in a system which contains small highly ordered domains it will have two significant advantages: (1) a more efficient integration over larger ($q_{||}$,$\hbar\omega$) ranges, enabling the enhancement of small signals; and (2) a reduction of the coherently summed scattering volume.

The energy and momentum resolution of the TAS is dictated by: (1) the incident energy of the neutron beam; (2) the divergence of the neutron beam; and (3) the wavelength resolution of the monochromator and analyzer. For the experiments detailed in Papers V and VI, the collimation was kept constant and the high and low-energy resolution setups were achieved by varying the energy of the incoming neutrons.

It is important to realize that the neutron energy, energy resolution, momentum resolution, and coherence length are not independent parameters. Thus, changing one will inevitably have an effect on the others, as can be seen by the parameters displayed in Table 5.1. The low-energy resolution setup (Table 5.1 ①) is used to obtain high-spatial resolution data and is capable of detecting small ordered domains in the membrane system. The high-energy resolution setup (Table 5.1 ②) uses the standard configuration of the TAS, but is not able to detect these small ordered structures.

X-ray scattering experiments obtain diffraction data by integrating over all possible energies, because the detected photons are not energy discriminated. However, the structural features of the small ordered domains that are observed in the low-energy resolution neutron data have not been reported from X-ray scattering experiments. By comparing energy, momentum resolution and coherence length of the different techniques in Table 5.1, one can argue that this might be the effect of the X-ray beam's long coherence length. Our experiments using low-energy/high-spatial resolution (LE/HSR) neutron diffraction present experimental evidence that the coherence length of the neutron beam plays a crucial role in resolving small, nanometer size structures.

Setup	λ (Å)	E (meV)	ΔE (meV)	ΔQ (Å^{-1})	ξ (Å)
①	1.44	39.5	3.521	0.034	32.3
①	1.49	36.8	3.173	0.032	34.6
②	2.37	14.6	0.757	0.020	91.3
Neutron Diffraction	4.2	4.66	∞	0.005	420
X-ray Diffraction	1.54	$8.041{\cdot}10^6$	∞	0.001	$\sim$3000

Table 5.1: Instrumental parameters for the low (①) and high (②) energy resolution setups used for TAS experiments in Papers V and VI. The monochromator and analyzer were PG(002) crystals. The collimation was set to (c1-c2-c3-c4): 30-18-28-60 (in minutes). Typical values for energy, energy resolution, momentum resolution, and coherence length for (cold) neutron diffraction and X-ray diffraction experiments are also included for comparison.

5.3 Paper V: Co-Existence of Gel and Fluid Lipid Domains in Single-Component Phospholipid Membranes

Clare L. Armstrong, Matthew A. Barrett, Laura Toppozini, Norbert Kučerka, Zahra Yamani, John Katsaras, G. Fragneto, and Maikel C. Rheinstädter *"Co-existence of gel and fluid lipid domains in single-component phospholipid membranes"*, Soft Matter, **8**, 4687-4694, 2012.

5.3.1 Preface to Paper V

The initial experiment to test the LE/HSR technique was performed on a single-component DPPC lipid bilayer sample. The presence of domains was induced by examining the system close to its main transition temperature, creating coexisting fluid and gel phases. This allowed the nanoscale membrane structure to be modified simply by changing the temperature, rather than creating an assay of dual component samples with different lipid concentrations. Although this system was thought to exhibit a pseudo-critical behaviour, indicative of a second order phase transition, evidence suggesting that it possesses a coexistence of phases at its main transition temperature was observed in the dynamics data presented in Paper IV.

To enhance the in-plane and out-of-plane scattering from the lipid tails, the sample studied was a highly oriented membrane stack composed of chain deuterated lipids. Measurements were taken with the sample in the gel phase (low temperature), fluid phase (high temperature), and in a coexisting phase state at T_m using both the standard high-energy resolution TAS setup and the LE/HSR setup. The experiment was conducted using the N5 TAS at the Chalk River National Laboratory.

The out-of-plane data obtained using high-energy resolution suggests the lipid bilayer has a single, gradually shifting d_z-spacing as the system is heated though the transition temperature. This implies that the system only has one uniformly changing phase, pointing to a second order phase transition. However, it should be noted that the width of the Bragg peaks are much broader than the Q resolution of the spectrometer.

When the same system, at the same temperature, was examined using the LE/HSR setup, the increased spatial resolution allowed for the observation of several Bragg peaks, corresponding to multiple lamellar d_z-spacings. This suggests that the system is undergoing a classical first order phase transition, and that the presence of these coexisting domains could not be resolved by the standard TAS setup.

This increased spatial resolution does come at the price of coherent intensity. Because a shorter coherence length means that the neutrons are not coherently scattering off of as many periodicities, there is a loss in signal. However, the increased sensitivity to short-range order makes it a valuable tool to probe small ordered patches in systems that do not possess long-range structural order, in particular, biological systems.

Author Contributions

- *Designed research:* Maikel C. Rheinstädter
- *Sample fabrication:* **Clare L. Armstrong**, Laura Toppozini, and Matt A. Barrett
- *Sample environment development:* Giovana Fragneto and Maikel C. Rheinstädter
- *Performed experiment:* **Clare L. Armstrong**, Laura Toppozini, Norbert Kučerka, Zahra Yamani, and Maikel C. Rheinstädter

- *Analysed data:* **Clare L. Armstrong**
- *Wrote the manuscript:* **Clare L. Armstrong**, John Katsaras, and Maikel C. Rheinstädter

Soft Matter

Dynamic Article Links

Cite this: *Soft Matter*, 2012, **8**, 4687

www.rsc.org/softmatter

PAPER

Co-existence of gel and fluid lipid domains in single-component phospholipid membranes

C. L. Armstrong,[*a] M. A. Barrett,[a] L. Toppozini,[a] N. Kučerka,[b] Z. Yamani,[b] J. Katsaras,[bc] G. Fragneto[d] and M. C. Rheinstädter[*ab]

Received 11th November 2011, Accepted 21st February 2012
DOI: 10.1039/c2sm07158d

Lateral nanostructures in membranes, so-called rafts, are believed to strongly influence membrane properties and functions. The experimental observation of rafts has proven difficult as they are thought to be dynamic structures that likely fluctuate on nano- to microsecond time scales. Using neutron diffraction we present direct experimental evidence for the co-existence of gel and fluid lipid domains in a single-component phospholipid membrane made of DPPC as it undergoes its main phase transition. The coherence length of the neutron beam sets a lower limit for the size of structures that can be observed. Neutron coherence lengths between 30 and 242 Å used in this study were obtained by varying the incident neutron energy and the resolution of the neutron spectrometer. We observe Bragg peaks corresponding to co-existing nanometer sized structures, both in out-of-plane and in-plane scans, by tuning the neutron coherence length. During the main phase transition, instead of a continuous transition that shows a pseudo-critical behavior, we observe the co-existence of gel and fluid domains.

1 Introduction

Clusters, rafts, nanodomains, and patches have become a central issue in cell membrane studies.[1–4] The heterogeneous organization of membrane constituents is not only believed to be essential for cellular functions such as signalling, trafficking and adhesion,[5–7] but also impacts material properties.[8] However, the experimental observation of these heterogeneities has proven to be challenging, as they are thought to be short-lived.[9–12] As such, in order for experimental techniques to unambiguously observe such structures, they must be capable of simultaneously accessing small length scales and fast (nano to microsecond) time regimes.

Lipid bilayers are established model systems for studying dynamics and functional aspects of complex biological membranes.[13,14] They also allow the investigation of heterogeneous structures, which mimic "rafts". Submicron sized domains in ternary mixtures of phospholipids and cholesterol have been observed using small angle neutron scattering (SANS).[15–19] Selective deuteration was used in these experiments to enhance the scattering of the heterogeneities, and domains in the range 20–200 nm radius were observed. Domains in these so-called raft forming lipid mixtures are thermodynamically stable and quasi-static, *i.e.*, changing on slow time scales of seconds or minutes. Heterogeneous structures have also been reported in single component lipid membranes: Rappolt *et al.* observed gel- liquid crystal phase co-existence in a DPPC membrane by driving the system far from equilibrium by an infrared temperature jump.[20] Pabst *et al.* observed co-existence of orthorhombic and hexagonal lamellar gel phases in single component DSPG membranes.[21] The experiments point, however, to a kinetically trapped, out-of-equilibrium state, which lead to an interdigitated, stable (on the time scale of the experiments) phase. The origin of the driving force behind phase separation in artificial and biological membranes is highly debated, as "rafts", thus far, have primarily been experimentally observed in either raft forming mixtures or far from equilibrium. Phase separation in biological membranes has very recently been related to non-equilibrium fluctuations of the cytoskeleton,[22] which are coupled to the local membrane curvature. Microdomains, on the order of 10–100 nm, have been theoretically predicted and small (75 nm), transient (250 msec) domains have indeed been observed in a biological membrane *in vivo* using particle tracking techniques.[23]

The aim of this work was to experimentally prove the existence of heterogeneities in a lipid membrane, which are (1) "small" (3–50 nm), (2) transient and (3) occur in thermal equilibrium under conditions that mimic physiological conditions, such as high hydration and high temperature. Those domains would be very difficult to "see" with standard techniques, however, they are speculated to occur in biological membranes and thought to be

[a]*Department of Physics and Astronomy, McMaster University, Hamilton, ON, L8S 4M1, Canada. E-mail: armstc5@mcmaster.ca; rheinstadter@mcmaster.ca; Fax: +(905)546-1252; Tel: +(905)525-9140 ext.23134*
[b]*Canadian Neutron Beam Centre, National Research Council, Chalk River, ON, K0J 1J0, Canada*
[c]*Neutron Scattering Science Division, Oak Ridge National Laboratory, Oak Ridge, TN, 37831-6100, USA*
[d]*Institut Laue-Langevin, 6 rue Jules Horowitz, B.P. 156, 38042 Grenoble Cedex 9, France*

physiologically relevant.[1–4] It has been speculated that small transient domains in phospholipid model membranes are responsible for the so-called pseudo-critical behaviour, without experimental proof so far.

Phospholipid bilayers are known to undergo an acyl-chain melting transition, the so-called main transition, from an ordered gel to a disordered fluid phase. Critical fluctuations and critical swelling—most likely due to co-existent gel and fluid domains—have been reported close to this phase transition.[24–38] These lipid bilayers are, therefore, ideal model systems for the study of domain formation. The system can be tuned through the gel-fluid phase co-existence region, simply by changing the temperature, as sketched in Fig. 1.

In this paper we use the coherence length of the neutron beam to clearly show direct experimental evidence for the co-existence of gel and fluid nanodomains in the temperature range of the main phase transition. While a continuous transition between the gel and fluid phase, and a pseudo-critical behaviour have been previously reported in the literature,[24–38] we observe co-existing gel and fluid domains indicative of a first order phase transition.

In most natural systems partially coherent waves are common. X-rays and neutrons have coherence lengths that are usually significantly longer than molecular lattice spacings, including protein-protein distances in biological membranes. The coherence of waves in periodic systems (lattices) is critical with regard to their dynamics, as interference effects, such as Bragg reflections, largely determine their propagation. Additionally, in less well ordered systems, the coherence length of the probe, ξ, may play an important role in the investigation of small structures, *i.e.*, when ξ is comparable to the size of the object in question.

A collimated beam of neutrons obtained by Bragg reflection from a single crystal, or a pair of phased Fermi choppers, is never 100% monochromatic. With regard to their wave properties, their longitudinal coherence length, ξ, is defined by eqn (1):[39]

$$\xi = \frac{\lambda^2}{\Delta\lambda}. \quad (1)$$

The energy of a neutron (in meV) with wavelength λ (in Å) is given by $E = 81.81/\lambda^2$,[40] such that

$$\frac{\Delta E}{E} = 2\,\frac{\Delta\lambda}{\lambda}, \quad (2)$$

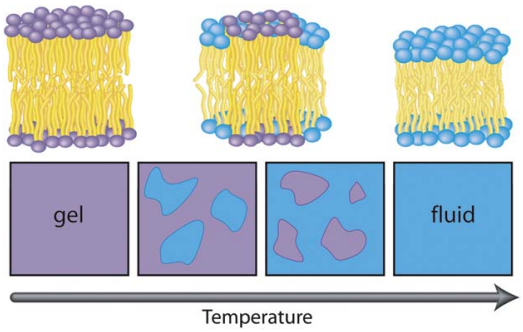

Fig. 1 Schematic of the gel-fluid transition in phospholipid membranes with co-existing gel and fluid domains.

where E is the incident neutron energy and ΔE is the instrumental energy resolution and will be discussed in more detail below. ξ can now be written as a function of E and ΔE, as follows:

$$\xi = \frac{2E}{\Delta E}\,\lambda = \frac{2E}{\Delta E}\sqrt{\frac{81.81}{E}} \sim \frac{18\sqrt{E}}{\Delta E}. \quad (3)$$

For cold neutrons with energies of ~4.5 meV and a typical monochromaticity by single crystal reflection of about 2%, the longitudinal coherence length is calculated to be approximately 450 Å (using eqn (3)). † Note, that the reason for the typically low monochromaticity of neutron beams is to avoid further compromising the already low flux "white" neutron beam, a situation that is very different for synchrotron X-rays. The longitudinal coherence length of X-rays reflected from a Si(111) monochromator with a wavelength resolution of $\Delta\lambda/\lambda \approx 1 \times 10^{-4}$ and $\lambda = 1$ Å is of the order of $\xi_{xray} = 10{,}000$ Å. The coherent properties of the scattering probe may play an important role for the investigation of small structures, such as nanoscale domains, comparable to or smaller than a given ξ – structures smaller than ξ may give spatially averaged values of, *e.g.*, peak positions and widths.

We investigated the packing and correlations of the lipid acyl chains in multi-lamellar phospholipid bilayers using neutron diffraction. DPPC, with two fully saturated acyl chains (di-16 : 0), was chosen for this study. Chain deuterated DPPC (DPPC-d62) was used to enhance out-of-plane and in-plane Bragg diffraction. By varying the coherence length of the incident neutron beam, we present direct experimental evidence for the co-existence of nanometer sized domains in single-component phospholipid membranes at temperatures close to the main phase transition. This technique can, in the future, be used to study rafts in membranes containing cholesterol and other lipid mixtures, and eventually in biological membranes.

2 Materials and methods

2.1 Sample preparation

Highly oriented multi-lamellar stacks of 1,2-dipalmitoyl-sn-*glycero*-3-phosphocholine (DPPC) were prepared on 2″ single-side polished Si wafers with a thickness of 300 μm. The coherent scattering of the lipid hydrocarbon chains was enhanced by using partially, tail deuterated lipids, *i.e.*, DPPC-d62. A solution of 20 mg mL^{-1} DPPC-d62 in 1 : 1 chloroform and 2,2,2-trifluoroethanol (TFE) was prepared. The Si wafers were cleaned by alternate 12 min sonications in ultra pure water and ethanol at 313 K. This process was repeated twice. 1 mL of the lipid solution was deposited on each Si wafer and allowed to dry. The wafers were kept in vacuum overnight to remove all traces of the solvent. The samples were then hydrated with heavy water, D_2O, and annealed in an incubator at 303 K for 24 h. Following this

† Note that the transverse coherence length ξ_t can be estimated to be $\xi_t \sim \lambda/\alpha$, where α is the divergence of the neutron beam. Long transverse coherence lengths of several micrometers are achieved in small angle neutron scattering (SANS) instruments by using small pinholes. The transverse coherence length in our setup is of the order of ~5 Å and small compared to the longitudinal coherence, as given in the Table to Fig. 2.

protocol, each wafer contained roughly 3 000 highly oriented stacked membranes with a total thickness of ~10 μm.

Twenty such Si wafers were stacked with 0.6 mm aluminium spacers placed in between each wafer to allow for the membranes to be hydrated. The "sandwich" sample was kept in a temperature and humidity controlled aluminium chamber. Hydration of the lipid membranes from the vapour phase was achieved by separately adjusting the temperature of the heavy water reservoir, the sample and the chamber cover. Temperature and humidity sensors were installed close to the sample. A water bath was used to control the temperature of the water reservoirs, and the temperature of the sample and its cover was controlled using Peltier elements. d_z-spacings of $d_z^{gel} = 70$ Å at 303 K and $d_z^{fluid} = 56$ Å at 315 K were achieved using this set-up. From values for d_z as function of relative humidity (RH) published for DMPC,[41] the hydration of the DPPC bilayers in this experiment can be estimated to better than 99.6%, close to full hydration. The main transition temperature, T_m, of deuterated DPPC is 310.5 K,[42] a value slightly lower than its protonated counterpart (T = 314.4 K).[24,42] The temperature of the pre-transition from the L_β to the $P_{\beta'}$ phase in deuterated DPPC-d62 was determined to be 302.9 K.[42] All measurements in this work were, therefore, done in the $P_{\beta'}$ and fluid L_α phase.

The samples were mounted vertically in the neutron beam such that the scattering vector (**Q**) could either be placed in the membrane plane ($\mathbf{q}_\parallel$), or perpendicular to the membrane ($\mathbf{q}_z$). Out-of-plane and in-plane structure could be measured by simply rotating the sample by 90 degrees.

2.2 Neutron experiment

Experiments were conducted using the N5 triple-axis spectrometer at the Canadian Neutron Beam Centre (Chalk River, ON, Canada). The three axis of the spectrometer refer to the axis of rotation of the monochromator, the sample and the analyzer. The incident and final neutron energies are defined by the Bragg reflections from pyrolytic graphite (PG) crystals. The divergence of the neutron beam is controlled by several neutron Soller collimators. A schematic of the instrument configuration is shown in Fig. 2. To achieve the different coherence lengths (eqn (3)) the energy of the incident neutrons and the energy resolution of the spectrometer must be varied. The incident energy is determined by the angle of reflection of the monochromator. To avoid higher order contributions, which also fulfil the Bragg condition, *i.e.*, λ/2, λ/3, a PG filter was used after the monochromator. Two incident energies were available using this setup, 14.5 meV and 42.3 meV, corresponding to neutron wavelengths of 2.37 Å and 1.39 Å respectively.

The energy resolution of a neutron triple-axis spectrometer is determined by: (1) the incident energy of the neutron beam; (2) the divergence of the neutron beam; and (3) the wavelength resolution of the monochromator and analyzer. The collimation was defined in four different regions of the beam path (c1, c2, c3, c4), as shown in Fig. 2. The tighter the collimation the better the energy resolution, however, this is achieved at the cost of a reduced neutron flux. In addition, the choice of a Bragg reflection plays a role in the energy resolution. In the case of PG

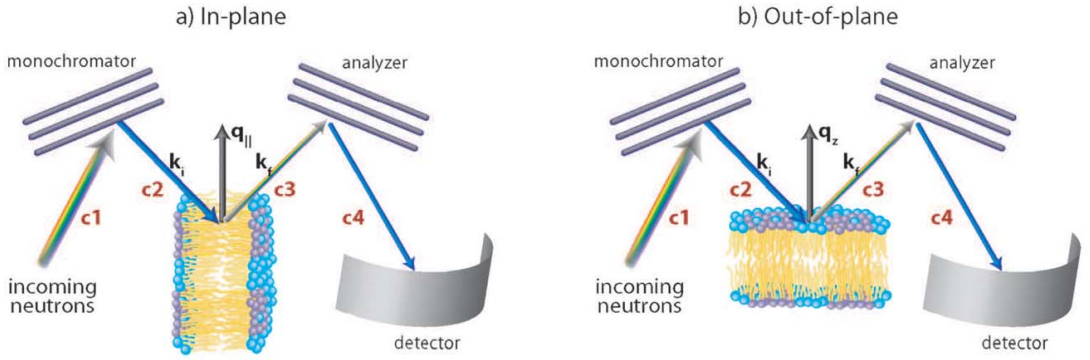

ξ (Å)	Monochromator	Analyzer	Collimation (minutes) (c1-c2-c3-c4)	Wavelength (Å)	Incident Energy (meV)	Energy Resolution ΔE (meV)	Q Resolution ΔQ (Å^{-1})
30	PG(002)	PG(002)	30-18-28-60	1.39	42.3	3.915	0.032
33	PG(004)	PG(002)	30-18-28-60	1.39	42.3	3.504	0.032
46	PG(002)	PG(004)	30-18-28-60	1.39	42.3	2.524	0.032
64	PG(004)	PG(004)	30-18-28-60	1.39	42.3	1.821	0.033
103	PG(004)	PG(002)	30-18-28-60	2.37	14.5	0.6643	0.018
152	PG(002)	PG(004)	30-18-28-60	2.37	14.5	0.451	0.019
242	PG(004)	PG(004)	30-18-28-60	2.37	14.5	0.2836	0.019

Fig. 2 Geometry of the triple axis spectrometer. a) Orientation of the sample for in-plane scans, such that **Q** is in the plane of the membrane ($\mathbf{q}_\parallel$). b) Orientation of the sample for out-of-plane scans, such that **Q** is perpendicular to the plane of the membrane ($\mathbf{q}_z$). The table displays the instrumental settings used to achieve the different coherence lengths, ξ, using eqn (3). k_i and k_f are the incident and final neutron wave vectors ($k = 2\pi/\lambda$).

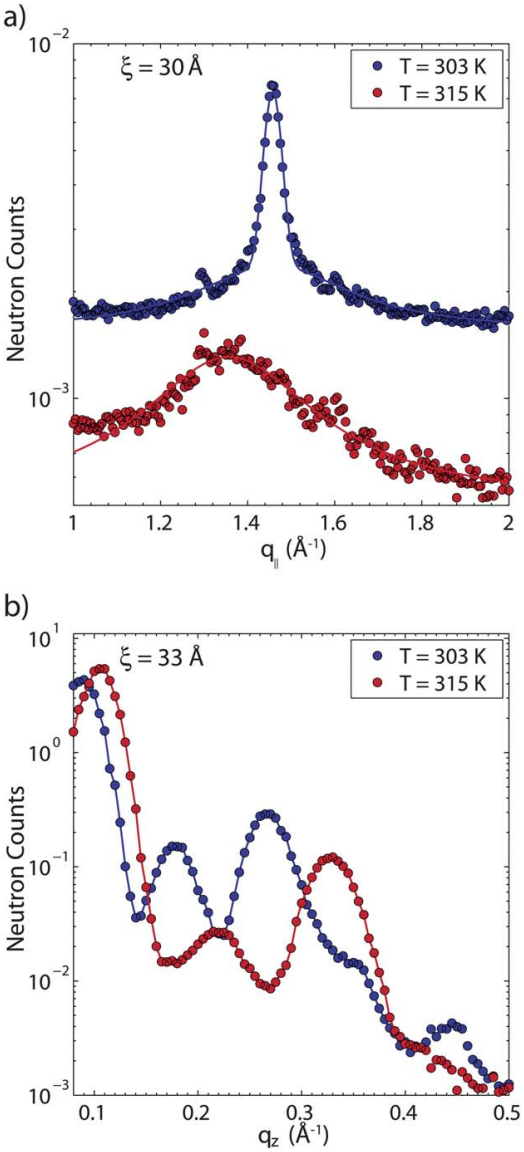

Fig. 3 Scans of gel and fluid DPPC bilayers at $T = 303$ K and $T = 315$ K, respectively. a) In-plane ($q_{||}$) scan showing the lipid acyl chain correlation peak. b) Out-of-plane (q_z) curves displaying the change in d_z-spacing between gel and fluid phase bilayers.

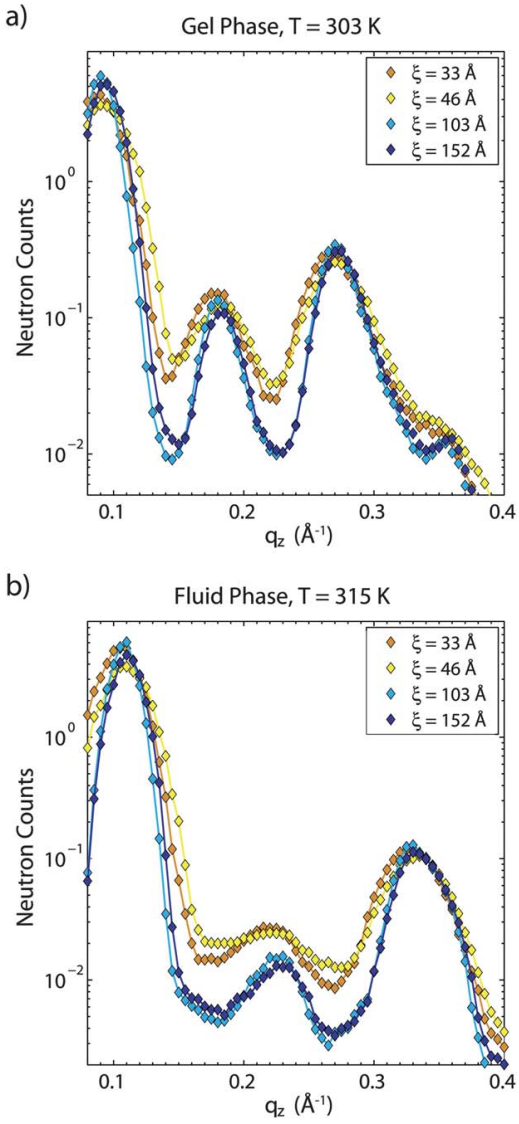

Fig. 4 Out-of-plane scattering curves of stacked DPPC-d62 membranes probed with different coherence length neutrons (33 Å< ξ < 152 Å). a) Gel phase and b) fluid phase bilayers. Curve shapes change as a function of q_z resolution, as listed in the Table to Fig. 2.

crystals, both the PG(002) and PG(004) reflections can be used for monochromatization. According to Bragg's law, the energy resolution is improved with higher angles of reflection (*i.e.* PG(004)), which also happens to reduce neutron flux. The table in Fig. 2 lists the different configurations used and their corresponding coherence lengths.

Collimation was kept constant during the course of the experiment. Coherence lengths between 30 and 242 Å were achieved by using different incident energies and two different PG reflections. The momentum resolution, ΔQ, is also given in the Table to Fig. 2. A good Q resolution usually implies the use of fine collimation and a corresponding large coherence length. In order to enable small nanometer sized structures to become visible, poor energy and Q resolution are needed, which at first sounds counter intuitive – to be discussed later.

3 Results

Fig. 3 shows the in-plane (a) and out-of-plane (b) measurements of gel phase ($T = 303$ K) and fluid phase ($T = 315$ K) DPPC

membranes. The in-plane scan depicts the lipid acyl chain correlation peak, which is the result of the close packed lipid tails making up the hydrophobic membrane core. The correlation peak occurs at 1.46 $Å^{-1}$ in the gel phase, and at 1.37 $Å^{-1}$ in the fluid phase, corresponding to nearest neighbour distances of 4.3 Å and 4.6 Å. The narrow width of the gel peak indicates a well-ordered structure; the peak broadens significantly and loses intensity in the fluid phase of the bilayers due to increased fluctuations.[38] The d_z-spacing between two neighbouring membranes in the stack can be determined from the spacing between the well developed Bragg reflections ($d_z = 2\pi/\Delta q_z$) in the out-of-plane curves in Fig. 3 (b). d_z-spacings of 70 Å and 56 Å are observed for gel and fluid DPPC bilayers, respectively, and the data were obtained with a neutron coherence length of 33 Å.

Fig. 4 depicts out-of-plane curves in the gel and fluid phase measured at different coherence lengths. The peaks are well described by Gaussian peak profiles. The broadening of the peaks changes slightly due to the difference in q_z resolution, as listed in the Table in Fig. 2. However, the position of the Bragg peaks in the different out-of-plane curves does not change as a function of ξ. The resolution (and coherence properties) of the neutron spectrometer are, therefore, not crucial in determining membrane structure deep in the gel or the fluid phase.

The in-plane structure of bilayers in the vicinity of the main phase transition temperature, T_m, was investigated in more detail (Fig. 5). Only one correlation peak at $q_{\|} = 1.46$ $Å^{-1}$, corresponding to the gel phase is observed at $T = 303$ K. When increasing the temperature, a second correlation peak appears at

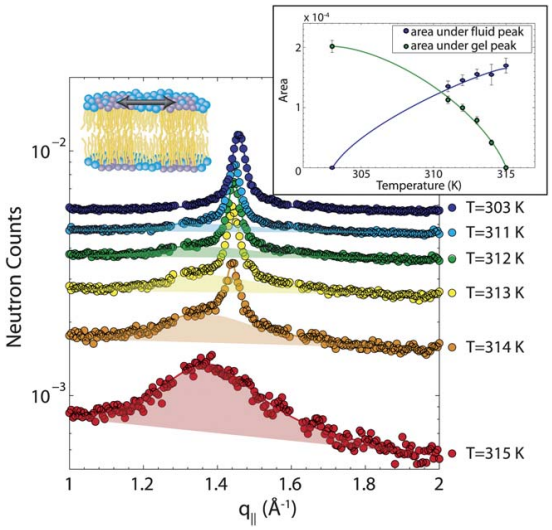

Fig. 5 In-plane scans of DPPC-d62 bilayers at 303 K<T<315 K. (Aluminium Bragg peaks from the humidity chamber were cut out at around $q_{\|} = 1.3$ and 1.6 $Å^{-1}$ for clarity.) Correlation peaks corresponding to co-existing gel and fluid phases are observed close to the main transition temperature, T_m ($\xi = 30$ Å). The inset to the figure displays the area under the fluid and gel peaks, determined from fits of Lorentzian profiles, as a function of temperature. Note that the in-plane scans are plotted on a logarithmic scale to make the broad lipid peak more visible. The corresponding areas are displayed using a linear y-axis.

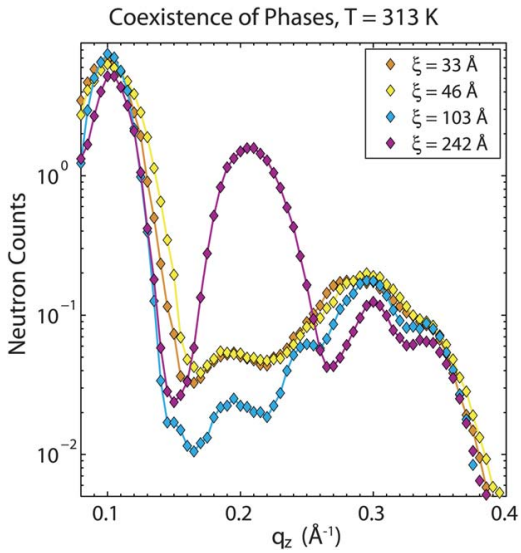

Fig. 6 Out-of-plane scattering curves resulting from stacked DPPC membranes near the main transition temperature ($T_m = 313$ K), probed with different neutron coherence lengths, ξ. The three well-developed, out-of-plane Bragg peaks observed with $\xi = 242$ Å split when the coherence length is reduced to $\xi \leq 103$ Å.

the nominal fluid position ($q_{\|} = 1.37$ $Å^{-1}$). The intensity of the gel peak is reduced with increasing temperature, while the fluid peak increases. Only the fluid peak is observed at $T = 315$ K. The data in Fig. 5, measured using a small coherence length, show the co-existence of the gel and the fluid peaks with increasing temperature. The area under the correlation peaks, which was determined from fits of Lorentzian peak profiles, is proportional to the volume of their respective phases, and are graphically depicted in the inset to Fig. 5. The fluid phase grows when heating through the transition at the cost of gel phase domains. Based on this data, the co-existence region extends from ~311–314 K.

Out-of-plane curves at $T = 313$ K are shown in Fig. 6. The data measured at high energy and q_z resolution, with a ξ of 242 Å, show three well-defined Bragg peaks with a d_z spacing of 63 Å. We note that this d_z-spacing is the average between d_z^{gel} and d_z^{fluid} ((70 Å + 56 Å)/2 = 63 Å) as determined from gel and fluid phase data (in Fig. 3 (b)). At smaller coherence lengths ξ, however, a peak splitting is observed. Each of the out-of-plane Bragg peaks splits into several separate reflections. The splitting occurs between 103 Å< ξ < 242 Å. Although the width of the Bragg reflections is resolution limited, the Bragg width of the ξ = 242 Å reflection is considerably broader than the instrumental resolution (given in the Table of Fig. 2). Significant peak broadening with improving q_z resolution is consistent with the averaging of individual Bragg peaks.

4 Discussion

The transition from gel ($P_{\beta'}$) to fluid (L_α) phospholipid bilayers has previously been reported to show critical behavior ("critical

swelling").[24–38] The lamellar spacing d_z, but also the nearest neighbour distance of lipid molecules in-the-plane of the membrane, mimic the critical behaviour observed in second order magnetic order-disorder transitions.[38] Critical behaviour is expected in second order phase transitions, with no co-existence of low and high temperature phases. However, a latent heat has been found in the main transition of phospholipid bilayers, which clearly identifies this transition as being of first order.[24–26] The observation of a pseudo-critical behaviour has, therefore, been puzzling and has resulted in a lively and ongoing debate in the literature.

Experimental evidence for co-existing gel and fluid domains has been reported. Inelastic neutron experiments on DMPC previously reported evidence for the co-existence of small nanometer gel and fluid domains in the temperature range of the main phase transition[38] – based on the co-existence of the corresponding excitations in the spectra. The long wavelength dispersion relation, as measured with a neutron spin-echo spectrometer, showed a pronounced soft mode at a length scale of about 420 Å.[8] It was speculated that domains may be responsible for the extreme softness, *i.e.*, the very low value for the bending modulus of phospholipid bilayers in the range of the phase transition, known as "critical softening".[34] Bending of the membrane most likely occurs at the interface between two nanodomains, which costs less energy than bending a pure gel or fluid domain. The diameter of these domains can be estimated to be 420 Å from this experiment. The relaxation rate of domain pattern fluctuations of aqueous solutions of vesicles near the fluid-gel phase transition temperature was found to show a pronounced slowing near the main phase transition in ultrasonic spectra.[10] Finally, co-existing gel and fluid domains in single-component lipid membranes were also reported from computer simulations.[12,43]

The two in-plane Bragg peaks shown in Fig. 5 present direct experimental evidence for co-existing gel and fluid domains in single-component phospholipid bilayers in the range of the main phase transition. Based on the lengths scales accessible in this experiment, limits for the domain size can be determined. The longest coherence length available in this experiment indicates that the lower limit for the size of those domains is ~242 Å in diameter, which is in good agreement with estimated values determined by the neutron spin-echo measurements.[8] However, because the smallest available neutron coherence length was 30 Å, our experiment can not rule out the existence of even smaller structures that include only a few lipid molecules. Instead of a critical behaviour with a continuously shifting peak, as was reported by Rheinstädter *et al.*,[38] we observe the co-existence of gel and fluid like domains, with their ratio changing as a function of temperature. The main transition in phospholipid membranes was, therefore, found to show the characteristics of a first order phase transition, in agreement with calorimetric experiments[24–26]

In out-of-plane scattering experiments, with good momentum resolution and corresponding high neutron coherence length, a continuous change of the lamellar d_z spacing is observed, as depicted in Fig. 6 for a coherence length of $\xi = 242$ Å, while a splitting of the Bragg peaks is observed at smaller coherence lengths. In the pure gel or fluid phase, all neighbouring membranes are in the same state, although different scenarios may develop in the transition region. The two neighbouring

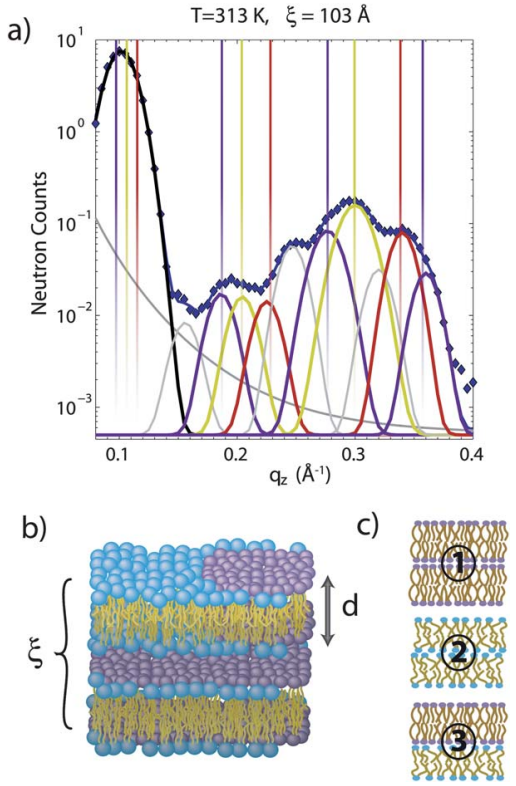

Fig. 7 a) Out-of-plane scattering curves of stacked DPPC membranes near the transition temperature ($T = 313$ K), probed with a coherence length of $\xi = 103$ Å. Fitting of the data reveals Bragg peaks from the different phases: fluid, gel, and intermediate phases. No fine structure of the first Bragg peak at around $q_{\|} = 0.10$ Å^{-1} could be resolved; it is, therefore, fit by a single peak (black line). Bragg peaks corresponding to the gel phase bilayers are shown in purple, those corresponding to fluid phase bilayers are shown in red, and those corresponding to mixed phase bilayers are shown in yellow. Additional peaks are shown in grey. b) Sketch of the multi-lamellar membrane patch with co-existing gel and fluid domains. c) Illustration of the three possible stacking scenario. Scenario 3 results in a d_z space which is the average of the fluid and gel spacing.

membranes may be: (1) both in the gel phase; (2) both in the fluid phase; or (3) one in the gel phase and the other in the fluid phase. The three scenarios are depicted in Fig. 7 c). When a gel region of the bilayer happens to be next to a fluid region, a long neutron coherence length (greater than $d_z^{gel} + d_z^{fluid}$) will average over the two d_z-spacings and result in an average d_z value between d_z^{gel} and d_z^{fluid}. The d_z spacing of 63 Å at $T = 313$ K, therefore, points to a multi-lamellar membrane structure with neighbouring gel and fluid domains. Based on this assumption, the critical coherence length ξ can be estimated to equal 126 Å. For ξ less than 126 Å, the neutron coherence only covers a single membrane, as shown in Fig. 7 b).

Fig. 7 shows a fit of the out-of-plane scattering curve measured at $\xi = 103$ Å (Fig. 6). Eleven Bragg peaks can be identified and could be fit to the data and assigned to different d_z spacings and

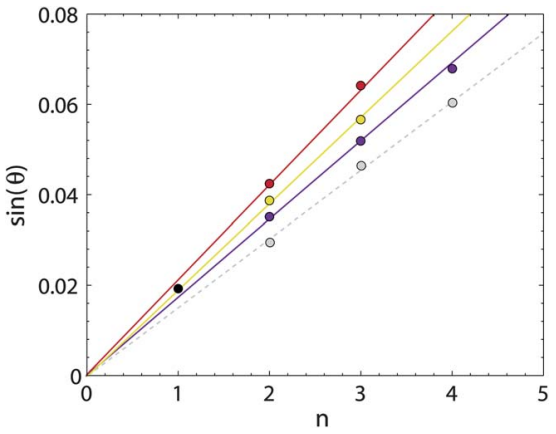

Fig. 8 Plot of $s\,i\,n\,(\theta) = \lambda n/2\,d$. Peaks belonging to the same d_z-spacing fall on a straight line through the origin. The 11 Bragg peaks fit in Fig. 7 a) can be assigned to 4 different d-spacings, namely, 56 Å, 63 Å, 70 Å, and 77 Å.

phases. To assign the peaks to different phases, Bragg's law can be re-written as $s\,i\,n\,(\theta) = \lambda n/2\,d$. Therefore, by plotting $sin(\theta)$ *vs.* the (estimated) order of the different Bragg reflections (n), peaks which belong to the same d_z-spacing will fall on a straight line through the origin. This plot is shown in Fig. 8. The 11 Bragg peaks can be assigned to 4 different d_z-spacings, namely, 56 Å, 63 Å, 70 Å, and 77 Å. The d_z spacings of 70 Å and 56 Å agree perfectly with the d_z spacings found in gel and fluid phase. The intermediate phase, with a d_z spacing of 63 Å, can be assigned to scenario (3), with neighbouring gel and fluid domains in the membrane stack. There is an additional series of reflections in Fig. 8. These peaks fall on a line through the origin with a slope corresponding to a d_z spacing of 77 Å. This d_z spacing does not correspond to one of the three proposed scenarios, gel, fluid and gel–fluid. However, it is well known that unexpected or quasi-forbidden Bragg peaks can appear in soft materials[44] to adapt to macroscopic constraints. The melting of a membrane patch from the gel to the fluid state inside a stack of membranes is sketched in Fig. 7 b). The size difference between d_z^{gel} and d_z^{fluid} would create a distortion of the multi-lamellar structure. Because the membrane stack is an elastic medium, this is associated with an energy cost. One way for the system to comply with the macroscopic constraints is to try to keep the overall thickness constant, by creating membranes with a larger d_z spacing to compensate for the difference $d_z^{gel} - d_z^{fluid}$. The observed spacing of $d_z = 77$ Å may correspond to the thickness of a DPPC bilayer where all the lipids are in all-*trans* configuration (*i.e.*, fully stretched out). This type of structure is not energetically favourable at high temperatures and just a consequence of the macroscopic constraints given by the membrane stack.

A comment is in order. Following the Gibbs' Phase Rule in condensed systems (without a co-existing gas phase) the number of independent intensive properties (F), such as temperature and pressure, depends on the number of components (C), and the number of co-existing phases in thermal equilibrium (P): $F = C - P + 1$. The observation of co-existing domains over a given temperature interval in a single lipid system implies $F = 0$, *i.e.*, a single point in temperature-pressure phase space (critical point). This observation of co-existing gel and fluid domains over a certain temperature range, therefore, seems to contradict the phase rule. Gibbs' rule, however, does not apply to *transient*, short lived domains, as discussed by Ehrig *et al.*[11] The fluctuation period of these transient domains was determined to be ~10 ns from experiment[10] (DMPC bilayers) and MD simulations[12] (DPPC bilayers). By tuning the energy resolution ΔE in the Table in Fig. 2, the neutron diffraction experiments can also become temporally sensitive. Time resolution is defined by $\tau = \hbar/\Delta E$. As the energy resolution is ~1 meV, only structures which fluctuate at times slower than 1 picosecond will lead to correlation peaks. The lower limit for the lifetime of the fluctuating structures observed in our experiment is, therefore, determined to be ~1 picosecond, in agreement to the MD simulations.

While this experiment proves the co-existence of domains in single-component phospholipid bilayers, future experiments will be conducted in multi-component lipid membranes and membranes containing cholesterol to detect possible raft structures. By scanning the neutron coherence length ξ, the size of those structures will be determined using the technique developed in this work.

5 Conclusions

The coherent properties of photons and neutrons are used to study structure and dynamics in elastic and inelastic X-ray and neutron scattering experiments. Matching the coherent properties of the scattering probe with those of the sample becomes important in soft-matter and biology because of: (1) the missing long ranged order; and (2) the large length scales involved. Good monochromaticity is a prerequisite for atomic resolution in crystal and protein structure determinations. Such radiation is also highly coherent with large coherence lengths, of the order of several thousands of Angstroems. A large coherence length may, however, average over small structures, such as nanoscale domains. By controlling ξ in a neutron diffraction experiment, we present direct experimental evidence for co-existing gel and fluid domains in a phospholipid bilayer. Instead of a continuous phase transition from the well ordered gel into the fluid phase, which adheres to a well-known critical behaviour, we observe a first order transition with a co-existence of gel and fluid domains.

Nanodomains are not only important to understand fundamental properties of model membranes, but also to better understand complex biological membranes and the formation and function of lipid rafts.[4,45,46] Additional examples are the recently emerging nanoferroelectrics[47] and nanoscale magnetic domains in thin magnetic films.[48] The development of neutron instrumentation which enables the control of the neutron coherence length can be envisioned for the future. Such an instrument would not only be important for the investigation of biological materials, but in all systems where fluctuating nanodomains determine material properties.

Acknowledgements

We thank the Canadian Neutron Beam Centre for the allocation of beam time and the staff at CNBC for their support. This

research was partially funded by the Natural Sciences and Engineering Research Council of Canada (NSERC), the Canada Foundation for Innovation (CFI), the Ontario Ministry of Economic Development and Innovation, and the National Research Council Canada (NRC). John Katsaras is supported through ORNL's Laboratory Directed Research and Development (LDRD), and Program Development programs.

References

1 D. M. Engelman, *Nature*, 2005, **438**, 578–580.
2 D. Lingwood and K. Simons, *Science*, 2009, **327**, 46–50.
3 K. Simons and E. Ikonen, *Nature*, 1997, **387**, 569–572.
4 C. Eggeling, C. Ringemann, R. Medda, G. Schwarzmann, K. Sandhoff, S. Polyakova, V. N. Belov, B. Hein, C. von Middendorf, A. Schönle and S. W. Hell, *Nature*, 2009, **457**, 1159–1162.
5 P.-F. Lenne and A. Nicolas, *Soft Matter*, 2009, **5**, 2841–2848.
6 T. Apajalahti, P. Niemelä, P. N. Govindan, M. S. Miettinen, E. Salonen, S.-J. Marrink and I. Vattulainen, *Faraday Discuss.*, 2010, **144**, 411–430.
7 E. Watkins, C. Millerb, J. Majewski and T. Kuhl, *Proc. Natl. Acad. Sci. U. S. A.*, 2011, **108**, 6975–6980.
8 M. C. Rheinstädter, W. Häussler and T. Salditt, *Phys. Rev. Lett.*, 2006, **97**, 048103.
9 P. S. Niemel, S. Ollila, M. T. Hyvnen, M. Karttunen and I. Vattulainen, *PLoS Comput. Biol.*, 2007, **3**, e34.
10 B. Bruning, E. Wald, W. Schrader, R. Behrends and U. Kaatze, *Soft Matter*, 2009, **5**, 3340–3346.
11 J. Ehrig, E. P. Petrov and P. Schwille, *New J. Phys.*, 2011, **13**, 045019.
12 T. Murtola, T. Róg, E. Falck, M. Karttunen and I. Vattulainen, *Phys. Rev. Lett.*, 2006, **97**, 238102.
13 G. Pabst, N. Kučerka, M.-P. Nieh, M. C. Rheinstädter and J. Katsaras, *Chem. Phys. Lipids*, 2010, **163**, 460–679.
14 G. Fragneto and M. Rheinstädter, *C. R. Phys.*, 2007, **8**, 865–883.
15 J. Pencer, T. Mills, V. Anghel, S. Kruegar, R. Epand and J. Katsaras, *Eur. Phys. J. E*, 2005, **18**, 447–458.
16 J. Pencer, V. Anghel, N. Kucerka and J. Katsaras, *J. Appl. Crystallogr.*, 2006, **39**, 791–796.
17 V. Anghel, N. Kucerka, J. Pencer and J. Katsaras, *J. Appl. Crystallogr.*, 2007, **40**, 513–525.
18 J. Pencer, V. Anghel, N. Kucerka and J. Katsaras, *J. Appl. Crystallogr.*, 2006, **39**, 791–796.
19 C. Nicolini, P. Thyagarajan and R. Winter, *Phys. Chem. Chem. Phys.*, 2004, **6**, 5531–5534.
20 M. Rappolt, G. Pabst, G. Rapp, M. Kriechbaum, H. Amenitsch, C. Krenn, S. Bernstroff and P. Laggner, *Eur. Biophys. J.*, 2000, **29**, 125–133.
21 G. Pabst, S. Danner, G. Deutsch and A. Raghunathan, *Biophys. J.*, 2007, **93**, 513–525.
22 P. Sens and M. Turner, *Phys. Rev. Lett.*, 2011, **106**, 238101.
23 A. Sergé, N. Bertaux, H. Rigneault and D. Maruet, *Nat. Methods*, 2008, **5**, 687–694.
24 S. Mabrey and J. Sturtevant, *Proc. Natl. Acad. Sci. U. S. A.*, 1976, **73**, 3862–3866.
25 S. Andersen, A. Jackson and T. Heimburg, *Prog. Neurobiol.*, 2009, **88**, 104–113.
26 T. Heimburg and D. Jackson, *Proc. Natl. Acad. Sci. U. S. A.*, 2005, **102**, 28.
27 P. Mason, J. Nagle, R. Epand and J. Katsaras, *Phys. Rev. E: Stat. Phys., Plasmas, Fluids, Relat. Interdiscip. Top.*, 2001, **63**, 030902.
28 G. Pabst, J. Katsaras, V. A. Raghunathan and M. Rappolt, *Langmuir*, 2003, **19**, 1716–1722.
29 R. Zhang, W. Sun, S. Tristram-Nagle, R. L. Headrick, R. M. Suter and J. F. Nagle, *Phys. Rev. Lett.*, 1995, **74**, 2832–2835.
30 J. Lemmich, K. Mortensen, J. Ipsen, T. Hø nger, R. Bauer and O. Mouritsen, *Phys. Rev. Lett.*, 1995, **75**, 3958.
31 F. Chen, W. Hung and H. Huang, *Phys. Rev. Lett.*, 1997, **79**, 4026–4029.
32 J. Nagle, H. Petrache, N. Gouliaev, S. Tristram-Nagle, Y. Liu, R. Suter and K. Gawrisch, *Phys. Rev. E: Stat. Phys., Plasmas, Fluids, Relat. Interdiscip. Top.*, 1998, **58**, 7769–7776.
33 G. Fragneto, T. Charitat, E. Bellet-Amalric, R. Cubitt and F. Graner, *Langmuir*, 2003, **19**, 7695–7702.
34 N. Chu, N. Kučerka, Y. Liu, S. Tristram-Nagle and J. F. Nagle, *Phys. Rev. E: Stat., Nonlinear, Soft Matter Phys.*, 2005, **71**, 041904.
35 T. Salditt, *J. Phys.: Condens. Matter*, 2005, **17**, R287–R314.
36 T. Salditt, *Curr. Opin. Colloid Interface Sci.*, 2000, **5**, 19–26.
37 M. Vogel, C. Münster, W. Fenzl and T. Salditt, *Phys. Rev. Lett.*, 2000, **84**, 390–393.
38 M. Rheinstädter, C. Ollinger, G. Fragneto, F. Demmel and T. Salditt, *Phys. Rev. Lett.*, 2004, **93**, 108107.
39 H. Rauch, *Found. Phys.*, 1993, **23**, 7–36.
40 G. Squires, *Introduction to the theory of thermal neutron scattering*, Dover Publications, Inc., Mineola, New York, 1978.
41 N. Kučerka, Y. Liu, N. Chu, H. I. Petrache, S. Tristram-Nagle and J. F. Nagle, *Biophys. J.*, 2005, **88**, 2626–2637.
42 J. Katsaras, R. F. Epand and R. M. Epand, *Phys. Rev. E: Stat. Phys., Plasmas, Fluids, Relat. Interdiscip. Top.*, 1997, **55**, 3751–3753.
43 S. Leekumjorn and A. Sum, *Biochim. Biophys. Acta, Biomembr.*, 2007, **1768**, 354–365.
44 S. Förster, A. Timmann, C. Schellbach, A. Frömsdorf, A. Kornowski, H. Weller, S. Roth and P. Lindner, *Nat. Mater.*, 2007, **6**, 888–893.
45 J. Oelke, A. Pasc, A. Wixforth, O. Konovalov and M. Tanaka, *Appl. Phys. Lett.*, 2008, **93**, 213901.
46 H. J. Risselada and S. J. Marrink, *Proc. Natl. Acad. Sci. U. S. A.*, 2008, **105**, 17367–17372.
47 J. Scott, *Science*, 2007, **315**, 954–959.
48 O. Shpyrko, E. Isaacs, J. Logan, Y. Feng, G. Aeppli, R. Jaramillo, H. Kim, T. Rosenbaum, P. Zschack, M. Sprung, S. Narayanan and A. Sandy, *Nature*, 2007, **447**, 68–71.

5.4 Paper VI: The Observation of Highly Ordered Domains in Membranes with Cholesterol

Clare L. Armstrong, Drew Marquardt, Hannah Dies, Norbert Kučerka, Zahra Yamani, Thad A. Harroun, John Katsaras, An-Chang Shi, and Maikel C. Rheinstädter *"The Observation of Highly Ordered Domains in Membranes with Cholesterol"* (submitted to PLoS ONE).

5.4.1 Preface to Paper VI

The previous paper introduced the LE/HSR technique that was used to resolve a coexistence of small, fluctuating domains in a single-component lipid membrane. The next step for this project was to implement this technique to study membrane systems containing cholesterol.

Again, using the N5 TAS at Chalk River, an experiment was performed on a fluid DPPC bilayer containing ∼30 mol% cholesterol. Upon examining the in-plane data obtained using the standard high-energy resolution setup (with a wavelength that would yield a long coherence length) we found evidence for uniform fluid disordered phase, as is usually reported in the literature. The in-plane scan showed a broad fluid peak, corresponding to the lipid tail spacing, which is often observed in pure lipid samples at high temperature and near full hydration.

When the same system was examined using the LE/HSR setup (with a neutron wavelength that would give a short coherence length), not only was the broad fluid background present, but also a number of well defined peaks. The peaks that were confirmed to be the result of scattering from the sample were found to correspond to a highly ordered phase with a monoclinic structure. The absence of these peaks in the pure DPPC data indicates that the cholesterol is causing small domains of lipids to order. The lack of long-range order in this system is evident from the fact that this structure is not observable using the high-energy resolution setup or in X-ray scattering experiments.

In an effort to confirm the results obtained from neutron scattering, a simulation of the experiment was designed. The simulated system was composed of disordered fluid phase lipid tails, modelled by Gaussian randomized, hexagonally packed scat-

tering sites, and small highly ordered domains, which possess the same monoclinic structure measured from the neutron experiment. The effect of probing the system with the high and low-energy resolution setups was simulated by using large and small integration areas over which the scattering contributions were coherently summed in the theoretical scattering function. When using a large integration area (corresponding to the high-energy resolution setup) there is no evidence of the existence of highly ordered domains in the system, and only the disordered fluid phase is observed. Using the small integration area, however, did give rise to peaks reflecting the structure of the ordered domains in the system.

This supports the theory that there are highly ordered lipid domains in the sample; however, probing the system using the standard high-energy resolution setup misleadingly suggests that the system is in a uniform fluid disordered phase.

Author Contributions

- *Designed research:* Maikel C. Rheinstädter
- *Sample fabrication:* **Clare L. Armstrong** and Hannah Dies
- *Performed experiment:* **Clare L. Armstrong**, Hannah Dies, Drew Marquardt, Norbert Kučerka, Zahra Yamani, Thad A. Harroun, and Maikel C. Rheinstädter
- *Developed simulation:* An-Chang Shi and Maikel C. Rheinstädter
- *Analysed data:* **Clare L. Armstrong**
- *Wrote the manuscript:* **Clare L. Armstrong**, John Katsaras, and Maikel C. Rheinstädter

The Observation of Highly Ordered Domains in Membranes with Cholesterol

Clare L. Armstrong,[1,*] Drew Marquardt,[2,3] Hannah Dies,[1] Norbert Kučerka,[3] Zahra Yamani,[3] Thad A. Harroun,[2] John Katsaras,[4,3,5] An-Chang Shi,[1] and Maikel C. Rheinstädter[1,3,†]

[1] *Department of Physics and Astronomy, McMaster University, Hamilton, ON, Canada*
[2] *Department of Physics, Brock University, St. Catherines, ON, Canada*
[3] *Canadian Neutron Beam Centre, National Research Council of Canada, Chalk River, ON, Canada*
[4] *Neutron Sciences Directorate, Oak Ridge National Laboratory, Oak Ridge, USA*
[5] *Joint Institute for Neutron Sciences, Oak Ridge, TN 37831, USA*

(Dated: April 10, 2013)

Rafts, or functional domains, are transient nano- or mesoscopic structures in the exoplasmic leaflet of the plasma membrane, and are thought to be essential for many cellular processes. Using neutron diffraction and computer modelling, we present evidence for the existence of highly ordered lipid domains in the cholesterol-rich (32.5 mol%) liquid-ordered (l_o) phase of dipalmitoylphosphatidylcholine membranes. The liquid ordered phase in one-component lipid membranes has previously been thought to be a homogeneous phase. The presence of highly ordered lipid domains embedded in a disordered lipid matrix implies non-uniform distribution of cholesterol between the two phases. The experimental results are in excellent agreement with recent computer simulations of DPPC/cholesterol complexes [Meinhardt, Vink and Schmid, Proc. Natl. Acad. Sci. U.S.A., doi:10.1073/pnas.1221075110], which report the existence of nanometer size l_o domains in a liquid disordered lipid environment.

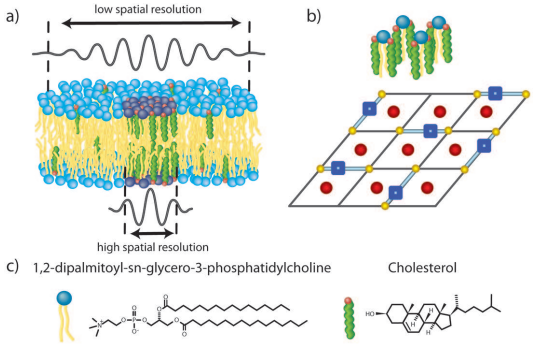

FIG. 1. a) Schematic of a lipid bilayer containing a lipid domain as studied by neutron scattering techniques using a low (top) and high (bottom) spatial resolution setup. b) In-plane representation of saturated hydrocarbon-chain lipid-cholesterol interactions in accordance with the umbrella model, whereby each lipid is associated with 2 cholesterol molecules. This structural arrangement results when the cholesterol content is 66 mol%. The blue squares represent lipid head groups, the yellow circles correspond to lipid tails, and the red circle are cholesterol molecules. c) Schematic molecular structures of DPPC and cholesterol molecules.

It is widely believed that in the plasma membrane sphingolipids and cholesterol molecules assemble into functional domains, or so-called *rafts* (Figure 1 a) and b)). They are thought to take part in membrane-associated events such as signal transduction, cell adhesion, signalling, cell trafficking and lipid/protein sorting [1–13].

* armstc5@mcmaster.ca
† rheinstadter@mcmaster.ca

While the size, shape, and even the existence of liquid-ordered domains in cell membranes is still a subject of much debate, it is generally agreed that domains coalesce upon cross-linking to form signalling and sorting platforms [14]. Anomalies in raft composition have been associated with various diseases, including atherosclerosis, muscular dystrophy and neurodegenerative disorders, such as Alzheimer's. Specific proteins associated with disease, such as the amyloid beta (Aβ) [15] and prions protein [16], as well as various signalling proteins [17–19], have been shown to accumulate in rafts. Recently, the membrane's physical properties have also been suggested to play an important role in modulating protein-protein interactions in rafts [20–24].

Cholesterol (Figure 1 c)) is an essential component of eukaryotic cell membranes, and is capable of modulating the membrane's permeability [25]. In association with rafts, cholesterol has been implicated in cell signalling processes [1, 26–29]. The phase separation of cholesterol and other biomolecules (e.g., sphingolipids, phospholipids, proteins) into domains is a key element with regard to raft formation in biological systems.

Experimental observations of membrane heterogeneities have proven challenging, as they are thought to be both small and short-lived [4, 30–32]. Therefore, in order for experimental techniques to unambiguously observe such structures, they must be capable of simultaneously accessing small (nanometer to micrometer) length scales and fast (nano to microsecond) time regimes. To date, the detection of functional domains in living cells has relied on indirect methods, such as detergent extraction and cholesterol depletion, as they are now believed to be too small to be observed with the presently available microscopy techniques [33].

In this paper we report on neutron scattering and computer modelling experiments that show the existence of

nanoscopic domains in the liquid-ordered (l_o) phase of dipalmitoylphosphatidylcholine (DPPC) membranes. This newly developed neutron scattering technique has recently been used to observe co-existing transient nanometer sized domains in a single-component phospholipid membrane at temperatures close to its main phase transition [34].

RESULTS

Neutron Experiment

To determine the lateral molecular structure, in-plane neutron diffraction was used to measure the liquid-ordered phase of DPPC bilayers at T=50°C and a D_2O relative humidity of ∼100%, ensuring full hydration of the membranes. Highly oriented, solid supported DPPC membranes containing 32.5 mol% cholesterol were used in this study.

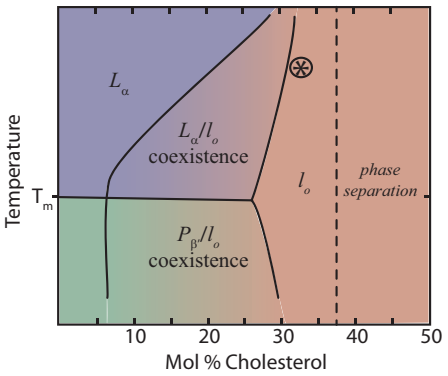

FIG. 2. Phase diagram of phospholipid/cholesterol complexes, such as DMPC/cholesterol and DPPC/cholesterol, as reported by, for example, [35–40]. Besides the well known gel and fluid phases, the so-called liquid-order phase is observed at high cholesterol concentrations. The 32.5 mol% sample, as depicted by the ⊛, was determined to be in the l_o phase.

A schematic phase diagram of a phospholipid/cholesterol system is shown in Figure 2. Although much is known about lipid-cholesterol mixtures, there is much activity in this area of study due to cholesterol's role in domain formation [35–40]. It has been speculated that the stiff cholesterol molecules align parallel to the hydrocarbon lipid tails and suppress lipid tail fluctuations [41], in turn affecting the membrane's dynamical properties. Most lipid/cholesterol studies agree that, depending on temperature and cholesterol concentration, three phases are observed, namely: 1) the rigid gel $P_{\beta'}$ (ripple) phase [42]; 2) the fluid L_α phase; and 3) the liquid-ordered l_o phase. The gel and fluid phases are well known from single component phospholipid bilayers. The l_o phase is only observed at high concentrations of cholesterol. This phase is somewhat peculiar as it appears to be well ordered (similar to the gel phase), however, the lipids exhibit a diffusion coefficient that is similar to that measured in fluid bilayers.

At low cholesterol content, the bilayers undergo a phase transition from the gel to the fluid phase, as is observed in pure lipid bilayers, and the temperature of the main transition, T_m, is slightly shifted towards higher temperatures. However, at high cholesterol concentrations ($\gtrsim$30 mol%), the main transition of liquid-ordered membranes is suppressed, while at intermediate cholesterol concentrations (i.e., between about 10-30 mol%), most studies report a coexistence between gel and l_o, or L_α and l_o phases. The location on the phase diagram of the sample composition used in the present study is shown in Figure 2. Because the phase boundaries of the phase diagram are not well known, additional experiments were conducted to verify the exact phase of the membranes. The corresponding data is included in the Supplementary Material: Specific heat capacity measurements are shown in Figure S1; X-ray reflectivity of a DPPC/37.5 mol% sample is shown in Figure S2; Neutron reflectivity is shown in Figure S3.

Two different neutron scattering setups, were used to study the membranes, namely: (1) a conventional, high energy and momentum resolution setup (i.e. small ΔE and ΔQ); and (2) a low energy and momentum resolution setup (i.e. large ΔE and ΔQ), with a high spatial resolution capable of detecting small structures and weak signals. The two setups could be readily switched by changing the incoming neutron wavelength, λ, thus eliminating the need for re-aligning the sample. The experiment was predominantly sensitive to the molecular structure and arrangement of the lipid acyl chains, and their contribution to the scattering signal was enhanced by using the chain perdeuterated lipid DPPC-d62. The sample was aligned in the neutron beam such that the scattering vector, Q, was always in the plane of the membrane, as depicted in Figure 6. This in-plane component of the scattering vector is referred to as $q_{||}$.

Data taken using the conventional setup are shown in Figure 3 a). The data show a diffraction pattern typical of fluid single and multi-component lipid bilayers [43–52]. The broad correlation peaks are signatures of a disordered, fluid structure, with three broad peaks, observed at $q_{||}$ ∼1.36 Å^{-1},2.28 Å^{-1}, 2.65 Å^{-1}, corresponding to the packing of the lipid acyl chains in the membrane's hydrophobic core. Peaks were fitted using Gaussian profiles and could be indexed by a planar hexagonal unit cell with parameters a=b=5.58 Å and γ=120°. Fitting was done using the Powdercell software package [53, 54]. The area per lipid molecule was calculated from the unit

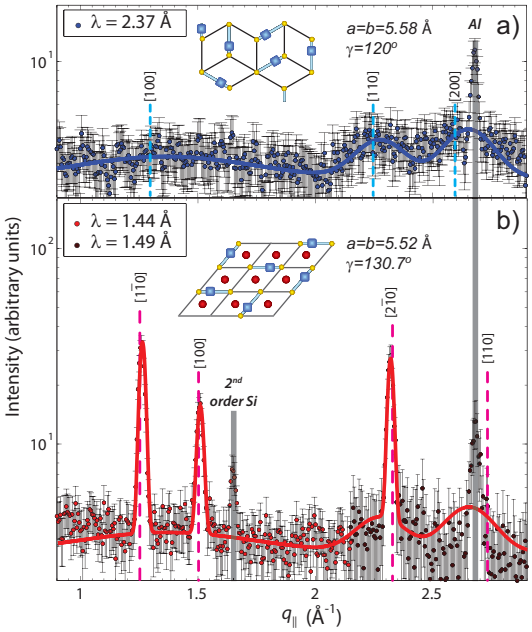

FIG. 3. A comparison between the in-plane scans of DPPC-d62 bilayers with 32.5 mol% cholesterol using (a) the conventional high energy resolution (small ΔE) setup and (b) the low energy resolution (large ΔE) setup. The data are denoted by circles with the fit shown as a solid line. A disordered structure was observed in (a), while the sharp features in (b) are indicative of the presence of highly ordered lipid domains. A top view of the corresponding molecular structures are shown in the insets to the figure using the same symbols as in Figure 1 b); the quasi-Bragg reflections are indicated by vertical dashed lines and their associated Miller indices, [*hkl*]. Peaks resulting from the silicon substrates and the aluminum sample chamber (as described in the Materials and Methods Section) are highlighted in grey, but not accounted for in the fit.

cell parameters to be $A_{lipid} = 2 \times (5.58)^2 \sin(120°) = 53.9$ Å^2 (one unit contains 1 lipid tail and 1/2 headgroup, so the area is doubled in order to represent one lipid molecule). This area per lipid is significantly smaller than the 63.1 Å^2 [55] and 64.2 Å^2 [56] found in liquid crystalline DPPC bilayers at 50°C. The cartoon in Figure 3 a) depicts the unit cell and a possible arrangement of the lipid molecules. While the lipid tails were found to arrange on a hexagonal lattice, no long range order was observed for the lipid head groups, unlike the case if DPPC bilayers in the sub gel phase where the lipid headgroups form a two-dimensional lattice [57–59].

The diffraction pattern obtained using the low energy resolution (large ΔE) setup is shown in Figure 3 b). In addition to the broad disordered components, three pronounced narrow correlation peaks are visible, indicating the presence of a co-existing, well ordered structure. The positions of the peaks ($q_{||}$ = 1.26, 1.51, and 2.32 Å^{-1}) are best described by a monoclinic unit cell of parameters a=b=5.52 Å and γ=130.7°. The cartoon depicts a possible molecular structure. The monoclinic unit cell allows for each lipid to be associated with two cholesterol molecules, in accordance to the umbrella model (discussed below).

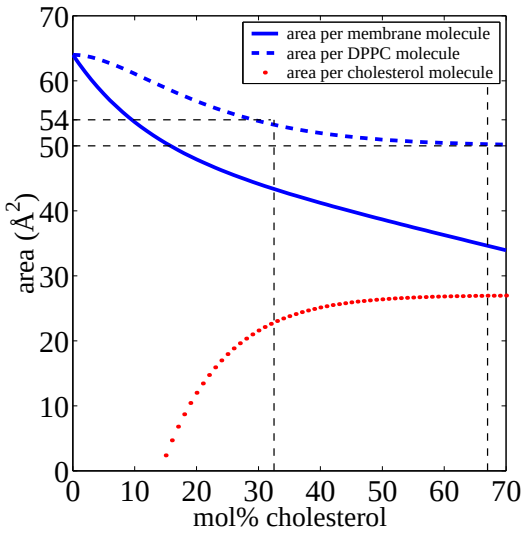

FIG. 4. Area per molecule and partial areas for DPPC and cholesterol molecules as function of cholesterol concentration. Curves were calculated using Eq. (1) [60].

The areas determined from the two experimental setups can be compared to a model by Edholm and Nagle [60]. The total area per membrane molecule for a DPPC/cholesterol can be written as the sum of the partial areas of lipid and cholesterol molecules:

$$a(x) = (1-x)\left[a^0_{DPPC} - \Delta a\left(1-e^{-nx}\right)\right] + x a_{chol}, \quad (1)$$

where a_{chol} (=27 Å^2) is cholesterol's area, and does not change as a function of concentration, x, and a^0_{DPPC} (=64 Å^2) is the area for DPPC at 0 mol% cholesterol. Δa (14 Å^2) is the change in DPPC area when in contact with cholesterol and n (=7.5) is the maximum number of DPPC molecules that can be condensed by a single cholesterol molecule.

The partial areas of cholesterol and lipid molecules were determined to be $a_{chol}(x) = a(x) + (1-x)a'(x)$ and $a_{DPPC}(x) = a(x) - xa'(x)$; the result of which is plotted in Figure 4. Deuterium labelling was used in our experiment to highlight the structure of the lipid tails. The areas determined in Figure 3 are, therefore, partial lipid areas. The area of 54 Å^2 for the disordered structure in Figure 3 a) is in excellent agreement with the area per DPPC molecule in Figure 4 in the presence of 32.5 mol% cholesterol. The area per lipid molecule in

the the highly ordered domains in Figure 3 b) is calculated to be $A_{lipid} = 2 \times (5.52)^2 \sin(130.7^\circ) = 46.2$ Å^2. This lipid area is consistent with high concentrations of cholesterol, where lipid condensation reaches a maximum, and is in-line with the umbrella model. We note that this area is also close to the area per lipid published by Tristram-Nagle *et al.* [61], for gel phase DMPC membranes (∼47 Å^2). The lipids in the highly ordered patches can thus be speculated to have a gel-like structure, with the acyl tails in an all-trans configuration, as will be discussed below.

The equilibrated lipid area is governed by a balance of forces resulting from the headgroup and hydrocarbon chains. In the infinitely long chain length regime, where lipid chain-chain van der Waals attractive interactions dominate (i.e., headgroup electrostatic interactions are negligible), the headgroup has a minimum area due to the steric interactions between the interfacial glycerol-carbonyl groups. However, the observed minimal area is still larger than the optimum packing for all-trans chains of about 40 Å^2 [62], indicating that the overall lipid area is determined by the headgroup steric limit [63].

The presence of broad correlation peaks in the small ΔE setup and the appearance of additional, sharp reflections in the large ΔE setup are the signature of small, highly ordered lipid domains embedded in a disordered matrix.

Computer Modelling

The primary reason that small, nanometer sized domains in the l_o phase have not been previously reported by scattering techniques may be related to the fact that the X-ray and neutron probes coherently average over a given area or volume. Small structures are thus not visible because only coherent spatial averages are observed. A computer simulation can easily model the high and low coherence length setups by calculating the in-plane structure factor, $S(q_{||})$, over different areas and comparing the resulting patterns to the experimental diffraction patters in Figure 3.

A snapshot of a typical system used for the calculations is schematically shown in Figure 5 c): It consists of a disordered lipid matrix with 2 highly ordered lipid domains. The positions of the lipid acyl chains are represented by dots, as shown by Figure 5 d). The lattice parameters of the disordered and ordered phases were taken from the experiment. Positional disorder was added by introducing a random displacement of the tails from their nominal position: a large amplitude of this random displacement mimics a highly disordered structure, while small or no displacements resulted in highly ordered structures. The aim of the computer model was not to produce an independent model of the structure of the l_o phase, but to demonstrate the effect that coherent averaging over different areas has on the observed scattering.

The high and low energy resolution setups in the neutron experiment were simulated by calculating the scattering function, $S(q_{||})$, over different simulation areas (Figure 5 c)). The large integration area corresponds to the high energy resolution setup (small ΔE). The low energy resolution setup (large ΔE), with a higher spatial resolution, on the other hand, was simulated by integrating over an area corresponding to a single domain.

The diffraction pattern in Figure 5 a) shows the result of integrating over an area of 250×250 Å^2 (containing ∼1350 lipid molecules), as indicated by the blue rectangle in Figure 5 c). The blue area is comprised of the lipid matrix and the embedded domains, resulting in the observation of broad correlation peaks. The obtained scattering pattern, characteristic of a disordered system, is the *coherent* average result, which is comprised of the fluid matrix and the ordered domains.

Figure 5 b) shows the integration of an area corresponding to a single ordered domain (70×70 Å^2 which includes ∼110 lipid molecules), as indicated by the red rectangle in Figure 5 c). The fit of the experimental diffraction pattern is also shown in b); the calculated peaks positions from Powdercell are marked by the vertical dashed lines. While the computer model well reproduces the positions of the correlation peaks, i.e., the unit cell structure (see Table S1 and Figure S4 in the Supplementary Materials for a detailed comparison), the model is too simple to also reproduce the corresponding peak intensities (the form factors). The $[1\bar{1}0]$ was found to be systematically extinct in the computer model while the [110] produced a strong peak, not clearly observed in the experimental data. The most important result was that in both, experiment and computer model, pronounced correlation peaks were observed at a small coherence length indicating the existence of well ordered lipid structures.

DISCUSSION

The molecular structure of the l_o phase in a DPPC membrane containing 32.5 mol% cholesterol was studied using different spatial resolution neutron scattering techniques. Computer modelling revealed that the observed scattering patterns are consistent with a heterogeneous structure composed of ordered nanometer sized lipid domains residing within a disordered liquid matrix.

Initially, the lateral membrane structure was studied by operating the neutron diffractometer in the commonly used low spatial resolution mode, where ΔE and ΔQ are small (Figure 3 a)). In these experiments neutrons with a long coherence length are used, spatially averaging all in-plane features of the membrane [34].

The scattering pattern from the low spatial resolution setup was indicative of lipids and cholesterol being in a uniform, fluid-like state, as has been previously reported [43–47, 50, 52]. The absence of any sharp features in the diffraction pattern indicated that the cholesterol is uniformly distributed in the lipid matrix, with the lipid

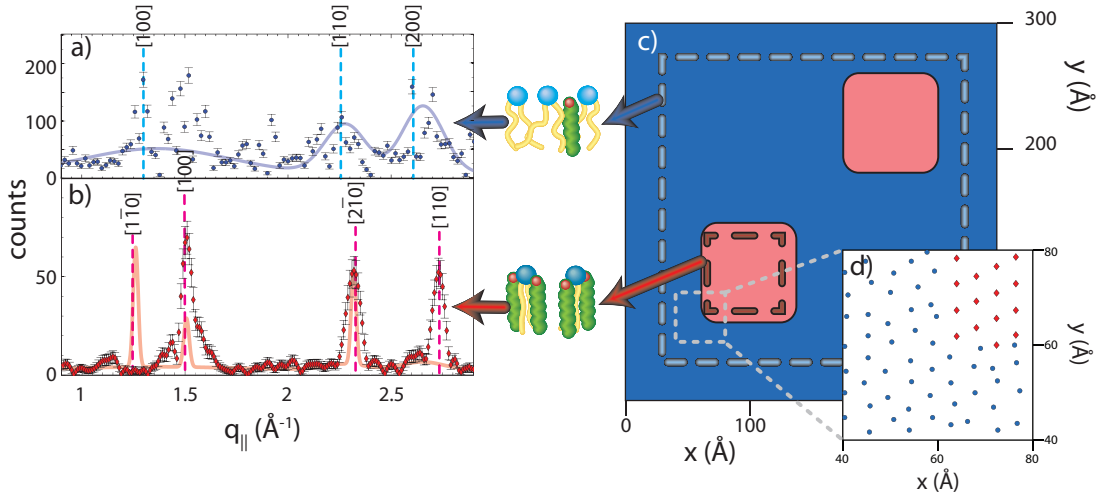

FIG. 5. a) The scattering function $S(q_{||})$ integrated over an area of 250×250 Å^2, resulting in a diffraction pattern indicative of fluid, disordered bilayers. b) $S(q_{||})$ for an ordered lipid domain of size 70×70 Å^2. Three sharp correlation peaks are observed. The dots represent data obtained from the computer model, while the solid lines correspond to the fits obtained from the neutron scattering experiment in Figure 3 a)and b). Areas of integration are indicated by the blue and red rectangles shown in c). c) Snapshot of a typical configuration in the computer model. The blue region corresponds to the disordered lipid matrix, and the red regions to ordered lipid domains. The total system size was 300×300 Å^2 and contained ∼2000 lipid molecules, or ∼4000 lipid tails. The ordered domains were ∼ 70 × 70 Å^2 in size and included ∼110 lipid molecules. d) A close up view of the computer model system, where the blue circles represent lipid tails in the fluid disordered state and the red diamonds are tails in the l_o phase.

tails arranging themselves in a hexagonally packed structure on a lattice with parameters $a = b$=5.58 Å and an area per lipid of A_{lipid} = 53.9 Å^2. As mentioned, this area per lipid is significantly smaller than that observed in pure DPPC bilayers at $T = 50$°C (63.1 Å^2 [55] and 64.2 Å^2 [56]), and is a result of cholesterol's condensation effect (i.e., ordering of a lipid's hydrocarbon chains). [38, 39] In fact, this area per lipid is in excellent agreement with the partial lipid area determined by the model proposed by Edholm and Nagle [60], which is plotted in Figure 4.

In the case of the high spatial resolution setup, however, distinct sharp peaks were observed in both experiment (Figure 3 b)) and computer model (Figure 5 b)). In the case of the experiment, the integration area was determined by the instrumental ΔE and ΔQ, and the corresponding neutron coherence length, ξ. In the simulation, the size of the coherently added area was defined by the length of the distance vector $\vec{r}_{nm}$ between two lipid tails in the summation of the structure factor $S(q_{||})$. Importantly, both techniques detect the presence of ordered domains embedded in a disordered matrix. In this case, the lipid tails were found to form a monoclinic structure in these domains with lattice parameters a=b=5.52 Å and γ=130.7°, and a lipid area of A_{lipid} = 46.2 Å^2.

Several models describing the interaction between lipids and cholesterol are currently being discussed. Of these, the most prevalent are: the umbrella; the complex; and the superlattice model [39, 64]. In the umbrella model [65, 66], each lipid head group can "host" two cholesterol molecules, thus shielding the mostly hydrophobic cholesterol molecule from the aqueous environment. Based on the model for partial areas of lipid and cholesterol molecules by Edholm and Nagle [60, 67] (Figure 4), the partial lipid area decreases significantly towards higher cholesterol concentrations. At the maximum theoretical solubility of 66 mol% cholesterol [65, 68], a partial lipid area of ∼50 Å^2 is calculated, comparable to the ∼47 Å^2 lipid area of DPPC in gel phase membranes [61]. M'Baye *et al.* addressed this point [69] and concluded that cholesterol, due to its specific H-bonding interactions with lipids and its ability to fill voids in lipid bilayers, may efficiently expel water molecules from the highly ordered gel phase to form the l_o phase. As early as 1987, Hjort Ipsen *et al.* [70] reported that the bilayer at high cholesterol concentrations behaves as a liquid with greatly reduced membrane-area compressibility. NMR measurements have shown that the deuterium order parameters approach a value of 0.5, typical of an all-trans rotating hydrocarbon chain. The hydrocarbon chain organization determined from the correlation peaks observed by experiment in Figure 3 b) is consistent with an ordered structure containing elevated amounts of cholesterol, where all the voids in the monoclinic lipid lattice are filled with cholesterol molecules, as depicted in the cartoons to Figures 1 b) and 3 b). This suggests that the

lipid domains are comprised of lipids with highly ordered hydrocarbon chains.

Recent observations have suggested that in the mammalian plasma membrane, small domains residing within ordered lipid phases are in dynamic equilibrium with the less ordered portions of the membrane [8]. Armstrong *et al.* studied the nanoscale dynamics of the lipids making up domains [52]. They reported that on the nanometer length scale, cholesterol rich domains seem to be softer than fluid phase bilayers, and at the same time, are better ordered than lipids in the gel phase. The present data taken together with the study by Armstrong *et al.* [52], add significant weight to the recently proposed plasma membrane model.

We note that it is not straightforward to directly relate the coherence length of the neutron beam to domain size. The coherence length of a neutron beam was first measured by Kaiser, Werner and George [71] by neutron interferometry. In one dimension (1D), a neutron in the neutron beam can be described by a 1D wave package, $\psi(r,t) = \int_{-\infty}^{\infty} dk\ a(k)e^{-i(kr-\omega t)}$. If the amplitude, $a(k)$, is approximated by a Gaussian amplitude function, $a(k) = a_0 e^{-(k-k_0)^2/(2\sigma^2)}$, the wave package will have a Gaussian shape [71]. In this simple model, the coherence length, ξ, can be thought of as the $FWHM$ of the Gaussian wave package, $FWHM = 2\sqrt{2\ln(2)}\sigma \approx 2.35 \times \sigma$. The intensity measured at the detector is the result of the superposition of the different scattered waves; for two waves: $I = |\psi_1 + \psi_2|^2 = |\psi_1|^2 + |\psi_2|^2 + \psi_1^*\psi_2 + \psi_2^*\psi_1$. The first two terms describe incoherent scattering. Coherent, Bragg scattering is the result of the cross terms in the equation. If there is no overlap between the wave function, only incoherent scattering takes place. The two wave functions will certainly overlap if they are closer together than the $FWHM$, which corresponds to the coherence length. However, the total spatial extent of the wave function is larger than the $FWHM$.

Additionally, the wave functions are commonly approximated by Gaussian functions as these are limited in space, and their Fourier Transform can easily be calculated. In a more realistic model, the wave package may fall off much more slowly than a Gaussian package, which would drastically increase the spatial extent of the package, making the cross terms observable at distances much larger than the coherence length (the FWHM) of the wave package.

It is, therefore, non-trivial and, at this point, not possible to quantitatively relate the domain to the coherence length of the neutron beam. The full width at tenth of maximum of a Gaussian ($FWTM$), $FWTM = 2\sqrt{2\ln(10)}\sigma \approx 4.29 \times \sigma$, contains 90% of the Gaussian area and might give a more appropriate estimate of the domain size. The experimental neutron coherence length of ∼35 Å would then give a tentative domain size of ∼65 Å. As a result, domain sizes of ∼70 Å were used in the computer simulations in order to compare to experiment.

Our results can be compared to a recent computer simulation study by Meinhardt, Vink and Schmid [72] of a DPPC/cholesterol system. By using a coarse grained model that included 20,000 lipid molecules, a microemulsion-type state was observed that contained nanometer-sized l_o domains in a liquid disordered environment. The liquid ordered phase in lipid membranes was previously modelled as a homogenous phase. The computational work has two important results. Firstly, raft formation was observed in a binary system, while it was previously thought that raft-mixtures required the presence of several different types of lipids and cholesterol. Secondly, small, nanometer sized domains on the order of 100 Åwere observed. These findings are in excellent agreement to the experimental results presented here. Based on the width of the correlation peaks in the computer model and the correlation length, the domains in our experiments can roughly be estimated to be on the order of 70 Å. In future experiments the size of the domains will be determined from measurements of the corresponding structure factor using small angle neutron or X-ray scattering experiments.

CONCLUSION

By combining neutron scattering and computer modelling we present evidence suggesting that the liquid-ordered, l_o, phase in DPPC membranes contains highly ordered lipid domains. DPPC bilayers with 32.5 mol% cholesterol were prepared in their high cholesterol l_o phase, but below the critical concentration at which phase separation takes place. Experiments and simulations were performed using two different spatial resolutions. A small ΔE and ΔQ neutron setup, which integrated over large areas of membrane, gave rise to a diffraction pattern typical of fluid-like, disordered systems. Similar data were reported previously from neutron and X-ray scattering experiments, and suggest a homogeneous distribution of cholesterol molecules within the lipid matrix.

Increasing the spatial resolution of the experiment by using a configuration with a large ΔE and ΔQ resulted in a drastic decrease of the coherence length of the neutron beam, enabling smaller membrane patches to be studied. This setup resulted in distinct correlation peaks due to a local ordering of the lipid acyl chains. The reflections could be modelled using a simulated system of small, ordered nanoscopic lipid domains. We speculate that these domains are saturated with cholesterol molecules, i.e., two cholesterol molecules per lipid molecule, as suggested by the umbrella model. The elastic neutron scattering experiments taken in this study, together with recent inelastic experiments [52] suggest that small domains in ordered lipid phases are in dynamic equilibrium with the less ordered parts of the membrane.

Materials and Methods

Sample Preparation

Chain perdeuterated 1,2-dipalmitoyl-sn-glycero-3-phosphocholine (DPPC-d62) was used to enhance the intensity of the coherent out-of-plane and in-plane neutron Bragg diffraction peaks. Highly oriented multilamellar stacks of DPPC with 32.5 mol% cholesterol were prepared on 2″ single-side polished Si wafers of thickness 300 μm. A solution of 16.7 mg/mL DPPC-d62 with 32.5 mol% cholesterol in 1:1 chloroform and 2,2,2-trifluoroethanol (TFE) was prepared. The Si wafers were cleaned by alternate 12 minute sonications in ultra pure water and methanol at 313 K. This process was repeated twice. The cleaned wafers were placed on a heated sample preparation surface, which was kept at 50°C. This temperature is well above the main phase transition for DPPC, thus the heated substrates ensured that the lipids were in the fluid phase after deposition. 1.2 mL of the lipid solution was deposited on each Si wafer and allowed to dry. The wafers were kept under vacuum overnight to remove all traces of the solvent. Samples were then hydrated with heavy water, D_2O, and annealed in an incubator at 328 K for 24 hours. Following this protocol, each wafer contained ∼3,000 highly oriented stacked membranes with a total thickness of ∼10 μm. Sixteen such Si wafers were stacked with 0.6 mm aluminum spacers placed in between each wafer to allow for the membranes to be properly hydrated. The "sandwich" sample was kept in a sealed temperature and humidity controlled aluminum chamber. Hydration of lipid membranes from water vapour was achieved by independently adjusting the temperature of the heavy water reservoir, the sample and the chamber cover. Temperature and humidity sensors were installed close to the sample. A water bath was used to control the temperature of the different water reservoirs, and the temperatures of the sample and its cover were controlled using Peltier elements. The hydration of the sample was estimated from the lamellar spacing d_z to better than 99.6%.

The samples were mounted vertically in the neutron beam such that the scattering vector, Q, could either be placed in the plane of the membrane ($q_{||}$), or perpendicular to it (q_z). The out-of-plane and in-plane structures could be measured by simply rotating the sample by 90 degrees, as shown in Figure 6.

The main transition temperature, T_m, of DPPC-d62 was reported to occur at 310.5 K, [73] a value slightly lower than its protonated counterpart (T = 314.4 K) [73, 74]. The temperature of the pre-transition from the $L_{\beta'}$ to the $P_{\beta'}$ phase in deuterated DPPC-d62 was determined to be 302.9 K [73]. All measurements reported here were done at T = 323.2 K (50°C), well above T_m.

Neutron Experiment

Setup	λ (Å)	E (meV)	ΔE (meV)	ΔQ (Å^{-1})	ξ (Å)
①	1.44	39.5	3.521	0.034	32.3
①	1.49	36.8	3.173	0.032	34.6
②	2.37	14.6	0.757	0.020	91.3
Neutron Diffraction	4.2	4.66	∞	0.005	420
X-ray Diffraction	1.54	$8.041{\cdot}10^6$	∞	0.001	∼3000

TABLE I. Instrumental parameters for the low (①) and high (②) energy resolution setups used. PG(002) crystals were used for both the monochromater and analyzer. The collimation was set to (c1-c2-c3-c4): 30-18-28-60 (in minutes). For comparison, typical values for energy, ΔE, ΔQ, and coherence length for (cold) neutron diffraction and X-ray diffraction experiments are also included.

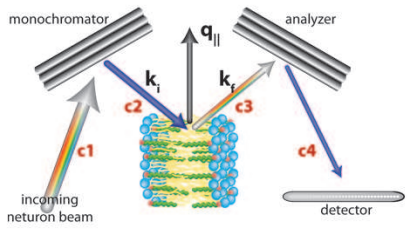

FIG. 6. Geometry of the triple axis spectrometer. Orientation of the sample for in-plane scans, such that the scattering vector, Q, lies in the plane of the membrane ($q_{||}$). k_i and k_f are the incident and final neutron wave vectors ($k = 2\pi/\lambda$) and the c's denote the location of collimators along the beam line.

Experiments were conducted using the N5 triple-axis spectrometer at the Canadian Neutron Beam Centre (Chalk River, ON, Canada). The three axes of the spectrometer refer to the axis of rotation of the monochromator, the sample and the analyzer. The incident and final neutron energies are defined by the Bragg reflections from pyrolytic graphite (PG) crystals. The divergence of the neutron beam was controlled by Soller collimators. A schematic of the instrument's configuration is shown in Figure 6. The instrumental parameters for the two setups used in this experiment are listed in Table I.

The ΔE and ΔQ of a neutron triple-axis spectrometer are determined by: (1) the incident energy of the neutron beam; (2) the divergence of the neutron beam; and (3) the wavelength resolution of the monochromator and analyzer. Collimation was kept constant during the course of the experiment. Small and large ΔE setups were achieved by varying the incident energy of the incoming neutrons. The longitudinal coherence length of the neutron beam, ξ, is defined by $\xi = \lambda^2/\Delta\lambda$ [75]. For a neutron spectrometer with incident neutron energy E and instrumental energy resolution ΔE, ξ can be estimated to be $\xi \sim 18\sqrt{E}/\Delta E$ [34], where E and ΔE are

in meV. The transverse coherence length ξ_t can be estimated to be $\sim \lambda/\alpha$, where α is the divergence of the neutron beam. Long transverse coherence lengths of several micrometers are achieved in small angle neutron scattering (SANS) instruments by pinholes. The transverse coherence length in our setup was of the order of ∼5 Å, and is small compared to the longitudinal coherence. Note, that the reason for the typically low monochromaticity of neutron beams is to avoid further compromising the already low flux "white" neutron beam, a situation that is very different for synchrotron X-rays.

Switching between the high and low energy resolution setups was done by changing instrumental settings of the neutron triple-axis spectrometer, which has an effect on ΔQ and ΔE of the beam. A smaller neutron wavelength leads to strongly relaxed ΔQ and ΔE. In addition, the longitudinal coherence length of the neutron beam decreases. The most significant changes between the high and low energy resolution setups are: (1) a more efficient integration over larger $q_{||}$ ranges to enhance small signals; and (2) a reduction of the coherently added scattering volume.

Typical values for ΔE, ΔQ, and coherence length for (cold) neutron diffraction and X-ray diffraction experiments are also included in Table I. Typical X-ray photon energies are between ∼4 and ∼20 keV, with wavelength resolutions of $\Delta\lambda/\lambda \sim 10^{-3} - 10^{-4}$, which are achieved by silicon monochromators. Cold neutrons are usually used for experiments in biological materials, with typical energies of 4.2 meV and a monochromatization of ∼1%. While these techniques appear to be favourable to pick up small signals from small domains (because of their large ΔE and at the same time, small ΔQ, the long coherence length ξ prevents high spatial resolution. Previously, setup ① was successfully used in [34] for the study of lipid nanodomains in membranes.

In-plane peak assignments

Figure 7 shows in-plane diffraction over an extended range of in-plane momentum transfers, (1 Å^{-1} < $q_{||}$ <3 Å^{-1}), measured at neutron wavelengths of λ=1.44 Å and λ=1.49 Å. Several Bragg peaks are observed at $q_{||}$-positions of $q_{||}$=1.26 Å^{-1}, 1.51 Å^{-1}, 1.65 Å^{-1}, 2.32 Å^{-1} and 2.70 Å^{-1}. In order to unambiguously assign scattering signals to the membrane system, the origin of the peaks was determined.

The observed Bragg peaks can be the result of: (1) scattering from the sample; (2) scattering from the aluminum sample environment or the silicon substrate; or (3) the result of multiple scattering. The positions of the aluminum and silicon Bragg reflections were calculated based on their known crystal structures. Aluminum forms a face-centred cubic lattice (space group 203) with lattice parameter a=4.0497 Å. Silicon forms a cubic lattice (space group 227) with lattice parameter a=5.4309 Å. The positions of the corresponding aluminum and silicon Bragg peaks are shown in Figure 7. The Bragg peak at $q_{||}$=2.70 Å^{-1} can be assigned to aluminum, most likely from the windows of the humidity chamber and sample holder that were used to house the silicon wafers.

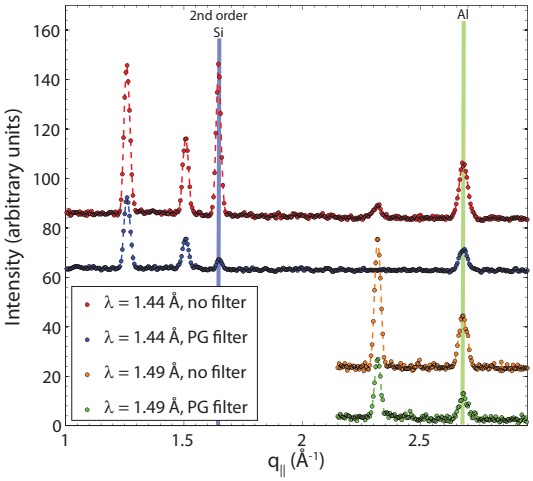

FIG. 7. In-plane diffraction data and peak assignments. Data were taken with and without a PG filter, which was used to suppress higher order reflections.

The Bragg equation $2d\sin(\theta) = n\lambda$ allows for Bragg peaks at integer values of n. This is a particularly relevant point when crystal monochromators are used to monochromate the incoming neutron beam, as was the case in our experiment. If the instrument is set up for a wavelength of λ=2.37 Å, for example, $2 \times \lambda$ and $3 \times \lambda$ also happen to fulfil Bragg's law, leading to reflections at approximately one half and one third of the original calculated positions. The reflection at $q_{||}$=1.65 Å^{-1} fulfils this condition, agreeing with the position of the silicon [220] reflection peak measured at a wavelength of 2λ. Higher order wavelengths can be suppressed in neutron experiments by using filters that only transmit the original wavelength and strongly absorb all other wavelengths. Figure 7 also includes data measured with a PG filter [76]. While the intensity of all peaks decreased, the peak at $q_{||}$=1.65 Å^{-1} was drastically reduced in the presence of the filter, and was therefore assigned to a second order Bragg reflection from the silicon substrate. We note that the silicon wafers used in this experiment were single crystals. However, due to multiple scattering events [77], Bragg reflections can be observed even when the corresponding crystal axis is not aligned in the scattering plane.

Based on the above analysis, three peaks in Figure 7, namely those at $q_{||}$=1.26 Å^{-1}, 1.51 Å^{-1} and 2.32 Å^{-1}, can be unambiguously assigned to scattering from the membrane structure, and were the only ones used to determine the lipid tail structure.

Supplementary Material to: The Observation of Highly Ordered Domains in Membranes with Cholesterol

Clare L. Armstrong,[1,*] Drew Marquardt,[2,3] Hannah Dies,[1]
Norbert Kučerka,[3] Zahra Yamani,[3] Thad A. Harroun,[2]
John Katsaras,[4,3,5] An-Chang Shi,[1] and Maikel C. Rheinstädter[1,3,†]

[1]*Department of Physics and Astronomy, McMaster University, Hamilton, ON, Canada*
[2]*Department of Physics, Brock University, St. Catherines, ON, Canada*
[3]*Canadian Neutron Beam Centre, National Research Council of Canada, Chalk River, ON, Canada*
[4]*Neutron Sciences Directorate, Oak Ridge National Laboratory, Oak Ridge, USA*
[5]*Joint Institute for Neutron Sciences, Oak Ridge, TN 37831, USA*

(Dated: March 28, 2013)

* armstc5@mcmaster.ca
† rheinstadter@mcmaster.ca

VERIFICATION OF THE LIQUID-ORDERED STATE

Additional measurements were conducted to verify that the DPPC/32.5 mol% cholesterol sample was in the l_o phase. Measurements of specific heat capacity are sensitive to phase transitions. In particular the pre- and main transitions of lipid membranes are easily detected and have distinct signals [1]. Thermograms were collected using a Shimadzu DSC-60 and a TA-60WS Thermal Analyzer. The calorimeter was calibrated using octadecane, which has a melting temperature of 27.95°C. An indium (In) standard was used in the heater power calibration, with a transition enthalpy of 28.6 J/g. Data were collected at a scan rate of 5°C/min and a sampling time of 1 second.

DPPC and cholesterol (at a concentration of 32.5 mol%) were co-dissolved in organic solvent and the solvent was removed by a gentle stream of N_2 followed by several hours under vacuum. The mixture was hydrated with ultra pure water to a DPPC concentration of 0.166 mg/μL. It was then put through 5 freeze/thaw cycles. An aluminum hermetically sealed pan was loaded with 30 μL of the lipid/cholesterol solution. The same procedure was followed for a pure DPPC sample. Background was determined by a scan containing only 30 μL of ultra pure water.

Heat capacity data are shown in Figure S1. A pure DPPC membrane was measured as a reference and shows signals consistent with the pre- and main transitions of DPPC bilayers, in excellent agreement with literature values: The main transition temperature, T_m, of DPPC was determined to be T = 314.4 K [2, 3]; the temperature of the pre-transition ($L_{\beta'}$ to the $P_{\beta'}$) was determined to be 303.1 K [3]. The absence of a transition in DPPC bilayers with 32.5 mol% cholesterol is indicative that the cholesterol concentration of 32.5 mol% is high enough to induce l_o phase.

As marked in the schematic phase diagram shown in Figure 2 of the main paper, phase separation has been speculated at cholesterol concentrations of ∼40 mol% and above.

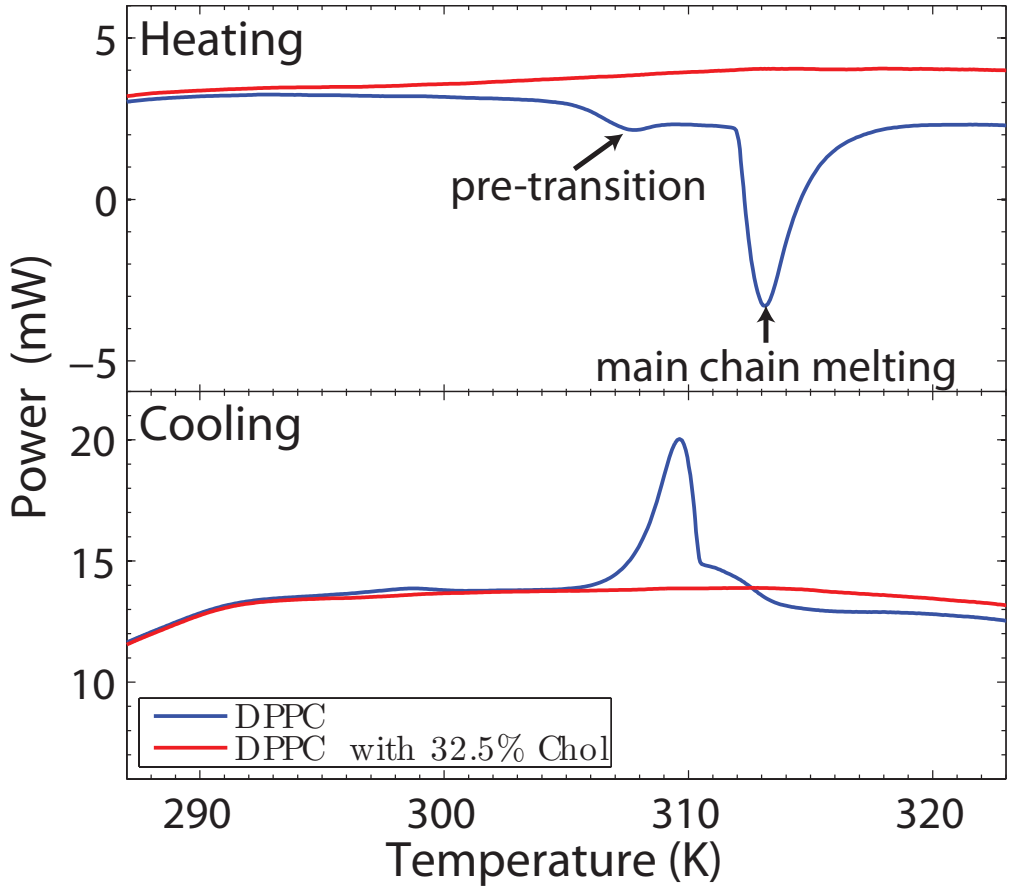

FIG. S1. Specific heat capacity data measured upon heating and cooling. A pure DPPC bilayer scan is included for comparison. While the DPPC sample (blue) shows signals corresponding to the pre- and main transition observed in a variety of lipids, no transition was observed in DPPC bilayers containing 32.5 mol% cholesterol (red).

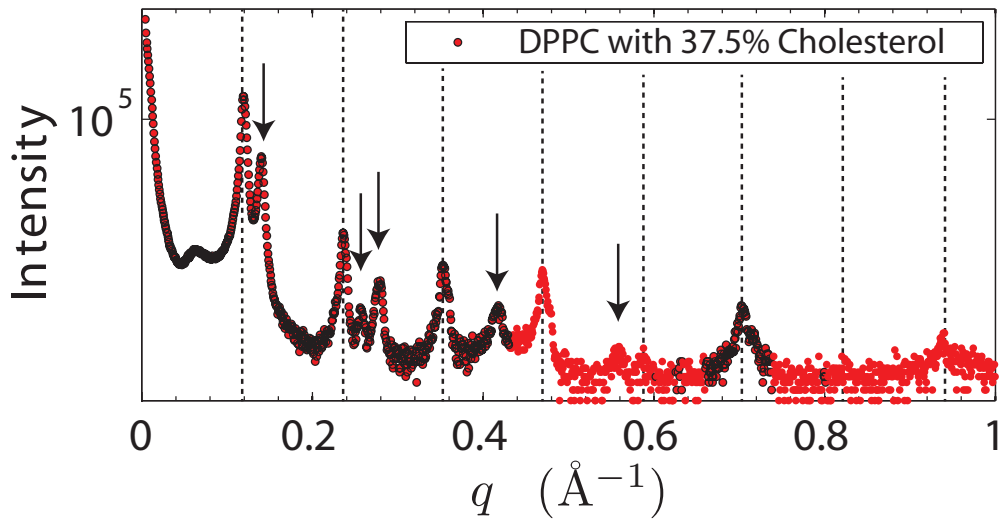

FIG. S2. X-ray reflectivity for DPPC with 37.5 mol% cholesterol. Peaks due to the lamellar structure are marked by vertical lines. Additional peaks are observed and marked by arrows, an indication of a phase separated structure.

X-ray reflectivity is an excellent probe for determining resultant structures. X-ray scattering data was obtained using the Biological Large Angle Diffraction Experiment (BLADE) in the Laboratory for Membrane and Protein Dynamics at McMaster University. BLADE uses a 9 kW (45 kV, 200 mA) CuKα rotating anode at a wavelength of 1.5418 Å. Both source and detector are mounted on movable arms, such that the membranes remain horizontal during the measurements. Focusing multi-layer optics yield a high intensity parallel beam with monochromatic X-ray intensities up to 10^{10} counts/(mm$^2\times$s). This beam geometry provides optimal illumination of the solid supported membrane samples, thus maximizing the scattering signal. A reflectivity scan of the 32.5 mol% sample used in this study was taken at 20°C and 50% relative humidity. A number of pronounced Bragg peaks due to the lamellar membrane structure were observed, indicative of a well organized and uniform lamellar morphology.

A sample with a higher cholesterol concentration (37.5 mol%) was prepared for comparison. The X-ray reflectivity curve from this sample is shown in Figure S2. Additional peaks are observed at this cholesterol concentration, which are indicative of co-existing, phase separated structures, as was previously discussed [4]. Taking into account this data, it is safe to

assume that the 32.5 mol% cholesterol sample is in the l_o phase, as indicated on the phase diagram (Figure 2).

The quality and structure of the 32.5 mol% cholesterol sample was also checked using out-of-plane neutron reflectivity scans. Reflectivity was measured on N5 in-situ using the same setup as for the in-plane measurements. This was accomplished by simply rotating the sample by 90°. Figure S3 a) shows reflectivity scans measured before and after sample

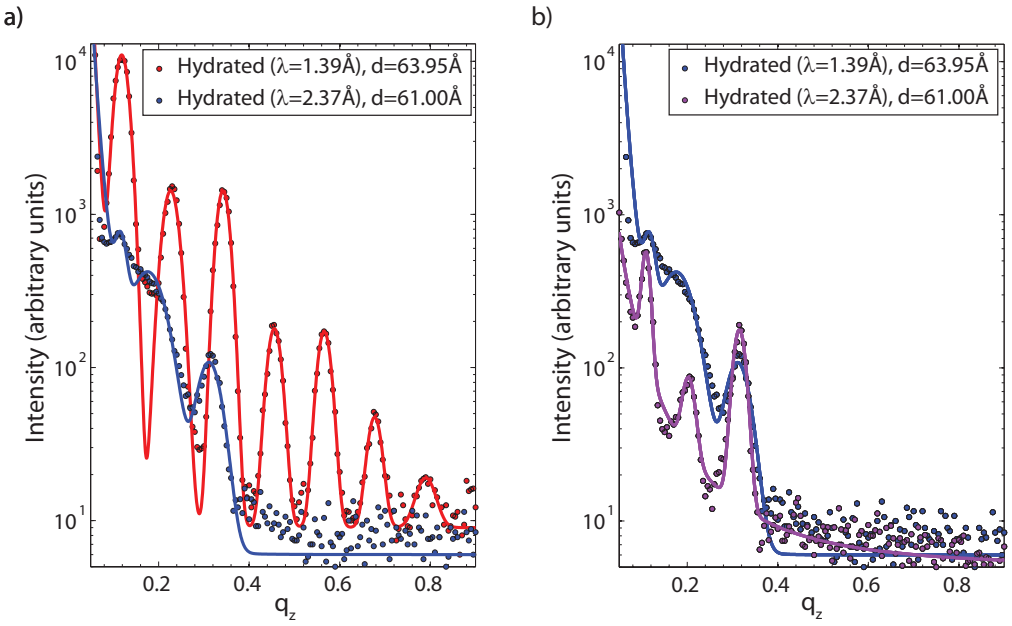

FIG. S3. Out-of-plane neutron reflectivity data measured in parallel to the in-plane data. a) A dry and a hydrated DPPC sample with 32.5 mol% cholesterol. b) Reflectivity data from the hydrated sample measured using the high and low resolution setup.

hydration. Data were collected at a temperature of 50°C. Seven orders of lamellar Bragg peaks are observed for bilayers in the dry state, and a d_z-spacing of d_z=56.1 Å can be determined from the symmetric and equally spaced reflections. After hydration, the higher order reflections were found to be strongly suppressed, indicative of the onset of strong bilayer fluctuations induced by the water. A d_z-spacing of d_z=64.0 Å was determined.

Figure S3 b) depicts neutron reflectivity scans measured using the two different setups (① and ②) used for the in-plane investigations. While the Bragg peaks can be well resolved using the high resolution setup, peaks appear significantly broader when using the low

Chapter 6

Future Outlooks and Concluding Remarks

6.1 Lipid Diffusion in Membranes

Building upon the work presented in this thesis regarding lateral lipid diffusion in the bilayer, there are two specific lateral $q_{||}$ ranges that warrant further examination: (1) the high $q_{||}$ transition region between continuous and ballistic flow-like motion ($q_{||}$=2 - 3 Å^{-1}); and (2) the low $q_{||}$ ($q_{||} < 0.3$ Å^{-1}) values corresponding to long length scales, greater than ∼60 Å.

In more carefully examining the high $q_{||}$ transition region with increased statistics, it should be possible to determine whether the change in the character of motion is abrupt, as it appears in the IN13 data presented in Paper II, or if there is, more likely, a gradual transition from continuous to flow-like motion. The development of a more complete short-range diffusion model could include the characterization of how this transition occurs, in addition to the theory suggesting the existence of sub-diffusive regime thought to be present at these length scales, based on observations from MD simulations [62].

The motion at low $q_{||}$, corresponding to long length scales, is an important region to re-examine in order to resolve discontinuities between diffusion coefficients measured using neutron scattering and macroscopic experimental techniques. A preliminary experiment to probe long-range lipid diffusion was presented in Paper III; however,

this served primarily as a feasibility test. The initial data obtained in that experiment, along with the insight gained regarding strengths and limitations of incoherent NSE, will aid in the design and execution of future experiments using this technique to elucidate the lipid diffusion processes over mesoscopic length scales. The experimental gap between neutron scattering and fluorescence microscopy will not be completely eliminated with the use of NSE, but it will be reduced.

6.2 Lipid/Cholesterol Domains

The next step in the study of lipid bilayers containing cholesterol is to probe how the structure of the system is effected by cholesterol concentration. Paper IV presented energy dispersion curves obtained from low and high cholesterol samples, both of which showed evidence for a l_o phase. The observation of highly ordered structures in a low cholesterol sample would further strengthen the notion of non-uniform cholesterol distribution in the bilayer, but also may bring to light whether or not there is a critical cholesterol concentration required for the formation of l_o lipid domains.

A sample has already been prepared, composed of chain deuterated DPPC and 5 mol% cholesterol, ready for the next available beam time on the N5 spectrometer in Chalk River. In addition to this, another high cholesterol sample has been constructed made of protonated DPPC and tail-end deuterated cholesterol. The experiment presented in Paper VI shows data which corresponds to the ordering of the lipid tails and, from this, the location of the cholesterol is inferred. A sample with deuterated cholesterol could allow for the direct observation of the cholesterol structure. However, because the cholesterol molecule is only "tail-end" deuterated, it is unclear as to whether the coherent signal will be detectable, especially when considering the increased incoherent background as a result of a protonated lipid bilayer.

6.3 LE/HSR Triple-Axis Spectrometry

The development of the LE/HSR technique opens the door to a variety of possibilities for measuring small ordered structures in biological systems. Before pursuing the measurement of complex biological samples, it is important to fully characterize how

the coherence length of the neutron probe relates to the size of the observable structures in the system. This will allow for a quantifiable measurement of the domain size, in addition to its structure.

6.4 Conclusions

The experimental work presented in this thesis involves the measurement of structure and dynamics in model biological systems with the use of various neutron scattering techniques.

State of the art neutron backscattering spectrometry allowed for the measurement of lateral lipid diffusion in single supported lipid bilayers. This experiment not only demonstrated that the lipid diffusion coefficient in this system is similar to that measured in stacked bilayer systems, but also that an appreciable neutron scattering signal could be obtained from as little as $\sim$1 mg of sample material.

The characteristic of short-range lipid motion was probed in a diffusion experiment extending to higher than typically measured $q_{||}$-values. In this work, the continuous diffusion process over nanometer length scales was confirmed by the observation of a Lorentzian quasi-elastic energy broadening with a $q_{||}^2$ dependence. At lengths scales below $\sim$1/3 the lipid nearest-neighbour distance there was a distinct change in the character of motion. The short-range lipid motion exhibited a flow-like quality rather than continuous diffusion, or a rattling-in-the-cage motion.

Extending the diffusion window in the opposite direction, long-range lipid motion was examined with the use of incoherent NSE spectrometry. This study demonstrated the low $q_{||}$-range over which an incoherent signal could be obtained using an oriented, fully protonated lipid sample. Preliminary data was collected, which showed evidence for two diffusive processes over mesoscopic length scales: a slow processes thought to be related to the diffusion of loosely bound, coherent clusters of lipids, and a fast process corresponding to individual lipid diffusion.

Evidence supporting the existence of highly ordered domains in cholesterol containing lipid bilayers was observed in both the structure and dynamics of these systems. Three distinct energy dispersion curves, corresponding to the fluid phase, gel phase, and what is believed to be a liquid ordered phase, were observed in both the

low (5 mol%) and high (40 mol%) cholesterol samples. This strongly suggests that there is not only a coexistence of fluid and gel phases in the system, but that the cholesterol is non-uniformly distributed throughout the bilayer.

The coexistence of fluid and gel domains in a single-component lipid bilayer system was confirmed by an experiment designed to have increased spatial resolution, such that it would be sensitive to small, transient structures. This technique was then implemented to detect the presence of highly ordered domains induced by the presence of cholesterol in a lipid bilayer system. The result of this experiment emphasized how the quality of the probe influences the measurement of a system. Using the standard high-energy resolution setup, data was obtained suggesting that the lipid/cholesterol system was in a uniform fluid disordered state. However, by solely changing to a low-energy/high-spatial resolution setup, highly ordered lipid domains could be resolved, in addition to the fluid background. This technique offers a viable method for probing small ordered domains in systems that do not possess long-range order, a scenario often encountered in the field of biophysics.

Appendix A

ΔE to τ Conversion

The relationship between energy broadening (ΔE) and relaxation time (τ) can be obtained by simply Fourier transforming the self intermediate scattering function (ISF). Some useful equations to be aware of are the definition of a Lorentzian function:

$$L(x) = \frac{1}{\pi}\left(\frac{\gamma}{\gamma^2 + (x - x_o)^2}\right), \tag{A.1}$$

where the HWHM is γ and the function is centered about x_o; and the following integral of a single exponential function:

$$\int_0^\infty x^n e^{-\frac{x}{a}} dx = n! a^{n+1}. \tag{A.2}$$

Begin with a single exponential self ISF, with a relaxation time of τ,

$$I(q,t) = e^{-t/\tau}. \tag{A.3}$$

Fourier transform this function to obtain the incoherent scattering function:

$$S(q,\omega) = \frac{1}{2\pi\hbar}\int I(q,t)\ \exp(-i\omega t)\ dt \tag{A.4}$$

$$= \frac{1}{2\pi\hbar}\int_{\infty}^{\infty} e^{-t/\tau}\ e^{-i\omega t}\ dt \tag{A.5}$$

$$= \frac{1}{2\pi\hbar}\int_{\infty}^{\infty} e^{-\left(\frac{1}{\tau}+i\omega\right)t}\ dt \tag{A.6}$$

$$= \frac{1}{2\pi\hbar}\left(\int_{0}^{\infty} e^{-\left(\frac{1}{\tau}+i\omega\right)t}\ dt + \int_{0}^{\infty} e^{-\left(\frac{1}{\tau}-i\omega\right)t}\ dt\right) \tag{A.7}$$

$$= \frac{1}{2\pi\hbar}\left(\frac{\tau}{1+i\omega\tau} + \frac{\tau}{1-i\omega\tau}\right) \tag{A.8}$$

$$= \frac{1}{2\pi\hbar}\left(\frac{\tau(1-i\omega\tau)+\tau(1+i\omega\tau)}{(1+i\omega\tau)(1-i\omega\tau)}\right) \tag{A.9}$$

$$= \frac{1}{2\pi\hbar}\left(\frac{2\tau}{1-\omega^2\tau^2}\right) \tag{A.10}$$

$$= \frac{1}{\pi\hbar}\left(\frac{\frac{1}{\tau}}{\left(\frac{1}{\tau}\right)^2+\omega^2}\right)\times\frac{\hbar^2}{\hbar^2} \tag{A.11}$$

$$= \frac{1}{\pi}\left(\frac{\frac{\hbar}{\tau}}{\left(\frac{\hbar}{\tau}\right)^2+(\hbar\omega)^2}\right). \tag{A.12}$$

Equation A.12 is a Lorentzian function with a HWHM of $\frac{\hbar}{\tau}$. Therefore the FWHM energy broadening of the scattering function is:

$$\Delta E_{FWHM} = \frac{2\hbar}{\tau}. \tag{A.13}$$

To convert this expression into units of μeV and ns for the energy broadening and relaxation time, respectively, the above expression can be written as:

$$\Delta E_{FWHM} = \frac{2\hbar}{\tau}\cdot\frac{10^{15}}{e} = \frac{2}{1.52\tau}. \tag{A.14}$$

Appendix B

Mol% Calculation for Sample Preparation

B.1 Two Component System

Nomenclature

$n_T \equiv$ total number of moles in system

$n_1 \equiv$ number of moles of component 1

$n_2 \equiv$ number of moles of component 2

$m_T \equiv$ total mass in system

$m_1 \equiv$ mass of component 1

$m_2 \equiv$ mass of component 2

$M_1 \equiv$ molar mass of component 1

$M_2 \equiv$ molar mass of component 2

$x_1 \equiv$ mol% of component 1

$x_2 \equiv$ mol% of component 2

Relations

$$1 = x_1 + x_2$$

$$n_T = n_1 + n_2, \qquad m_T = m_1 + m_2$$

$$n_1 = \frac{m_1}{M_1}, \qquad n_2 = \frac{m_2}{M_2}$$

Calculate $\mathbf{m_1}$ for specified mol% = $\mathbf{x_1}$

$$n_1 = n_T x_1$$

$$\frac{m_1}{M_1} = \left(\frac{m_1}{M_1} + \frac{m_2}{M_2}\right) x_1$$

$$\frac{m_1}{M_1} = \left(\frac{m_1}{M_1} + \left[\frac{m_T - m_1}{M_2}\right]\right) x_1$$

$$\frac{m_1}{M_1} = m_1 \left(\frac{M_2 - M_1}{M_1 M_2}\right) x_1 + \frac{m_T}{M_2} x_1$$

$$m_1 \left[\frac{1}{M_1} - \left(\frac{M_2 - M_1}{M_1 M_2}\right) x_1\right] = \frac{m_T}{M_2} x_1$$

$$m_1 \left(\frac{M_2 - M_2 x_1 + M_1 x_1}{M_1 M_2}\right) = \frac{m_T}{M_2} x_1$$

$$\boxed{m_1 = \frac{m_T x_1}{M_2} \left(\frac{M_1 M_2}{M_2 - M_2 x_1 + M_1 x_1}\right)}$$

Bibliography

[1] M.D. Kaye, K. Schmalzl, V.C. Nibali, M. Tarek, and M.C. Rheinstädter. Ethanol enhances collective dynamics of lipid membranes. *Phys. Rev. E*, 83:050907, 2011.

[2] T. Elston, H. Wang, and G. Oster. Energy transduction in atp synthase. *Nature*, 391:510–513, 1998.

[3] S.J. Singer and G.L. Nicolson. The fluid mosaic model of the structure of cell membranes. *Science*, 175:720–731, 1972.

[4] K. Simons and E. Ikonen. Functional rafts in cell membranes. *Nature*, 387:569–572, 1997.

[5] K. Simons and E. Ikonen. How cells handle cholesterol. *Science*, 290:1721–1726, 2000.

[6] D.M. Engelman. Membranes are more mosaic than fluid. *Nature*, 438:578–580, 2005.

[7] P.S. Niemelä, S. Ollila, M.T. Hyvönen, M. Karttunen, and I. Vattulainen. Assessing the nature of lipid raft membranes. *PLoS Comput. Biol.*, 3:e34, 2007.

[8] L.J. Pike. The challenge of lipid rafts. *J. Lipid Res.*, 50:S323, 2009.

[9] D. Lingwood and K. Simons. Lipid rafts as a membrane organizing principle. *Science*, 327:46–50, 2009.

[10] C. Eggeling, C. Ringemann, R. Medda, G. Schwarzmann, K. Sandhoff, S. Polyakova, V.N. Belov, B. Hein, C. von Middendorf, A. Schönle, and S.W. Hell. Direct observation of the nanoscale dynamics of membrane lipids in a living cell. *Nature*, 457:1159–1162, 2009.

[11] P.-F. Lenne and A. Nicolas. Physics puzzles on membrane domains posed by cell biology. *Soft Matter*, 5:2841–2848, 2009.

[12] T. Apajalahti, P. Niemelä, P.N. Govindan, M.S. Miettinen, E. Salonen, S.-J. Marrink, and I. Vattulainen. Concerted diffusion of lipids in raft-like membranes. *Faraday Discuss.*, 144:411–430, 2010.

[13] E.B. Watkins, C.E. Millerb, J. Majewski, and T.L. Kuhl. Membrane texture induced by specific protein binding and receptor clustering: active roles for lipids in cellular function. *Proc. Natl. Acad. Sci. USA*, 108:6975–6980, 2011.

[14] M. Ruiz. Cell membrane detailed diagram (digital image). Wikimedia Commons, Jan. 2007.

[15] N.A. Campbell and J.B Reece. *Biology, 8th ed.* Benjamin Cummings, San Francisco, 2008.

[16] R. Phillips, T. Ursell, P. Wiggins, and P. Sens. Emerging roles for lipids in shaping membrane-protein function. *Nature*, 459:379–385, 2009.

[17] C.L. Armstrong, E. Sandqvist, and M.C. Rheinstädter. Protein-protein interactions in membranes. *Protein and Peptide Lett.*, 18:344–353, 2011.

[18] E. Fahy, S. Subramaniam, H.A. Brown, C.K. Glass, A.H. Merrill Jr., R.C. Murphy, C.R.H. Raetz, D.W. Russell, Y. Seyama, W. Shaw, T. Shimizu, F. Spener, G. van Meer, M.S. VanNieuwenhze, S.H. White, J.L. Witztum, and E.A. Dennis. A comprehensive classification system for lipids. *J. Lipid Res.*, 46:839–861, 2005.

[19] G. Pabst, N. Kučerka, M.-P. Nieh, M.C. Rheinstädter, and J. Katsaras. Applications of neutron and x-ray scattering to the study of biologically relevant model membranes. *Chem. Phys. Lipids*, 163:460–479, 2010.

[20] G.S. Smith, E.B. Sirota, C.R. Safinya, R.J. Plano, and N.A. Clark. Xray structural studies of freely suspended ordered hydrated dmpc multimembrane films. *J. Chem. Phys.*, 92:4519–4529, 1990.

[21] W.J. Sun, R.M. Suter, M.A. Knewtson, C.R. Worthington, S. Tristram-Nagle, R. Zhang, and J.F. Nagle. Order and disorder in fully hydrated unoriented bilayers of gel phase dppc. *Phys. Rev. E*, 49:4665–4676, 1994.

[22] J. Katsaras and V.A. Raghunathan. *Aligned Lipid-Water Systems*, pages 25–45. Lipid Bilayers: Sturcute and Interactions. Springer, Heidelberg, 2000.

[23] N. Kučerka, Y. Liu, N. Chu, H.I. Petrache, S. Tristram-Nagle, and J.F. Nagle. Structure of fully hydrated fluid phase DMPC and DLPC lipid bilayers using x-ray scattering from oriented multilamellar arrays and from unilamellar vesicles. *Biophys. J.*, 88:2626–2637, 2005.

[24] S. Tristram-Nagle, Y. Liu, J. Legleiter, and J.F. Nagle. Structure of gel phase dmpc determined by x-ray diffraction. *Biophys. J.*, 83:3324–3335, 2002.

[25] J.F. Nagle, R. Zhang, S. Tristram-Nagle, W. Sun, H.I. Petrache, and R.M. Suter. X-ray structure determination of fully hydrated Lα phase dipalmitoylphosphatidylcholine bilayers. *Biophys. J.*, 70:1419–1431, 1996.

[26] M. Weik, U. Lehnert, and G. Zaccai. Liquid-like water confined in stacks of biological membranes at 200 K and its relation to protein dynamics. *Biophys. J.*, 89:3639–3646, 2005.

[27] M.C. Rheinstädter, T. Seydel, F. Demmel, and T. Salditt. Molecular motions in lipid bilayers studied by the neutron backscattering technique. *Phys. Rev. E*, 71:061908, 2005.

[28] S. Mabrey and J.M. Sturtevant. Investigation of phase transitions of lipids and lipid mixtures by high sensitivity differential scanning calorimetry. *Proc. Natl. Acad. Sci. USA*, 73:3862–3866, 1976.

[29] J. Katsaras and K. R. Jeffrey. Evidence of the hydration force in gel phase lipid multibilayers. *Europhys. Lett.*, 38:43–48, 1997.

[30] J. Huang and G.W. Feigenson. A microscopic interaction model of maximum solubility of cholesterol in lipid bilayers. *Biophys. J.*, 76:2142–2157, 1999.

[31] J. Dai, M. Alwarawrah, and J. Huang. Instability of cholesterol clusters in lipid bilayers and the cholesterol's umbrella effect. *J. Phys. Chem. B*, 114:840–848, 2010.

[32] C.L. Armstrong, M.A. Barrett, A. Hiess, T. Salditt, J. Katsaras, A.-C. Shi, and M.C. Rheinstädter. Effect of cholesterol on the lateral nanoscale dynamics of fluid membranes. *Eur. Biophys. J.*, 41:901–913, 2012.

[33] E. Falck, M. Patra, M. Karttunen, M.T. Hyvönen, and I. Vattulainen. Lessons of slicing membranes: Interplay of packing, free area, and lateral diffusion in phospholipid/cholesterol bilayers. *Biophys. J.*, 87:1076–1091, 2004.

[34] J. Pan, T.T. Mills, S. Tristram-Nagle, and J.F. Nagle. Cholesterol perturbs lipid bilayers nonuniversally. *Phys. Rev. Lett.*, 100:198103, 2008.

[35] T.T. Mills, J. Huang, G.W. Feigenson, and J.F. Nagle. Effects of cholesterol and unsaturated dopc lipid on chain packing of saturated gel-phase dppc bilayers. *Gen. Physiol. Biophys.*, 28:126–139, 2009.

[36] A.-J. Dianoux and G. Lander, editors. *Neutron Data Booklet*. Old City Publishing Group, Philadelphia, 2nd edition, 2003.

[37] M.C. Rheinstädter. Dynamics in soft-matter and biology studied by coherent scattering probes. *arXiv:0905.1636v2 [physics.bio-ph]*, 2009.

[38] J.K. Dhont, G. Gompper, and D. Richter, editors. *Soft Matter: Complex Materials on Mesoscopic Scales*. Forschungszentrum Jülich GmbH, Jülich, Germany, 2002.

[39] V.F. Sears. Neutron scattering lengths and cross sections. *Neutron News*, 3:26–37, 1992.

[40] E.T. Castellana and P.S. Cremer. Solid supported lipid bilayers: From biophysical studies to sensor design. *Surf. Sci. Rep.*, 61:429–444, 2006.

[41] E. Sackmann. Supported membranes: Scientific and practical applications. *Science*, 271:43–48, 1996.

[42] M. Tanaka and E. Sackmann. Polymer-supported membranes as models of the cell surface. *Nature*, 437:656–663, 2005.

[43] C. Hamai, T. Yang, S. Kataoka, P.S. Cremer, and S.M. Musser. Effect of average phospholipid curvature on supported bilayer formation on glass by vesicle fusion. *Biophys. J.*, 90:1241–1248, 2006.

[44] G. Shirane, S.M. Shapiro, and J.M. Tranquada. *Neutron Scattering with a Triple-Axis Spectrometer*. Cambridge Univeristy Press, New York, 2002.

[45] T. Salditt and M.C. Rheinstädter. *Structure and Dynamics of Model Membrane Systems Probed by Elastic and Inelastic Neutron Scattering*, pages 503–530. Neutron Scattering in Biology, Techniques and Applications. Springer, Heidelberg, 2006.

[46] E. Mamontov and K.W Herwig. A time-of-flight backscattering spectrometer at the spallation neutron source, BASIS. *Rev. Sci. Instrum.*, 82:085109, 2011.

[47] F. Mezei, editor. *Neutron Spin Echo*. Springer, Berlin, 1980.

[48] D. Richter, M. Monkenbusch, A. Arbe, and J. Colmenero. *Neutron Spin Echo in Polymer Systems*. Springer, Heidelberg, 2005.

[49] M.C. Rheinstädter. *Lipid Membrane Dynamics*, pages 263–286. Dynamics of Soft Matter: Neutron Applications. Springer, New York, 2012.

[50] P. Lagüe, M.J. Zuckermann, and B. Roux. Lipid-mediated interactions between intrinsic membrane proteins: dependence on protein size and lipid composition. *Biophys. J.*, 81:276–284, 2001.

[51] N. Kahya, D. Scherfel, K. Bacia, B Poolman, and P. Schwille. Probing lipid mobility of raft-exhibiting model membranes by fluorescence correlation spectroscopy. *J. Biol. Chem.*, 278:28109, 2003.

[52] R. Macháň and M. Hof. Lipid diffusion in planar membranes investigated by fluorescence correlation spectroscopy. *Biochim. Biophys. Acta.*, 1798:1377–1391, 2010.

[53] S. König, W. Pfeiffer, T. Bayerl, D. Richter, and E. Sackmann. Molecular dynamics of lipid bilayers studied by incoherent quasi-elastic neutron scattering. *J. Phys. II France*, 2:1589–1615, 1992.

[54] M.C. Rheinstädter, J. Das, E.J. Flenner, B. Brüning, T. Seydel, and I. Kosztin. Motional coherence in fluid phospholipid membranes. *Phys. Rev. Lett.*, 101:248106, 2008.

[55] S. Busch, C. Smuda, L.C. Pardo, and T. Unruh. Molecular mechanism of long-range diffusion in phospholipid membranes studied by quasielastic neutron scattering. *J. Am. Chem. Soc.*, 132:3232–3233, 2010.

[56] D.M. Owen, D.J. Williamson, A. Magenau, and K. Gaus. Sub-resolution domains exist in the plasma membrane and regulate protein diffusion and distribution. *Nat. Commun.*, 3:1256, 2012.

[57] K. Simons and M.J. Gerl. Revitalizing membrane rafts: new tools and insights. *Nat. Rev. Mol. Cell Biol.*, 11:688–699, 2010.

[58] S.W. Hell and J. Wichmann. Breaking the diffraction resolution limit by stimulated emission: stimulated-emission-depletion fluorescence microscopy. *Opt. Lett.*, 19:780–782, 1994.

[59] E. Drolle, R.M. Gaikwad, and Z. Leonenko. Nanoscale electrostatic domains in cholesterol-laden lipid membranes create a target for amyloid binding. *Biophys. J.*, 103:L27–L29, 2012.

[60] G.L. Squires. *Introduction to the theory of thermal neutron scattering.* Dover Publications, Inc., Mineola, New York, 1978.

[61] H. Rauch. Reality in neutron interference experiments. *Foundation of Physics*, 23:7–36, 1993.

[62] E. Flenner, J. Das, M.C. Rheinstädter, and I. Kosztin. Sub-diffusion and lateral diffusion coefficient of lipid atoms and molecules in phospholipid bilayers. *Phys. Rev. E*, 79:011907, 2009.